Final Report

Electrochemical Processes for In-situ Treatment of Contaminated Soils

Submitted to
Department of Energy

by:

C.P. Huang (Principal Investigator)
Daniel Cha (Co-Investigator)
Jih-Hsing Chang (Graduate Research Assistant)
Zhimin Qiang (Graduate Research Assistant)

University of Delaware, Newark, DE
May 2001

Part I

Removal of Selected Hazardous Organic Compounds from Soils by Electrokinetic Process

TABLE OF CONTENTS

ABSTRACT

Contamination of soils by toxic organic pollutants is an environmental concern. The in-situ electrokinetic (EK) technology is an emerging process to remediate the contaminated soils. Since the electro-osmotic (EO) flow rate and sorption behaviors of pollutants are two critical factors of the process, this study focuses on understanding the partition of nonionic organic contaminants in soil-water system, mechanisms of the EO flow, and the transport of organic compounds under an externally applied electrostatic field. The target compounds include chlorinated organic compounds and polycyclic aromatic hydrocarbons (PAHs). In order to improve the treatment efficiency, surfactant and bio-surfactant were used. A thermodynamic concept, fugacity, was introduced to illustrate the interactions between organics and the soil. A semi-empirical equation was derived to describe the EO flow rate in unsaturated soils. Moverover, the diffusion-advection-sorption model was used to simulate the transport of nonionic organic contaminants in the presence of an electrostatic field.

The sorption experiments were conducted with various initial solute concentrations and different soil to solution ratios. The selected chlorinated organics include tetrachloroethylene (PCE), trichloroethylene (TCE), carbon tetrachloride, and chloroform. Results show that Langnuir isotherm can be used to express the distribution behavior of these chlorinated organic compounds in the soil-water system. In addition to the hydrophobicity (K_{ow}), the concentration of organic compound and soil to solution ratio can influence the distribution behavior also. In order to illustrate the effects of the organic concentration and soil to solution ratio, the activity coefficient was used. The activity coefficient, γ, a relative interaction based on chosen reference state, is a useful means to express the quantitative feature of the organic-soil interaction without detailed information of their interaction mechanisms. By comparing the activity coefficients, γ_w and γ_s (i.e., X_s/X_w), one can illustrate the trend of organic distribution at the soil-water interfaces.

The concentration effect can be explained by the changes in the adsorption of organic onto the soil surface. Based on the experimental results, when increasing the organic compound concentrations, the activity coefficient, γ_w, can be considered as a constant and γ_s increases due to the increase of interaction energy. The change of γ_s makes the sorption isotherms of PCE, TCE, carbon tetrachloride, and chloroform non-linear. According to γ_s, it can be seen that the sorption between these selceted chlorinated organics and the soil is exothermic.

The effect of soil to solution ratio can be attributed to the presence of dissolved organic matter (DOM) in the liquid phase. DOM enhances the organic dissolution, which in turns increases the organic concentration, i.e., X_w. Therefore, the partition coefficients of these chlorinated compounds, i.e., X_s/X_w, decrease with increasing the soil to solution ratio, i.e., high soil concentration. It is found that the activity coefficients between organic chemicals and water, $\ln(\gamma_w)$, exhibits a linear relationship with respect to the TOC concentration, that is, $\ln\gamma_w = m - n[TOC]$. In the absence of TOC, m is the $\ln\gamma_w$ value and n is an interaction coefficient. Based on the experimental results, the n values of PCE, TCE, carbon tetrachloride, and chloroform are ca. 0.15, 0.04, 0.03, and 0.08, respcetively.

For the PAHs desorption experiments, it was to explore the solubilization of PAHs in the presence of surfactants, sorption of surfactants onto soils, and PAHs distribution in a surfactant-soil-water system. The target PAH compounds studied include fluorene,

phenanthrene, anthracene, fluoranthene, and pyrene. The surfactants include an synthetic surfactant (Triton X-100) and a biosurfactant, i.e., rhamnolipid.

The partition can be considered as the main driving force for the distribution of PAHs in the micelle-water system. The partition coefficient between micelle and water phase (K_m) can be related to the partition coefficient of PAHs in octanol-water phase (K_{ow}). Accordingly, $K_m = \beta K_{ow}$ where β, a constant, can be obtained experimentally. The β values for Triton X-100 and rhamnolipid are 0.4 and 0.44, respectively. In addition, an empirical equation for estimating β can be established based on the number of "hydrophobic" carbons, y_1, and the number of "hydrophilic" groups, y_2. The empirical equaiton can predict β values of both Triton X-100 and rhamnolipid systems, $\beta = (0.031y_1 - 0.0058y_2)$.

Both surfactants exhibit strong attraction to the soil phase. The Triton X-100 sorption on the soil can be described by the Langmuir isotherm and can be attributed to a partition process. However, the sorption of rhamnolipid is a linear isotherm and can be attributed to an interfacial interaction. It is seen that the sorption density of both surfactants decreases with increasing PAHs contamination in the soil. This is because the sorption competition between the PAHs and the surfactant onto the soil.

The apparent partition coefficient of PAHs, $K_{d,cmc}$, can be expressed as, $K_{d,cmc} = \frac{\alpha K_{ow} f_{oc}^*}{(1+\beta K_{ow}[S])}$. In this equation, both α and β are constants, K_{ow} is the octanol number of PAHs, f_{oc}^* represents the total soil organic carbon, and [S] is the micelle concentration in the solution. Based on experimental results, the $K_{d,cmc}$ in Triton X-100 system can be related to the reciprocal concentration of surfactant, i.e., $K_{d,cmc} = K/[S]$, in the concentration range of surfactant 10 to 20 CMC, where CMC stands for the critical micelle concentration. However, the $K_{d,cmc}$ of the rhamnolipid system is a constant.

In EO experiments, various factors, including solution pH, electric field strength, soil water content, and electrolyte concentration were studied. Results indicate that the EO flow rate, Q, is proportional to the electrokinetic charge density, σ_e, and the electric field strength, E_0/L. Inert-electrolyte has no significant effect on the EO flow rate. A parabolic relationship between the EO flow rate and the water content, ω, was observed. Based on the finite plate model, the EO flow rate, can be expressed as a function of electrokinetic charge density, field strength, and soil water content, i.e $Q = K\sigma_e(E_0/L)\omega^2$. The characteristic coefficient, K, is a collection of several physical properties of the soil-water system including the fluid density, ρ, the specific surface area, Σ, width of the water layer, w, and the fluid viscosity, η, i.e., $K = (kfw)/(\eta\rho^2\Sigma^2)$. A K value of 57 $cm^3 \cdot \mu C^{-1} \cdot V^{-1}$ was observed.

EK experiments were conducted to study the in-situ removal of organic contaminants in unsaturated soils. In this study, chlorinated organic contaminats and PAHs contaminated soils were treated with water and surfactant solution respectively using the EK process. A diffusrion-advection-sorption model was used to simulate the transport of organic contaminats during the EK treatment. Results indicate that PCE, TCE, chloroform, and carbon tetrachloride can be removed effectively from the soil mass with a removal efficiency ranging from 85% to 98% in two weeks. The release of PCE, TCE, chloroform, and carbon tetrachloride from unsaturated soils follows a first-order rate expression. The rate constants are 0.61, 0.70, 1.15, and 1.03 day^{-1}, respectively, for PCE, TCE, chloroform, and carbon tetrachloride. For phenanthrene, the removal efficiency can reach to 30% with the surfactnant

addition versus 1% in the absence of surfactant after two-months. In general, the mobility of these chlorinated organic compounds in soils increases with increasing water solubility.

A diffusion-advection-sorption model based on linear sorption isotherm at equilibrium is able to simulate the movement of chlorinated organic contaminants in the unsaturated soil. According to this model, the partition coefficient is the major factor controlling the organic transport. Based on the model simulation, the fitted partition coefficient in the EK system is greater than that in over-saturated soil-water system. This can be attributed to the effect of soil to solution ratio on the organic sorption behavior. In addition, the fitted partition coefficients increase with increasing operation time due to the concentration effect.

In contrast, the diffusion-advection-sorption model based on the linear sorption isotherm at non-equilibrium condition is able to simulate the movement of phenanthrene during the EK treatment in the presence of Triton X-100. A desorption rate constant of 10^{-3} hr^{-1} was obtained. However, the d-a-s model does not predict well the distribution of phenanthrene in the presence of rhamnolipid. The presence of rhamnolipid apparently promotes microbial growth in the soil-water system which may bring about biodegradation of phenanthrene. As a result, the desorption behavior of phenanthrene is non-equilibrium.

1. INTRODUCTION

1.1. Significance of the Research

Throughout United States and the world, many organic chemicals such as solvents and petroleum derivatives were disposed improperly. Among these hazardous chemicals, chlorinated organics commonly used as industrial solvents are the major sources for soil contamination. The EPA, in a survey of 466 public water supply wells, found that one or more volatile organic compounds (VOCs) were detected. The VOCs found most often in this survey were trichloroethylene and perchloroethylene (Westrick etc., 1983). In a survey of 7000 wells conducted in California from 1984 through 1988 (Mackay and Smith, 1990), the most common chemicals detected were perchloroethylene, trichloroethylene, chloroform, 1,1,1-trichloroethane, and carbon tetrachloride. Additionally, according to survey results of potential pathways for the release of chemicals (EPA, 1988), transport through soils was cited as the primary pathway of contaminants. As a result, chlorinated organic compounds become one of the major pollutants in the soil.

In addition, polycyclic aromatic hydrocarbons (PAHs) found in the petroleum derivatives also induce an environmental concern. The typical PAHs in the contaminated soil include fluorene, phenanthrene, fluoranthene, and pyrene. These hydrophobic organic chemicals including chlorinated organics and PAHs are carcinogens on the list of U.S. EPA priority pollutants. They are related to some health problems such as cancer and chronic illnesses. Therefore, it is urgent to clean waste sites contaminated by the organic pollutants.

Many remediation techniques have been applied to remove toxic chemicals from contaminated soils. Among the various remediation alternatives, in-situ application is the most attractive option. Many methods have been suggested for the in-situ remediation of contaminated soils such as air stripping, pump and treat, and electrokinetics. Among these alternatives, electrokinetics can separate and extract heavy metals, radionuclides, and organic contaminants from saturated or unsaturated soils, sludges, and sediments. A low intensity direct current is applied across electrode pairs that have been implanted in the ground on each side of the contaminated soil mass. The electrical current causes electroosmosis and ion migration, which move the aqueous phase contaminants in the subsurface from one electrode to the other. Contaminants in the aqueous phase or contaminants desorbed from the soil are transported towards respective electrodes depending on their charge. The contaminants may then be extracted to a recovery system or deposited at the electrode.

Electrokinetic (EK) remediation technology has recently made significant advance. The company, Geokinetics (The Netherlands), has successfully completed several field studies. Electrokinetics, Inc., (Baton Rough, LA) has completed several large-scale pilot studies using 2-4 ton soil specimens (Acar and Alshawabkeh, 1993). With more emphasis now placed on in-situ technologies, the EK process is emerging as one of the most promising remediation techniques. Major advantages of this method are: a possible utilization in- or ex-situ; a low power consumption (i.e., low operational costs); and a potential applicability to a wide range of contamination situations.

Although EK process has made significant achievement in cleaning up contaminated sites, it is noted that most cases focused on the soil contaminated by heavy metals. However, the experimental information about the removal of organic pollutants is limited. In addition, the factors controlling the removal efficiency of organics during the EK treatment is not understood. In order to predict the transport of organics during the EK treatment, the

quantification of the sorption reaction and electro-osmotic flow rate is necessary. Through this study, one can obtain the information about the sorption of orgaincs and electro-osmotic flow rate to aid the model simulation for the organic removal.

1.2. Literature Review

1.2.1. Sources of Nonionic Organic Compounds in Soils

Soils at waste sites may be contaminated by hazardous organic chemicals, heavy metals and radionuclides. Typical hazardous organic contaminants include chlorinated solvents such as trichloroethylene (TCE), tetrachloroethylene (PCE), chloroform, and carbon tetrachloride, and PAHs such as fluorene, phenanthrene, anthracene, fluoranthene, and pyrene. The treatment of nonionic organic contaminants among these hazardous chemicals is the focus of this study.

Chlorinated hydrocarbons (CHCs), commonly used as industrial solvents, are a significant category of hazardous organic compounds. Chlorination has become a widespread industrial practice because it yields compounds of lower flammability, higher density, higher viscosity, and improved solvent properties compared to nonchlorinated solvents (Watts, 1998). Chlorinated solvents are mainly used for degreasing and cleaning a large range of products, from machine parts to computer chips. Although CHCs are highly volatile, they can also migrate through the subsurface. The chlorinated solvents are mobile in groundwater systems due to the properties of high density, relatively high water solubility, and low biodegradability (Watts, 1998). They also adsorb to soil surfaces, which results in a high contamination level at some specific sites. The most common chemicals detected in the monitering wells in United States were PCE, TCE, chloroform, 1,1,1-trichloroethane, and carbon tetrachloride (Mackay, 1990). In addition, at National Priorities List (NPL) sites the contaminants that are most frequently found include TCE (42%) and PCE (28%) (ATSDR, 1989).

PAHs are found in the heavy fractions of petroleum products (e.g., lubricating oils, asphalt, and tarlike materials) as well as automobile exhaust. The leaking of petroleum underground storage tanks may result in serious contamination of subsurface soils with PAHs, and eventual contamination of groundwater. Though these tanks are made of relatively durable materials, soil is a corrosive environment and, after a certain peroid of time (from 5 to 25 years), the tanks rust, corrode, and leak (Shwendeman *et al.*, 1987). Other major sources of PAH contamination are gas plants, which produce gas from coal and oil. Soils around these gas plants are difficult to remediate because of high concentrations of PAHs, long chain aliphatics, and phenolics (Michelcic *et al.*, 1988). It is well known that PAHs chemically induce cancer.

1.2.2. Sorption of Nonionic Compounds on the Soil

For the assessment of organic fate, transport, and health risk in the natural soil-water system, the sorption reaction is one of the most important factors. Therefore, an understanding of the organic sorption is required for the accurate assessment. The sorbent in the soil for the organic contaminant can be divided into two parts: the mineral material and the soil organic matter (SOM). Generally, the uptake of the organic on the surface of the mineral solid is called as “adsorption”. The uptake of a organic contaminant without reference to a specific mechanism is denoted as “sorption”. In fact, the terms, sorption and adsorption, have been used interchangeably to describe the distribution behavior of the

organic contaminant between soil and aqueous phase. As the content of soil organic matter is abundant, the partition process always plays a predominant role to the orgnaic sorption (Sabbah et al., 1997). The term, partition or partitioning, is used to describe the sorption process in which the sorbed organic chemical is considered to dissolves in the SOM. This can be analogous to a extraction process in which the organic solute tranports from the water phase into the organic solvent.

The extent of organic contaminants uptaken by the soil mianly depends on the SOM content of the soil (Karickhoff, 1984). The sorption appear to exhibit the partition process as long as the fraction of soil organic matter (w/w) is greater than 0.2% to 0.4% (Schwarzenbach and Westall, 1981, Banerjee et al., 1985). The organic sorption capacity is related to the extent and types of the soil organic matter. Chiou et. al. (1979) observed the linear sorption isotherm for nonionic compounds onto soils and attributed this to a simple partition process to SOM. However, many researchers reported a nonlinear sorption iostherm of some hydrophobic organics (Weber et al., 1992; Graber and Borisover, 1998; Xia and Ball, 1999). Some authors proposed that SOM comprises two different domains including a soft, highly amorphous, and swollen domain (rubbery component) and a hard, relatively condensed domains (galssy component) (Huang and Weber, 1997a; Graber and Borisover, 1998). Since the organic sorption on the rubbery and glassy domain are different, therefore, the organic distribution is nonlinear in the soil-water system.

A variety of conceptual and empirical equilibrium models for representing nonlinear sorption processes are available. A "distributed reactivity" sorption model (Huang et al., 1997b) and a dual-mode sorption model (Xing and Pignatello, 1997) have been proposed to elucidate the organic distribution in the two different domains. These models can be well-fitted to experiments results of some hydrophobic organics. However, Graber and Borisover (1998) reported that the glassy/rubbery model cannot account for the sorption of H-bonding organics in SOM. In addition, this model dose not necessarily result in the nonlinear sorption. Some other sorption models have been used to describe the sorption nonlinearity regardless of the SOM compositions, that is, the Langmuir and Freundlich isotherms.

In addition to SOM, the dissolved organic matter (DOM) in the aqueous can also influence the organic sorption in the soil-water system (Carter and Suffet, 1982; Landrum et al., 1984). Some research reported that the partition coefficient of the organic is often underestimated due to the presenc of DOM (Gschwend and Wu, 1985). The organic interacts with DOM from various sources, which results in various partition coefficients of the organic pollutant. In addition, Gauthier et al., (1987) reported that the organic interaction with DOM is not a function of DOM concentration. Accordingly, they suggested that the suructure and composition of the DOM can influence the sorpiton of organic pollutants.

Based on the above illustration, the sorption of nonionic organic in the soil-water system is mainly controlled by the presence of SOM and DOM. In addition to the extent of SOM and DOM, the compositions of SOM and DOM can affect the organic sorption as well. However, the specification of SOM and DOM is a difficult task. The other alternative for descrbing the sorption is that one can regard the solution (with DOM) and SOM as two homogeneous phases. Then, by analyzing the partition coefficient or the parameters of sorption isotherms, one can gain insight into the organic sorption in the soil-water system.

1.2.3. Desorption of PAHs in the Presence of Surfactant

PAHs is a highly hydrophobic organic group and exhibits a low water solubility. Due to this property, PAHs has the difficulty to be removed from the contaminated soil. The surfactant can increase the solubility of the hydrophobic organic, thereby, it has been applied to the soil remediation technology (e.g., pump-and-treat). However, the surfactant can also be adsorbed on the soil surface, which results in increasing the sorption capacity of the soil. Moreover, the adsorbed surfactnat may induce another environmental concern if it is hazardous.

The surfactant concentration increases to a certain value, where the surfactant molecules will aggregate, i.e., micelles. This surfactant concentration is referred to as critical micelle concentration, i.e., CMC. Micelles are highly dynamic colloids and their typical sizes are ca. several nanometers (Attwood and Florence, 1983). The solubility of hydrophobic organics increases with increasing the micelle concentration proportially (Rosen, 1989). The solpe of this increase solubility versus the surfactant concentration is defined as the solubilization capacity. The solubilization capacity of surfactants varies with the type, the hydrophobity, and the micelle structure of surfactants.

For the consideration of surfactant adsorption on the soil, Cluinie and Ingram (1983) reported that a five stages adsorption of nonionic surfactant onto a solid surface. They suggested that the orientation of surfactant molecules on the soil varies from the monolayer to the multilayer type with different surfactant concentrations. A similar sorption behaviors were observed by Partyka et al., (1984). These studies indicates two categories of surfactant sorption, that is, monomer-surface interactions and monomer-monomer interactions. Howeve, Carberry et. al., (1977) proposed that the sorption of nonionic surfactants on soils is not multilayer but micelle-type sorption. When the micelle is the sorbate, the sorption interaction of the surfactant with the soil surface can be regarded as a dissolution process. In other words, the micelle sorption can be described by the partition process. Nevertheless, the micelle formed by various type surfactants (e.g., anionic surfactant) may not follow this rule completely. Noordman et. al., (2000) reported that the adsorption of rhamnolipid (anionic biosurfactant) on the soil is driven by the hydrophobicity but not a partition process.

Means et al., (1980) expolred the sorption of PAHs onto 14 different materials and reported a sorption correlation with the organic carbon content of the soil. The partition coefficients were found to be independent of all other soil properties. However, surfactant adsorption on the soil is the additional source of soil organic carbon, which increases the PAHs sorption density the soil. In order to account for the sorption increase by surfactants, the PAHs sorption computatios are based on an effective organic carbon content (Edwards et al., 1994). Consequently, the PAHs distribution in the presence of surfactant should consider the hydrophobicity of organics, the solubilization capacity of surfactants and the surfactant adsorption on the soil.

1.2.4. Electro-Osmotic Flow

The EK phenomena take place when an electric field is applied to a porous medium, which invokes the electro-osmosis process (Mitchell 1991). Electro-osmosis is the movement of the liquid (water in most cases) induced by the excess surface charge on the porous media. Generally, the soil surface is negatively charged, which induces a net excess of positive ions in the adjacent water layer. As these excess positive ions move under the influence of the applied field they will draw the liquid in soil pores along with them (Hunter, 1981).

Many investigations about the principle of electro-kinetic flow have been reported (Smoluchowski, 1921; Gray and Mitchell, 1967; Yeung and Datla, 1995). Among these previous studies, two theories were commonly used to describe the electrokinetic flow, that is, Helmholtz-Smoluchowski and Schmid. According to the Helmoltz-Smoluchowski theory (Helmholtz, 1879, Smoluchowski, 1921), the electro-osmotic flow rate (Q_e), moving in a capillary of length, L, under an electrostatic field (externally applied voltage), E, is:

$$Q_e = (\varepsilon \zeta E)/(4\pi\eta L) \quad [1.1]$$

where ε, E, ζ, and η are the dielectric constant, field strength, electrokinetic (zeta) potential and water viscosity, respectively. Schmid (1950) proposed that the electro-osmotic flow rate is:

$$Q_e = (r^2 qFE)/(8\eta L) \quad [1.2]$$

where r, q, and F are the radius of capillary pores, volumetric charge density in the pores, and Faraday constant, respectively. The Helmoltz-Smoluchowski theory predicts an electro-osmotic flow rate that is independent of the pore size. In contrast, Schmid theory indicates that the flow rate is proportional to the cross sectional area of the pores.

An equation accommodates both the Helmoltz-Smoluchowski and the Schmid theories was developed by Erig and Majtenyi (1966), that is:

$$Q_e = (1/2)\ln(1+\kappa/r)(r^2/\eta)\sigma(E/L) \quad [1.3]$$

where σ and κ are the average mobile surface charge density and the parametric characterizing the double layer, respectively. Among all electro-osmotic theories, it is noted that the surface charge of the soil particles is the common factor controlling the electro-osmotic flow rate. The electro-osmotic flow rate is directly proportional to the surface charge density (or zeta potential of the soil particle). For the field practice, the electro-osmotic flow rate were always expressed as a function of the cross-sectional area of the flow:

$$Q_e = K_e i_e A \quad [1.4]$$

where K_e, i_e, and A are the electrokinetic permeability, the electrical potential gradient, and electrode surface area. Casagrande (1957) has determined the electrokinetic permeability of various soils and found that the K_e values vary only within one order of magnitude with an average value of 5×10^{-5} cm^2/sec-V. Therefore, this equaiton was applied to all sites regardless of the compositions of the soil.

1.2.5. Electrokinetic Remediation Process

During the electrokinetic treatment, electrolysis reactions dominate the chemical properties of the pore fluid. When the chemical properties of the process fluid are not controlled externally (i.e., unenhanced electrokinetic treatment), application of direct electric current results in oxidation at the anode, generating an acid front, while reduction at the cathode produces a base front by

$$2H_2O - 4e^- \rightarrow O_2 + 4H^+ \quad E_o\text{=-1.229 (anode)} \quad [1.5]$$

$$2H_2O + 2e^- \rightarrow H_2 + 2OH^- \quad E_o\text{=-0.828 (cathode)} \quad [1.6]$$

where E_o is the standard reduction electrochemical potential. Secondary reactions may exist depending upon the concentration of available species, such as:

$$H^+ + e^- \rightarrow \frac{1}{2}H_2 \quad [1.7]$$

$$M_e^{n+} + ne^- \rightarrow M_e \quad [1.8]$$

$$M_e(OH)_n(s) + ne^- \rightarrow M_e + nOH^- \quad [1.9]$$

where M_e refer to as metals. The type of electrolysis reactions occuring at the electrodes depends on the availability of the chemical species and the electrochemical potential of this reaction. Although some other secondary reactions might be favored at the cathode because of their lower electrochemical potentials, the water reduction half reaction (H_2O/H_2) is dominant at early stages of the process.

In unenhanced electrokinetic remediation and at the early stages of the process, electrolysis reactions of water will generate an acidic medium at the anode and an alkaline medium at the cathode. The pH will drop at the anode to below 2 and it will increase at the cathode to above 12 depending on the total current applied (Acar and Alshawabkeh, 1993). The acid front will advance toward the cathode by transport mechanisms including migration caused by electrical gradients; pore fluid advection caused by electro-osmotic flow, any externally applied or internally generated hydraulic potential differences; and diffusion caused by generated chemical gradient.

The removal of soil contaminants is also via these transport mechanisms. The movement of chemical species in a porous medium under an electrostatic field can be described by the following equation:

$$\partial C_i / \partial t = -\nabla J_i + R_i \quad [1.10]$$

where C_i is the chemical concentration in pore fluid; J_i is the chemical flux, R_i is the decay rate of the ith chemical species. In dilute systems and in the presence of an electric field, the flux is expressed (Shapiro and Probstein, 1993):

$$J_i = -v_i z_i F C_i \nabla E - D \nabla C_i + u C_i - (\rho / n) S_i \quad [1.11]$$

where v_i is the mobility, which is related to the diffusivity of the Nernst-Einstein equation, i.e. $v_I = D_i / (RT)$; z_i is the charge number; D_i is the diffusivity coefficient; E is the applied electric potential; F, is the Faraday constant; u is the average mass (electrokinetic) velocity; ρ is the density of the soil particles; n is the porosity of the soil matrix; and S_i is the concentration of the contaminant on the soil surface. The relationship between the concentration of the contaminant species in the solution phase, C_i, and in the solid phase, S_i, is determined by the appropriate adsorption or sorption isotherm. The following isotherms are most frequently used to describe the adsorption of contaminants onto solid surfaces:

$$S_I = S_m K_L C_i / (1 + K_L C_i) \text{ (Langmuir isotherm)} \quad [1.12]$$

$$S_i = K C_i \text{ (Linear isotherm)} \quad [1.13]$$

$$S_I = K_f C_i^m \text{ (Freundlich isotherm)} \quad [1.14]$$

By combining the above equations, one has the expression of concentration change of the chemical contaminant in the water phase:

$$\partial C_i / \partial t = v_i z_i F C_i \nabla^2 E + D \nabla^2 C_i - u \nabla C_i + (\rho / n) \nabla S_i + R_i \quad [1.15]$$

Mathematical models can be established to solve the above equation under given initial and boundary conditions. For the mobilization of nonpolar organic compounds from the surface by electrokinetic force, it is noted that the electrostatic attraction becomes unimportant.

1.3. Objectives

Under applied electrokinetic remediation, transport of nonionic organic compounds through soils is a complex and poorly understood phenomenon. Transport mechanisms may depend on the variable geologic formation conditions, electro-osmotic flow, and the physical

chemical properties of the organic compounds. As such, this complexity often increases the difficulty of research work on determining transport mechanism. One of the crucial factors is the sorption reaction. Although the sorption of nonionic organics has been studied over several decades, the available information from the literature may not suitable for the specific contaminated soils.

The main objective of this study is to obtain information pertaining to the transport of nonionic organic compound in contaminated soil with electrokinetic remediation. Since the organic sorption on the soil is the main factor of the transport, a series sorption experiments were conducted. In Chpater 3, the determination of the partition coefficients of chlorinated organics including PCE, TCE, chloroform, and carbon tetrachloride with various organic concentrations and soil to solution ratios was conducted. In Chapter 4, the PAHs , fluorene, phenanthrene, anthracene,fluoranthene, and pyrene, distribution in the presence of surfactants were investigated. The other important factor for the organic transport is the electro-osmotic flow rate, which was studied in Chapter 5. A quantitative equation was developed to predict the flow rate based on the physico-chemical properties of the soil. For the organic transport, a numerical model was used to quantify the removal behavior of organic compounds in the unsaturated soil shown in Chapter 6. Through modeling, one can estimate the extent of organic pollutant in the soil throughout the operation period. This information is important to help in the design and implementation of clean-up strategies.

In order to assess the partition coefficients of selected nonionic organic compounds, K_d (i.e., the sorption density to organic concentration at equilibrium), a series of batch sorption experiments have been conducted. The extent of partition coefficient may depend on the following factors: (1) chemical properties of organic compound (2) the concentration of organic compounds (3) soil to solution ratio (4) surfactant effect. These factors were tested and results were analyzed to illustrate the organic partition process between the soil and the solution.

The other task is to study electrokinetic process for the in-situ treatment of contaminated soils. Several different electrokinetic systems were designed to study important parameters controlling the mobilization and the transport of selected organic chemicals in soils by the electrokinetic process. Important factors such as field strength (applied voltage and power requirement), pH control, soil water moisture content, soil composition, zeta potential), and ionic strength that may affect the electro-osmotic flow rate were studied. A mathematical model was established to predict the movement of water in the unsaturated porous media. The transport of the nonionic organic compounds was simulated by a diffusion-advection-sorption based mathematical model.

1.4. Research Approach

Works in this research followed the executive flowchart shown in Figure 1.1 At first, soil materials were characterized for soil composition (clay, slit, and sand), organic matter content, moisture content, porosity, hydraulic conductivity, concentrations of organic contaminants, soil pH, and zeta potential. With the exception of specific surface area, pH_{ZPC}, and hydraulic permeability, all the other characterization procedures are extracted from the Methods of Soil Analysis, (Agricultural Experimental Station, University of Delaware (1991)).

The sorption characteristics of selected organic contaminants in soils were determined using batch reactors. A given amount of soil material would be mixed with a solution

containing the selected organic. Since it is expected that the association between the chemical contaminants and the soil particles can be affected by soil to solution ratio, tentatively, soil to solution ratio ranges at 1:5, 1:10, 1:20, 1:50, and 1:100 were chosen. Effect of the initial organic concentrations were determined by the concentration ranging from 0.1 C_s to 0.8 C_s, where C_s is the water solubity of the organic. The sorption isotherms and the partitioning coefficients can be obtained from these sorption experiments.

In order to enhance the mobilization and the movement of contaminants in soils, research effort was made to evaluate the effectiveness of surfactant as soil flushing agents. The selection of surfactant was made based on the following criteria: mobilization, dispersion, water solubility, and foam formation. Mobilization is the extent of the surfactant's ability to release the specific organic contaminants from the soil surface. Dispersion is an indication of the extent small soil colloids which are brought into the solution by the surfactant. Water solubility is an indication of the solubility of the surfactant. The foam formation is a test of the degree of foam produced by the surfactant. The ideal surfactant has high mobilization capacity, low colloid dispersion potential, high water solubility and low foam formation characteristics. Effect of surfactant type and surfactant concentration on the release of organic pollutants from the soil were determined.

The electro-osmotic flow influences the movement of organic contaminant directly due to advection. Important factors such as field strength (applied voltage and power requirement), pH control, soil surface properties (soil water moisture content, soil porosity, zeta potential), ionic strength were studied. During the experiments, the effluent quantity, the addition of electrolyte, the dose of acid or base, and pH value of working solution were measured with time until the flow rates approached a stable state.

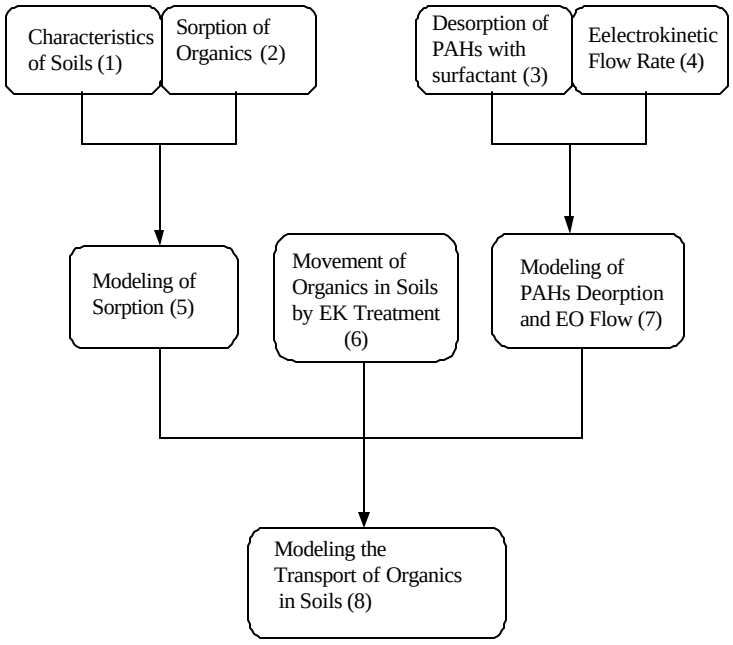

Figure 1.1. The flowchart of research approach.

The soil characterization and sorption experiments can provide the information about the physicochemical properties of soils and distribution ratio of organics at equilibrium, respectively. The electro-osmotic flowrate experiments provide water transport speed in the unsaturated soil under different electrokinetic conditions. Moreover, the study of the mobilization of organic contaminants in the contaminated soil using the electrokinetic remediation process give us the movement profile as a function of time. By combination of the above experimental data, we can build up and solve the organic compound transport model of electrokinetic remediation. As a result, the removal efficiency of organic, required time for cleaning up, and the cost of electrokinetic operation can be estimated. A transport model of the organic contaminant under

electrokinetic treatment was developed and written as a computer program by MATLAB. This mathematical program is used to predict the movement of organic contaminants in the soils by input of the necessary parameters.

1.5. References

1. Acar, Y. B. and A. N. Alshawabkeh (1993), Principles of Electrokinetic Remediation, Environ. Sci. Technol., Vol. 27, No. 13, 2638-2646.
2. ATSDR Biannual Report to Congress: October 17, 1986 ~ September 30, 1988. Agency for Toxic Substances and Disease Registry, U. S. Public Health Service, Atlanta, GA, 1989.
3. Attwood, D. and A. T. Florence, Surfactant Systems: Their Chemistry, Pharmacy and Biology, Chapman and Hall, New York, NY, 1983.
4. Banerjee, S., M. D. Piwoni, and K. Ebeid (1985), Sorption of Organic Contaminants to a Low Carbon Subsurface Core, Chemosphere, Vol. 8, 1057-1067.
5. Carberry, J. B, C. J. Twardowski, and D. K. Eberhart (1977), Clay Adsorption Treatment of Non-Ionic Surfactants in Wastewaters, J. Wat. Pollut. Control Fed., Vol. 49, 452-459.
6. Carter, C. W. and I. H. (1982), Binding of DDT to Dissolved Humic Materials, Environ. Sci. and Technol., Vol. 16, No. 11, 735-740.
7. Casagrande, L. (1957), Review of Past and Current Work on Electro-Osmotic Stabilization of Soils, December 1953, with Supplement of June 1957, Harvard Soil Mechanics Series No. 45.
8. Chiou, C. T., L. J. Peters, and V. H. Freed (1979), A Physical Concept of Soil-Water Quilibria for Nonionic Organic Compounds, Science, Vol. 206, 831-832.
9. Clunie, J. S. and B. T. Ingram, Adsorption from Solution at the Solid/Liquid Interface, Academic Press, New York, NY, 1983.
10. Edwards, D. A., Z. Adeel, and R. G. Luthy (1994), Distribution of Nonionic Surfactant and Phenanthrene in a Sediment/Aqueous System, Environ. Sci. and Technol., Vol. 28, No. 8, 1550-1560.
11. Esrig, M. I. And S. Majtenyi (1966), A New Equation for Electro-Osmotic Flow and Its Implications in Porous Media, Highway Research Record, No. 111, 31-41.
12. Gauthier, T. D., W. R. Seitz, and C. L. Grant (1987), Effects of Structural and Compositional Variations of Dissolved Humic Materials on Pyrene K_{oc} Values, Environ. Sci. and Technol., Vol. 21, No. 3, 243-248.
13. Graber, E. R. and M. D. Borisover (1998), Evaluation of th eGlassy/Rubbery Model for Soil Organic Matter, Environ. Sci. Technol., Vol. 32, No. 21, 3286-3292.
14. Gray, D. H. And J. K. Mitchell (1967), Fundamental Aspects of Electro-Osmosis in Soils, Journal of the Soil Mechanism and Foundations Division, November, 209-235.
15. Gschwend, P. M. and S. Wu (1985), On the Constancy of Sediment-Water Partition Coefficients of Hydrophobic Organic Pollutants, Environ. Sci. and Technol., Vol. 19, No. 1, 90-96.
16. Helmholtz, H. (1879), Ann. Physik, Vol. 7, 137.
17. Huang, W. and W. J. Weber, Jr. (1997a), Thermodynamic Considerations in the Sorption of Organic Contaminats by Soils and Sediments. 1. The Isosteric Heat Approach and Its Application to Model Inorganic Sorbents, Environ. Sci. and Technol., Vol. 31, No. 11, 3238-3243.

18. Huang, W., T. M. Young, M. A. Schlautman, H. Yu, and W. J. Weber Jr. (1997b), A Distributed Reactivity Model for Sorption by Solids and Sediments. 9. General Isotherm Nonlinearity and Applicability of the Dual Reactive Domain Model, Environ. Sci. and Technol., Vol. 31, No. 6, 1703-1710.
19. Hunter, R. J., Zeta Potential in Colloid Science Principles and Applications; Academic Press: Orlando, FL, 1981.
20. Karickhoff, S. W. (1984), Organic Pollutant Sorption in Aquatic System, J. Hydraulic Eng., Vol. 110, 707-735.
21. Landrum, J. P., S. R. Nihart, B. J. Eadie, and W. S. Garden (1984), Reverse-Phase Separation Method for Determining Pollutant Binding to Aldrich Humic Acid and Dissolved Organic Carbon of Natural Waters, Environ. Sci. and Technol., Vol. 18, No. 3, 187-192.
22. Mackay, D. M., and L. A. Smith (1990), Agricultural Chemicals in groundwater: Monitoring Management in California, J. Soil Water Conservation, Vol. 45, 253-255.
23. Means, J. C., S. G. Wood, J. J. Hassett, W. L. Banwart (1980), Sorption of Polynuclear Aromatic Hydrocarbons by Sediments and Soils, Environ. Sci. and Technol., Vol. 14, No. 12, 1524-1528.
24. Michelcic J. r., and Luthy, R. C. (1988). Degradation of Polycyclic Aromatic Hydrocarbon Compounds under Various redox Conditions in Soil-Water Systems, Applied Environmental Microbiology, Vol. 54, 1182 – 1187.
25. Mitchell, J. K., Fundamentals of Soil Behavior; 2nd Ed., John Wiley & Sons: New York, NY, 1991.
26. Noordman, W. H., M. L. Brusseau, and D. B. Janssen (2000), Adsorption of a Multicomponent Rhamnolipid Surfactant to Soil, Environ. Sci. Technol., Vol. 34, No. 5, 832-838.
27. Partyka, S., S. Zaini, M. Lindheimer, and B. Brun (1984), Adsorption of Non-Ionic Surfactants on a Silica Gel, Colloids and Surfaces, Vol. 12, No. 3-4, 255-270.
28. Report to Congress: Solid Waste Disposal in the United Stated (1988), Vol. II, EPA/530-SW011B, U. S. Environmental Protection Agency, U. S. Government Printing Office, Washington DC.
29. Rosen, M. J., Surfactants and Interfacial Phenomena. 2nd ed. John Wiley & Sons Inc., New York, NY, 1989.
30. Sabbah, I. and M. Rebhun, (1997), Adsorption-Desorption of Trichlorophenol in Water-Soil Systems, Water Environ. Research, Vol. 69, No. 5, 1032-1038.
31. Schmid, G. (1950), Zhurnal fur Electrochemie, Vol. 54, 424.
32. Schwarzenbach, R. P., J. Weatall (1981), Transport of Nonpolar Organic Compounds from Surface water to Groundwater: Laboratory Sorption Studies, Environ. Sci. Technol., Vol. 15, 1360-1367.
33. Shapiro, A. P. and R. F. Probstein (1993), Removal of Contaminants from Saturated Clay by Electroosmosis, Environ. Sci. and Technol., Vol. 27, No. 2, 283-291.
34. Shwendeman, T. D., and Wilcox, H. K., Underground Storage Systems: Leak Detection and Monitoring, Lewis publishers, Chelsea, MI. 1987.
35. Sims, J.T. and S. E. Heckendorn (1991). Methods of Soil Analysis, University of Delaware, Agricultural-Experimental Station Cooperative Extension, Newark.
36. Smoluchowski, von M. (1921), Handbuch der Elektrizitat und der Magnetismus II, Vol. 2, 366-428.

37. Watts, R. J. (1998). Hazardous Wastes: Sources, Pathways, Receptors. John Wiley and Sons, Inc., New York.
38. Weber, W. J., Jr., P. M. McGinley, and L. E. Katz (1992), A Distributed Reactivity Model for Sorption by Soils and Sediments. 1. Conceptual Basis and Equilibrium Assessments, Environ. Sci. Technol., Vol. 26, No. 10, 1955-1962.
39. Westrick, J. J, J. W. Mills, and R. F. Thomas (1983), The Ground Water Supply Survey: Summary of Volatile Organic Contaminant Occurrence Data, U. S. EPA, Office of Drinking Water, Cincinnati, OH.
40. Xia, G. and W. P. Ball (1999), Adsorption-Partitioning Uptake of Nine Nonpolar Organic Chemicals on Natural Geological Material, Environ. Sci. Technol., Vol. 33, No. 2, 262-269.
41. Xing, B. and J. J. Pignatello (1997), Dual-Mode Sorption of Low-Polarity Compounds in Glassy Poly(Vinyl Chloride) and Soil Organic Matter, Environ. Sci. and Technol., Vol. 31, No. 3, 792-799.
42. Yeung, A. T. and S. Datla (1995), Fundamental Formulation of Electrokinetic Extraction of Contaminants from Soils, Can. Geotech. J., Vol. 32, 569-583.

2. PHYSICAL-CHEMICAL CHARACTERIZATION OF SOILS

2.1. Composition

The composition of soil sample was analyzed by the sedimentation (hydrometer) method. The procedures are as follows: grind soil samples with mortar and pestle and sieve to make sure that all the diameters of the soil particles are less than 2 mm.

a) Take 50 gram of the ground soil sample and add 100 mL of 5% sodium hexametaphosphate.
b) Transfer the suspension to a sedimentation cylinder, insert a plunger and mix the contents thoroughly.
c) About 15 seconds after mixing the suspension, lower the hydrometer into suspension, and after 40 seconds, read the scale at the top of the meniscus.
d) Record the hydrometer value.
e) Record temperature of the sample and blank at the 40 seconds time mark. From these values, the percentage of sand can be calculated.
f) After 2 hours of standing lower the hydrometer into the sedimentation cylinder and record the hydrometer value, then record the temperature of sample and blank. From these values, the percentage of clay can be calculated.

The equations for the calculation of the soil composition are as follows:

$$\%\ \text{Sand} = 100 - \left\lceil \frac{100 \times (\text{hydrometer reading at } 40 \text{ seconds})}{(\text{Corrected weight of Soil})} \right\rceil$$

$$\%\ \text{Clay} = \frac{100 \times (\text{hydrometer reading at } 2 \text{ hours})}{(\text{Corrected weight of Soil})}$$

$$\%\ \text{Silt} = 100 - (\%\ \text{Sand} + \%\ \text{Clay})$$

where: Corrected Weight of Soil = $\dfrac{\text{oven dry weight of subsample} \times 50\text{g}}{\text{Air} - \text{dried weight of subsample}}$. Table 2.1. shows the results of composition analysis obtained by using the sedimentation method for the soil sample received. Clay and silt are the major components in all soil samples which indicates that the application of electro-osmosis technology will be feasible for these soils.

2.2. pH

The pH measurements were made in 0.01 M $CaCl_2$ solution. The samples were air dried and sieved through 2 mm sieve to remove the coarse soil fraction. Weigh 10 gram of the pretreated soil sample and mix with 10 mL of 0.01 M $CaCl_2$. Mix thoroughly and let the sample stand for at least 1 hour. Record the pH value by using a pH meter. The results shown in Table 2.1 indicate that most of the soil samples are in the neutral region (pH is equal to 7.6).

Table 2.1. Physical-chemical characteristics of the soil sample.

Physical-chemical Characteristics	Result	Method
Sand (%)	14.0	Hydrometer
Silt (%)	38.0	Hydrometer
Clay (%)	48.0	Hydrometer
PH	7.6	In 0.01M $CaCl_2$
ECEC (meq/100g)	20.5	The sum of exchangeable K,Ca,and Mg
Organic Matter(%)	1.7	Heating at 105 ^oC for 2 hours, then at 360 ^oC for 2 hours
Moisture (%)	13.6	Heating at 105 ^oC for 24 hours
Hydraulic Conductivity (10^{-8}cm/s)	2.5	Constant-head
pH_{zpc}	2.2	pH meter and Zetameter
Specific Surface Area (m^2/g)	10.7	Coccine Dye Adsorption

ECEC: effective cation exchange capacity

2.3. Organic Matter

The soil organic matter was determined by the loss of weight on ignition (L. O. I.) method. Take 1 cm^3 of air dried and sieved through 2mm sieve soil sample and place it into a 30 mL beaker. Dry the soil sample at 105 ^oC for two hours. Record the weight of soil sample plus beaker with an accuracy of +0.001 g. Heat the sample in oven at 360^o C for two hours. Cool the sample to 105 ^oC and maintain at this temperature until weighing. Weigh the beaker with the ash in a draft-free environment to ±0.001 g.

$$O.M.(\%) = \frac{(W_{bs} - W_b) - (W_{ba} - W_b)}{W_{bs} - W_b} \times 100$$

where: W_b = weight of beaker, W_{bs} = weight of beaker plus soil before ashing, W_{ba} = weight of beaker plus ashed soil.

Table 2.1. shows the results of organic matter content. The organic matter content is around 1.7 % by weight

2.4. Effective Cation Exchange Capacity

The experimental procedures of soil effective cation exchange capacity are as follows:

a) Determination of the exchangeable cations
   Weigh 10 g of soil sample into a 100 mL polyethylene cup and add 50 mL of 1 N ammonium acetate (NH_4OAc) to the cup as a buffer solution to maintain the solution pH at 7.0. Shake the cup for 30 minutes. Filter the suspension with No. 40 filter paper (Whatman) and add 25 ml of 1 N NH_4OAc again to wash the filter paper. Collect the filtrate and determine the K, Ca and Mg concentrations by atomic absorption spectrophotometer.
b) Determination of exchangeable acidity
   Weigh 10 g of soil sample into a 125 mL Erlenmeyer flask, add 25 ml of 1 N KCl solution and mix well. Filtrate the suspension into a 300 mL Erlenmeyer flask. Add 4 drops of phenolphthalein indicator to the KCl solution. Titrate the KCl

solution with the standard 0.01 N NaOH. At the end point of titration, record the volume of NaOH used. Get the exchangeable acidity in (meq/100g).

c) Effective cation exchangeable capacity (ECEC)
The sum of the concentrations of exchangeable K, Ca, Mg and the exchangeable acidity is the effective cation exchangeable capacity (ECEC).

Table 2.1 shows the results of effective cation exchange capacity (ECEC) of soil samples, the measured ECEC range is 20.5 meq/100g.

2.5. Moisture Content

Weigh the empty aluminum plate. Weigh 1 g of soil on the aluminum plate. Measure and record the weight of plate with soil and record it. Put the soil sample in oven at 105 ^{o}C for 24 hours to get rid of soil moisture. Take these samples from the oven to the desiccator and cool. Weigh of the dried soil.

The moisture content is calculated as follows:

$$M(\%) = \frac{W_{\text{wet soil}} - W_{\text{dry soil}}}{W_{\text{wet soil}} - W_{\text{plate}}} \times 100$$

where: M(%) = moisture content, percentage by weight, $W_{\text{wet soil}}$ = weight of original soil sample + aluminum plate, $W_{\text{dry soil}}$ = weight of the ashed soil + aluminum plate, W_{plate} = weight of the aluminum plate. The moisture content results are shown in Table 2.1. The moisture content is from 13.6 % by weight.

2.6. Specific Surface Area

The dye adsorption method (Smith and Coachley, 1983) was selected to determine the specific surface area of siols in this study. A commercially available dye, coccine acid red #18 (Aldrich Chemical Company, Inc.), was used as an adsorbate. This dye has a molecular weight of 604.48 and a flat molecular area of 196 $\text{A}^{o\,2}$. Its structure is shown in the following figure.

A monolayer coverage is assumed for this dye adsorption onto the soil surface. The experimental procedures for specific surface area measurement were as follows:

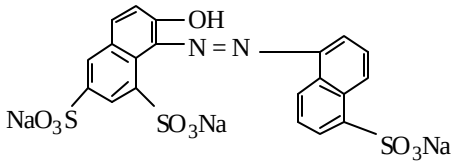

The structure of new coccine dye

a) Weigh a certain amount of air dried soil (typically 2~3 g/L) into a 1000 mL beaker. Add distilled water to the 1000 mL mark.
b) Adjust the pH of soil sample to 2 by adding $HClO_4$ stock solution. Adjust ioni strength if necessary.
c) Measure the suspended solids (SS) concentration .
d) Distribute 100 (or 50) mL soil sample to a series of 125 mL plastic bottles.

e) Add different amounts of stock dye solution into these bottles. The following initial dye concentration are suggested: $1x10^{-6}$, $2.5x10^{-6}$, $5x10^{-6}$, $7.5x10^{-6}$, $1x10^{-5}$, $1.25x10^{-5}$ M.
f) Shake the bottles in a shaker for 30 minutes to achieve equilibrium.
g) Centrifugate each mixture at 15,000 rpm (550g) for 10 minutes to separate the soil from supernatant.
h) Prepare a series of standard stock solution with known concentrations of coccine dye for the purpose of calibration.
i) Read and record the absorbance of the standard solutions and the sample supernatant by colorimetric method using a visible spectrophotometer (Hach model DR/2000, Hach Co., Loveland CO) at a wavelength of 505 nm.
j) Calculate the concentration of the dye remained in samples using the linear regression equation obtained from the calibration curve.
k) Calculate the maximum dye adsorption density, Γ_m using a multilayer adsorption equation.
l) Compute the surface area by the following equation:

$$S = \Gamma_m NA$$

where: S is the specific surface area of the soil (m^2/g); Γ_m is the maximum monolayer dye adsorption density (mole/g); N is the Avogadro's number ($6.023x10^{23}$ molecules/mole); A is the area occupied by a single dye molecule (m^2/molecule).

The multilayer adsorption model developed by Wang and Huang (1997) can be expressed as:

$$\Gamma = \frac{\Gamma_m K_1 C}{(1 - K_2 C)[1 + (K_1 - K_2)C]}$$

where: Γ = overall dye uptake density (mole/g-SS), Γ_m = monolayer uptake density (mole/g-SS), K_1 = constant related to the adsorption energy for binding to the particle surface (M^{-1}), K_2 = constant related to the adsorption energy for multilayer adsorption (M^{-1}). From the experimental data of the Γ - C relationship, the constants K_1, K_2, as well as Γ_m can be obtained by a nonlinear regression method. Table 2.1 shows the specific surface area of the soil samples tested.

2.7. pH_{ZPC}

Take the soil samples from the containers, dry at 105 ^oC, grind and then sieve through a mesh No.100 (150 μm). For each sample, prepare a solution of 0.1 g/L of the pretreated soil in 0.05 M $NaClO_4$. The zeta potential was measured with a zetameter (Laser Zee model 500) as a function of pH values ranging from 2 to 9. Plot the ζ values vs. pH and then the pH_{ZPC} is obtained at the pH of zero zeta potential. Since the application of electro-osmosis were investigated in this study, it is crucial to know the microscopic electrical properties of the soil samples. Table 2.1 shows the zeta potential for all soil samples tested, the measured value is approxinmately 2.2.

2.8. Hydraulic Conductivity and Hydraulic Permeability

A constant-head permeameter was used to measure hydraulic conductivities as shown in the below Figure 2.1. Water entered the medium cylinder from the bottom and was collected as overflow after passing upward through the soils.

From Darcy's law it follows that the hydraulic conductivity can be obtained from:

$$K = \frac{VL}{Ath}$$

where V = flow volume in time t, A, L and h are shown in figure.Hydraulic permeablity, k, can be caculated by the equation:

$$k = \frac{K\mu}{\rho g}$$

where K = hydraulic conductivity, μ = dynamic viscosity, ρ = the fluid density, g = acceleration of gravity.

The hydraulic conductivity of the soil is important, because the electro-osmosis technique is favorably applied to contaminated soils with low hydraulic conductivity (around 10^{-5} cm/sec). The result of hydraulic conductivity of the soil samples is shown in Table 2.1., the measured value is 2.5×10^{-5} cm/sec.

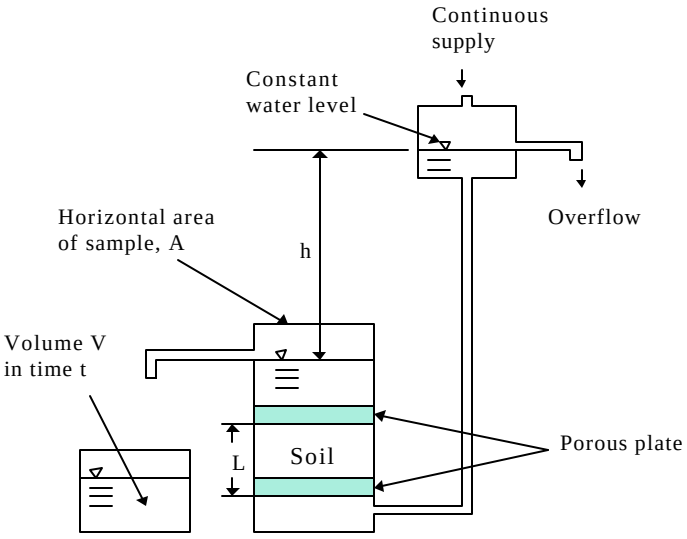

Figure 2.1. The schematic diagram of the constant-head permeameter.

3. SORPTION OF CHLORINATED ORGANIC COMPOUNDS IN SOIL-WATER SYSTEMS

3.1. Introduction

Understanding the interaction between organic contaminants and soil materials is important to assessing of the mobility and fate of these compounds in the environment. In general, the sorption behavior of organics on soils is governed by two major factors, namely, the hydrophobicity of the organic contaminants and the soil organic matter content (Sabbah et al., 1997). In many studies (Chiou et al., 1990; Rutherford et al., 1992; Seth et al., 1999), the fraction of organic carbon in soils is regarded as the main sorbent and the role of minerals is largely ignored. In other words, the partition (dissolution) instead of the adsorption (surface reaction) process dominates the sorption behaviors of organic pollutants in soils. The organic adsorbed by minerals is negligible when the soil organic matter is less than 0.2% by weight (Schwarzenbach and Westall, 1981).

Chiou et al. (1979) observed linear isotherms for nonionic organic compounds sorbing onto soils and attributed this to a simple partition process brought by the soil organic carbon. According to the partition concept, there exists an linear expression between the normalized partition coefficient, K_{oc}, and the octanol number of pollutant, K_{ow}. That is:

$$\log K_{oc} = a \log K_{ow} + b \qquad [3.1]$$

where K_{oc} is the normalized organic carbon partition coefficient and a and b are constants. It is noted that K_{oc} is related to the solute partition coefficient, K_d, and soil organic content (%), x, i.e., $K_{oc} = K_d/x$. Type of organic compound governs the values of a and b (Schellenberg et. al., 1984).

However, Mingelgrin and Gerstl (1983) argued that linearity is not evidence for the partition mechanism. Among the non-linear isotherms for organic compounds distribution in soil-water systems reported, (Voice et al., 1983; Weber et al., 1983), many appeared to follow that of the Freundlich type (Equation 3.2):

$$q_e = K_f C_e^{1/n} \qquad [3.2]$$

where q_e is the concentration in soil phase, C_e is the chemical concentration in aqueous phase, K_f is the Freundlich constant and n is a coefficient. The linear isotherm is only a special case of the Freundlich isotherm when n is equal to 1. The other common non-linear isotherm is the Langmuir (Equation 3.3). The Langmuir isotherm predicates an asymptotic approach to a specific maximum sorption density, q_{max}, and a factor, b, which is related to the affinity of the solute for the surface, that is:

$$q_e = \frac{q_{\max} b C_e}{(1 + bCe)} \qquad [3.3]$$

Based on the partition concept, the hydrophobicity of the organic contaminant plays the major rolw in the sorption process. As a result, the sorption process would be described by a linear isotherm. When sorption follows a non-linear sorption isotherms, it implies that other factors, in addition to hydrophobicity, must be responsible for the sorption process. Generally, the linear isotherm is observed at low initial adsorbate concentrations. The distribution of the adsorbate between the soil and the solution phase may decrease with increasing organic concentration (Mingelgrin and Gerstl, 1983). Accordingly, solute

concentration can be considered as one of the important factors influencing the sorption phenomenon.

The other important factor, not considered by any partition model is the soil to solution ratio. This effect has been observed in phosphate adsorption on soils (Barrow and Shaw, 1979). It has been reported that phosphate adsorption increases as soil to solution ratio increases (Fordham 1963; Barrow et al., 1965; and White, 1966). Hope and Syers (1976), however, reported that high soil to solution ratio resulted in a low phosphate adsorption. In fact, the "soil to solution ratio" affects the sorption behavior for a vareity of contaminants such as heavy metals, organic pollutants, and radioactive materials. Routson and Serne (1972) and Weiss and Colombo (1979) have found that the partition coefficient of low-level radioactive elements decreases with an increase of the soil to solution ratio. Fotoval et al. (1997) have reported that a decreasing soil to solution ratio increases the amount of cations adsorbed per unit weight of soil. Puls et al. (1991) also proposed that K_d increases with decreasing soil to solution ratio for Pb and Cd sorption on kaolinite. Accordingly, there must be some physicochemical processes occuring as the soil is mixed with water at different ratios, which results in a change of partition behavior. In this study, the effect of soil to solution ratio on the sorption of nonionic organic contaminants on soils was investigated. The adsorption capacity was discovered to closely corelate the presence of dissolved organic matter (DOM) in the aqueous phase.

The objective of this study is to assess the partition coefficient, K_d, of selected chlorinated organics, namely, tetrachloroethylene (PCE), trichloroethylene (TCE), carbon tetrachloride, and chloroform with various initial solute concentrations and soil to solution ratios. By the analysis of the partition coefficient variation, it may provide the information about the non-linear sorption of organics, i.e., the organic concentration effect. In addition, the soil to solution effect can be also explained by the K_d investigation. In order to analyze the partition coefficient of organic contaminants, it is necessary to characterize thermodynamically the organic compounds in both aqueous and the soil phases (McCall et al., 1985). The fugacity concept was introduced to characterize the organic in the soil-water system, which can determine the organic activity coefficient in the soil and aqueous phase respectively. Furthermore, the organic interaction with the soil and the solution can be quantified based on the magnitude of the activity coefficient. Therefore, one can gain insight into the concentration and soil to solution effects on the organic sorption in the soil-water system.

3.2. Theoretical Aspects

Figure 3.1 is a conceptual presentation of the sorption of nonionic chlorinated compounds in the soil-water system. In the system, the liquid phase consists of two components, namely, the water and the dissolved organic matter (DOM). The DOM in solution is derived from its dissolution of the soil organic matter due to rain and groundwater movement. In this case, DOM is a cosolvent and interacts with organic contaminants directly. Consequently, DOM will influence the distribution of organic contaminants in the soil-water system. As a result, the measured partition coefficient will be an apparent value rather than a true constant due to the presence of DOM. The DOM extent can be attributed to the soil concentration in the system. The DOM concentration increases with increasing the soil concentration, i.e., the soil to solution ratio. In this study, the presence of DOM was introduced to explain the soil to solution ratio effect on the organic sorption.

In addition to DOM, the extent of organic concentration is another factor controlling its sorption behavior. The organic contaminants are mainly sorbed in the soil organic matter (SOM). Generally, the sorption reaction is a partition process, which results in a linear isotherm. However, the sorption isotherm may be non-linear at the high organic concentration (Weber et al., 1992). The non-linear sorption behaviors can be attributed to the variation of the organic interaction with SOM. In this study, the non-linear sorption, i.e., the concentration effect, was illustrated by assessing the partition coefficient with various organic concentrations. Partition coefficient is the sole parameter used to describe the distribution of organic contaminant in the soil-water system. The partition coefficient usually on the mass basis, K_d, is defined as the ratio between the concentration of the organic compound in the solid phase and in the liquid phase, respectively, i.e.,

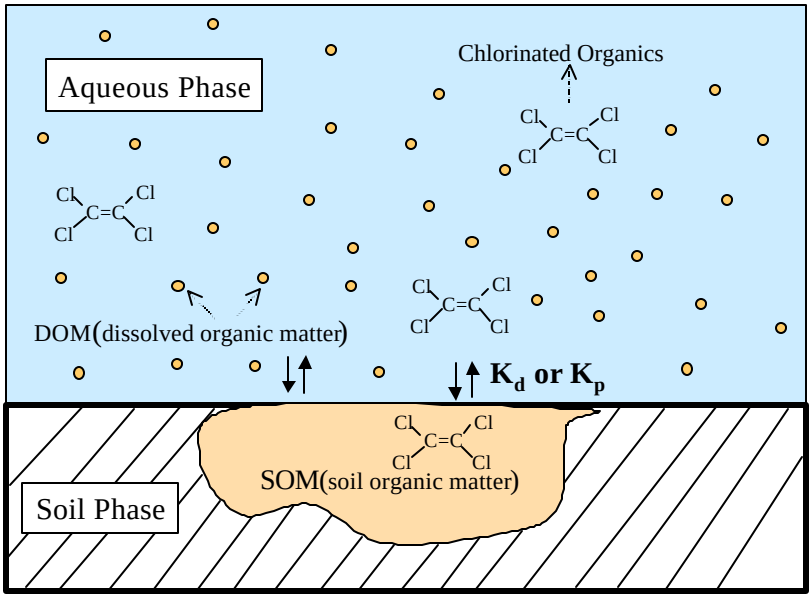

Figure 3.1. Schematic representation of the organics-water-soil system.

$$K_d = \frac{q_e}{C_e} \qquad [3.4]$$

where q_e (mg/Kg) is the organic concentration in the soil phase and C_e (mg/L) is the solute concentration in the aqueous phase. A linear sorption isotherm means that K_d is a constant, whereas, the partition coefficient is varying when the sorption behavior is non-linear.

However, in order to incorporate with the fugacity concept, one can redefine the partition coefficient on a molar basis, K_p:

$$K_p = \frac{X_s}{X_w} \qquad [3.5]$$

where X_s and X_w are the mole fraction of solute in aqueous and soil phase, respectively. The partitioning process is driven by the relative fugacity of the organics in each phase. The partition coefficient represents the organic distribution behavior at equilibrium whereas the relative fugacity of organic in each phase is identical.

The partial molar free energy or chemical potential μ of a compound in a given phase ϕ at a specific temperature and pressure can be expressed by:

$$m_f = m^o + RT \ln \frac{f_f}{f^o} \qquad [3.6]$$

where μ^o = chemical potential at standard state, f_ϕ = fugacity in phase ϕ, f^o = fugacity at standard state. Since the fugacity in the liquid phase can be replaced by $\gamma_\phi x_\phi$, Equation 3.6 yields:

$$m_f = m^o + RT \ln g_f x_f \qquad [3.7]$$

where γ_ϕ = the activity coefficient, x_ϕ = the mole fraction concentration of compound in phase ϕ. The term, $\gamma_\phi x_\phi$, is a measurement of how "active" the compound is relative to its reference state. For the sake of simplicity, the pure liquid compound is usually chosen to be the reference state at the stated temperature and pressure of the system. The term, $\gamma_\phi x_\phi$, is therefore referred to the activity of the solute compound. Obviously a high activirty indicates high relative fugacity. At equilibrium, the partial molar free energy of a compound (fugacity) in each phase must be equal, i.e., $\mu_s = \mu_w$. The subscripts w, and s, are designated for aqueous phase and soil phase, respectively. Accordingly, one has:

$$g_s X_s = g_w X_w \qquad [3.8]$$

By arranging Equation 3.8., it yields:

$$\frac{X_s}{X_w} = \frac{g_w}{g_s} \qquad [3.9]$$

By substituting Equation 3.9 into Equation 3.5, the partition coefficient is expressed:

$$K_p = \frac{g_w}{g_s} \qquad [3.10]$$

The molar fraction of organic in aqueous and soil phase, X_w and X_s, can be obtained by experimental measurements. In a diluted solution, the activity coefficient of organic compunds in aqueous phase, γ_w, can be estimeated by its water solubility. According to Equation 3.8, the activity coefficient of an organic compound sorbed in soils, γ_s, can be determined. The value of γ_s can provide the characteristic interaction information between the soil and the organic contaminant. Likewise, when γ_s, was determined in the diluted solution, then, the γ_w can account for the organic affinity at various concentrations toward the liquid phase.

The soil organic carbon (SOC) was considered as the major sorbent for the organic sorption. To calculate the molar fraction of organic in SOC, X_s, the molar volume and the density of the SOC are required. In this study, the SOM extent , 1.7% (by weight), can be measured experimentally. The soil organic content is 2 grams organic matter/gram organic carbon (Schwarzenbach et al., 1993), the density of organic carbon is calculated to be 0.6 g/cm^3. Accordingly, the volume of SOC per gram soil is: $0.017/(2\text{x}0.6) = 1.4\text{x}10^{-2}$ cm^3. Chiou and co-workers (1983) reported that the molar volume of the organic polymer phase is around 10^4 to 10^6 (cm^3/mole) and it was applied as the SOC molar volume. The mole number of SOC per gram soil can be obtained: $1.4\text{x}10^{-2}/10^4 = 1.4\text{x}10^{-6}$ mole. This value was used for the X_s calculation in this study.

3.2.1. Concentration Effect

Based on the partition concenpt, many researchers assumed that the activity coefficient of the partitioning chemical is independent of its concentration in the aqueous phase (Schwarzenbach, 1993). This assumption is reasonable at a low aqueous concentration where interactions among organic molecules is small that its influence may be negligible. However, this interaction may become significant at high organic concentration. Likewise, the activity

coefficient of sorbed organic compound may change when one treat the soil organic carbon as a solvent. Compared to the organic concentration in aqueous phase (dilluted solution), the concentration of the organic compound sorbed is much higher (concentrated solution). Accordingly, the γ_s value will vary with the concentration of organic compound and that γ_w can be considered a constant during the sorption process.

In the diluted solution, the activity coefficient, γ_w, is approximately equal to its value at saturation, γ_w^{sat}. The activity coefficient at saturation can be computed by following equation:

$$g_w^{sat} = \frac{1}{X_w^{sat}} \qquad [3.11]$$

The term, X_w^{sat}, in the diluted solution is equal to $V_w C_w^{sat}$ approximately, where V_w is the molar volume of water, 0.018 and C_w^{sat} (mole/L) is the water solubility of the solute. Equation 3.11 can be rewitten as:

$$g_w^{sat} \cong \frac{1}{V_w C_w^{sat}} \qquad [3.12]$$

The molar volume of water is 0.018 L/mole, Equation 3.12 yields:

$$g_w^{sat} \cong \frac{1}{0.018 C_w^{sat}} \qquad [3.13]$$

The magnitude of X_w and X_s can be obtained experimentally. According to Equation 3.8, the activity coefficient of organic with soil organic carbon, γ_s, is obtained. The γ_s values at various orgnaic concentrations were used for the illustration fo the concentration effect.

3.2.2. Soil to Solution Ratio Effect

When the soil to solution ratio increases, i.e., the increase of soil concentration, in a soil-water system, the DOM extent will increase. The mixture of DOM and water can be considered as a homogeneous phase. The presence of DOM serves as a cosolvent to increase the solubility of the organic comound. Accordingly, the organic interaction with the solution will vary with the DOM concentration, i.e., the soil to solution ratio. The effect of soil to solution ratio can be attributed to the presence of DOM in the soil-water system.

For assessing the effect of soil to solution ratio, in this study, the activity coefficient of organic in the liquid phase, γ_w, at different soil concentrations was investigated. According to Equation 3.8, the γ_w can be determined if X_w, X_s and γ_s were already known. Terms, X_w and X_s, can be obtained experimentally. The value of γ_s can be obtained by conducting the soprtion test under the diluted condition. Then, by substituting γ_s, X_s, and X_w, into Equation 3.9, the activity coefficients of organics in the liquid phase, γ_w, can be obtained at various soil to solution ratios. The activitry coefficient, γ_w, reflects the affinity between DOM solution and the organic, which was used for the explanation of the soil to solution ratio effect.

3.2.3. Interaction between Organic Contaminants and Soil

The activity coefficient indicates the compatibility between the the organic solute and the solvent. A high activity coefficient for the solute presents low degree of sollubilization to the solvent. To evaluate the interaction between the organic contaminant and the soil, the SOC has been regarded as a solvent and its sorption characteristics are similar to that of a polymer (Weber et al., 1992). Flory and Hocker (1971) proposed an equation to compute the activity "a" of small solute molecules in a polymer:

$$\ln a = \ln f_1 + \left(1 - \frac{V_1}{V_2}\right) f_2 + c f_2^2 \qquad [3.14]$$

where subscript 1 represents the solute phase, subscript 2 represents the polymer, ϕ_i is volume fraction concentration, V_i is molar volume, and χ is called the Flory interaction parameter.

Flory-Huggins theory has been used to describe the thermodynamics of organic contaminants in a soil-water system (Chiou, 1983; Chin, 1989; Spurlock,1994) and it was always simplified as:

$$\ln g = 1 + c \qquad [3.15]$$

The interaction parameter, χ, is an indication, like the activity coefficient, of the compatibility between the organic solute and the soil. A high χ value presents the low compatibility, which indicates unfavorable solute-soil interactions. Thererfore, the interaction parameter, χ, is a characterization parameter to express the interaction between various organic contaminants and soils. In analogy to the excess Gibbs free energy in the solute-solvent system, the residual chemical potential, μ_1^R, has been used to quantify the interaction energy between the organic contaminant and SOC (Spurlock, 1994). The excess Gibbs free energy is the combination of the combinatorial term (entropic contribution to the excess energy) and the residual term, μ_1^R, (enthalpic contribution to the excess energy). The combinatorial entropic contribution to the excess energy has been reported as a constant for the partition of organic compounds in a soil-water system (Chiou, 1983). As a result, the residual chemical potential, μ_1^R, is able to provide the information of the sorption enthalpic energy for various organic compounds in soils. Flory (1971) suggested an equation to determine the residual chemical potential, that is:

$$m_1^R = RTc \qquad [3.16]$$

3.3. Methodology

Soil samples were collected from a specific DOE waste site. The characteristics of soil including particle size distribution, pH, ECEC, organic matter, soil moisture, hydraulic conductivity, zeta potential, pH_{zpc}, and specific surface area were analyzed. All the experimental results of soil properties are shown in chapter 2. The organic chemicals were purchased from Aldrich Co (Milwaukee, WI). The purity of PCE, TCE, carbon tetrachloride, and chloroform is ca. 99.0%. Table 3.1 lists the major features of these organic chemicals including molecular formula, molecular weight, saturation water solubility (at 25 ^oC), and $\log K_{ow}$.

Table 3.1. The physical properties of PCE, TCE, carbon tetrachloride, and chloroform.

Physical Property	PCE	TCE	carbon tetrachloride	chloroform
Molecular Formula	C_2Cl_4	C_2HCl_3	CCl_4	$CHCl_3$
Molecular Weight	165.8	131.4	153.8	119.4
Saturation Solubility (mg/l)	110	1,100	800	8,000
$\log K_{ow}$	2.88	2.42	2.73	1.93

Experimental Procedures

Figure 3.2 shows the sorption experimental procedure for chlorinated organic compounds in soil-water system. Batch sorption experiments were conducted with PCE, TCE, carbon tetrachloride, and chloroform at various soil to solution ratios (by weight) ranging from 1:5 to 1:100. The initial concentrations of organic compounds range from $0.1C_s$ to $0.8C_s$ with C_s being the saturation water solubility. To a series of glass tubes (tube volume is 12 mL), a desired amount of soil and organic compound in solution of constant ionic strength electrolyte (0.05M $NaNO_3$) were added. The tubes were placed in a shaker and shaken constantly for 48 hours to reach the equilibrium condition. The mixtures were then centrifuged at 2,500 rpm (1,000 g) for 10 minutes using a centrifuge (Prescion Scientific Co. model K-9, Chicago, IL) to separate the soil from the solution. The residual concentration of the organic compound in the centrate was analyzed. The samples were extracted one time in hexane then determined with a GC/ECD (Hewlett-Packard, model 5890 series II, Wilmington DE). In order to obtain the magnitude of the dissolved organic carbon in soil solution, a series of glass tubes were used to contain the soil-water mixture without contamination at different soil to solution ratios. These samples were also shaken for 48 hours and centrifuged at 1,000g for 10 minutes. Then, the total organic carbon (TOC) of the supernatants were measured by a total organic carbon analyzer (Rosemount Analytical Inc., model DC-190, Santa Clara, CA).

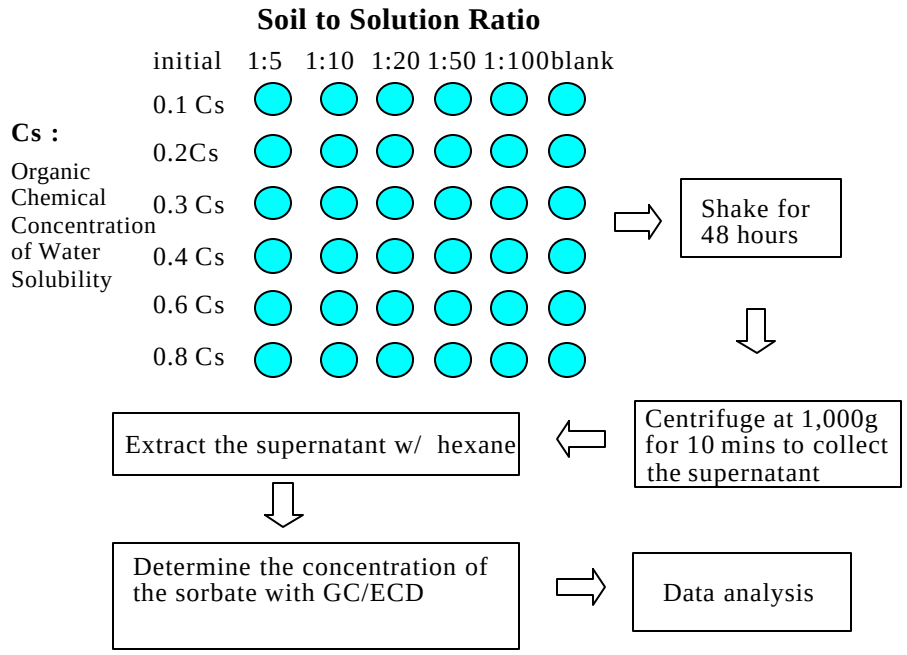

Figure 3.2. Flowchart of the sorption experimental procedure for chlorinated organic compounds.

3.4. Results

Figure 3.3 and Figure 3.4 show the sorption isotherms of PCE and TCE, respectively. Both of PCE and TCE isotherms can be closely fitted by the Langmuir equation, whereas the TCE isotherms can be also closely fitted by the linear sorption equation. For PCE, the major sorption force on soils is speculated to be van der Waals since it is a strong nonpolar organic compound. Generally, the van der Waals force introduces a low sorption capacity in the soil. When using the solubility as the initial concentration, the sorption density may approach to its maximal value. Accordingly, PCE sorption on the soil exhibits a Langmuir isotherm.

As for TCE which is a relatively polar organic compound, the forces responsible for its sorption can be dipole and van der Waals. Its sorption capacity is higher than PCE. The sorption density is not close to its maximal value even applying the solubility of TCE as the initial concentration. Therefore, TCE sorption behaviors can be fitted by both Langmuir and linear equations. In fact, the Langmuir isotherm is nearly linear in the relative low equilibrium concentration range. The different polarities can be seen from their water solubility (PCE 110 mg/l and TCE 1,100mg/l). Generally, the oragnic compound with higher water solubility has the higher polarity. The various sorption densities can be attributed to the interaction between the different polarity of organics and soil characteristics.

Figure 3.3 also shows the non-linear sorption isotherms of PCE at various soil to solution ratios. Results indicate that all experimental data at various soil to solution ratios can be fitted by the Langmuir equation. In Figure 3.4, Langmuir and linear sorption modes can fit experimetnal results of TCE at different soil to solution ratios. This may imply that the interaction mechanisms between organic contaminants and the soil does not change with the soil-solution ratio but only the interactiion extent does. Therefore, Langmuir isotherm is still applicable to describe the sorption of PCE and TCE at various soil to solution ratios.

Figures 3.5 (PCE) and 3.6 (TCE) show partition coefficients as a function of equilibrium concentration. Results indicate that the partition coefficients increase with decreasing the soil to solution ratio (i.e., low soil concentration). This is known as "soil to solution ratio effect". This can be attributed to the presence of DOM in the liquid phase. In this study, the centrifugation used for phase separation can not remove DOM in the solution during the sourption tests. The liquid phase actually contains two componants such as water and DOM. Apparently, when the soil concentration was increased, more amount of DOM would be dissolved from the soil phase to the liquid phase. The presence of DOM can change the organic chemical concentration in the liquid phase. Consequently, the soil to solution influences the distribution of organic compounds in the soil-water system.

At various soil to solution ratios (ranging from 1:5 to 1:100), the K_d values are from 20 to 240 l/kg for PCE and from 5 to 40 l/kg for TCE, respectively. According to Equation 3.1, $\log(\frac{K_d}{x}) = a \log K_{ow} + b$, the organic partition coefficient is proportional to its octanol-water partition coefficient in log scale. In other words, the organic contaminant with high hydrophobicity always has high partition coefficient. Accordingly, the partition coefficient of PCE ($\log K_{ow}$=2.88) is greater than that of TCE ($\log K_{ow}$=2.42).

Figure 3.7 shows sorption isotherms of carbon tetrachloride. These sorption isotherms can be closely fitted by the Langmuir equation. The major sorption force on soils for carbon tetrachloride is mainly attributed to be van der Waals like PCE. Figure 3.8 shows the sorption isotherms of chloroform. Results indicate that these sorption isotherms can be closely fitted by both Langmuir and linear equation like TCE. The explanation of different sorption

isotherms for carbon tetrachloride and chloform is the same as that for PCE and TCE, respectively. The different polarities can be seen from their water solubility (carbon tetrachloride 800 mg/l, chloroform 8000mg/l), which results in different sorption behaviors.

Figure 3.7 shows the non-linear sorption isotherms of carbon tetrachloride at various soil to solution ratios. Results show that experimental data at all soil to solution ratios can be fitted by the Langmuir equation. Likewise, chloroform follows the Langmuir equation at various soil to solution ratios (shown in Figure 3.8). This implies that the interaction mechanisms between organics (carbon tetrachloride and chloroform) and the soil is independent of the soil to solution ratio. Only the extent of the organic interaction change with the soil to solution ratio.

Figures 3.9 (carbon tetrachloride) and 3.10 (chloroform) show partition coefficients as a function of the equilibrium concentration. Results show that the partition coefficient increases with decreasing soil to solution ratio, i.e., low soil concentration. This can be seen from the sorption experiments of PCE and TCE as well, which is attributed to the presence of DOM in the aqueous phase. DOM can enhancess the organic concentration in the aqueous phase due to the interaction between DOM and organic contaminants. The partition coefficient is calculated according to the chemical concentration ratio between lsolid and liquid phase, $K_d = q_e/C_e$. The increase of the organic concentration in liquid phase results in decreasing the partition coefficient. Therefore, the partition coefficients of organics decrease with increasing soil to solution ratio.

The K_d values range from 10 to 170 l/kg for carbon tetrachloride and from 1 to 10 l/kg for chloroform based on experimental results. In the comparison of all selected chlorinated organic compounds, it is seen that the order of the partition coefficients is PCE (10 to 100 l/kg) ≅ carbon tetrachloride (10 to 170 l/kg) > TCE (3 to 35 l/kg) > chloroform (1 to 10 l/kg). This order is the reverse order of their water solubility (PCE: 110 mg/L, carbon tetrachloride: 800 mg/L, TCE: 1,100 mg/L, chloroform: 8,000 mg/L). This indicates that the hydrophobicity of organic compound dominates its distribution in the soil-water system.

The partition coefficient is used to describe the distribution behavior of chemical contaminant in the soil-water mixture. In addition, it also serves as a crucial parameter in the estimation of retardation factor for the organic transport. The partition coefficient of organic contaminant measured in the sorpiton experiment was usually expected to be applicable to the transport model. However, the water content is ca. 10% to 15% by weight in the real site, which is far less than that in a over-saturated soil-water system applied to sorption experiments. Due to the effect of the soil to solution ratio, the partition coefficient determined by the sorption experiment can not represent the organic distribution in the field. In order to obtain the feasible partition coefficient, thereby, it is necessary to study the effect of soil to solution ratio on the sorption reaction.

Figure 3.11 shows the concentration of total organic carbon (TOC) as a function of the soil concentration. Results indicate that TOC (reguarded as DOM) concentration increases proportionally to the soil concentration. This indicates that the increase of soil to solution ratio (high soil concentration) increases the DOM extent in the liquid phase. The linear relationship implies that SOM contain a certain fraction of soluble organics. The slope of the straight line, 0.12 mg/g, represents the fraction of soluble organics in the soil. According to Table 2.1, the total organic matter is ca. 17 mg per gram soil. Based on results shown in Figure 3.11, each gram of soil produces 0.012 mg organic carbon in the solution.

Consequently, the fraction of soluble organics in SOM can be determined by the ratio, i.e., 0.12/17 x 100% = 0.7% (by weight).

3.5. Discussion

According to Eqaution 3.10, $K_p = \frac{g_w}{g_s}$, the distribution of organics is related to the activity coefficients, γ_w and γ_s. The activity coefficient can reflect the interaction of the solute with the solvent. In this study, the organic concentration and soil to solution ratio are two

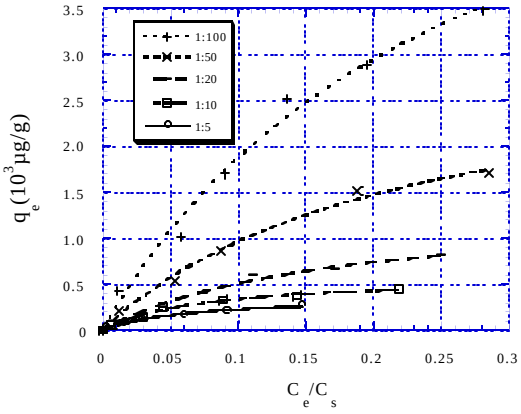

Figure 3.3. The isotherms of PCE at various soil to solution ratios. The curves are fits of the data to the Langmuir equation. Cs = 110 mg/l.

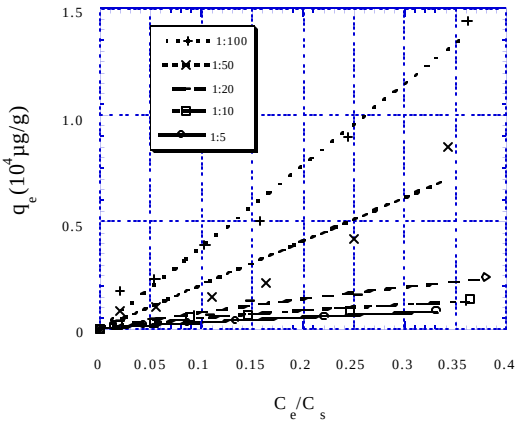

Figure 3.4. The isotherms of TCE at various soil to solution ratios. The lines are fits of the data to the Langmuir and linear equation. Cs = 1,100 mg/l.

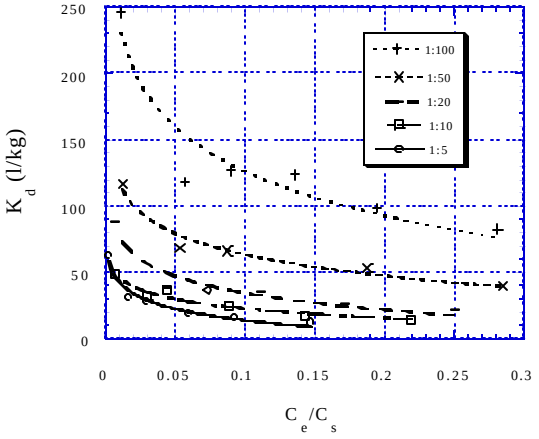

Figure 3.5. The partition coefficients, K_d, of PCE; (soil to solution ranging from 1:5 to 1:100); C_e = equilibrium concentration; C_s=water solubility of PCE (110 mg/L).

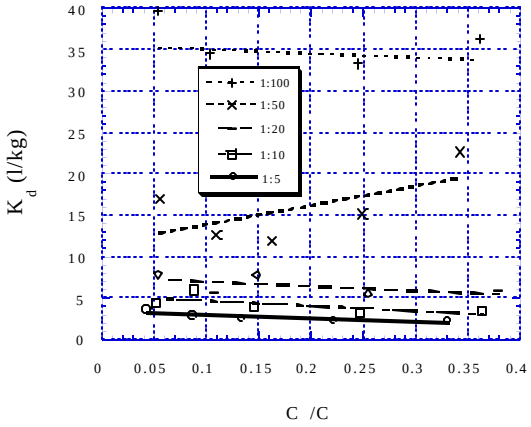

Figure 3.6. The partition coefficients of TCE; (soil to solution ranging from 1: 5 to 1:100); C_e = equilibrium concentration; C_s=water solubility of PCE (1,100 mg/L).

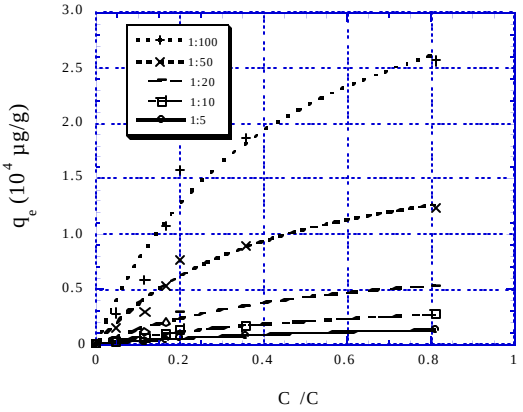

Figure 3.7. The isotherms of carbon tetrachloride at various soil to solution ratios. The curves are fits of the data to the Langmuir equation. Cs = 800 mg/l.

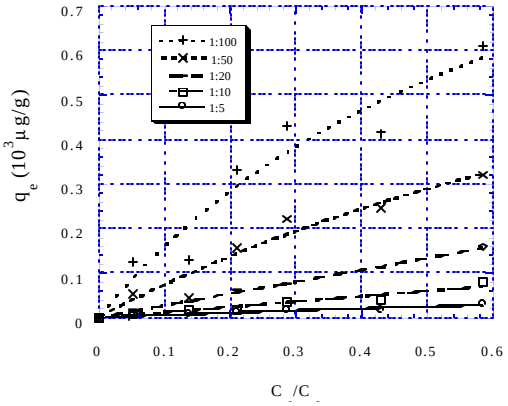

Figure 3.8. The isotherms of chloroform at various soil to solution ratios. The lines are fits of the data to the Langmuir and linear equation. Cs = 400 mg/l.

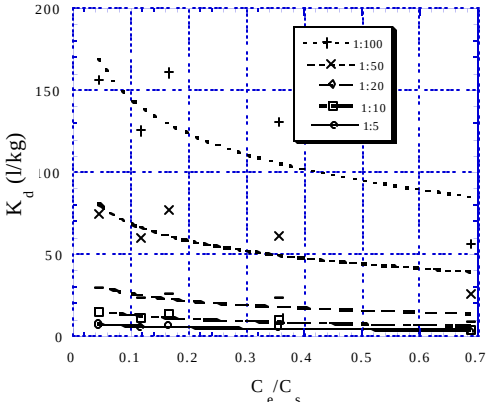

Figure 3.9. The partition coefficient of carbon tetrachloride.

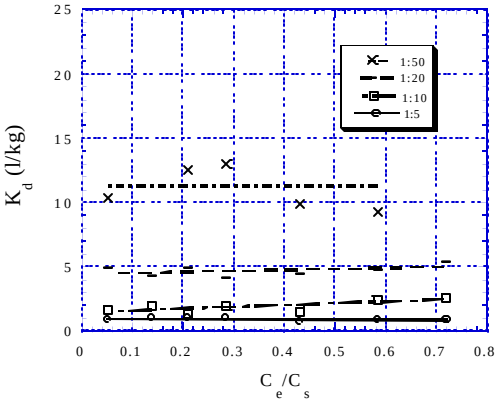

Figure 3.10. The partition coefficient of chloroform.

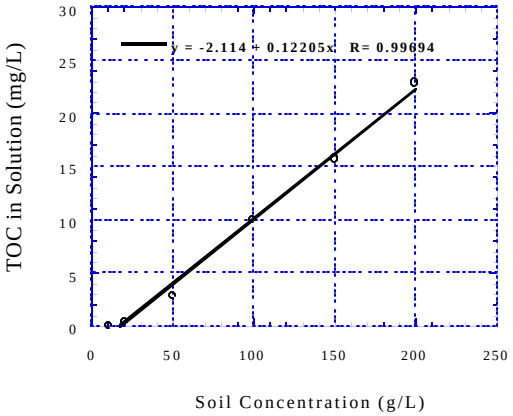

Figure 3.11. The total organic carbon in solution as a function of soil concentration.

major factors controlling the sorption of chlorinated organic compounds in the soil-water system. The analysis of activity coefficient is a useful approach to elucidate the effects of these sorption factors. It can provide the information of fundamnetal interaction between the organic contaminant and the soil.

3.5.1. Concentration Effect

In this study, the activity coefficient of organics in the soil, γ_s, at various organic concentrations was used to illustrate the concentration effect, i.e., non-linear sopriton isotherm. According to Figure 3.11, TOC is almost absent from the solution at the 1:100 soil

to solution ratio, i.e., soil concentration is 10 g/L.. The solution can be considered to consist only of pure water. Accordingly, the activity coefficient of organic in the solution, γ_w, is approximaely equal to that in the water. The value of γ_w can be computed by Equation 3.13, $\gamma_w = 1/0.018C_w^{sat}$. By substituting γ_w, X_w, and X_s, into Equation 3.9, $\frac{X_s}{X_w} = \frac{g_w}{g_s}$, the γ_s value was given. The terms, X_w and X_s, are the molar fraction of organic compound in aqueous phase and soil phase, respectively. They can be obtained based on the experimental results of the organic sorption. Furthermore, the Flory interact parameter, χ, can be determined by Equation 3.15, $\ln g = 1 + c$. The residual partial molar free energy, μ_1^R, was obtained from Equation 3.16, i.e., $m_1^R = RTc$.

Table 3.2. Solute activity coefficients, Flory interaction parameters, and the residual partial molar free energies for various solute concentrations.

Sorbate	$\ln\gamma_s$	χ	μ_1^R (KJ/mol)
PCE			
0.1 C_s	-6.0	-7.0	-17.3
0.2 C_s	-5.1	-6.1	-15.1
0.3 C_s	-4.4	-5.4	-13.3
0.4 C_s	-3.5	-4.5	-11.2
0.6 C_s	-3.0	-4.0	-9.9
0.8 C_s	-1.5	-2.5	-6.3
Carbon Tetrachloride			
0.1 C_s			
0.2 C_s	-3.7	-4.7	-11.7
0.3 C_s	-3.0	-4.0	-9.8
0.4 C_s	-2.0	-3.3	-8.1
0.6 C_s	-1.8	-2.8	-6.9
0.8 C_s	-1.8	-2.8	-6.9
	-1.6	-2.6	-6.4
TCE			
0.1 C_s	-3.7	-4.7	-11.6
0.2 C_s	-3.3	-4.3	-10.7
0.3 C_s	-2.6	-3.6	-8.8
0.4 C_s	-2.1	-3.1	-7.6
0.6 C_s	-0.8	-0.2	-0.4
0.8 C_s	-1.4	-0.4	0.9
Chloroform			
0.1 C_s	-5.6	-6.6	-16.3
0.2 C_s	-5.5	-6.5	-16.1
0.3 C_s	-4.6	-5.6	-14.0
0.4 C_s	-4.4	-5.4	-13.3
0.6 C_s	-4.4	-5.4	-13.3
0.8 C_s	-4.0	-5.0	-12.4

Note: all data calculated at 1: 100 soil to solution ratio.

Based on experimental results, Table 3.2 lists the organic activity coefficient, $\ln\gamma_s$, Flory interaction parameter, χ, and the residual partial molar free energy, μ_1^R, at various organic concentrations for PCE, carbon tetrachloride, TCE, and chloroform, respectively. It is seen that the χ value increases with increasing organic concentration. The Flory interaction parameter, χ, is an indication for the organic-soil interaction; a high χ value exhibits an unfavorable interaction. Consequently, the interaction between the organic and the soil becomes more unfavorable with increasing organic concentration. Since the μ_1^R is the enthalpic contribution to the excess mixing Gibbs free energy, the negative value of μ_1^R shown in Table 3.2 indicates that the the interaction between chlorinated organics and the soil is exothermic. Table 3.2 also shows the variance of Flory interaction parameters from 0.1 to 0.8 water solubility for each chlorinated organic compound. The various χ values of PCE, carbon tetrachloride, TCE, and chloroform range from –7.0 to -2.5, -4.7 to –2.6, -4.7 to –0.4, and –6.6 to -5.0, respevtively. Among all selected organics, the concentration effect on PCE is most significant due to its greatest variance (4.5). In contrast to PCE, the concentration effect on chloroform is relatively insignificant because the χ variance is only 1.5. The order of the concentration effect is PCE > carbon tetrachloride ≅ TCE > chloroform, which follows order of their hydrophobicity. This indicates that SOC is a relatively low hydrophobicity material compared with these chlorinated organics. Therefore, the concentration effect on the organic with high hydrophobicity becomes significant.

Figure 3.12 and 3.13 show the Flory interaction parameter, χ, and residual partial molar energies, μ_1^R, versus the molar fraction of organic in the soil phase, respectively. Results indicate that both of the χ, and μ_1^R increase with increasing organic concentration. It is noticed that the interaction energy is expected to reach an infinite value when the molar fraction of solute approaches to 1.0. This is because the organic can not overcome the repulsive interaction energy from the soil at a very high molar fraction.

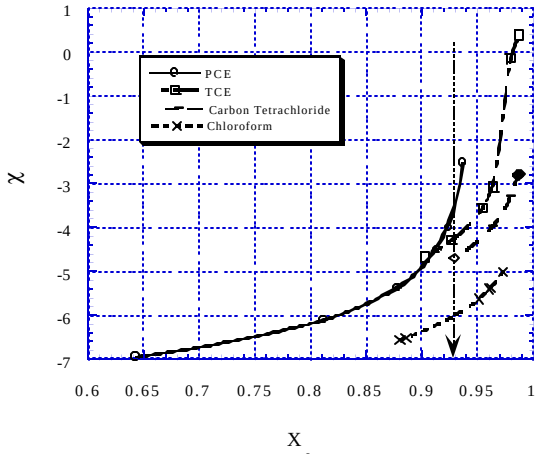

Figure 3.12. The c as a function of solute molar fraction with soil organic carbon. The arrow indicates the molar fraction at which all four compounds are compared.

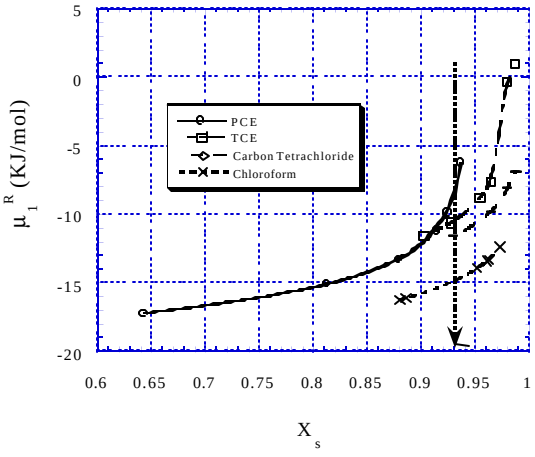

Figure 3.13. The μ_1^R as a function of solute molar fraction with soil organic carbon. The arrow indicates the molar fraction at which all four compounds are compared.

To compare the interaction energy of different chlorinated organic compounds, Figure 3.13 shows μ_1^R values of various chlorinted organics at an identical molar fraction. The order of the interaction energy is PCE > TCE ≅ carbon tetrachloride > TCE, which is in reverse

order of the water solubility. This indicates that the organic contaminant with higher hydrophobicity (e.g., PCE) has weaker interaction with SOC. Since most organic matter in natural soils is polar with a combination of hydroxy- and oxy-moieties exposed to their exterior (Schwarzenbach, et al., 1993), the nonpolar compounds in soil matrix are unfavorably bound compared with polar ones. Accordingly, the interaction energy of sorption reaction between organics and soils follows the order of the organic hydrophobicity.

Although organic compound with high hydrophobicity (e.g., PCE) presents weak interaction with soils, the order of the partition coefficients, PCE > carbon tetrachloride ≅ TCE > chloroform, is still the same as that of the hydrophobicity..According to Equation 3.9, $K_p = \frac{g_w}{g_s}$, the partition coefficient is obtained by comparing the organic interaction in liquid and solid phase at equilibrium. High hydrophobic compounds may have high partition coefficient when the interaction in liquid phase is significant (i.e., γ_w value is great). In this study, the $\ln\gamma_s$ value of PCE at 0.3 C_s (-4.4) is the same as that of chloroform at 0.4 C_s, shown in Table 3.2. The γ_w value of PCE (9×10^4) is far greater than that of chloroform (800) according to Equation 3.13, $\gamma_w = 1/0.018C_w$. Accordingly, the K_d value of PCE is greater than that of chloroform. This indicates that the distribution of organic not only depends on the organic interaction with the soil but also on its interaction with the solution. Since the organic interaction in the aqueous phase is significant, the high hydrophobic organic exhibits high partition coefficient.

3.5.2. Soil to Solution Ratio Effect

Based on experimental results, Table 3.3 lists the organic activity coefficients in the liquid phase, γ_w, and the solubility ratio, $\log(C/C^{sat})$ at various soil to solution ratios. The γ_w computation was based on experiments conducted at of 0.1 C_s organic concentration, where the concentration effect is negligible. It is seen that the organic concentration, (C/C^{sat}), increases experimentally with increasing the soil concentration, i.e., high soil to solution ratio. The increase of soil concentration increases the DOM concentration in the solution. DOM serves as "a cosolvent", thereby, the organic concentration in the aqueous phase increases with the soil concentration. According to Table 3.3, the activity coefficient, γ_w, decreases experimental with increasing the soil concentration. The activity coefficient reflects the affinity between the solute and solvent and its low value exhibits a high affinity. The decrease of the activity coefficient, $\ln\gamma_w$, exhibits the increase of the affinity due to the presence of DOM.

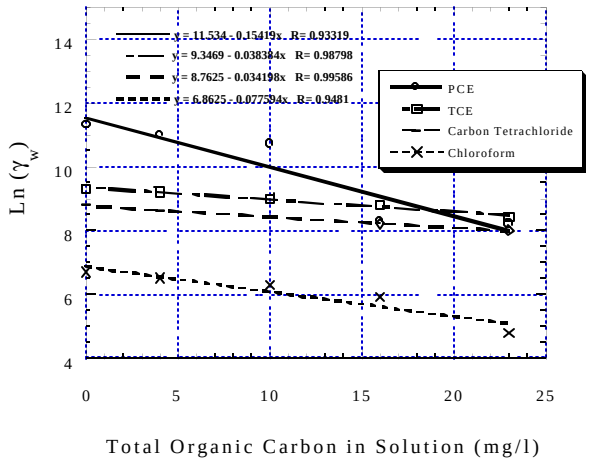

Figure 3.14. The $\ln g_w$ as a function of total organic carbon in solution.

Figure 3.14 shows the log value of the activity coefficients, $\ln\gamma_w$, as a function of TOC in the solution. TOC concentration

can be an indication to present the DOM extent and corelated to the activity coefficient. Results show that a linear relationship between TOC and $\ln\gamma_w$, that is:

$$Ln\gamma_w = m\text{-}n[TOC] \qquad [3.17]$$

where m is the $\ln\gamma_w$ value in the absence of TOC, n is a interaction coefficient. The interaction coefficient, n, indicates the compatibility between the organic and TOC (or DOM). A high n value indicates a favorable interaction between the organic and the solution. According to Figure 3.15, the n values of PCE, TCE, carbon tetrachloride, and chloroform are ca. 0.15, 0.04, 0.03, and 0.08, respcetively.

Table 3.3. Solute activity coefficients in liquid phase, ln g_w, and the solubility ratio at various soil to solution ratio.

Sorbate	$\ln\gamma_w$	$\log(C/C^{sat})$
PCE		
1:5	8.2	1.37
1:10	8.3	1.33
1: 20	10.7	0.25
1: 50	11.0	0.16
1:100	11.3	0.00
TCE		
1:5	8.4	0.33
1:10	8.8	0.25
1:20	9.0	0.19
1:50	9.2	0.08
1:100	9.3	0.00
Carbon Tetrachloride		
1:5	8.0	0.39
1:10	8.2	0.22
1:20	8.4	0.13
1:50	8.6	0.04
1:100	8.8	0.00
Chloroform		
1:5	4.8	0.85
1:10	5.9	0.35
1:20	6.3	0.17
1:50	6.5	0.09
1:100	6.7	0.00

Note: the data calculated under the 0.1 C/Cs condition.

3.6. Summary

The use of the fugacity concept is useful for illustrating the partition behavior of organic compounds in the soil-water system. This approach is not only able to analyze the non-linear sorption isotherms (concentration effect) but also explain the soil to solution ratio effect. The activity coefficient is a useful means to describe the quantitative feature of the organic-soil interaction without detailed information of their interaction mechanisms. By comparing the

activity coefficients, γ_w and γ_s, one can illustrate the trend of organic distribution between the soil and water phase.

In addition to the hydrophobicity (K_{ow}) of organic contaminant and SOM, the organic compound concentration and the soil to solution ratio can influence the organic distribution as well. As increasing the organic compound concentration, the activity coefficient, γ_w, can be considered as a constant and γ_s increases due to the increase of the repulsive force from the soil phase. The change of γ_s makes the sorption isotherms of organic contaminants non-linear. According to the interaction interpretation of γ_s, it can be found that the sorption reaction between these selceted chlorinated organics and the soil is exothermic.

Based on experimental results, the soil to solution effect can be attributed to the presence of the DOM in the liquid phase. DOM can act as a cosolvent in liquid phase, which results in the increase of the organic concentration. Accordingly, the partition coefficients ($= X_s/X_w$) of these chlorinated compounds decrease with increasing the soil to solution ratio. It is seen that the organic activity coefficient in the solution, $\ln\gamma_w$, presents a linear relationship with the TOC concentration. The linear expression is $\ln\gamma_w = m-n[TOC]$, where m is the $\ln\gamma_w$ value in the absence of TOC, n is an interaction coefficient. Based on the experimental results, the n values of PCE, TCE, carbon tetrachloride, and chloroform are ca. 0.15, 0.04, 0.03, and 0.08, respcetively.

3.7. References

1. Adamson, A. W., Physical Chemistry of Surfaces, John Wiley & Sons, Inc., 5th edition, Canada, 1990.
2. Barrow, N. J., P. G. Ozanne, and T. C. Shaw (1965), Nutrinet Potential and Capacity. I. The Concepts of Nutrient Potential and Capacity and their Application to Soil Potassium and Phosphorus, Australian J. Agricul. Res., Vol. 16, 61 - 76.
3. Barrow, N. J. and T. C. Shaw (1979), Effects of Soil: Solution Ratio and Vigour of Shaking on the Rate of Phosphate Adsorption by Soil, J. Soil Sci., Vol. 30, 67 - 76.
4. Chin, Y. P. and W. J. Weber, Jr. (1989), Estimating the Effects of Dispersed Organic Polymers on the Sorption of Contaminants by Natural Solids. 1. A predictive Thermodynamic Humic Substance-Organic Solute Interaction Model, Environ. Sci. Technol., Vol. 23, 978-984.
5. Chiou, C. T., L. J. Peters, and V. H. Freed (1979), A Physical Concept of Soil-Water Equilibria for Nonionic Organic Compounds, Science, Vol. 206, 831 - 832.
6. Chiou, C. T., J. F. Lee, and S. A. Boyd (1983), Partition Equilibria of Nonionic Organic Compounds between Soil Organic Matter and Water, Environ. Sci. Technol., Vol. 17, No. 4, 227-231.
7. Chiou, C. T., J. F. Lee, and S. A. Boyd (1990), The Surface Area of Soil Organic Matter, Environ. Sci. Technol., Vol. 24, 1164-1166.
8. Flory, P. J. and H. Hocker (1971), Thermodynamics of Polystyrene Solutions Part 1. - Polystyrene and Methyl Ethyl Ketone, Trans. Faraday Soc., Vol. 67, 2258-2269.
9. Fordham, A. W. (1963), The Measurement of Chemical Potential of Phosphate in Soil Suspensions, Australian J. Agricul. Res., Vol. 1, 144 - 156.
10. Fotovat, A., R. Naidu, and M. E. Sumner (1997), Water:Soil Ratio Influence Aqueous Phase Chemistry of Indigenous Copper and Zinc in Soils, Australian J. Soil Research, Vol. 35, 687 - 709.

11. Hope, G. D. and Syers, J. K. (1976), Effects of Solution: Ratio on Phosphate Sorption by Soil, J. Soil Sci., Vol. 27, 301 -306.
12. McCall, P. J. and G. L. Agin (1985), Desorption Kinetics of Picloram as Affected by Residence Time in the Soil, Environ. Toxicol. Chem., Vol. 4, 37-44.
13. Mingelgrin, U. and Z. Gerstl (1983), Reevaluation of Partitioning as a Mechanism of Nonionic Chemicals Adsorption in Soil, J. Environ. Quality, Vol. 12, No. 1, 1-11.
14. Puls, R. W., R. M. Powell, D. Clark, and C. J. Eldred (1991), Effects of pH, Soil/Solution Ratio, Ionic Strength, and Organic Acids on Pb and Cd Sorption on Kaolinite, Water, Air, and Soil Pollution, Vol. 57, 423 - 430.
15. Routson, R. C. and R. J. Serne (1972), Experimental Support Studies for the Percol and Transport Model, BNWL-1719.
16. Rutherford, D. W. and C. T. Chiou (1992), Effect of Water Saturation in Soil Organic Matter on the Partition of Organic Compounds, Environ. Sci. Technol., Vol. 26, 965-970.
17. Sabbah, I. and M. Rebhun (1997), Adsorption-Desorption of Trichlorophenol in Water-Soil Systems, Wat. Environ. Res., Vol. 69, No. 5, 1032 - 1038.
18. Schellenberg, K., C. Leuenberger, and R. P. Schwarzenbach (1984), Sorption of Chlorinated Phenols by Natural Sediments and Aquifer Materials, Environ. Sci. and Technol., Vol. 18, 652-657.
19. Schwarzenbach, R. P., and J. Westall (1981), Transport of Nonpolar Organic Compounds from Surface Water to Groundwater. Laboratory Sorption Studies, Environ. Sci. Technol. Vol. 15, 1360-1367.
20. Schwarzenbach, R. P., P. M. Gschwend, and D. M. Imboden, Environmental Organic Chemistry, New York, 1993.
21. Seth, R., D. Mackay, and J. Muncke (1999), Estimating the Organic Carbon Partition Coefficient and its Variability for Hydrophobic Chemicals, Environ. Sci. Technol., Vol. 33, 2390-2394.
22. Spurlock, F. C. and J. W. Biggar (1994), Thermodynamics of Organic Chemical Partition in Soils. 1. Development of a General Partition Model and Application to Linear Isotherms, Environ. Sci. Technol., Vol. 28, No.6, 989-995.
23. Voice, T. C. and W. J. Weber Jr (1983), Sorption of Hydrophobic Compounds by Sediments, Soils and Suspended Solids-I Theory and Background, Wat. Res., Vol. 17, 1433-1441.
24. Weber Jr, W. J., T. C. Voice, M. Pirbazari, G. E. Hunt, and D. M. Ulanoff (1983), Sorption of Hydrophobic Compounds by Sediments, Soils and Suspended Solids-II Sorbent Evaluation Studies, Wat. Res., Vol. 17, 1443-1452.
25. Weber Jr, W. J., P. M. McGinley, L. E. Katz (1992), A Distributed Reactivity Model for Sorption by Soils and Sediments. 1. Conceptual Basis and Equilibrium Assessments, Environ. Sci. Technol., Vol. 26, No.10, 1955-1962.
26. Weiss, A. J. and P. Colombo (1979), Evaluation of Isotope Migration-Land Burial Water Chemistry at Commercially Operated Low-Level Radioactive Waste Disposal Sites, NUREG/CR-1289.
27. White, R. E. (1966), Studies of the Phosphate Potentials of Soil. IV. The Mechanisms of the Soil / solution ratio effect, Australian J. Agricul. Res., Vol. 4, 77 - 85.

4. DESORPTION OF POLYCYCLIC AROMATIC HYDROCARBONS IN THE PRESENCE OF SURFACTANT

4.1. Introduction

The subsurface contamination by hazardous organic pollutants is an important environmental issue. Among various organic contaminants, polycyclic aromatic hydrocarbons (PAHs) are of special concern due to their high toxicity and hydrophobicity. By nature of high hydrophobicity, PAHs are strongly sorbed to soil or sediments (Karickhoff, 1984). In other words, the soils contaminated by PAHs are difficult to clean up. From the view point of removal efficiency, the desorption of PAHs plays a key role in the the remediation process. The removal efficiency is enhanced upon the increase in the desorption rate of PAHs in soil-solution systems. Since surfactant has the high solubility for organics, it is expected that surfactant can increase the desorption rate of hydrophobic contaminants in soils. It has been reported that surfactants have been used in soil-washing, soil-flushing, and pump-and-treat techniques (Mackay and Cherry, 1989). Generally, aggregates of surfactant molecules (micelles) can increase the dissolution and mobility of organic contaminants in the water and soil phase, respectively (Edwards et al., 1991). Nonetheless, the surfactant can be sorbed by the soil and becomes part of the soil organic matter (SOM). Therefore, the sorbed surfactant can increase the organic sorption density of the soil, thereby increasing the stability of the organic contaminants in soils. In addition, the sorbed surfactant, if it is toxic or hazardous, may cause another environmental problems. When applied in remediation process, surfactant, especical anionic surfactant, may precipitate which can significantly impact the removal efficiency (Rouse et al., 1993). Precipitation can be minimized by the use of selecting the appropriate anionic surfactants. Another way to avoid the precipitation is by mixing the nonionic surfactant with the anionic surfactant. Mixing two different surfactants can reduce the overall CMC, thereby decreasing the surfactant precipitation (Sabatini, 1991). According to the above illustration, some disadvantages will occur when the surfactant application is not well-designed. Therefore, it is necessary to study the desorption behavior of contaminants in the presence of surfactant.

This work explores the solubilization of PAHs in an artificial synthetic surfactant, Triton X-100, and in a biosurfactant, rhamnolipid, respectively. The compounds of PAHs studied include fluorene, phenanthrene, anthracene, fluoranthene, and pyrene. The partition coefficients of PAHs in these two soil-surfactant systems were measured. A quantitative relationship between the partition coefficient and the octanol number of PAHs was developed by relating experimental data of PAHs solubilization. Additionally, the sorption behavior of the synthetic and the bio-produced surfactants on both uncontaminated and PAHs contaminated soils were investigated.

4.1.1. Fundamentals of Surfactants

A surfactant molecule consists of both hydrophilic and hydrophobic moieties. The molecular structure makes surfactants accumulate at interfaces, e.g., air-water, oil-water, and water-solid preferentially. The hydrophilic moiety of the surfactant prefers to stay in polar phase such as water. The hydrophobic moiety of surfactant will prefer the nonpolar phase like the oil. Therefore, surfactants can accumulate at an oil-water interface (West and Harwell, 1992). Many industrial applications takes advantatge of the amphiphilic

characteristic of surfactants. The accumulation of surfactants at water-oil interface can reduce the surface tension of water, which improves the wetting process.

Surfactants can be generally categorized into four groups including cationic, anionic, nonionic and zwitterionic, i.e., both cationic and anionic. This classification is based on the nature of their head group, i.e., the hydrophilic head. In the aqueous solution, surfactant molecules form micelles when the surfactant concentration exceeds a certain value. This concentration is called the critical micelle concentration, CMC. The CMC value of a surfactant is a function of surfactant type (nonionic surfactants generally have lower CMC than ionic surfactants) and system conditions, e.g., temperature and hardness (Rosen, 1989). Micelles consist of two portions: the hydrophilic exterior which is oriented toward water phase and the hydrophobic interior which is away from the water phase and oriented toward the center of micelles. Since hydrophobic organic compounds are soluble in the interior of micelle, the solubility in water will increase. This increasing "aqueous solubility" of organic compounds in micelles is referred as solubilization. The degree of organic solubilization depends on the class and the concentration of the surfactant.

Although the surfactant has the potential to increase the aqueous solubility of hydrophobic contaminants and to facilitate the organic removal efficiency, the accumulation at the soil-water interface may be the disadvantage to engineering applications. The surfactant sorption on the soil is undesirable. Among the four types of surfactant, cationic surfactants exhibit the strongest attraction to the soil surface. This can be attribued to the negative charge of the soil surface in a neutral pH environment. Generally, most surfactant sorptions displays three to four distinct regions in the sorption isotherm of which some regions can be fitted approximately by the Langmuir isotherm (Rosen, 1989).

4.1.2. Biosurfactant

Many bacterial species produce biosurfactants. There are a variety of biosurfactants, most of which can be classified as anionic or nonionic. In addition, biosurfactants can also be classified into several broad groups: glycolipids, lipopeptides, lipopolysaccharides, phospholipids, and fatty acids/neutral lipids (Fiechter, 1992). The largest and best-studied group of biosurfactants is glycolipids, which include the sophorose-, rhamnose-, trehalose-, sucrose-, and fructose-lipids. Many factors including growth conditions, culture medium nutrients, temperature, pH, and agitation control the production and purification of biosurfactants (Miller, 1995). Biosurfactants have a typical molecular weights range of approximately 500 to 1500 mw and CMC values of 1 to 200 mg/l (Lang and Wagner, 1987).

Like many other synthetic surfactants, biosurfactants can improve the removal efficiency of the organic contaminants. Compared to synthetic surfactant and in terms of remediation, biosurfactants have several advantages over synthetic ones. They are biodegradable, cost-effective, and can be produced in-situ at contaminated sites.

4.2. Theoretical Aspects

Figure 4.1 shows the conceptual scheme of equilibrium desorption of PAHs in the micelle-soil-water system. According to Figure 4.1, it is seen that PAHs compounds are distributed in three phases including water, micelle, and soil. Three reaction steps can be recognized:

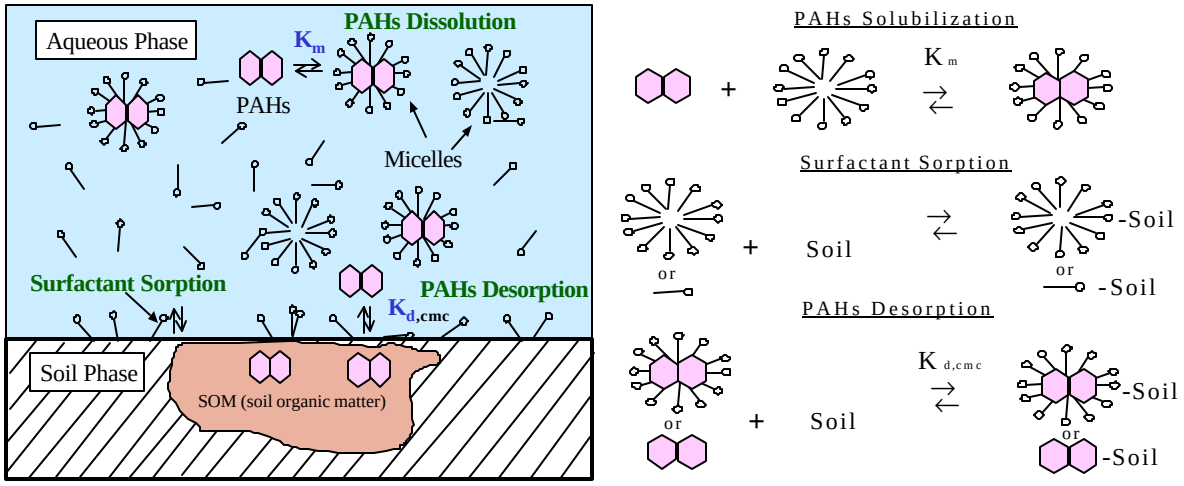

Figure 4.1. Schematic representation of the PAHs desorpiton in micelle-water-soil system.

(1) Solubilization of PAHs from the aqueous into the micelle phase:

$$P^w + M \xleftrightarrow{K_m} P - M \qquad [4.1]$$

where P^w is the PAHs in the water phase, M is the free micelle, P-M is the PAHs in the micelle, and K_m is the partition coefficient of PAHs between water and micelle phase. Since the solubilization of PAHs is a partition process between water phase and micelle phase, that is,

$$K_m = \frac{[P - M]}{[P^w]} \qquad [4.2]$$

(2) Sorption of surfactant on the soil including the sorption of both individual surfactant molecule and aggregates (micelle):

$$S + X \longleftrightarrow S - X \qquad [4.3]$$

where S represents the concentration of surfactant including individual molecule and aggregate in aqueous phase, X is the soil surface, S-X is the surfactant-soil associates. Since the surfactant sorption is an interfacial interaction, it can not been regarded as a partition process. As a result, the surfactant sorption on the soil surface may be described by the Langmuir or linear isotherm (Rosen, 1989).

(3) Partition of PAHs between the aqueous and the soil phase:

$$P^* + X^* \xleftrightarrow{K_{d,cmc}} P^* - X^* \qquad [4.4]$$

where P^* is the PAHs concentration in the solution, i.e., both water and micelle phase, X^* is the soil phase containing the sorbed surfactants, P^*-X^* is the PAHs concentration in the soil phase. The term, $K_{d,cmc}$, is the apparent partition coefficient of PAHs in the soil-micelle-water system. That is:

$$K_{d,cmc} = \frac{[P^* - X^*]}{[P^*]} \qquad [4.5]$$

According to Equation 4.5, the PAHs desorption in the presence of surfactant is associated with both the solubilization capacity and soil sorption of the surfactant. Therefore, in order to

describe the PAHs desorption, an integrated relationship among the solubilization of PAHs, sorption of surfactants, and the apparent partition of PAHs is necessary.

4.2.1. PAHs Solubilization in the Micelle Phase

As mentioned above, the solubilization of PAHs from water phase into micelle phase is one of the three major steps for PAH's desorption. The solubilization of micelle can enhance the PAHs solubility in the aqueous phase, which increases the desorption of PAHs in the soil-water system. According to Equation 4.5, the PAHs concentration in the presence of micelle, P^*, should be determined to compute the apparent coefficient of PAHs, $K_{d,cmc}$. The partition coefficient in the micelle-water phase, K_m, can use to calculate the PAHs concentration in the micelle phase, then, one can obtain the P^* value. Therefore, the effect of the solubilization of the surfactant can be involved into the quantification of $K_{d,cmc}$ when introducing K_m into Equation 4.5.

According to the definition of the partition coefficient in micelle-water phase, i.e., $K_m = \frac{[P-M]}{[P^w]}$, Jafvert (1991) derived that K_m and the octanol number of PAHs, K_{ow}, can be correlated by a linear equation. Almgren et al. (1979) determined the micelle-water partition coefficient (K_m) of 10 aromatic hydrocarbons in the micelle solution. These values also can be correlated to a linear relationship with a corresponding K_{ow}. That is:

$$K_m = \beta K_{ow} \qquad [4.6]$$

where β is a constant. During the derivation by Jafvert (1994), β was independent of the specific PAHs compound but only depends on the characteristic of the surfactant. This equation was used to incorporate with Equation 4.5 to compute the $K_{d,cmc}$.

4.2.2. Surfactant Sorption on the Soil

The sorption of surfactant onto soil surface is the part of the soil organic matter. In other words, the sorbed surfactant can increase the sorption density of the soil for PAHs contaminants. Accordingly, the magnitude of the sorbed surfactants must be involved into the computation of the apparent partition coefficient, $K_{d,cmc}$. The surfactant sorptions can be fitted by the Langmuir or linear equation. The Langmuir expression is:

$$[S-X] = \frac{q_{max} b[S]}{1+b[S]} \qquad [4.7]$$

where , q_{max} is the maximum sorption density in the soil phase and b is an indicator of the affinity for various organic compounds to the soil. The linear isotherm of the surfactant sorption is:

$$[S-X] = c + d[S] \qquad [4.8]$$

where c and d are the regression constants. Therefore, Langmuir or linear isotherm was used to incorporate with Equation 4.5 to compute the $K_{d,cmc}$.

4.2.3. Partition of PAHs between the Aqueous and the Soil Phase

The partition coefficient of PAHs in the presence of surfactants, $K_{d,cmc}$ is defined as the ratio between the concentration of the PAHs in the soil phase and in the liquid phase. Since the aqueous phase consists of water and micelle phase, Equation 4.5 can be rewritten as:

$$K_{d,cmc} = \frac{[P^* - X^*]}{[P^w] + [P^m]} \quad [4.9]$$

where the superscription w and m stands for water phase and micelle phase, respectively. It must be noted that the liquid phase also comprises the other componant such as the dissolved organic matter (DOM). Compared to the micelle concentration, we assume that the effect of DOM on PAHs desorption is relatively small and can be neglected. Equation 4.9 can be divided by $[P^w]$, one has:

$$K_{d,cmc} = \frac{[P^* - X^*]/[P^w]}{1 + [P^m]/[P^w]} \quad [4.10]$$

where $[P^*\text{-}X^*]/[P^w]$, is the partition coefficient of PAHs, K_d^*, between soil and water phase and $[P^m]/[P^w]$ can be replaced by $K_m[S]$, Equation 4.10 can be written as follows:

$$K_{d,cmc} = \frac{K_d^*}{(1 + K_m[S])} \quad [4.11]$$

Generally, the sorbate is considered to be dissolved in the organic carbon of soil, a normalized partition coefficient, K_{oc}, can be used to express the distribution of contaminant between the water and organic carbon content, that is,

$$K_{oc} = \frac{[P^* - X^*]}{[P^w] f_{oc}^*} \quad [4.12]$$

where f_{oc}^* is the organic carbon content in soils containing the sorbed surfactant. According to the definition of K_d, $K_d^* = [P^*\text{-}X^*]/[P^w]$, Equation 4.12 becomes:

$$K_{oc} = \frac{K_d^*}{f_{oc}^*} \quad [4.13]$$

For PAHs compounds, their K_{oc} values can be always correlate to the corresponding K_{ow} values. In addition, PAHs sorption isotherms in soils always exhibit a linear expression (Karickhoof, 1984). Hessett et al. (1980) reported a near-zero intercept and a constant slope (α = 0.48) for the sorption of various PAHs onto 14 sediments and soils. The proportionality between K_{oc} and K_{ow} can be expressed as follows:

$$K_{oc} = \alpha K_{ow} \quad [4.14]$$

By combining Equation 4.13 and 4.14, one has:

$$K_d^* = \alpha f_{oc}^* K_{ow} \quad [4.15]$$

By substituting Equation 4.15 into Equation 4.11, it yields:

$$K_{d,cmc} = \frac{\alpha K_{ow} f_{oc}^*}{(1 + K_m[S])} \quad [4.16]$$

By substituting $K_m = \beta K_{ow}$ into Equation 4.16, one has:

$$K_{d,cmc} = \frac{\alpha K_{ow} f_{oc}^*}{(1 + \beta K_{ow}[S])} \quad [4.17]$$

The sorbed surfactant is the part of the organic carbon content in soils,thereby, f_{oc}^*, can be expressed:

$$f_{oc}^* = \gamma[S - X] + f_{oc} \quad [4.18]$$

where γ is the effective coefficient of the surfactant which has contributed to the sorption of organic contaminants, i.e., as the soil organic carbon. The term, f_{oc}, is the original organic carbon of the soil.

If the surfactant adsorption can be fitted by the Langmuir isotherm, by the combination of Equation 4.7 and 4.18, ond has:

$$f_{oc}^{*} = \frac{\gamma q_{\max} b[S]}{1 + b[S]} + f_{oc} \qquad [4.19]$$

By subtituting Equation 4.19 into Equation 4.17, the apparent partition coefficient, $K_{d,cmc}$, can be expressed:

$$K_{d,cmc} = \frac{\alpha K_{ow}\left[\frac{\gamma q_{\max} b[S]}{1 + b[S]} + f_{oc}\right]}{1 + \beta K_{ow}[S]} \qquad [4.20]$$

When the term, $\beta K_{ow}[S]$ is far greater than one, Equation 4.20 can be simplied to the following expression:

$$K_{d,cmc} = \frac{\alpha K_{ow}[\gamma q_{\max} + f_{oc}]}{\beta K_{ow}[S]} \qquad [4.21]$$

Then, K_{ow} can be cancelled in Eqaution 4.21, one has:

$$K_{d,cmc} = \frac{\alpha[\gamma q_{\max} + f_{oc}]}{\beta[S]} \qquad [4.22]$$

Since α, β, γ, q_{max}, and f_{oc} are constants in a specific soil-water system, Equation 4.22 can be written as follows:

$$K_{d,cmc} = K/[S] \qquad [4.23]$$

where K is an integrated coefficient, i.e., $K = \alpha[\gamma q_{max}+f_{oc}]/\beta$. According to Equation 4.23, the apparent partition coefficient, $K_{d,cmc}$, is inversely proportional to the surfactant concentration in the solution, [S].

If the surfactant adsorption is linear, one can subtitute Equation 4.8 into Equaiton 4.18 and has:

$$f_{oc}^{*} = \lambda(c + d[S]) + f_{oc} \qquad [4.24]$$

By subtituting Equation 4.24 into Equation 4.17, the apparent partition coefficient, $K_{d,cmc}$, can be expressed:

$$K_{d,cmc} = \frac{\alpha K_{ow}[\gamma(c + d[S]) + f_{oc}]}{1 + \beta K_{ow}[S]} \qquad [4.25]$$

4.3. Methodology

4.3.1. Qualitative Analysis of the Surfactant

In order to select the suitable surfactant for the removal of PAHs compounds from soils, a group of surfactant was screened based on the following properties: water solubility, clay particle dispersion, oil dispersion, and foam formation (Ellis et al., 1985). First, a surfactant must have high solubility in water phase. To determine the water solubility of surfactant, it begins by mixing 5 ml of surfactant (2% by weight) in 250 ml of distilled water for 5 minutes. The degree of surfactant dissolution was distinguished by visual observation.

A surfactant possesses the strong ability of clay particle dispersion may have adverse effect on the flushing process. Since high clay dispersion ability always mobilize small particles, these particles may resettle and clog the soil pores. As a result, both the flushing flow and the removal efficiency would decrease. High purity kaolinite and bentonite (Georgia Kaolin Company, Atlanta, GA) were used to evaluate the clay particle dispersion. A given amount of clay (250 mg) and 10 ml of the 2% (w/w) surfactant solution were mixed in a 15-ml vial. The vial was shaken for 5 minutes over a shaker then allowed to settle overnight. The visual cloudiness of the solution was indicative of the presence of suspended clay.

For removal PAHs from soils, a surfactant should have the high ability of oil dispersion. This will decrease the strong attraction between PAHs and soils. The oil dispersion tests were conducted by mixing 100 ml surfactant solutions and three drops of motor oil in a 250 ml beaker. The extent of the oil dispersion was determined by the visual cloudiness of the final solution. For the foam formation consideration, surfactant with a high foam formation tendency might have adverse effect on the remediation application. The foaming may block the flushing pathway in the sol matrix. To determine the extent of foam formation of surfactant, surfactant solutions were mixed vigorously for 2 minutes, then, the extent of the foaming was observed visually.

The precipitation of surfactant may block the pores of the soil, which is an adverse effect on the soil flushing process. To determine the extent of precipitation of surfactant, surfactant solutions were mixed with the calsium chloride solution (0.1 M). The mixtures were shaken for 24 hours, then, the extent of precipitation was obserbed visually. Table 4.1 lists type and manufacturer of various surfactants used in this study.

Table 4.1. The type and the manufacturer of surfactants studied.

No	Surfactant	Charge	Company
1	MERPOL A	Non	DuPont, Wilmington, DE
2	MERPOL SE	Non	DuPont, Wilmington, DE
3	MERPOL SH	Non	DuPont, Wilmington, DE
4	MERPOL 189S	Non	DuPont, Wilmington, DE
5	ZONYL FSK	AM	DuPont, Wilmington, DE
6	EMULPHO GENE BC-610	Non	Rhodia, Cranbury, NJ
7	IGEPAL CO-210	Non	Rhodia, Cranbury, NJ
8	IGEPAL CO-630	Non	Rhodia, Cranbury, NJ
9	LUBRHOPHOS LF-200	Non	Rhodia, Cranbury, NJ
10	Triton X-100	Non	Rohm and Haas, Philadelphia, PA
11	Triton X-405	Non	Rohm and Haas, Philadelphia, PA
12	Triton X-85	Non	Rohm and Haas, Philadelphia, PA
13	Triton QS-44	Non	Rohm and Haas, Philadelphia, PA
14	Triton GR-5	Non	Rohm and Haas, Philadelphia, PA
15	SDS	Non	Aldrich, Milwaukee, MI
16	Fluorochemical FC-143	A	3M, St. Paul, MN
17	Biosurfactant Rhamnolipid	A	Jeneil Biotech, Saukville, WI

Note: Non: nonionic AM: amphoteric A: anionic surfactant

4.3.2. PAHs Solubilization with Surfactants

Figure 4.2 shows the experimental procedures for the PAHs dissolution in the surfactant solution. Batch dissolution experiments were conducted with fluorene, phenanthrene, anthracene, fluoranthene, and pyrene at various CMC values ranging from 0 to 5. To a series of glass tubes, 10 ml surfactant solution and PAHs organic compound were added. The tubes were placed in a shaker and shaken constantly for 10 days to reach the equilibrium condition. The mixtures were then centrifuged at 2,500 rpm (1,000 g) for 10 minutes using a centrifuge (Prescion Scientific Co. model K-9, Chicago, IL) to separate the PAHs powder from the supernatant. Then, a superspeed refrigerated centrifuge (Sorvall, model RC-5, Wilmington, DE) was used to remove fine particles in the supernatant at the speed of 12,000 g. The concentration of the PAHs in the centrate was analyzed by a HPLC/FLD (Hewlett-Packard, model 1100 series, Wilmington, DE).

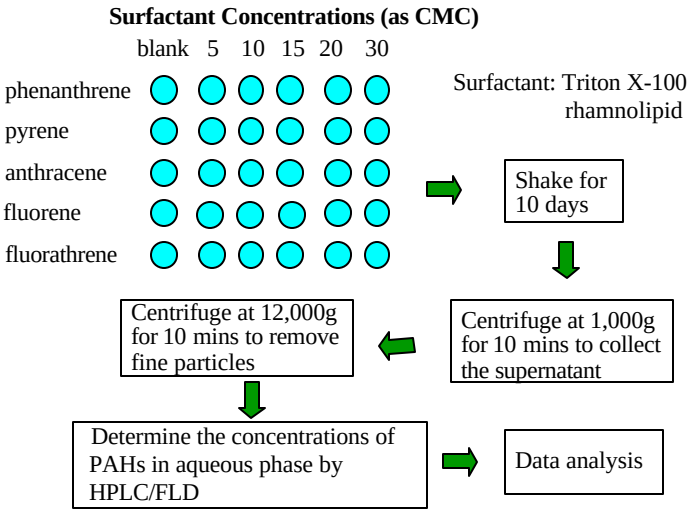

Figure 4.2. Flowchart of the experimental procedures for PAHs solubilization.

In solubilization experiments, Triton X-100 and the biosurfactant (rhamnolipid) were selected. Figure 4.3 shows the molecular structure, molecular weight, and CMC value of Triton X-100 and rhamnolipid, respectively. The PAHs were purchased from Aldrich Co (Milwaukee, WI). The purity of fluorene, phenanthrene, fluoranthene, and pyrene is 98.0% and that of anthracene is 97.0%. Table 4.2 lists the major features, including molecular formula, molecular weight, saturation water solubility, and $\log K_{ow}$ of PAHs studied.

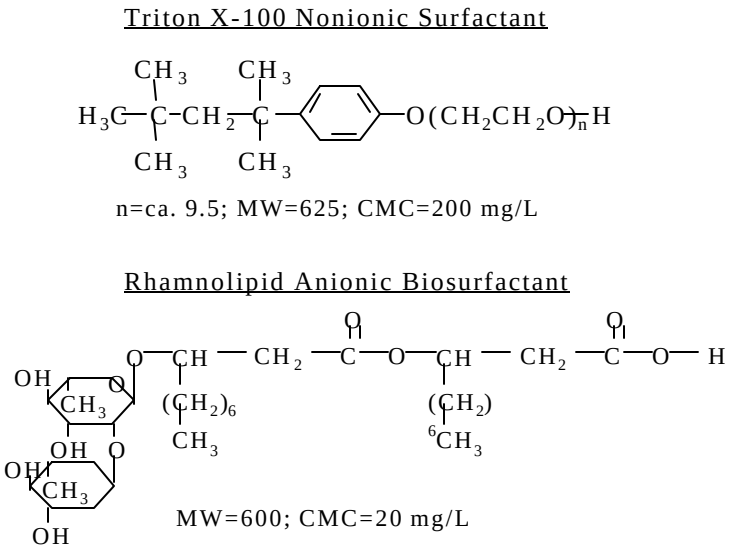

Figure 4.3. The molecular structure, molecular weight, and CMC value of Triton X-100 and rhamnolipid.

Table 4.2. Major physical properties of fluorene, phenanthrene, fluoranthene, pyrene, and anthracene (Schwarzenbach, 1993).

Physical Property	fluorene	phenanthrene	anthracene	fluoranthene	pyrene
Formula	$C_{13}H_{10}$	$C_{14}H_{10}$	$C_{14}H_{10}$	$C_{16}H_{10}$	$C_{16}H_{10}$
Molecular Weight	166.2	178.2	178.2	202.3	202.3
Solubility (mg/L)	1.8	1.1	0.1	0.2	0.1
$\log K_{ow}$	4.2	4.6	4.5	5.2	5.1

4.3.3. PAHs Desorption in the Presence of Surfactants

The characteristics of soil samples are listed in Chapter 2. Figure 4.4 shows the experimental procedures for PAHs desorption in the surfactant-soil-water system. Batch desorption experiments were conducted with fluorene, phenanthrene, anthracene, fluoranthene, and pyrene at various CMC values ranging from 0 to 5. The soil samples were pre-contaminated by PAHs, which concentrations in soils ranged from 25 to 200 µg/g. To prepare PAHs contaminated soil samples, a given amount of PAHs powder was dissolved into 100 ml hexane completely. The PAHs-hexane solution then was added into a soil mixer (Hobart, model CT-345, Lake Bluff, IL) with 100 g dried soils. After mixing for about 1 hour in the hood , hexane evaporated into the air phase and the nonvolatile PAHs remained in the soil.

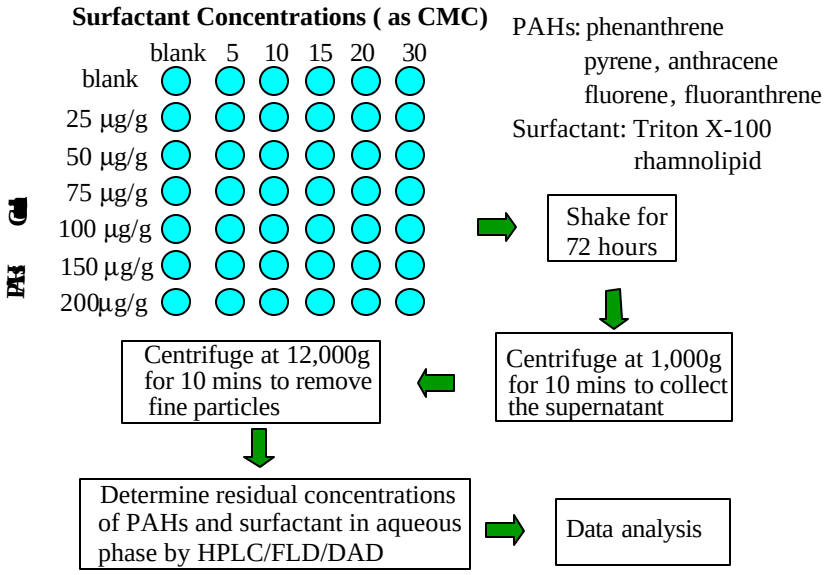

Figure 4.4. Flowchart of the experimental procedures for PAHs desorption.

To a series of glass tubes, PAHs (2g) contaminated soil samples and 10 ml of surfactant solution at various concentrations, 0 CMC to 30 CMC, were added. Two surfactants, Triton X-100 and rhamnolipid, were used to conduct the desorption experiments. The tubes were placed in a shaker and shaken constantly for 72 hours to reach the equilibrium condition. The mixtures were then centrifuged at 2,500 rpm (1,000 g) for 10 minutes using a centrifuge (Prescion Scientific Co. model K-9, Chicago, IL) to separate the coarse particles from the supernatant. Then, a superspeed refrigerated centrifuge (Sorvall, model RC-5, Wilmington, DE) was used to remove the fine particles in the supernatant at a speed of 12,000 g. The residual concentrations of PAHs and Triton X-100 in the centrate were analyzed with a HPLC/FLD and HPLC/DAD (Hewlett-Packard, model 1100 series, Wilmington, DE), respectively.

The concentration of rhamnolipid was determined by the surface tension method. Since pH may affect the surface tension measurements, the solution was buffered. This was done

by mixing 10 ml buffer solution (pH=7) with 10 ml rhamnolipid solution. The buffer solution was made of potassium phosphate (0.05 M) monobasic-Sodium hydroxide (Fisher Scientific, Pittsburgh, PA). The surface tension of all samples was determined by a tensiometer constructed with a platinum ring produced from (CSC Scientific company, Fairfax, VA) ring and a recorder (Coll-Parmer, Chicago, IL).

4.4. Results

4.4.1. Screening Tests

Table 4.3 lists the results of screen testing of surfactants in terms of water solubility, oil dispersion, clay dispersion, forming capacity, color, and precipitation degree. Results show that most surfactants have high water solubility. Since the surfactant would be used in the soil-water system to enhance the PAHs removal efficiency, the qualified candidates generally possess the features of high oil dispersion, low clay dispersion, low forming, clear color, and low precipitate. Based on results shown in Table 4.3, Triton X-100, SDS, and rhamnolipid are better surfactants.

Table 4.3. Results of screening testing of Surfactants.

No	Surfactant Name	A[a]	B[b]	C[b]	D[b]	E[c]	F[a]
1	MERPOL A	Y	H	L	L	w	N
2	MERPOL SE	Y	L	L	L	w	N
3	MERPOL SH	Y	H	M	M	c	N
4	MERPOL 189S	Y	L	H	H	y	Y
5	ZONYL FSK	Y	H	H	H	b	N
6	EMULPHO GENE BC-610	Y	H	L	H	w	N
7	IGEPAL CO-210	N	nd	nd	nd	nd	nd
8	IGEPAL CO-630	Y	H	L	H	c	N
9	LUBRHOPHOS LF-200	N	nd	nd	nd	nd	nd
10	***Triton X-100***	***Y***	***H***	***L***	***H***	***c***	***N***
11	Triton X-405	Y	M	M	H	c	N
12	Triton X-85	N	nd	nd	nd	nd	nd
13	Triton QS-44	Y	H	H	H	c	N
14	Triton GR-5	Y	H	H	H	w	Y
15	Fluorochemical FC-143	Y	L	L	L	c	N
16	SDS	Y	H	M	H	c	Y
17	***Biosurfactant-ramhnolipid***	***Y***	***H***	***H***	***M***	***c***	***Y***

Note: A: Solubility (2%), B: Oil Dispersion, C: Clay Dispersion, D: Forming, E: Color, F: Precipitation, a: Y=yes, N=no, b: H=high, M=moderate, L=low, c: w=white, c=clear, y=yellow, b=brown, Surfactants in bold type are selected for further experiment.

Figure 4.5 shows the surface tension of various surfactants as a function of concentration. Results show that the surface tension of all surfactants decreases with increasing concentration and reaches a minimum value, respectively. This specific minimum surface tension value is ca. 32, 30, and 28 dyne/cm for SDS, Triton X-100, and rhamnopilid, respectively. Results indicate that the CMC value of SDS, Triton X-100, and rhamnolipid is

roughly 500, 200, and 20 mg/L, respectively. There is no micelle formation when the surfactant concentration is below CMC.

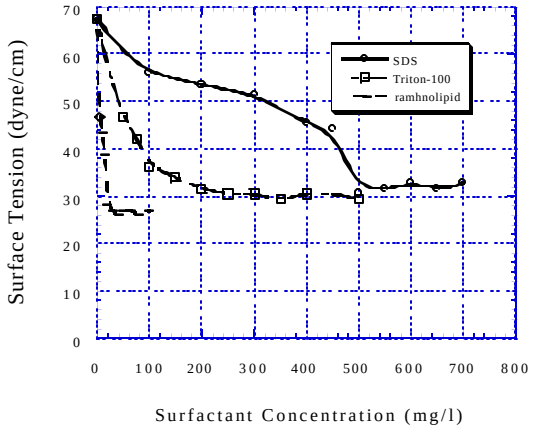

Figure 4.5. The surfactant tension as a function of surfactant concentration for SDS, Triton X-100, and rhamnolipid.

The Triton X-100 surfactant is a popular flushing agent in the soil remediaiton practice (Yeom et al, 1996; Sahoo et al., 1998). The SDS (sodium dodecyl sulfate) is also frequently applied in the soil washing treatment (Deshpande et al., 1999). However, the possibility of precipitation for Triton X-100 is lower than SDS because SDS is an anion surfactant. Accordingly, Triton X-100 was selected in this study. Rhamnolipid (anionic biosurfactant) may also cause the precipitation problems but it has the advantage of being biodegradable. In addition, the CMC value of the rhamnolipid (20 mg/L) is relatively low compared to that of SDS (500 mg/L). Since the solubilization of micelle is the main factor controlling the remediation efficiency, the surfactant with low CMC value may save the operation cost. Therefore, the Triton X-100 and rhamnolipid were selected as target surfactants for desorption experiments.

4.4.2. PAHs Dissolution in the Presence of Surfactants

Figure 4.6 shows the PAHs concentration as a function of Triton X-100 concentration. Results show that the PAHs concentration increases with increasing the surfactant concentration proportionally except at the surfactant concentration becomes greater than 30 CMC. Since the solubilization of PAHs mainly depends on the micelle concentration, the PAHs concentration is related to the surfactant concentration in terms of CMC. The non-proportional solubilization capacity can be attributed to the various micellar structures. In general, micelles are regarded to be roughly spherical, but micelles may become nonspherical at concentration greater than ten times CMC (Rosen, 1989). The nonspherical surfactant micelles consist of two parallel sheets (lamellar micelles) in which the individual molecules are oriented perpendicular to the plane of the sheet. Compared with spherical micelles, the lamellar micelles are aggregated by different number of surfactant molecules. Therefore, the solubilization capacity can be affected by different micellar formation.

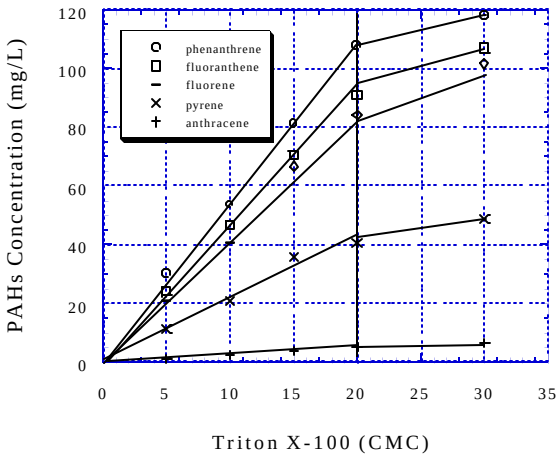

Figure 4.6. The PAHs concentration as a function of Triton X-100 concentration.

Results indicate that the degree of PAHs solubilization follows the order of water solubility except fluorene, that is, phenanthrene > fluoranthene > pyrene > anthracene. This degree reflects the solubilization capacity surfactants which can be expressed by the term, $[P-M]$. According to Equation 4.2, $K_m = \frac{[P-M]}{[P^w]}$, then, the solubilization degree can be written as: $K_m[P^w] = [P\text{-}M]$. Since K_m is a constant and $[P^w]$ is the PAH in water, the degree of various PAHs follows the order of their water solubility. Based on experimental results, the $K_m[P^w]$ value of fluorene, phenanthrene, fluoranthene, pyrene, and anthracene is 7.7, 5.0, 1.2, 0.7, and 0.3, respectively. The exceptional case of fluorene implies that the K_m value of fluorene is different from that of other PAHs.

Figure 4.7 shows the PAHs concentration as a function of rhamnolipid concentration. Results show that the PAHs concentration increases with increasing the surfactant concentration. Compared with Triton X-100, the solubilization proportionality of the rhamnolipid remain constant at the high concentration. This indicates that the structure of rhamnolipid micelle does not change throughout the concentrations tested. The CMC value of rhamnolipid (20 mg/L) is about ten times smaller than that of Triton X-100 (200 mg/L). For the surfactant with small CMC value, its micellar structure may not change its structure due to the relatively low concentration. This can account for the solubilization proportionality of PAHs in rhamnolipid solution.

Results also indicate that the slope ratio of PAHs solubilization in rhamnolipid solution follows the order of their water solubility except fluorene, that is, phenanthrene > fluoranthene > pyrene > anthracene. This can be interpretted by the same explanation for Triton X-100 results. The slope ratio is 0.65, 0.45, 0.45, 0.29, and 0.02 for phenanthrene, fluoranthene, fluorene, pyrene, and anthracene, respectively.

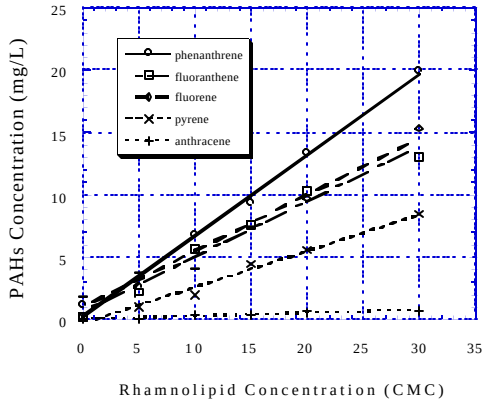

Figure 4.7. The PAHs concentration as a function of rhamnolipid concentration.

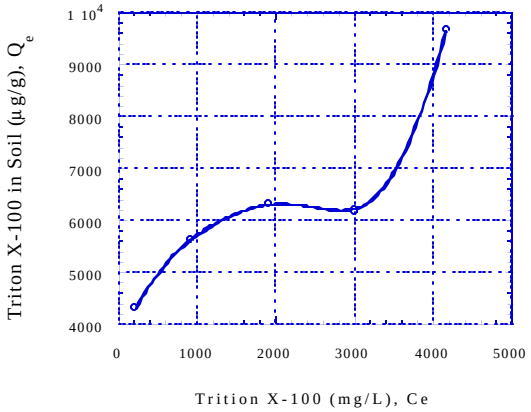

Figure 4.8. Triton X-100 sorption isotherms in uncontaminated soils.

4.4.3. Surfactant Sorption onto Soils

Figure 4.8 shows that the Triton X-100 sorption on the PAH-free soil. Results indicate that the sorption curve can be fitted by the Langmuir isotherm except data points at the highest equilibrium concentration. This result is in agreement with the report of Sun and Inskeep (1995). Their results showed that the sorption isotherms of Triton X-100 on Oshtemo soils exhibits the Langmuir type at the equilibrium concentration ranging from 0 to 600 mg/L. In this study, Langmuir isotherm can describe the sorption of Triton X-100 in the range of

equilibrium concentration from 0 to 3,000 mg/L. Although various soils exhibit different sorption capacity of surfactant, the sorption behavior of Triton X-100 basicly follows the Langmuir equation.

For the high equilibrium concnetration out of the Langmuir equation fitting range, it may be attributed to different micellar structures. Narkis and Ben-David (1985) investigated a series of nonionic surfactants sorption on the mineral clay. They reported that micelles may be sorbed on the soil directly. Carberry et. al., (1977) also suggested that the sorption of nonionic surfactants on soils is not multilayer but micelle-type sorption. When the micelle is the sorbate, the sorptive interaction of the surfactant with the soil surface can be regarded as a solubilization process. Accordingly, the sorption density has a maximal value, i.e., the saturation solubility of surfactant in soil phase. The surfactant sorption can be fitted by the Langmuir isotherm. Based on the solubilization concept, the sorption capacity varies with the hydrophobicities of solutes. The hydrophobicity of micelle may change with micellar structures. According to results from the solubilization experiments, the micellar structure of Triton X-100 may change from spherical to lamellar at 20 CMC. Figure 4.8 shows that the equilibrium concentration at 20 CMC (4,000 mg/L) can not be fitted by the Langmuir equation. This may demonstrate that Triton X-100 changes its micellar structures at ca. 20 CMC and that the surfactatant sorption can not be fitted by the Langmiur isotherm due to the presence of various micellar formations.

Figures 4.9, 4.10, 4.11, 4.12, and 4.13 show Triton X-100 sorption isotherms at various levels of PAH-contaminated soils including fluorene, phenanthrene, anthracene, fluoranthene, and pyrene, respectively. The contaminated PAH concentrations in the soils were from 25 to 200 μg/g. Results show that the sorption density of Triton X-100 decreases with increasing the PAHs contamination level in the soil. Since the interaction of both PAHs and surfactants with the soil can be regarded as a sollubilization process and soil organic matter is the only sorbent, PAHs molecules can occupy some available soil sites of the surfactant. In other words, the sorption of PAHs compounds and surfactants on soils are competitive. In addition, results show that PAHs types can influence the sorption density of surfactant. For various PAHs contaminated soils, the sorption densities of Triton X-100 at 200 μg/g are appromaxitely 6000, 5800, 5600, 4800, and 3000 μg/g for fluoranthene, anthracen, phenanthrene, pyrene, and fluorene, respectively. The order of sorption density is almost the same as their $\log K_{ow}$ values except pyrene, that is, fluoranthene ($\log K_{ow}$=5.2) > anthracen ($\log K_{ow}$=4.5) ≅ phenanthrene ($\log K_{ow}$=4.6) > fluorene ($\log K_{ow}$=4.2). Generally, the organic contaminant with low hydrophobicity exhibits strong sorption interaction with the soil. Therefore, the sorption density of surfactant is small on the soil contaminated by low $\log K_{ow}$ value PAHs.

Results show that the sorption density of surfactant decreases with increasing surfactant concentration except the lowest and highest equilibrium concentration. This may be attributed to the release of soil organic matter from soils. It is inevitable that the organic matter was dissolved from the soil to the aqueous phase due to the strong hydrophobic solubilization of micelles. Because of the loss of the soil organic matter, available soil sites for surfactant decreases. The soil organic matter is considered as the main domain for the

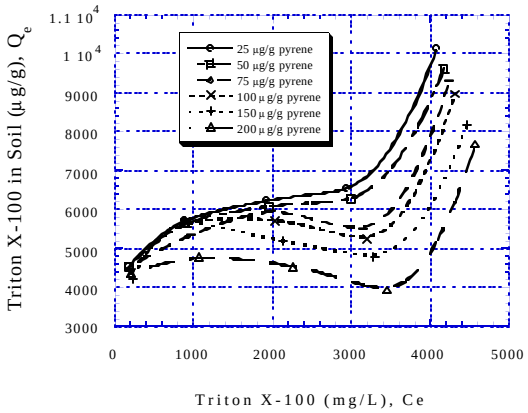

Figure 4.9. Triton X-100 sorption isotherms at various quantities of fluorene contaminated soils.

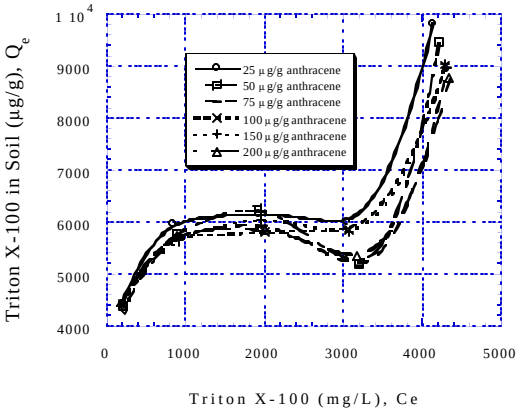

Figure 4.10. Triton X-100 sorption isotherms at various quantities of phenanthrene contaminated soils.

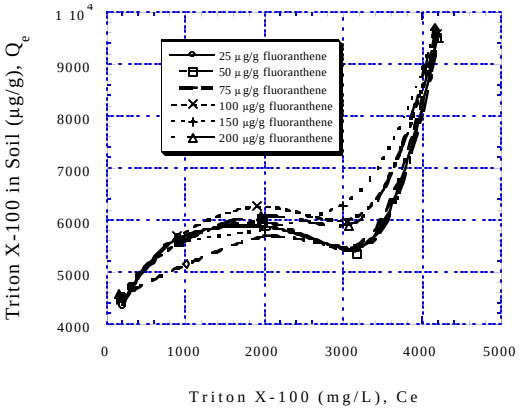

Figure 4.11. Triton X-100 sorption isotherms at various quantities of anthracene contaminated soils.

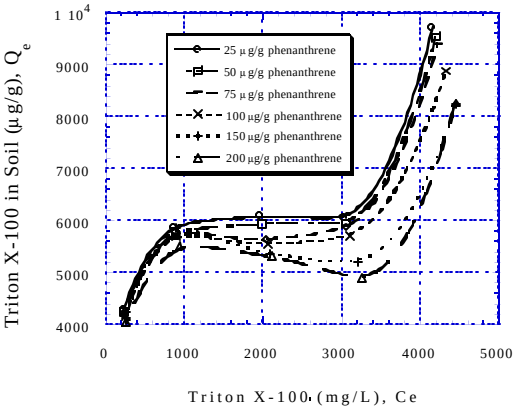

Figure 4.12. Triton X-100 sorption isotherms at various quantities of fluoranthene contaminated soils.

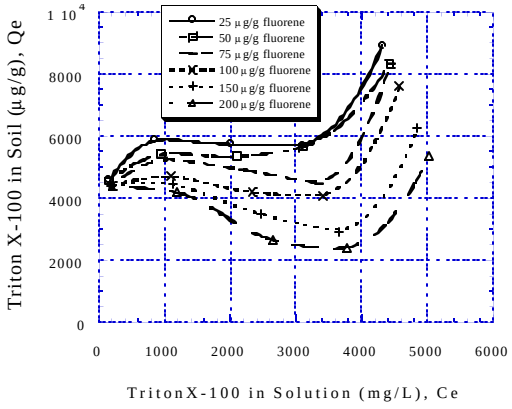

Figure 4.13. Triton X-100 sorption isotherms at various quantities of pyrene contaminated soils.

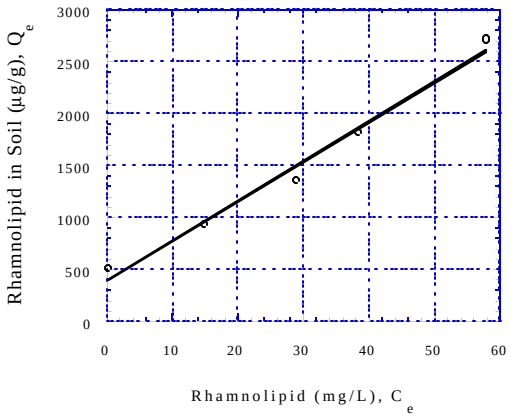

Figure 4.14. Rhamnolipid sorption isotherms in uncontaminated soils.

micelle sorption, therefore, the sorption density of surfactant decreases with increasing surfactant concentration.

Figure 4.14 shows that the rhamnolipid sorption in the PAH-free soil. Results show that the sorption curve can be fitted by a linear equation. Thangamanl and Shreve (1994) reported the same sorption behavior of rhamnolipid. Noordman et. al., (2000) reported that the adsorption of rhamnolipid on the soil is driven by the hydrophobicity of rhamnolipid but not by the partition process. This may be evidenced by the linear isotherm of the rhamnolipid sorption. If the pratition process is the only interaction between rhamnolipid and the soil, the sorption behavior should be related to the hydrophobicity of surfactant. According to experimental results, there exits the linearity even the micelle formed in the aqueous phase, i.e., the equilibrium concentration over 20 mg/L. The defference between the hydrophobicity of individual surfactant molecule and the micelle can not affect the surfactant sorption. This implies that the rhamnolipid sorption is mainly an interfacial adsorption process. Generally, the sorption drived by organic hydrophobicity is a partition process. The anionic character of the rhamnolipid may repel the organic attraction to the soil, which truns the partition reaction into an interfacial adsorption. The sorption densities of the rhamnolipid range from 500 to 2,500 µg/g and the partition coefficient is 34 L/Kg.

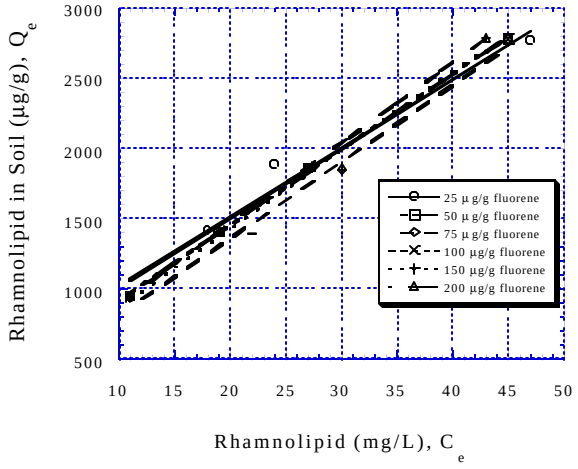

Figure 4.15. Rhamnolipid sorption isotherms various quantities of fluorene contaminated soils.

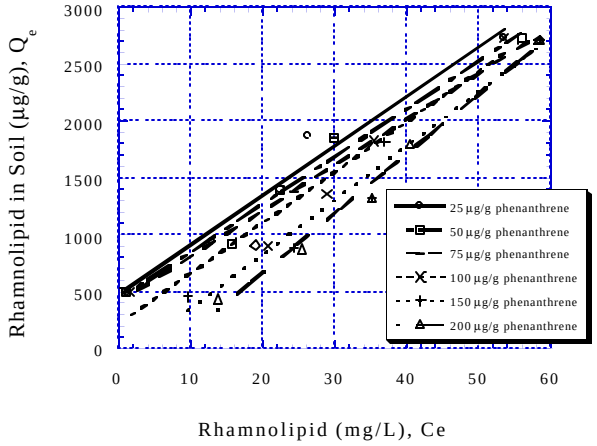

Figure 4.16. Rhamnolipid sorption isotherms at various quantities of phenanthrene contaminated soils.

Figures 4.15, 4.16, 4.17, 4.18, and 4.19 show rhamnolipid sorption isotherms versus various PAH contaminated soils including fluorene, phenanthrene, anthracene, fluoranthene, and pyrene, respectively. The contaminated PAH concentrations in the soils were from 25 to 200 µg/g.. Results show that the sorption density of rhamnolipid decreases slightly with increasing the PAHs contamination concentration. This may be attributed to the decrease of the soil specific surface area. When preparing PAHs contamination soils, PAHs were dissolved in hexane and mixed with the soil. After hexane evaporation, part of PAHs may be filled in the pores of the soil in addition to the sorption. Accordingly, the specific surface area of soils decreases with increasing the contamination concentration. Since the rhamnolipid sorption is an interfacial reaction, the sorption density decreases with increasing the soil

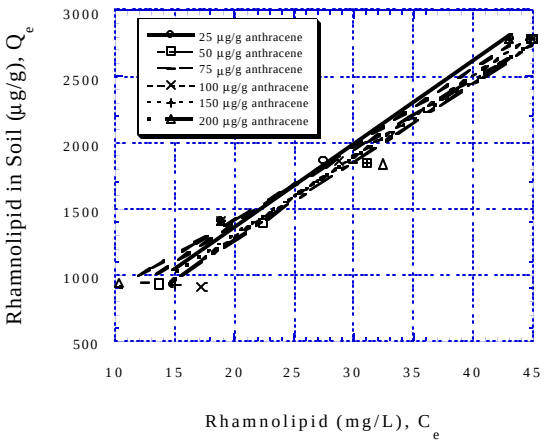

Figure 4.17. Rhamnolipid sorption isotherms at various quantities of anthracene contaminated soils.

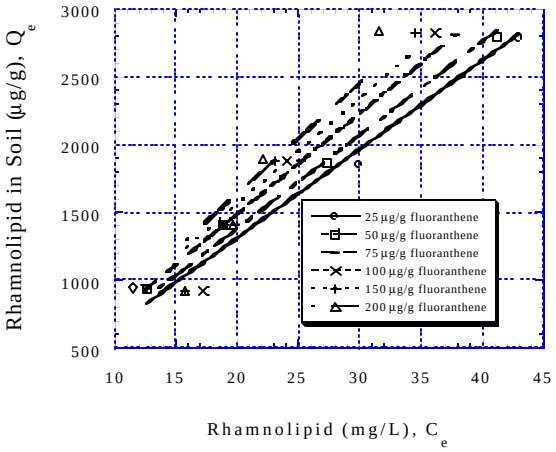

Figure 4.18. Rhamnolipid sorption isotherms at various quantities of fluoranthene contaminated soils.

contamination. Results show that the slopes of the linear isotherm are 54, 48, 59, 72, and 74 L/Kg for fluorene, phenanthrene, anthracene, fluoranthene, and pyrene, respectively. The slope reflects the sorption intensity of rhamnolipid with the contaminated soil. A high value of the slope exhibits the strong attraction to the soil surface. The order of the slope , fluorene ≅ phenanthrene < anthracene < fluoranthene < pyrene, almost follows that of the PAHs hydrophobicity. That is, pyrene ($\log K_{ow}$=5.1) ≅ fluoranthene ($\log K_{ow}$=5.2) > anthracen ($\log K_{ow}$=4.5) ≅ phenanthrene ($\log K_{ow}$=4.6) > fluorene ($\log K_{ow}$=4.2). This indicates that the adsorption of rhamnolipid is mainly driven by the hydrophobicity of the soil. Therefore, the sorption intensity of rhamnolipid increases with increasing the hydrophocity of PAHs contamination soils.

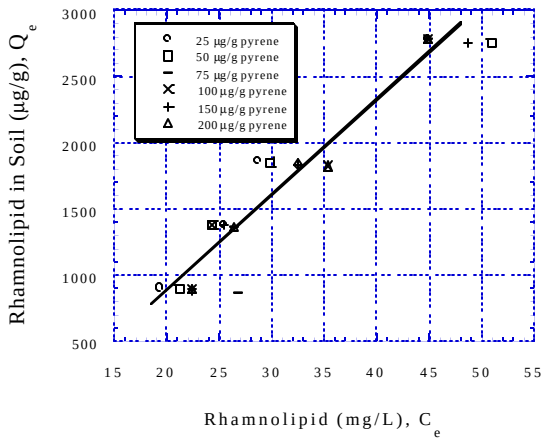

Figure 4.19. Rhamnolipid sorption isotherms at various quantities of pyrene contaminated soils.

4.4.4. PAHs Distribution in the Presence of Surfactants

Figures 4.20, 4.21, 4.22, 4.23, and 4.24 show the desorption isotherms at various Triton X-100 concentrations (0 to 30 CMC) for fluorene, phenanthrene, anthracene, fluoranthene, and pyrene, respectively. Results show that all desorption isotherms can be fitted by the linear equation and be described by the partition coeffcient. According to the definition of the partition coefficient, $K_d = q_e/C_e$, where K_d is the partition coefficient, q_e is the organic concentration in the soil phase, and C_e is the organic concentration in the aqueous phase. The partition coefficient can be related to the activity coefficient, γ_w/γ_s, (Chapter 3). The terms, γ_w and γ_s, are the activity coefficient of organics in the aqueous and soil phase, respectively. The

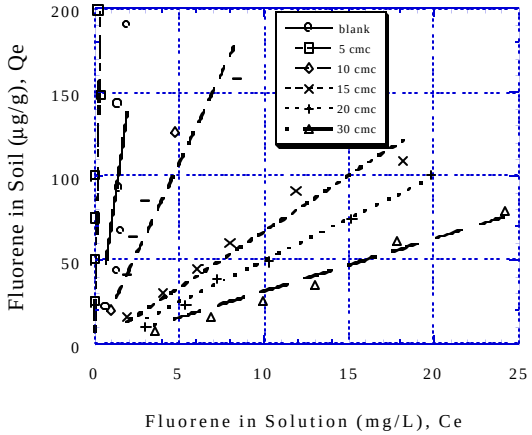

Figure 4.20. The fluorene isotherms with various CMC values in Triton X-100 solution-soil system.

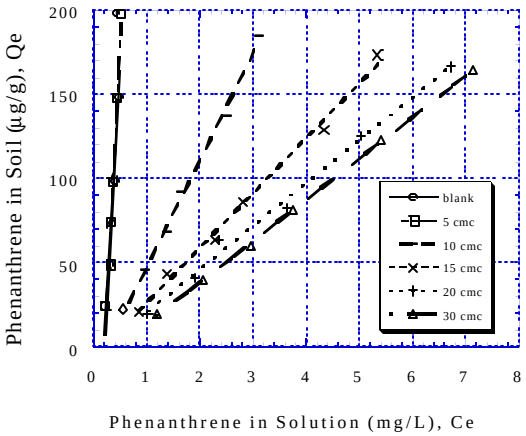

Figure 4.21. The phenanthrene isotherms with various CMC values in Triton X-100 solution-soil system

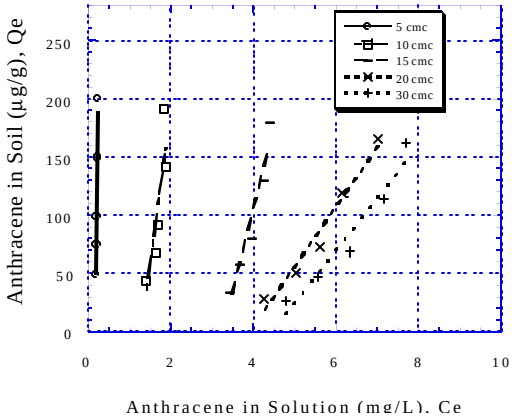

Figure 4.22. The anthracene isotherms with various CMC values in Triton X-100 solution-soil system.

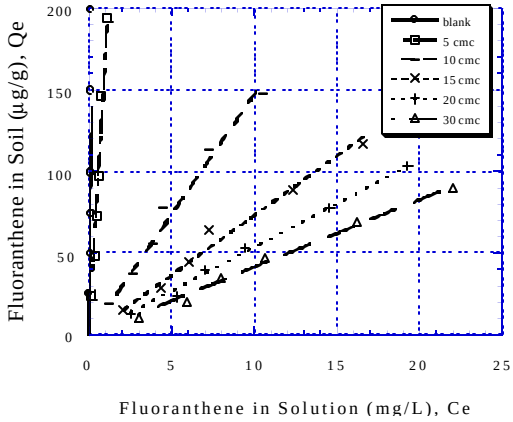

Figure 4.23. The fluoranthene isotherms with various CMC values in Triton X-100 solution-soil system.

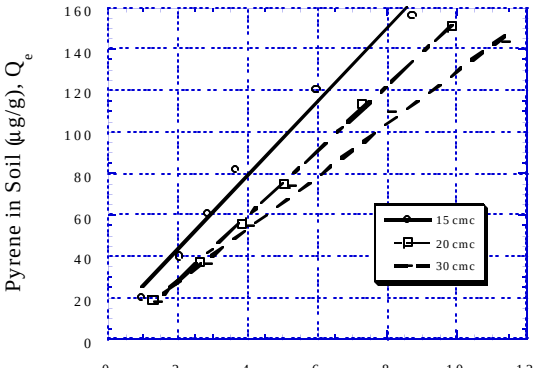

Figure 4.24. The pyrene isotherms with various CMC values in Triton X-100 solution-soil system.

linear isotherm indicates that the activity coefficients, γ_w and γ_s, are constant values. In other words, the PAHs interaction with surfactant solution and the soil are independent of the PAHs concentration.

Results show that apparent partition coefficient of PAHs, $K_{d,cmc}$, decreases with increasing the surfactant concentration. This observation is in agreement with the results reported by Sun and Boyd (1993). With the strong surfactant solubilization ability, the solubility of PAHs can be enhanced in the aqueous phase. Accordingly, the desorption capacity of PAHs increases with increasing surfactant concentration, which decreases the

partition coefficient. It is noticed that the desorption difference is insignificant in comparison with the desorption tests conducted by pure water and 5 CMC Triton X-100. According to results obtained from sorption experiments, most surfactant molecules are sorbed on the soil surface with use of the low surfactant concentration, i.e., 5 CMC. There are few or none micelles in the solution, which results in insignificant solubilization surfactant. Therefore, the surfactant applied to PAHs desorption at the low concentration is not effective.

The $K_{d,cmc}$ values of fluorene, phenanthrene, anthracene, fluoranthene, and pyrene are ca. 5~20, 25~55, 50~275, 5~15, and 20 L/Kg, respectively. The partition process is the main reaction for the PAHs distribution in the micelle-soil-water system. The driving forces of partition process contain the hydrophobicity of PAHs, surfactant, and soil organic matter. When using the same type of surfactant and soil during desorption tests, the hydrophobicity of PAHs is the only factor controlling the PAHs desorption. Based on this concept, the partition coefficient, $K_{d,cmc}$, should follow the order of the magninute of PAHs hydrophobicity. According to results, $K_{d,cmc}$ of PAHs does not follow this rule. In fact, the surfactant would sorbed on the soil surface and become a new sorbent for PAHs during the desorption process. This coupling reaction results in the PAHs partition coefficient not following the solubility order in the presence of surfactant.

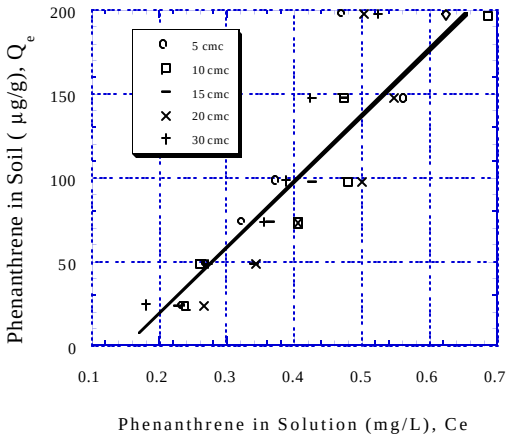

Figure 4.25. The fluorene isotherms with various CMC values in rhamnolipid solution-soil system.

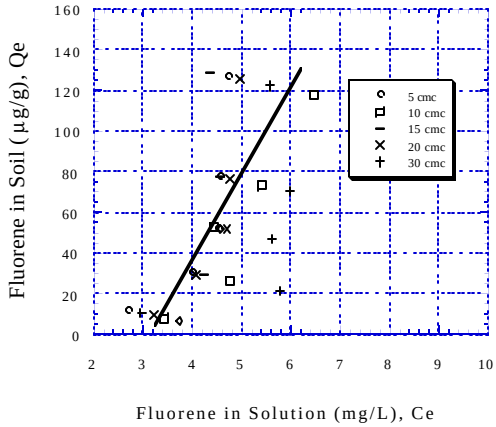

Figure 4.26. The phenanthrene isotherms with various CMC values in rhamnolipid solution-soil system.

Figures 4.25, 4.26, 4.27, 4.28 and 4.29 show desorption isotherms at various rhamnolipid CMC values for fluorene, phenanthrene, anthracene, fluoranthene, and pyrene, respectively. Results show that the desorption among various surfactant concentrations are insignificant except fluoranthene. This indicates that rhamnolipid concentration has no significant effect on the enhancement of PAHs desorption. The rhamnolipid concentration in the aqueous ranges only from 0 to 2 CMC approximately. In contrast, the initial rhamnolipid concentration was 5~30 CMC, therefore a great amount of biosurfactant molecules were sorbed by soils. As a result, the equilibrium concentration of PAHs are close to their water solubility level, which causes the desorption isotherm not to vary with the rhamnolipid concentration. In addition, the rhamnolipid adsorbed on the soil becomes part of sorbent for PAHs. The increasing content of the soil sorbent can reduce the solubilization of PAHs from the soil phase. Therefore, the desorption of PAHs is independent of rhamnolipid concentrations.

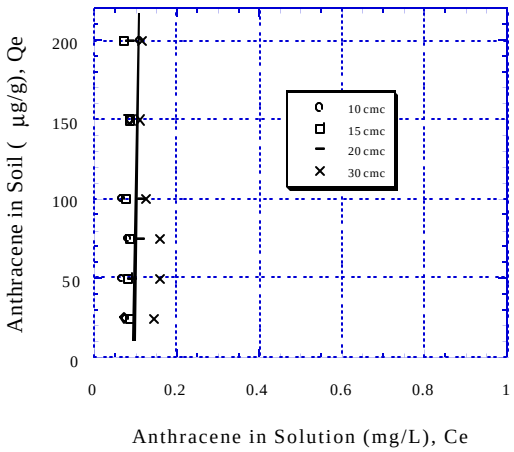

Figure 4.27. The anthracene isotherms with various CMC values in rhamnolipid solution-soil system.

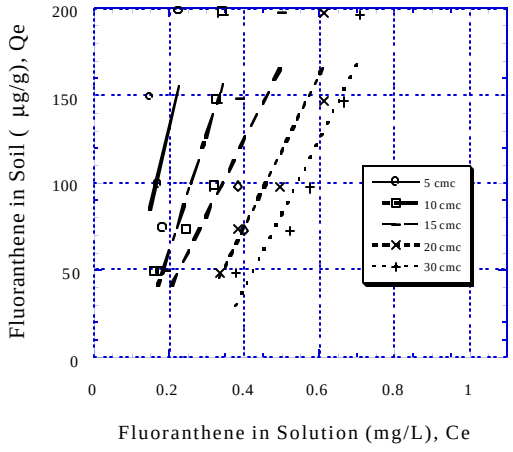

Figure 4.28. The fluoranthene isotherms with various CMC values in rhamnolipid solution-soil system.

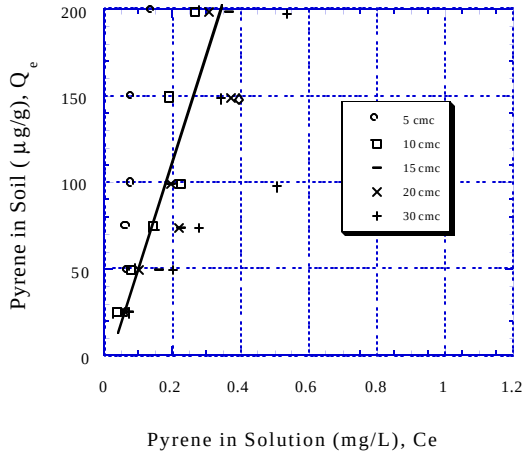

Figure 4.29. The pyrene isotherms with various CMC values in rhamnolipid solution-soil system.

Results show that all the desorption isotherms with rhamnolipid can be fitted by the linear equation. As discussed for Triton X-100, the linear isotherm indicates that the activity coefficients , γ_w and γ_s, are constant values. The PAHs interaction with rhamnolipid and soil are independent of the PAHs concentration. Results show that $K_{d,cmc}$ of fluorene, phenanthrene, anthracene, fluoranthene, and pyrene are ca. 50, 400, 2000, 1000, and 500 L/Kg, respectively. The sorption of rhamnolipid results in a random order in the PAHs partition coefficient.

4.5. Discussion

4.5.1. PAHs Dissolution in the Presence of Surfactants

Figure 4.30 shows the partition coefficient of PAHs in the micelle-water system, K_m, as a function of the partition coefficient of PAHs in the octanol-water system, K_{ow}. Results show that K_m can be correlated to the K_{ow} proportionally as expected, i.e., Equation 4.6: $K_m = \beta K_{ow}$. A high β value reflects the high solubilization capacity of the surfactant for hydrophobic organics. Results indicate that β values for Triton X-100 and for rhamnolipid are ca. 0.4 and 0.44, respectively. This means that the solubilization capacity of these two surfactants are similar to each other at an identical concentration. However, the CMC value of rhamnolipid (20 mg/L), is largely different from that of Triton X-100 (200 mg/L). This implies that the there is no correlation between the CMC and solubilization capacity of surfactant.

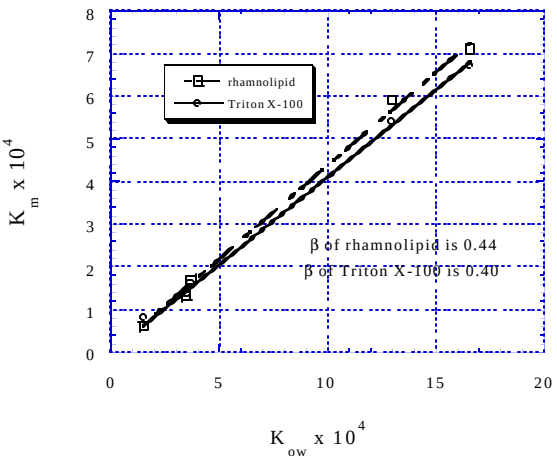

Figure 4.30. The partition coefficient of PAHs in micelle-water system versus their octanol number.

Edwards et al., (1991) reported that the β value of Triton X-100 for phenanthrene and pyrene is 0.38 which is in good agreement with results obtained in this study (0.40). According to Equation 4.6 (Jafvert, 1994), β values only depends on the surfactant characteristics such as molar volume and the dispersion force of surfactant. Jafvert et al., (1995) proposed an empirical equation to estimate the ratio, β, based on K_m and K_{ow} as follows:

$$K_m = (0.031y_1 - 0.0058y_2)K_{ow} \quad [4.26]$$

where y_1 = number of "hydrophobic" carbons (e.g., aromatic or aliphatic, straight or branched reduced carbons), y_2 = number of "hydrophilic" groups (e.g., sorbitan carbons (in C_6H_8 group), or ethoxy groups (C_2H_4O group)). Based on results shown in Figure 4.3, the number of "hydrophobic" carbons in Triton X-100 is 14 and number of "hydrophilic" groups (C_2H_4O group) is 9.5. The β can be computed as 0.031*14 - 0.0058*9.5 ≅ 0.38, which is close to our experimental result (0.40). Likewise, the number of "hydrophobic" carbons for rhamnolipid is 18 and the number of "hydrophilic" groups (sorbitan carbons) is 14. Therefore, the β value of the rhamnolipid was determined as ca. 0.47 which is also close to the experimental result (0.44). This indicates that Equation 4.26 is not only suitable to prediction of the β value for Triton X-100 but also for rhamnolipid.

4.5.2. PAHs Distribution in the Presence of Surfactants

The apparent partition coefficient of PAHs compounds in the surfactant-water-soil system can be expressed by Equation 4.20, $K_{d,cmc} = \dfrac{\alpha K_{ow}\left[\dfrac{\gamma q_{max} b[S]}{1+b[S]} + f_{oc}\right]}{1+\beta K_{ow}[S]}$. According to Equation 4.20 (Section 4.2.3), the apparent partition coefficient can be simplified to Equation 4.23, when the term $\beta K_{ow}[S]$ is much greater than 1.0. The integrated coefficient, K, is equal to $\alpha\gamma[q_{max}+f_{oc}]/\beta$. Figures 4.31, 4.32, 4.33, and 4.34 show the apparent partition coefficient, $K_{d,cmc}$, as a function of Triton X-100 concentration in the presence of fluorene, phenanthrene, anthracene, and fluoranthene, respectively. Results show that there is an inversely proportional relationship between $K_{d,cmc}$ and Triton X-100 concentration in the range from 10 to 20 CMC. This can be attributed to $\beta K_{ow}[S]$ being much greater than 1.0 in Triton X-100 solution-soil system. The K_{ow} of fluorene is ca. 15,000, with a β of 0.4, and Triton X-100 concentration of ca. 10^{-3} M. The product of these three parameters, $\beta K_{ow}[S]$, is ca. 6.0. Accordingly, the simplified equation, K/[S], is able to describe the partition behavior of PAHs relationship with the Triton X-100 concentration. Compared with fluorene, the desorption of other PAHs compounds studied can fit this equation due to their higher K_{ow} values.

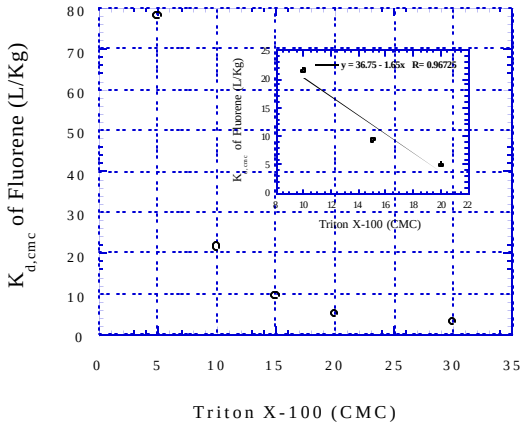

Figure 4.31. The apparent partition coefficient d fluorene as a function of Triton X-100 concentration.

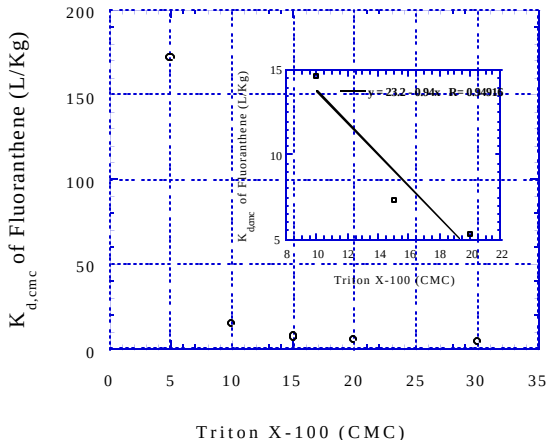

Figure 4.32. The apparent partition coefficient of phenanthrene as a function of Triton X-100 concentration.

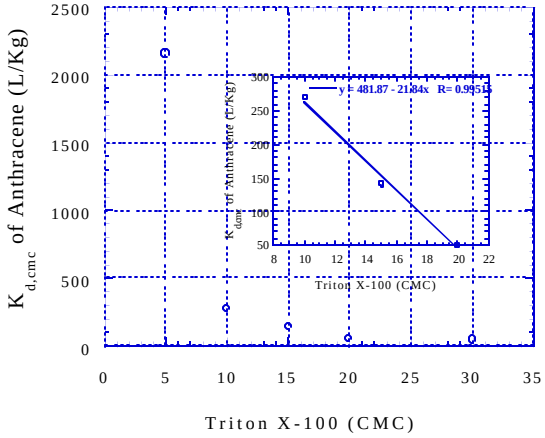

Figure 4.33. The apparent partition coefficient of anthracene as a function of Triton X-100 concentration.

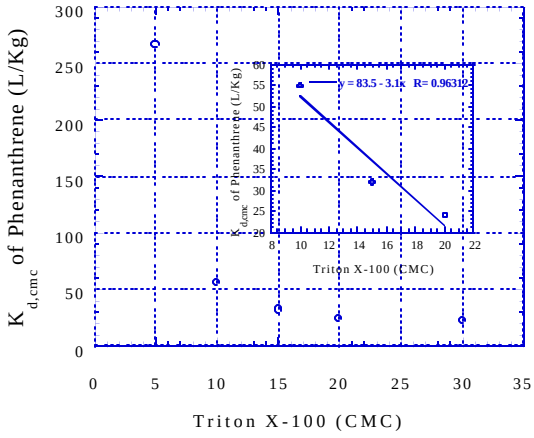

Figure 4.34. The apparent partition coefficient of fluoranthene as a function of Triton X-100 concentration.

Results indicate that the integrated coefficient, K, of fluorene, phenanthrene, anthracene, and fluoranthene is ca. 1.7, 3.1, 21.8, and 1.0 mol-Triton/Kg-soil, respectively. The integrated coefficient, K, is equal to $\alpha[\gamma q_{max}+f_{oc}]/\beta$. The term, α, is the proportionality between the K_{oc} and K_{ow}, which can be considered a constant. The term, γ, is the effective transformation coefficient of the surfactant which serves as the soil organic carbon. Since only Triton X-100 was used in these experiments, γ is a constnat. The original content of soil organic carbon, f_{oc}, is a constant due to the same soil sample used. The dissolution ratio, β, is a constant according to the experimental results. Consequently, the variation in K value can be only attributed to the maximal sorption density of surfactnat, q_{max}. Since K is proportional to q_{max}, a high q_{max} can yield a high K value. According to Figures 4.9, 4.10, 4.11, and 4.12, the q_{max} of Triton X-100 for various PAHs contaminated soils appromaxitely follows the same order: anthracen > phenanthrene > fluorene, as that of the K value except fluoranthene. This indicates that the Triton X-100 sorption on the soil can reduce PAHs desorption significantly.

According to the sorption results of surfactants, most surfactant molecules were sorbed in the soil when Triton X-100 concentration applied in the soil-water system was 5 CMC. Under this circumstance, there were few micelles in the solution, which causes the equaiton, $K_{d,cmc}$ = K/[S], being not valid. In addition, this equation is not feasible when the surfactant concentration applied was at 30 CMC. This can be attributed to the change of the micellar structure. Due to various micellar structures, the β value changed. Meanwhile, the sorption of Triton X-100 at this high concentration is not the Langmuir type. Consequently, this linear equation is only applicable in the range of Triton X-100 concentration from 10 to 20 CMC.

For the PAHs desorption in the Rhamnolipid solution, Equation 4.25: $K_{d,cmc} = \frac{\alpha K_{ow}[\gamma(c + d[S]) + f_{oc}]}{1 + \beta K_{ow}[S]}$ was used due to the linear sorption of rhamnolipid. The K_{ow} of fluoranthene is around 1.6×10^5, β is 0.44, and rhamnolipid concentration is around 2×10^{-6} M. The product of these three parameters, $\beta K_{ow}[S]$, is around 0.14. Since $\beta K_{ow}[S]$ is much less than 1.0, the apparent partition coefficient can be approximately simplified as: $K_{d,cmc} = \alpha K_{ow}[\gamma(c + d[S]) + f_{oc}]$. The terms, α, K_{ow}, γ, and f_{oc} are constant, thereby, the partition coefficient is proportational to the sorption denstiy of the surfactant. Figures 4.15 to 4.19 show that the sorption density of rhamnolipid increases with increasing equilibrium concnentration, [S]. This means that $K_{d,cmc}$ increases with increasing equilibrium concentration of rhamnolipid. However, results of Figures 4.25 to 4.29 show that the PAHs isotherms change slightly or negligibly with increasing rhamnolipid concentraion. This indicates that rhamnolipid sorption on the soil has no significant effect on the PAHs desorption. Therefore, the partition coefficient of PAHs is a constant in the presence of rhamnolipid.

4.6. Summary

The distribution of PAHs in the micelle-soil-water system can be considered as a partitioning process. The partition coefficient between micelle and water phase (K_m) can be related to the partition coefficient of PAHs in octanol-water phase (K_{ow}). The ratio of K_m over K_{ow}, i.e., β, only depends on the surfactant type and can be determined experimentally. The β value for Triton X-100 (synthetically nonionic surfactant) and rhamnolipid (anionic biosurfactant) is 0.4 and 0.44, respectively. An empirical equation for estimating the ratio, $\beta = (0.031y_1 - 0.0058y_2)$, is not only able to predict the β value of Triton X-100 but also that of rhamnolipid. The term, y_1, is the number of "hydrophobic" carbons and y_2 is number of "hydrophilic" groups.

The surfactant exhibits the strong attraction with the soil particle. The sorption of Triton X-100 can be described by the Langmuir isotherm except the sorption with the initial concentration at 30 CMC. The sorption of rhamnolipid shows a linear isotherm based on the tested initial concentration (0 ~ 30 CMC). According to experimental results, rhamnolipid has stronger sorption ability (K_d = 34 L/Kg) than Triton X-100 (K_d = 10 L/Kg) in the soil. The sorption density of both surfactants decreases with increasing PAHs concentration sorbed in the soil.

The apparent partition coefficient of PAHs in the presence of surfactant, $K_{d,cmc}$, can be described by an equaiton: $K_{d,cmc} = \frac{\alpha K_{ow} f_{oc}^*}{(1 + \beta K_{ow}[S])}$. The term, K_{ow}, is the partition coefficient

of PAHs in octanol-water phase, α is a constant for reflecting the affinity between the organic contaminant and the soil, f_{oc}^{*} is the total content of soil organic carbon, and [S] is the surfactant solution in the aqueous phase. For PAHs desorption in the presence of Triton X-100, $K_{d,cmc}$ can be related to the reciprocal of surfactant concentration, i.e., $K_{d,cmc} = K/[S]$ in a certain range of surfactant concentration (10~20 CMC). The integrated coefficient, K, is equal to $\alpha[\gamma q_{max}+f_{oc}]/\beta$. The term, q_{max}, is the sorption capacity of Triton X-100 on the soil. For the PAHs desorption in the presence of rhamnolipid, $K_{d,cmc}$ is invariant when increasing rhamnolipid concetration in the soil-water system.

4.7. References

1. Almgren, M, F. Grieser, J. K. Thomas (1979), Dynamics and Static Aspects of Solubilization of Neutral Arenes in Ionic Micellar Solutions, J. Am. Chem. So., Vol. 101, No. 2, 279-291.
2. Carberry, J. B, C. J. Twardowski, and D. K. Eberhart (1977), Clay Adsorption Treatment of Non-Ionic Surfactants in Wastewaters, J. Wat. Pollut. Control Fed., Vol. 49, 452-459.
3. Deshpande, S., B. J. Shiau, D. Wade, D. A. Sabatini, and J. H. Harwell (1999), Surfactant Selection for Enhancing Ex Situ Soil Washing, Wat. Res., Vol. 33, No. 2, 351-360.
4. Edwards, D. A., R. G. Luthy, and Z. Liu. (1991), Solubilization of Polycyclic Aromatic Hydrocarbons in Micellar Nonionic Surfactant Solutions, Environ. Sci. Technol., Vol. 25, No. 1, 127-133.
5. Ellis, W. D., J. R. Payne, and G. D. McNabb (1985), Treatment of Contaminated Soils with Aqueous Surfactants, U. S. Environmental Protection Agency, EPA-600/2-85-129.
6. Fiechter A. (1992), Biosurfactants: Moving towards Industrial Application. Trends Biotech, Vol. 10, 208-217.
7. Hassett, J. J., J. C. Means, W. L. Barnwart, and S. G. Wood (1980), Sorption Properties of Sediments and Energy-Related pollutants. U. S. Environmental Protection Agency, Athens, GA., EPA-600/3-80-041.
8. Jafvert, C. T. (1991), Sediment- and Saturated-Soil-Associated Reactions Involving an Anionic Surfactant (Dodecylsulfate). 2. Partition of PAH Compounds among Phases, Environ. Sci. Technol., Vol. 25, No. 6, 1039-1045.
9. Jafvert, C. T., J. K. Heath, and P. L. Van Hoof (1994), Solubilization of Non-Polar Compounds by Non-ionic Surfactant Micelles, Wat. Res., Vol. 28, No. 5, 1009-1017.
10. Jafvert, C. T., W. Chu, and P. L. Van Hoof (1995), A Quantitative Structure-Activity Relationship for Solubilization of Nonpolar Compounds by Nonionic Surfactant Micelles, ACS Symposium Series 594, 24-37.
11. Karickhoff, S. W. (1984), Organic Pollutant Sorption in Aquatic System, J. Hydraul. Eng., Vol. 110, No. 6, 707-735.
12. Lang, S. and F. Wagner, Structure and Properties of Biosurfactants. In: Biosurfactants and Biotechnology (Kosaric N, Cairns WL, Gray NCC, eds). New York: Marcel Dekker, 21-45.
13. Mackay, D. M. and J. A. Cherry (1989), Groundwater Contamination: Pump-and-Treat Remediation, Environ. Sci. Technol., Vol. 23, No. 6, 630-636.
14. Miller R. M. (1995), Biosurfactant-Facilitated Remediation of Metal-Contaminated Soils, Environ. Health Prospect., Vol. 103 (Suppl 1), 59-62.
15. Narkis, N. and B. Ben-David (1985), Adsorption of Non-Ionic Surfactants on Activated Carbon and Mineral Clay, Water Res. Vol. 19, No. 7, 815-824.

16. Noordman, W. H., M. L. Brusseau, and D. B. Janssen (2000), Adsorption of a Multicomponent Rhamnolipid Surfactant to Soil, Environ. Sci. Technol., Vol. 34, No. 5, 832-838.
17. Rosen, M. J., Surfactants and Interfacial Phenomena. 2nd ed. John Wiley & Sons Inc., New York, 1989.
18. Rouse, J. D., D. A. Sabatini, and J. H. Harwell (1993), Minimizing Surfactant Losses Using Twin-head Anionic Surfactants in Subsurface Remediation, Environ. Sci. Technol., Vol. 27, No. 10, 2072-2078.
19. Sabatini, D. A. and T. A. Austin (1991), Characteristics of Rhodamine WT and Fluorescein as Adsorbing Ground-Water Tracer, Ground Water, Vol. 29, No. 3, 341-349.
20. Shaoo D., J. A. Smith, T. E. Imbrigiotta, and H. M. Mclellan (1998), Surfactant-Enhanced Remediation of a Trichloroethene-Contaminated Aquifer. 2. Transport of TCE, Environ. Sci. Technol., Vol. 32, No. 11, 1686-1693.
21. Schwarzenbach, R. P., P. M. Gschwend, and D. M. Imboden, Environmental Organic Chemistry, New York, 1993.
22. Sun, S. and S. A. Boyd (1993), Sorption of Nonionic Organic Compounds in Soil-Water Systems Containing Petroleum Sulfonate-Oil Surfactants, Environ. Sci. Technol., Vol. 27, No. 9, 1340-1346.
23. Sun, S. and W. P. Inskeep (1995), Sorption of Nonionic Organic Compounds in Soil-Water System Containing a Micelle-Forming Surfactant, Environ. Sci. Technol., Vol. 29, No. 4, 903-913.
24. Thangamanl, S. and G. S. Shreve (1994), Effect of Anionic Biosurfactant on Hexadecane Partitioning in Multiphase Systems, Environ. Sci. Technol., Vol. 28, No. 12, 1993-2000.
25. West, C. C. and J. H. Harwell (1992), Surfactants and Subsurface Remediation, Environ. Sci. Technol., Vol. 26, No. 12, 2324-2329.
26. Yeom, I. T., M. M. Ghosh, and C. D. Cox (1996), Kinetic Aspect of Surfactant Solubilization of Soil-Bound Polycyclic Hydrocarbons, Environ. Sci. Technol., Vol. 30, No. 5, 1589-1595.

5. ELECTRO-OSMOTIC FLOW RATE IN UNSATURATED SOILS

5.1. Introduction

Electrokintics has found its applications in sludge dewatering, grout injection, in-situ generation of chemical reagents in soil remediation, groundwater flow barriers, and soil and groundwater decontamination (Mitchell, 1986). Since its development at the beginning of the 19th century, many theories have been advanced to explain the mechanism of electro-osmotic (EO) flow in the capillary and the porous media. Reuss (1809) was the first to discover that a water flow could be induced through a capillary by an external electric field. Later, Helmholtz (1879) incorporated electrical components into the electro-osmotic flow equation. Although the electric double layer theory can not totally explain the electro-osmotic behaviors, it is well received as a means to describe the electro-osmotic phenomenon in most capillary materials (Burgreen and Nakache, 1964).

Figure 5.1 illustrates the distribution of electro-osmotic flow based on the electric double layer theory. Since the surface charge of most soils is negative in typical soil-water system, it induces an excess counter-ion (cation) distribution in a thin water layer at the vicinity of the soil surface. When an electric field is imposed to the soil-water system, the cations will migrate to the cathode and the anions to the anode. As the cations and anions are always hydrated, a water momentum (or frictional drag) is produced by the movement of these ions (Yeung and Datla, 1995). In the presence of excess positive charges on the soil surface, a net electric driving force transports the water layer from the anode to the cathode (flow 1). In other words, the electro-osmotic flow that results from the fluid surrounding the soil particles is induced by ionic fluxes (Lyklema and Minor, 1998).

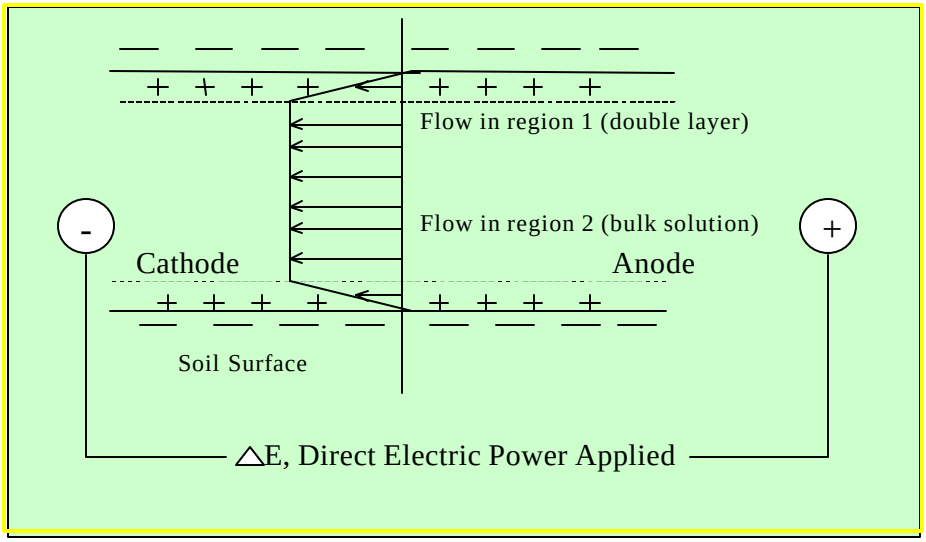

Figure 5.1. Schematical diagram of distribution of electro-osmotic flow based on the electric double layer theory.

In addition, the water molecules in bulk phase (flow in region 2) can be carried along with "flow in region 1" in the same flow direction. Interaction between "flow in region 1" and "flow in region 2" enables the movement of water in the bulk phase (i.e., by drag action). Therefore, the total observed electro-osmotic flow is attributed to the movement of these two water layers. In the absence of electrolyte or when both the cationic and anionic components are equivalent in concentrations, there will be no "flow in region 1". As a result, "flow in region 2" is not possible. Consequently, the overall electro-osmotic flow would be zero.

Based on above arguments, the zeta potential and the charge distribution in the fluid adjacent to the capillary wall play key roles in determining the electro-osmotic flow. Many researchers have reported that the zeta potential of the soil particle correlates well with the electro-osmotic flow (Quincke, 1861, Dorn, 1878, Helmholtz, 1879, Smoluchowski, 1921, Neal and Peters, 1946). The Helmholtz-Smoluchowski equation is the one of the earliest and still widely used models of electrokinetic processes (Helmholtz, 1879, Smoluchowski, 1921). The Helmholtz-Smoluchowski equation assumes the pore radii are relatively large compared to the thickness of the diffuse double layer and all of the mobile ions are concentrated near the soil-water interface. These assumptions are valid as long as soils with large pores are saturated with water or dilute electrolyte solutions. The Helmholtz-Smoluchowski equation has the following expression:

$$v_e = \frac{D\zeta}{4\pi\eta}\frac{E}{L} \qquad [5.1]$$

where v_e = velocity of electro-osmotic flow in soils ($m \bullet s^{-1}$), E = electric potential ($V \bullet m$), D = dielectric constant of the soil water ($C \bullet V^{-1} \bullet m^{-1}$), ζ = zeta potential of soil particle (V), η = viscosity of soil water ($N \bullet s \bullet m^{-2}$), L = electrode spacing (m). For small capillaries or unsaturated soils, where the thickness of electric double layer and the water layer radius are of the same order of magnitude, the Helmholtz-Smoluchowski equation is no longer applicable.

Furthermore, the zeta potential alone can not totally predict the EO flow rate. At the onset of EO flow, the electrostatic force is the only driving mechanism for water movement, i.e. "flow in region 1" (Vane and Zang, 1997). According to the Coulomb's law, the electrostatic force is a function of the intensity of electric field and the electrical charge. Therefore, the applied field (potential gradient) and excess charge at the soil-water interface must be included in modeling the osmotic water flow. The zeta potential, measured at the shear plane, can not directly represent the charge condition at the very surface of the soil particle. Consequently, zeta potential may not be a reliable parameter for predicting the electro-osmotic flow.

The surface charge density of soil surface has also been considered a contributing parameter to the electro-osmotic flow rate. Esrig and Majtenyi (1966) applied the Buchkingham π theorem to describe the electro-osmotic flow in porous media. They suggested that the average velocity is proportional to the surface charge density of the porous media. Schmid (1950) developed a quantitative model based on the concept of volume charge density. He assumed that the excess cations countering the negative charge of clay particles are uniformly distributed through the entire pore cross-sectional area. The Schmid equation has the following expression:

$$v_e = \frac{r^2 \rho_0 F}{8\eta}\frac{E}{L} \qquad [5.2]$$

where r = radius of pore (m), ρ_0 = volume charge density in the pore ($C \bullet m^{-3}$), F = Faraday constant (96,500 $C \bullet eq^{-1}$).

In dealing with the vadose zone (i.e., unsaturated), all the above models may not be applicable because these equations were derived under the scenario of saturated condition. Practically, the most widely used electro-osmotic flow equation for the under unsaturated subsurface system is proposed by Casagrande (1949):

$$Q = k_e i_e A \qquad [5.3]$$

where Q = electro-osmotic flow rate ($m^3 \bullet s^{-1}$), k_e = coefficient of electro-osmotic conductivity ($m^2 \bullet V \bullet s^{-1}$), i_e = applied electrical gradient ($V \bullet m^{-1}$), A = gross cross-sectional area perpendicular to water flow (m^2). The hydraulic conductivity of different soils can vary by several orders of magnitude; however, the coefficient of electro-osmotic conductivity is generally between 1 x 10^{-9} and 10 x 10^{-9} $m^2/(V\ s)$ and is independent of the soil type (Mitchell 1993). Therefore, an electrical gradient is a much more effective driving force than the hydraulic gradient. Although Equation 5.3 is considered a practical one, it can not account for the effect of various physical-chemical parameters of a soil-water system.

There is need to develop a simple and reliable electro-osmotic water flow equation that can be applied to unsaturated soils in terms of fundamental soil-water parameters, such as, the water content of the soil, the soil surface charge density, and the electrolyte concentration. The objective of this study was to develop a semi-empirical equation for the prediction of electro-osmotic flow rate in unsaturated soils. Several operational parameters were studied. There included the solution pH, the electric field strength, the soil water content, and the electrolyte concentration. It is hoped that the semi-empirical equation can provide a better tool for designing in-situ remediation of contaminated soils in the vadose zone.

5.2. Theoretical Aspects

The water flow behavior of the unsaturated soil is totally different from that of the saturated system. In the presence of an electrical field, a friction force is created when water molecules begin to move in the soil pores. The frictional stress decreases as the thickness of the water layer increases. For the unsaturated soil-water system, the water layer is extremely thin, usually ranging from 10^{-8}cm to 10^{-6}cm. Under such circumstance, all water molecules exhibit strong frictional interaction with the soil surface. In the case of saturated water-capillary system, the radii of capillaries are relatively large, ranging from 10^{-1}cm to 10^{-3}cm. As a result, most capillary water molecules do not interact physically or chemically with the capillary wall (Iwata et al., 1995). The circular capillary model would be useful for the prediction of EO flow rate, for saturated soils. However, for the unsaturated soil system, the finite plate model would be better for predicting the EO flow.

Figure 5.2. shows the basic concept of the finite plate model. According to the finite plate model, the soil matrix is conceptualized as a finite plate and all water molecules are evenly spread on the soil surface (surface/water). The water layer can be divided into two portions. One portion of the water layer between shear plane and soil surface is stagnant and its thickness is χ. The other water layer under the influence of a shear stress, τ, is moving at a velocity gradient, dv/dz, i.e., a Newtonian fluid. The thickness of this layer is θ. The proportionality constant is the coefficient of viscosity of the fluid. That is:

$$\tau = \eta(dv/dz) = \eta(v_0/\theta) \qquad [5.4]$$

where τ = shear stress ($erg \bullet m^{-2}$), η = viscosity of fluid ($erg \bullet s \bullet cm^{-2}$), dv/dz= velocity gradient of the fluid (s^{-1}), v_0 = the surface velocity of the water layer ($cm \bullet s^{-1}$), θ = average thickness of water layer between water surface and shear plane(cm).

When an aqueous solution moves tangentially across a charged surface, the thin water layer becomes a two-dimensional gel which macroscopically behaves as a rigid body (Lyklema et al., 1998a1). Figure 5.2 shows the conceptualized dimensions of the water layer of finite length, L, and width, w. The EO flow rate can be expressed by the following equation:

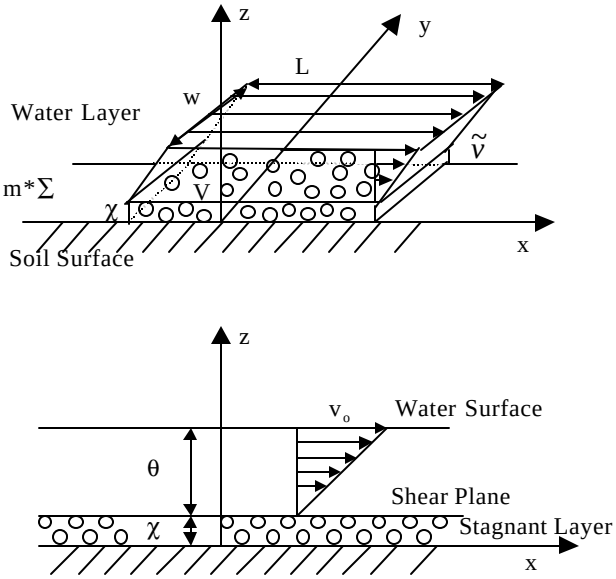

Figure 5.2. Illustration of EO flow behavior by the finite plate model.

$$Q = \tilde{v}A = \tilde{v}qw \qquad [5.5]$$

where Q = Electro-osmotic flow rate ($cm^3 \bullet s^{-1}$), $\tilde{v}$ = average velocity of the fluid ($cm \bullet s^{-1}$), A = the cross section area of the water layer (cm^2), w = width of the water layer (cm). The thickness of water layer can be expressed as following equation:

$$\theta = V/m\Sigma \qquad [5.6]$$

where V = total volume of the fluid (cm^3), m = total mass of soils (g), Σ = specific surface area of soils ($cm^2 \bullet g^{-1}$). By substituting Equation 5.6 into Equation 5.5, one has the following expression:

$$Q = \tilde{v}Vw/m\Sigma \qquad [5.7]$$

The average velocity can be related to the velocity at the water surface, v_0. That is,

$$\tilde{v} = fv_0 \qquad [5.8]$$

where f = a dimensionless ratio. By substituting Equation 5.8 into Equation 5.7, one has:

$$Q = fv_0Vw/m\Sigma \qquad [5.9]$$

By substituting Equation 5.6 into Equation 5.4, it yuelds:

$$\tau = \eta(v_0/\theta) = \eta v_0 m\Sigma/V \qquad [5.10]$$

Rearranging the above equation gives the following expression:

$$v_0 = \tau V/\eta m\Sigma \qquad [5.11]$$

By substituting Equation 5.11 into 5.9, the EO flow rate is:

$$Q = fv_0Vw/m\Sigma = fV^2\tau w/\eta m^2\Sigma^2 \qquad [5.12]$$

The "rigid" water layer includes water molecules in the region beyond the shear plane into the bulk phase. Therefore, the shear force is proportional to the electric force induced by the electrokinetic charge density (the accumulated space charges from the bulk phase to the zeta potential plane) and the applied electric field, that is:

$$k\sigma_e(E_0/L) = \tau \qquad [5.13]$$

where k = frictional coefficient, σ_e = electrokinetic charge density ($C \bullet cm^{-1}$), E_0 = the intensity of electric field (V), L = total length of water layer (cm). By substituting Equation 5.13 into Equation 5.12, the EO flow rate is written as follows:

$$Q = k\sigma_e(E_0/L)fV^2w/\eta m^2\Sigma^2 = k'\sigma_e(E_0/L)V^2 \qquad [5.14]$$

where $k' = kfw/\eta m^2\Sigma^2$. Since $\omega = \rho V/m$, where ω, ρ, and m are water content of the soil, fluid density and soil mass, respectively, the EO flow rate equation finally has the following form:

$$Q = k'\sigma_e(E_0/L)\omega^2m^2/\rho^2 = K\sigma_e(E_0/L)\omega^2 \qquad [5.15]$$

where K is a characterized coefficient, i.e., $K = kfw/\eta\rho^2\Sigma^2$. This characterized coefficient, K, collects several physical properties of the soil-water system such as the fluid density (ρ), the specific surface area (Σ), width of the water layer (w) and fluid viscosity (η).

5.3. Methodology

According to Equation 5.15, major variables controlling the EO flow rate are the electrokinetic charge density of the soil surface, electric field strength, and the water content. In order to verify Equation 5.15, experiments were conducted to measure the EO flow rate at various values of these parameters. The electrokinetic charge density of the soil surface is related to the zeta potential, which can be measured at different pH values and electrolyte concentrations. Therefore the effect of surface charge density on EO flow rate was determined under various pH values and electrolyte concentrations. Based on the EO flow rate data obtained under different pH, electrolyte concentration, and zeta potential, Equation 5.15 can be established. Table 5.1 lists the experimental conditions.

Electrokinetic Experiments:

Figure 5.3 shows the sketch of the laboratory electro-osmosis reactor. The electro-osmosis cell consists of an acrylic unit with a central cylinder of 11.5 cm in length and 8.9 cm in internal diameter. The volume of both the cathode and the anode compartments are 700 mL. To separate the soil from the water solution, a pair of nylon meshes (Spectrum model PP, mesh opening 149 μm) and a filter paper (Whatman No. 1) are placed between the soil sample and electrodes. Graphite disks (Carbon of America; grade 2020; 3.25 inches in diameter) were used as the electrodes and placed at each electrolytic compartment right behind the membranes.

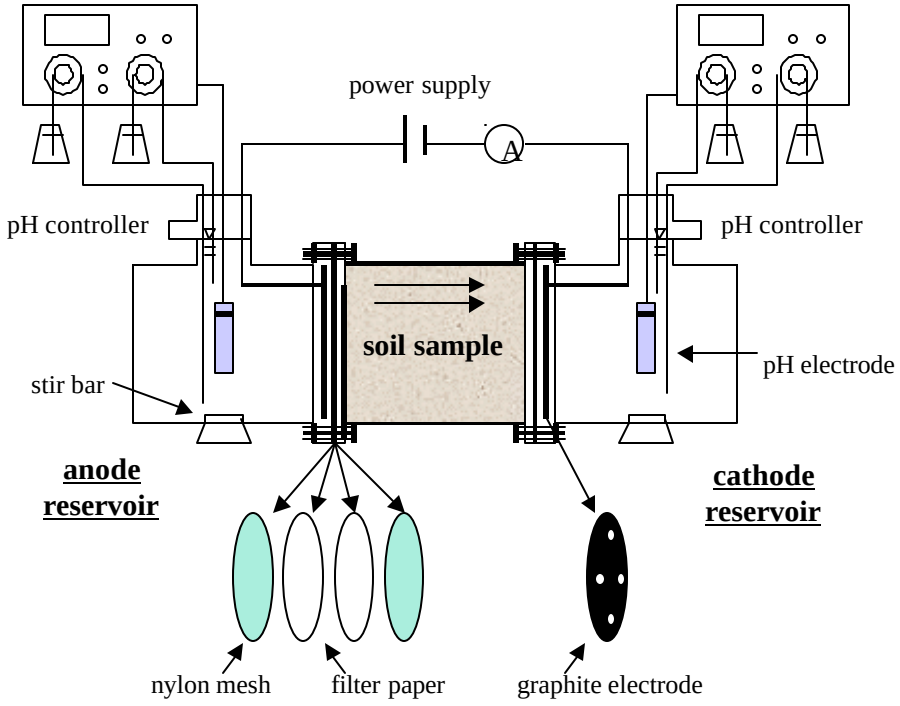

Figure 5.3. Schematic diagram of the electro-osmosis reactor.

The electro-osmotic flow experiments were conducted by changing four operational factors including the pH of the working solution, the electrolyte concentration, the water content of soils, and the intensity of electric field. Table 2 shows experimental conditions for each electro-osmotic experiment. In order to maintain pH constant throughout pH effect experiments, strong acid (1M HCl) was added to the cathode reservoir and strong base (1M NaOH) was added to the anode reservoir (Model pH-22, New Brunswick Scientific).

Table 5.1. Experimental conditions of electro-osmotic flow tests.

Test No.	pH of Solution	Field Strength (V/cm)	Electrolyte	Water Content (%)
1	4	12/10	$1x10^{-3}$M NaCl	20
2	6	12/10	$1x10^{-3}$M NaCl	20
3	7	12/10	$1x10^{-3}$M NaCl	20
4	9	12/10	$1x10^{-3}$M NaCl	20
5	*	6/10	$1x10^{-2}$M CH_3COONa	20
6	*	12/10	$1x10^{-2}$M CH_3COONa	20
7	*	24/10	$1x10^{-2}$M CH_3COONa	20
8	*	12/10	$1x10^{-3}$M NaCl	20
9	*	12/10	$1x10^{-3}$M CH_3COONa	20
10	*	12/10	$1x10^{-2}$M CH_3COONa	20
11	*	12/10	$5x10^{-2}$M CH_3COONa	20
12	*	12/10	$1x10^{-1}$M CH_3COONa	20
13	*	12/10	$1x10^{-2}$M CH_3COONa	5
14	*	12/10	$1x10^{-2}$M CH_3COONa	10
15	*	12/10	$1x10^{-2}$M CH_3COONa	15
16	*	12/10	$1x10^{-2}$M CH_3COONa	20
17	*	12/10	$1x10^{-2}$M CH_3COONa	25

*: uncontrolled pH

The electrodes were connected to a DC power supply (Model WP-705B, Vector-VID Instrument Division). During tests, parameters such as the amount of daily water flow, the intensity of electric current and field strength, pH of catholyte and anolyte were monitored continuously. At the end of a pre-selected time period, the soil sample in the cell was sliced into 10 equal sections. The pH value and the water content of each sector of the soil matrix was measured.

5.4. Results

To gain insight into the mechanism of the electro-osmotic flow it is first necessary to investigate the effect of surface charges on the flow rate. Several operational parameters such as pH, electrolyte type, and electrolyte concentration can affect the surface charge. The change in soil surface charges can dramatically affect EO flow rate. Other parameters studied were the intensity of electric field and soil water content.

5.4.1. Effect of pH

Figure 5.4 shows the daily EO flow as a function of time at various pH values. Results show that the EO water flow rate decreases with decreasing solution pH and ceases at pH around 2.2. The decrease in EO flow rate can be attributed to the decreasing surface charge density of the soils. The soil surface charge is rendered more positive as the pH decreases due to the preferential adsorption of hydronium ions (H^+) on the soil surface (Stana-Kleinschek et al., 1998). The electrostatic force driving the water molecules decreases and the EO flow decreases as the surface density approaches neutrality. According to Equation 5.15, the transport of water is attributed to the charge of the water layer between shear layer and water

surface, i.e., electrokinetic charge density. Since the electrokinetic charge density is balanced by the charge between the shear plane and soil surface, the electrokinetic charge density would change as the surface charge changes. The magnitude of the electrokinetic charge density at different pHs can be readily obtained from the zeta potential measurements. For symmetrical electrolytes, the electrokinetic charge density can be written as follows (Hunter, 1981):

$$\sigma_e = 11.74 c^{1/2} \sinh(19.46 z\zeta) \qquad [5.16]$$

where σ_e = electrokinetic charge density ($\mu C \bullet cm^{-2}$), c = electrolyte concentration (M), z = valance of electrolyte ion, ζ = zeta potential (V).

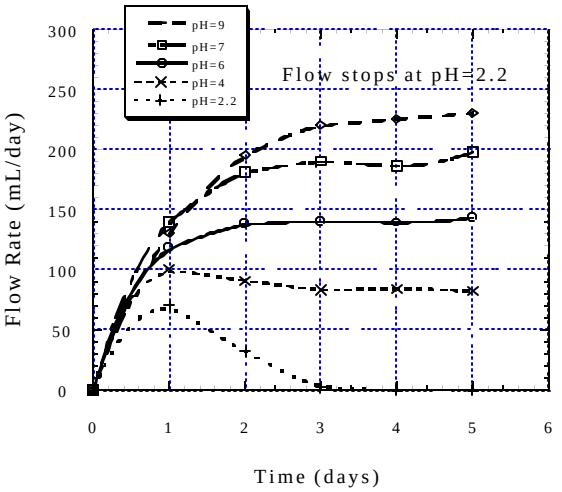

Figure 5.4. Influence of the pH on the electro-osmotic flow rate. Experimental conditions: electrolyte concentration = 10^{-3} M NaCl; voltage = 12 V; water content = 20% (w/w).

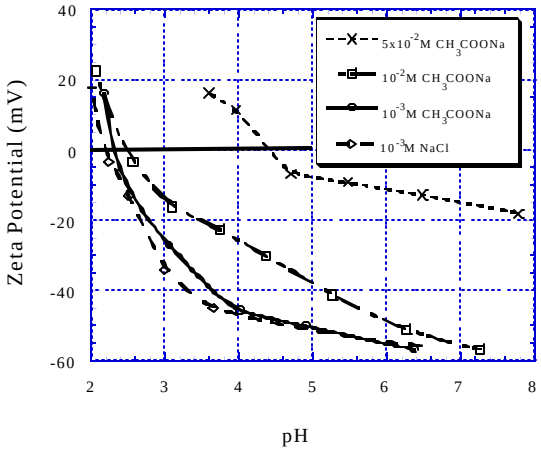

Figure 5.5. The zeta potential of soil particles as a function of pH at various electrolyte concentrations.

Figure 5.5 shows the zeta potential of soil particles as a function of pH at various electrolyte concentrations. Results show the absolute value of zeta potential decreases with decreasing the pH value and the pH_{ZPC} is around 2.2 at the electrolyte concentration of 10^{-3}M NaCl. Figure 5.6 shows the pH value of the soil as a function of normalized distance. The average pH value of the soil can be obtained from this graph, then, the zeta potential at different pH values can be found from Figure 5.5. According to Equation 5.16, then, the electrokinetic charge density of soil can be determined at the various pH conditions. The relationship between the EO flow rate and the electrokinetic charge density (at different pH) is shown in Figure 5.7. Results indicate that the EO flow is proportional to the electrokinetic charge density as expected in the EO flow model.

5.4.2. Effect of Electric Field

Figure 5.8 shows the daily flow as a function of time under various applied electric voltages. Results show that the EO flow rate increases with increasing the intensity of electric field. As predicted by Equation 5.15, EO flow rate is proportional to the electric potential. Figure 5.9 shows the linear relationship between the flow rate and the intensity of electric field. However, it is seen that the EO flow rate decreases with increasing operation time

(Figure 5.8). Since the solution pH was not controlled during tests, the protons produced at the anode neutralize the surface charge density of the soil. Meanwhile, the electrokinetic charge density decreases which results in the EO flow in the soil decreasing gradually.

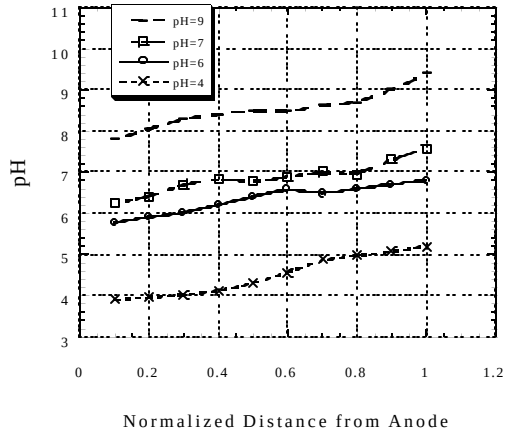

Figure 5.6. The pH value of the soil as a function of normalized distance. Experimental conditions: electrolyte concentration = 10^{-3} M NaCl; voltage = 12 V; water content=20% (w/w).

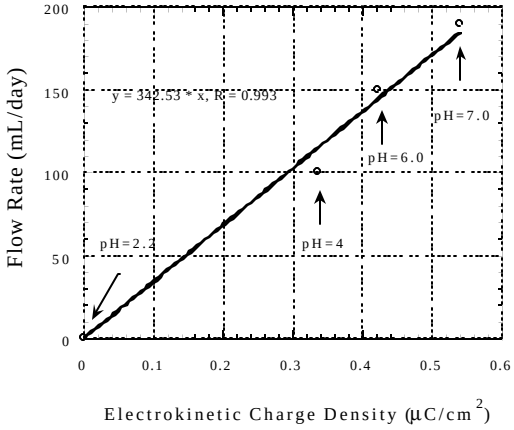

Figure 5.7. The electro-osmotic flow rate as a function of the electrokinetic charge density.

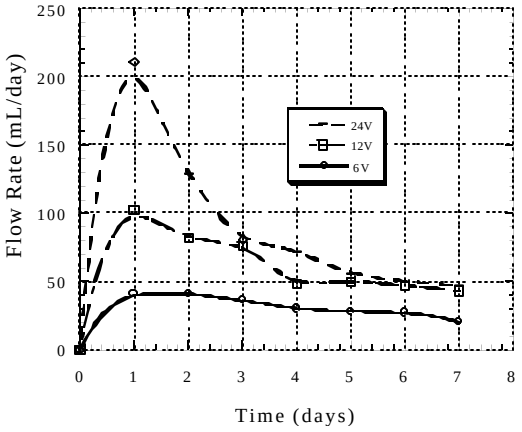

Figure 5.8. Influence of the intensity of electric field on the electro-osmotic flow rate. Experimental conditions: electrolyte concentration = 10^{-2} M CH_3COONa; water content = 20% (w/w). The pH was not controlled.

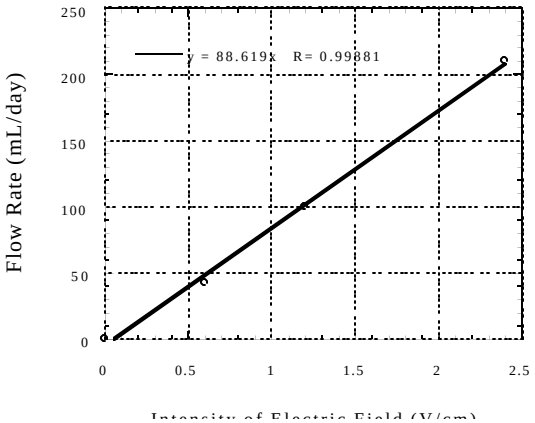

Figure 5.9. The electro-osmotic flow rate as a function of the field strength.

5.4.3. Effect of Electrolyte Concentration

Figure 5.10 shows the influence of the electrolyte concentration on the electro-osmotic flow rate. Results show that the electrolyte concentration has no effect on the EO flow rate at least during the one-day treatment. Moreover, the EO flow rate decreases with increase of operation time. This can be attributed in part to the acidification of soils. According to Figure 5.4, it is seen that the EO flow rate approaches a steady state even as the electrolyte concentration increase due to the addition of the strong acid/base for pH control. This

observation also implies that the electrolyte concentration has no effect on the EO flow rate as long as the electrolyte ions do not interact specifically with the soil (i.e., indifferent ions). However, the electrolytes that specifically adsorb on the soil can change the zeta potential and which in turn modifying its surface charge density.

From Figure 5.10, it is seen that the flow rate decreases with increasing the electrolyte concentration after several-days treatment. This can be attributed to the adsorption of the electrolyte ions onto the soil surface. From Figure 5.5, the electrolyte (sodium acetate) interacts specifically with the soil surface, as indicated by an increase in pH_{zpc} upon an increase of electrolyte concentration. Figure 5.11 shows the solution pH at various electrolyte concentrations. Based on data shown in Figures 5.5 and 5.11, it is seen that the absolute value

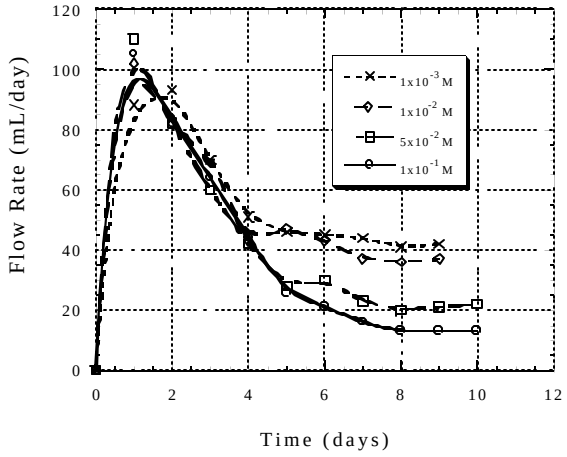

Figure 5.10. Influence of the electrolyte concentrations on the electro-osmotic flow rate. Experimental conditions: voltage = 12 V; water content = 20% (w/w). Electrolyte = CH_3COONa.

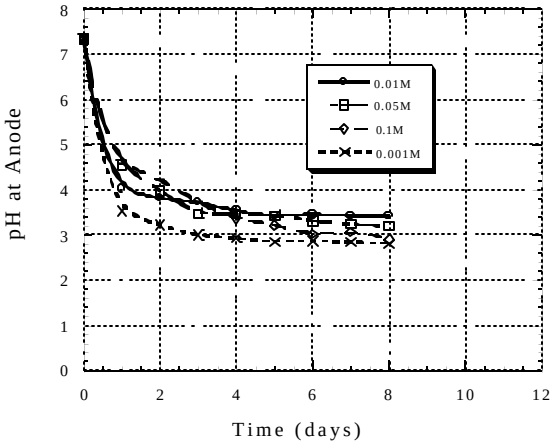

Figure 5.11. The pH value at anode as a function of time at various electrolyte concentrations. Experimental conditions: voltage = 12 V; water content = 20% (w/w).

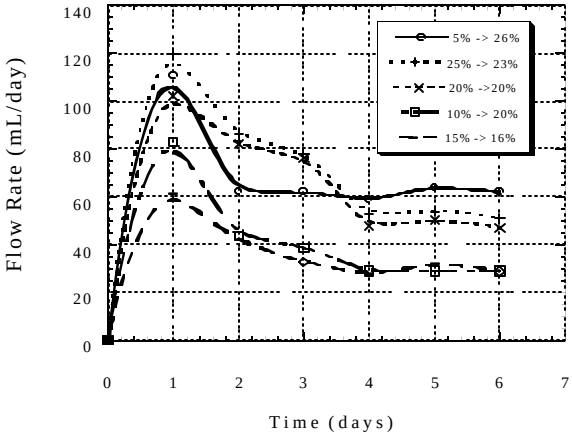

Figure 5.12. The final water content as a function of normalized distance at various initial water contents packed in the soil. Experimental conditions: electrolyte concentration = 10^{-2} M CH_3COONa; voltage = 12 V.

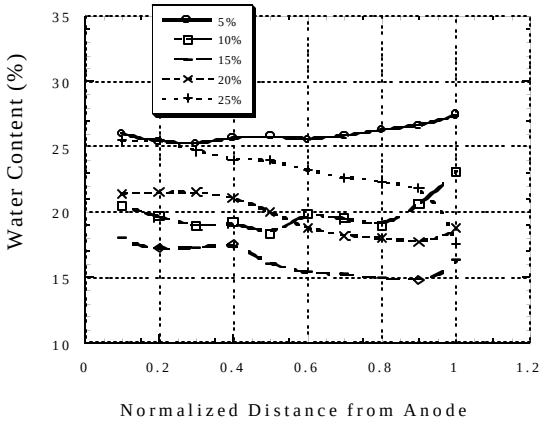

Figure 5.13. Influence of the water content on the electro-osmotic flow rate. Experimental conditions: electrolyte concentration = 10^{-2} M CH_3COONa; voltage = 12 V.

of zeta potential decreases with increasing ionic strength at a given pH. According to

Equation 5.16, the electrokinetic charge density decreases as zeta potential decreases. Therefore, the EO flow decreases with increasing electrolyte concentration as expected.

5.4.4. Effect of Water Content

Figure 12 shows the EO flow rate as a function of time at various initial water contents. Regardless of the initial water content, the EO flow rate increases to a maximum level then decreases gradually to reach a steady state value. The initial surge in EO flow can be attributed to the flux of H^+ ions into the soil column. When the H^+ flux stops, the pH value of the soil water system decreases, approaching the pH_{zpc} value of the soil. As a result, the EO flow rate decreases.

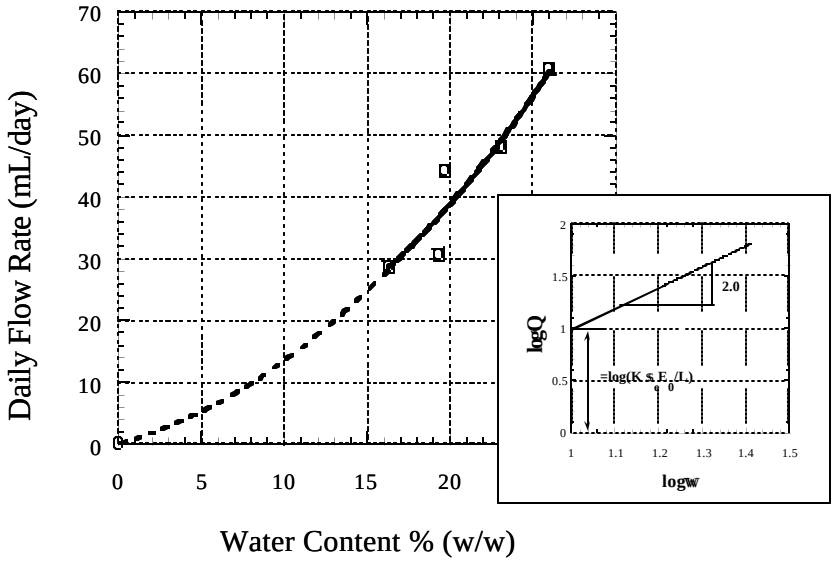

Figure 5.14. The electro-osmotic flow as a function of water content of the soil. Experimental conditions: electrolyte concentration = 10^{-2} M CH_3COONa; voltage = 12 V.

Figure 13 shows the water content of the soil as a function of the normalized distance at the 6^{th}-day, which is the steady state condition. Results show that the final water content is different from the initial value. As the EO system reached a hydraulic steady state, the water content of soil varies from 5% to 26%, 10% to 20%, 15% to 16%, 20% to 20%, and 25% to 23%, respectively. The diversity between initial and final water content can be attributed to various hydraulic properties of EO systems. The use of different initial water contents could change the hydraulic properties of soil samples such as infiltrate rate, porosity, and hydraulic conductivity, which results in different final water contents. However, the hydraulic properties of soil samples can not be controlled, therefore, there is no relationship between initial and final water content.

Figure 14 shows the EO flow rate versus final soil water content. Equation 5.15 clearly predicts that the EO flow rate is proportional to the square of the water content (i.e., $Q \propto \omega^2$). Accordingly, by plotting logQ versus logω, one can have a straight line which slope is 2.0 and the intercept of y-axis is log ($K\sigma_e E_0/L$). With information, specifically, σe and E_0/L given from experimental conditions, the K value was calculated to be 57 $cm^3 \bullet \mu C^{-1} \bullet V^{-1}$. Figure 14 shows that a straight line as predicted could fit experimental data. Furthermore, Gray and Mitchell (1967) reported a parabolic relationship between the EO flow and the water content in the soil-water system. Our observation was in agreement with what was reported by Gray and Mitchell.

5.5. Discussion

Based on experimental results, the semi-empirical equation of EO flow was developed: $Q = K\sigma_e(E_0/L)\omega^2$. Where Q, K, σ_e, E_0/L, and ω, are electro-osmotic flow rate, characterized coefficient, electrokinetic charge density, potential gradient, and soil water content, respectively. According to this equation, some practical aspects of electro-osmosis process must be of consideration.

The working solution and soils in practiacl electro-osmosis system should be relatively neutral because solution of low pH values cannot be injected into the subsurface according to U.S. EPA regulations (Lageman et. al., 1989). In addition, the electro-osmotic flow rate can be reduced in the acidic environment since the electrokinetic charge density decreases with decreasing pH. In order to maintain a long-term operation in a neutral environment, the chemical buffer can be induced to the electro-osmosis process.

Weak acids, such as acetic acid, can undergoes partial dissociation in water and can be served as a pH buffer in the anode chamber. It is beliveed that acetic acid is biodegradable and environmental safe (Alshawabkeh et. al., 1999). In addition, the acetic acid can be used at the cathode to neutralize the hydroxyl ions generated by electrolytic reduction of water (Puppala et al., 1997). There are two major advantages in using acetic acid to depolarize the hydroxyl ions produced in the cathode. First, the electrical conductivity of the soil-water mixture will not increase dramatically since the concentration of ions generated by dissociation of the acid is very low. Secondly, the prevention of a low electrical conductivity zone can be expected in the soil close to the cathode because most metal acetated are highly soluble.

Chemically inert and electrically conducting materials such as graphite, coated titanium, or platinum sholed be used as anode to prevent dissolution of the electrode and genetation of undesirable corrosion procudes in an acidic environment. In order to maintain a neutral pH, sacrificail electrodes can be used as anodes. For instance, the copper electrodes are used into a copper sulphate solution. When an electrical potential is applied, copper ions will dissolve into solution at the anode and deposit at the cathode to maintain the charge balance. Electrolytic reaction of water occurs insignificatantly, therefore, hydrogen and hydroxyl ions is negligible. Consequently, pH value of solution in both anode and cathode maintain constant (Yeung and Datla).

In comparison Figure 5.4 and 5.10, it is found that the electro-osmotic flow rate is different by using different electrolytes. Results show that the EO flow rate is around 150mL and 110 mL for sodium chloride and sodium acetate, respectively. This may be attributed to the different coordination number of water molecule (i.e., hydration number) with cations and anions. Since anions still exit in the double layer and their moving direction is against the cations, anions carring with some water molecules may decrease the electro-osmotic flow rate.

5.6. Summary

Based on experimental results, a semi-empirical equation for the EO flow rate in an unsaturated soil-water system was verified. A finite plate model was used to derive the EO flow rate in unsaturated soils. The derivation indicates that the EO flow rate is theoretically proportional to the extent of electrokinetic charge density, the intensity of electric field, and square of the soil water content in the soil-solution systems. Experimental results were in agreement with these predictions. For the effect of electrolyte concentration, results imply

that there is no significant effect on the EO flow rate as long as the electrolyte ions do not interact specifically with the soil. The semi-empirical equation of EO flow was developed: $Q = K\sigma_e(E_0/L)\omega^2$. Where Q, K, σ_e, E_0/L, and ω, are electro-osmotic flow rate, characterized coefficient, electrokinetic charge density, potential gradient, and soil water content, respectively. The K value was 57 $cm^3 \bullet \mu C^{-1} \bullet V^{-1}$ for the soil tested.

5.7. References

1. Alshawabkeh, A. N., A. T. Yeung, and M. R. Bricka (1999), Practical Aspecs of In-Situ Electrokinetic Extraction, Journal of Environmental Engineering, Vol. 125, No. 1, pp. 27-35.
2. Burgreen, D., F. R. Nakache (1964), Electrokinetic Flow in Ultrafine Capillary Slits, J. Phy. Chem., Vol. 68, 1084-1091.
3. Casagrande, I. L. (1949), The Application of Electro-Osmosis to Practical Problems in Foundations and Earthworks, Bautechnique, Vol. 1, 1-29.
4. Dorn, E. (1880), Wied. Ann., Vol. 10, 46.
5. Electrokinetics (EK) Inc. (1995), Assessment of Selected Enhancement Schemes in Electrokinetic Remediation, SBIR-Phase I Rep. Sibmitted to the U.S. Army Corp. of Engineers-Waterways Experiment Station(USAE-WES), Baton Route, La., 159.
6. Esrig, M. I. And S. Majtenyi (1966), A New Equation for Electroosmotic Flow and Its Implications for Porous Media, Highway Research Record, Vol. 111, 31-41.
7. Gray, D. H. and J. K. Mitchell (1967), Fundamental Aspects of Electro-Osmosis in Soils, J. Soil Mech. and Foun. Div., ASCE, Vol. 93, 209- 236.
8. Helmholtz, H. (1879), Ann. Physik, Vol. 7, 137.
9. Hunter, R. J. Zeta Potential in Colloid Science Principles and Applications; Academic Press: Orlando, FL, 1981.
10. Iwata, S.; Tabuchi, T.; Warkentin, B. P. Soil-Water Interactions: Mechanisms and Applications; Marcel Dekker: New York, NY, 1995.
11. Lageman, R., W. Pool, and G. Seffinga (1989), Electro-Reclamation in Theory and Practice, Rep. No. EPA/540/2-89/056, U.S. Environmental Protection Agency, Washington, D.C., 57-76.
12. Lyklema, J. and M. Minor (1998a), On Surface Conduction and Its Role in Electrokinetics, Coll. Surfaces A: Physicochemical Eng. Aspects, Vol. 140, 33-41.
13. Lyklema, J., S. Rovillard, and J. D. Coninck (1998b), Electrokinetics: The Properties of the Stagnant Layer Unraveled, Langmuir, Vol. 14, 5659-5663.
14. Mitchell, J. K. Workshop on Electrokinetics Treatment and Its Application in Environmental-Geological Engineering for Hazardous Waste Site Remediation, Seattle, WA, Aug 4-5, 1986, 20-31.
15. Mitchell, J. K., Fundamentals of Soil Behavior; 2nd Ed., John Wiley & Sons: New York, NY, 1991.
16. Neale, S. M. and R. H. Peters (1946), Electrokinetic Measurements with Textile Fibers and Aqueous Solutions, Farad. Soc. Trans., Vol. 42, 478-487.
17. Puppala, S., A. N. Alshawabkeh, Y. B. Acar, R. J. Gale, and R. M. Bricka (1997), Enhanced Electrokinetic Remediation of High Sorption Capacity Soils, J. Haz. Mat., Vol. 55 (1-3), 203-220.
18. Quincke, G. (1861), Ann. Physik., Vol. 113, 513.

19. Reuss, F. (1809), Memories Soc. Imp. Naturalistes, Vol. 2, 327.
20. Schmid, G. (1950), Zhurnal fur Electrochemie, Vol. 54, 424.
21. Smoluchowski, von M. (1921), Handbuch der Elektrizitat und der Magnetismus II, Vol. 2, 366-428.
22. Stana-Kleinschek, K. and V. Ribitsch (1998), Electrokinetic Properties of Processed Cellulose Fibers, Coll. Surfaces A: Physicochemical Eng. Aspects, Vol. 140, 127-138.
23. Vane, L. M. and G. M. Zang (1997), Effect of Aqueous Phase Properties on Clay Particle Zeta Potential and Electro-Osmotic Permeability: Implications for Electro-Kinetic Soil Remediation Processes, J. Haz. Mat. Vol. 55, 1-22.
24. Yeung, A. T. and S. Datla (1995), Fundamental Formulation of Electrokinetic Extraction of Contaminants from Soils, Can. Geotech. J., Vol. 32, 569-583.

6. ELECTROKINETICS OF NONIONIC ORGANICS IN SOILS

6.1. Introduction

Electrokinetic (EK) decontamination process has been one of the most promising in-situ technologies for the removal of heavy metals and organics from soils. The EK takes place when an electric field is applied to a porous medium, which invokes the electro-osmosis, electrophoresis, and electrolytic migration (Mitchell 1991). Electro-osmosis is the movement of the liquid (water in most cases) induced by the excess surface charge on the porous media. Electrophoresis is the motion of charged colloids in the soil-liquid mixture. The electrolytic migration is the migration of ionic species in the pore fluid. Based on different physico-chemical properties of contaminants and soils, the specific contaminant could be removed from soils by one or coupling of these mechanisms. The EK process can be applied to a variety of pollutants. Much research in EK treatment for heavy metals has been reported (Acar et al., 1994; Reed et al., 1996; Li et al., 1996). To date, information on the removal of organic contaminants is limited. Nevertheless, Bruell (1992) has demonstrated that benzene, toluene, ethylene, xylene (BETX compounds), and trichloroethylene loaded onto kaolinite can be moved toward the cathode by the electro-osmosis process. Experimental results on the transport and removal of polar organic species such as phenol (Acar et al., 1992) and acetic acid (Renaud and Probstein, 1987) have been reported. However, most previous research focused on the removal of highly soluble or ionic organic compounds. The transport information of nonionic organic compounds in the EK system is still limited.

In general, the transport of nonionic organic contaminants in the EK system can be simulated by the diffusion-advection-sorption (DAS) equation (Probstein and Hicks, 1993). For the simplificaiton of the transport simulation, the zeta potential of the soil surface was always assumed to be a constant. However, zeta potential is varying during the EK process because H^+ ions produced at the anode enter the soil-water mixtures. The variation in zeta potentials causes an unstable electro-osmotic flow rate. This can make the advection term in the DAS equation produce errors during the simulation process. In addition, there exist effects of organic concentration and soil to solution ratio on the sorption-desorption behavior of the organic contaminant. The sorption term of the DAS equation yields errors when ignoring these sorption effects. Therefore, in order to obtain an accurate transport simulation for nonionic organics, a stable electro-osmotic flow rate and the consideration of sorption effects are necessary. Another important issue about the transport simulation is the sorption-desorption behavior of the nonionic organics during the EK treatment. Many studies based on the equilibrium status to describe the pollutant transport (Shapiro and Probstein, 1993; Bruell et al., 1992). However, the application of equilibrium isotherms may not be applicable under some certain circumstances. It is possible that the sorption-desorption of the organic contaminant is under a non-equlibrium condition during the transport process. Consequently, both equilibrium and non-equilibrium conditions must be considered when studying the transport of nonionic organics.

In this study, nonionic chlorinated compounds including perchloroethylene (PCE), trichloroethylene (TCE), carbon tetrachloride, and chloroform treated by the EK process were investigated. A strong hydrophobic PAH contaminant, phenanthrene, was treated with the use of surfactants (Triton X-100 and rhamnolipid) in the EK system. A numerical solution of the DAS equation based on either equilibrium or non-equilibrium was used to fit experimental

results of the organic movement. Hopefully, the fitted parameters can provide the applicable information for the prediction of the EK decontamination process.

6.2. Theoretical Aspects

The transport of organic contaminants in soil-water system is a complex phenomenon. It consists of the following major processes: advection, molecular diffusion, hydrodynamic dispersion, and chemical sorption. Based on the principle of mass conservation, in an elementary control volume, the change of mass storage with time is equal to the mass inflow rate minus the mass outflow rate. The physical processes that control the flux into and out of the elementary volume are advection and hydrodynamic dispersion induced by electro-osmosis. Loss or gain of solute mass in the elementary volume can occur as a result of chemical or biochemical reactions. The equation of mass conservation for one dimension is usually written as (Van Genuchten and Cleary, 1982):

$$\frac{\partial C_i}{\partial t} = D_i^* \frac{\partial^2 C_i}{\partial x^2} + v\frac{\partial C_i}{\partial x} - \frac{\rho}{\phi}\frac{\partial q_i}{\partial t} \qquad [6.1]$$

where C_i = specific contaminant concentration in the water phase (g/cm^3), D^* = sum of dispersion and diffusion coefficients (cm^2/sec), v = electro-osmotic velocity (cm/sec), ρ = density of the soil (g/cm^3), ϕ = porosity of the soil, q = specific contaminant concentration in the soil phase (g/Kg).

The diffusion term, $D_i^*(\partial C^2/\partial x^2)$, essentially comprises of the molecular diffusion and the mechanical dispersion steps. For estimating the diffusion coefficient of organic compound in the aqueous phase, an emperical expression, based on the Stokes-Einstein equation, is proposed by Wilke and Chang (Werther, 1976):

$$\frac{D_A \mu_{AB}}{T} = 7.4x10^{-8}\frac{(xM_B)^{1/2}}{V_{mA}^{0.6}} \qquad [6.2]$$

where D_A = diffusion coefficient of the solute (cm^2/sec), μ_{AB} = viscosity of the aqueous solution (cP), T = absolute temperature (^{0}K), M_B = molecular weight of the solvent, V_{mA} = solute molecular volumes at the normal boiling point (cm^3/g-mole). According to Equation 6.2, the association parameter, x, allows for reflecting differences in various solvents. For water, the x value is equal to 2.6 (Drew et al., 1981).

For mechanical dispersion, only longitudinal dispersion is considered in the 1-D modeling. One important approximation is that the longitudinal dispersion is proportional to fluid velocity (Domenico and Schwartz, 1998):

$$D_L = \alpha v \qquad [6.3]$$

where D_L = longitudinal dispersion coefficient (cm^2/sec), α = longitudinal dispersity of the soil matrix (cm). At equilibrium, q is a function of solute concentration (C) and is independent of reaction time (t). The sorption isotherms should be considered in describing the total transport process. The sorption behavior of organic generally can be described by the following expressions, linear, Langmuir, and Freundlich isotherm, i.e.,:

$$q_i = K_d C_i \text{ (Linear isotherm)} \qquad [6.4]$$

$$q_I = q_{max}K_L C_i/(1+K_L C_i) \text{ (Langmuir isotherm)} \qquad [6.5]$$

$$q_I = K_f C_i^n \text{ (Freundlich isotherm)} \qquad [6.6]$$

where K_d, K_L, and K_f is the sorption coefficient for linear, Langmuir, and Freundlich isotherm, respectively. The term, q_{max}, is the maximal sorption capacity of the soil and n is the Freundlich number.

The sorption of organic compounds may be under a non-equilibrium condition during the EK process (Yeung and Mitchell, 1993). The desorption rate ($\partial q/\partial t$) of organic compound may be affected by soil properties including surface area, organic and water content, presence of surface metal oxides, soil type, soil pH, contamination time, and temperature (Fares et al., 1995). The desorption kinetics of organic contaminant is poorly understood due to its complexity. However, the desorption kinetics in the unsaturated soil can be described by a local equilibrium concept. Since the water layer on the soil surface is extremely thin, generally ranging from 10^{-8}cm to 10^{-6}cm, the local equilibrium may be reached in a short period of time. The desorption rate needs modification under the non-equilibrium sorption condition:

$$\partial q/\partial t = k_r (K_d C_i - q) \text{ (Non-equilibrium linear isotherm)} \quad [6.7]$$

$$\partial q/\partial t = k_r (q_{max} K_L C_i/(1+K_L C_i) - q) \text{ (Non-equilibrium Langmuir isotherm)} \quad [6.8]$$

$$\partial q/\partial t = k_r (K_f C_i^n - q) \text{ (Non-equilibrium Freundlich isotherm)} \quad [6.9]$$

where k_r is the desorption rate constant.

Mathematical tools can be established to solve the above equations under given initial and boundary conditions. The mathematical solution procedures based on equilibrium (Sung, 1998) and non-equilibrium linear sorption were shown in the section of Appendix (Hsieh, 1988). The solution of the diffusion-advection-sorption equation (Equation 6.2) was performed by MATLAB. The computation program was listed in the Appendix section as well.

6.3. Methodology

According to Equation 6.2, the diffusion coefficient of organic contaminants can be obtained. Table 6.1 lists the diffusion coefficients of PCE, TCE, chloroform, carbon tetrachloride, and phenanthrene. These values would be applied to the diffusion term in the DAS equation, i.e., Equation 6.1.

Table 6.1. The diffusion coefficient of selected organic compounds (Werther, 1976).

Organic Species	Molar Volume (cm^3/mole)	Diffusion Coefficient ($x10^{-6}$ cm^2/sec)	Diffusion Coefficient (cm^2/hour)
PCE	116.0	8.71	0.0314
TCE	98.1	9.63	0.0347
Chloroform	83.3	10.60	0.0382
Carbon Tetrachloride	101.2	9.45	0.0340
Phenanthrene	238.2	5.65	0.0203

Figure 6.1 shows the sketch of the laboratory EK reactor for the removal of chlorinated organic compounds. This reactor is the same as that used for measuring the EO flow rate (mentioned in Chapter 5). Soil samples and chemicals used for EK treatment were identical to those for previous experiments (e.g., sorption experiments). The air-dried soils were preheated at 105 ^oC for 24 hours, then, blended with 0.01M sodium acetate solution and chlorinated organic contaminants. The soil-solution mixtures (soil water content ca. 20%) were carefully packed into the center unit and a membrane set was placed on each side. Both sides of the centere unit are sealed with parafilm (American Nation Can, Chicago, IL) to prevent the chlorinated organics from evaporation. The unit is allowed to equilibrate overnight as to allow a uniform distribution of the testing compound.

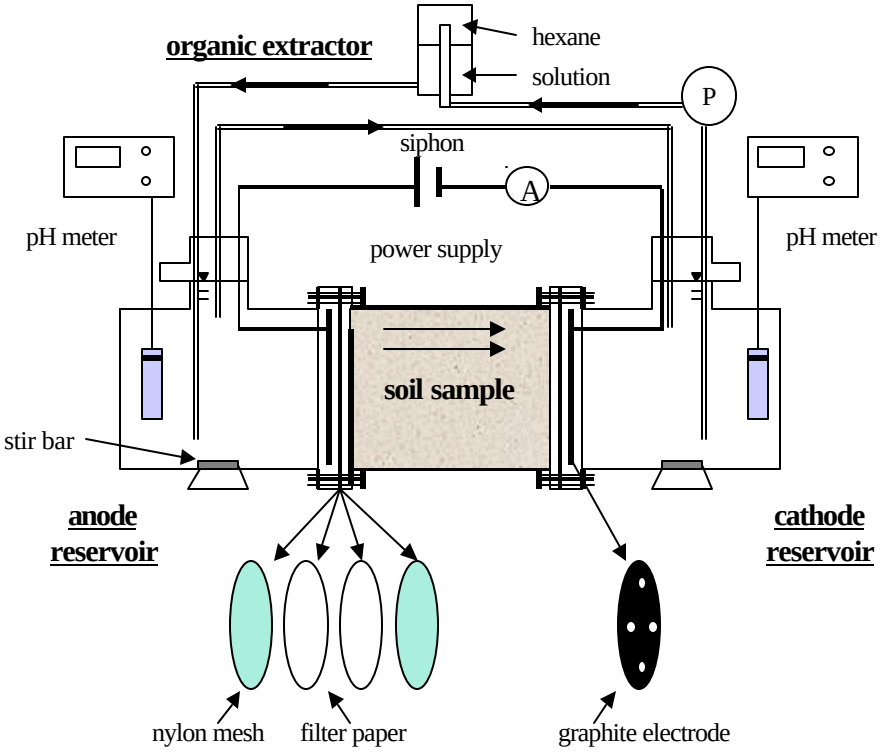

Figure 6.1. Schematic diagram of the electrokinetic system for removal of chlorinated organic contaminants from soils.

In order to better control the pH value, the system uses a circulation device (i.e., pumping and siphon) to neutralize the acid produced at the anodic electrode during EK operation. The concentration of the electrolyte was 0.01M sodium acetate (CH_3COONa). This electrolyte solution works as a buffer and it is cheap, biodegradable, and nontoxic (Baraud et. al., 1997). A liquid extractor with hexane was used to trap the released organic compounds from contaminated soils in the system. All EK experiments were applied at a constant voltage (12 V).

At the end of a pre-selected time period, i.e., 1, 3, 5, and 7 days, the soil sample in the cell were sliced into 10 equal sections. In order to extract the target organics from the soil, two grams of the treated soil sample was mixed with 2 mL 0.1 M sulfuric acid and 5 mL hexane for shaking 24 hours. Both the residual organics in the soil and in the extractor were determined by the gas chromatography equipped with an electron capture detector (GC/ECD) (Hewlett-Packard model 5890, DE, USA). The concentration profile was plotted and data were

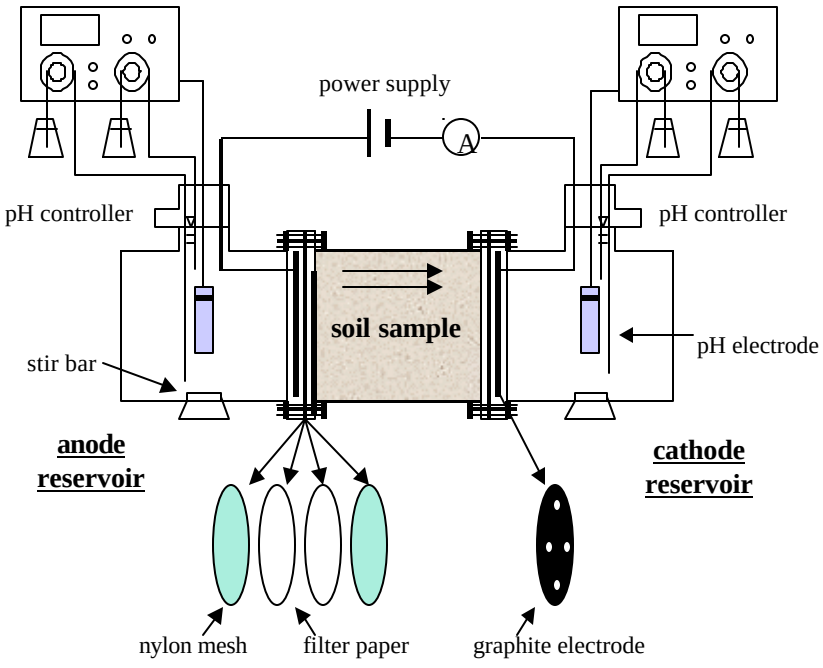

Figure 6.2. Schematic diagram of the electrokinetic system for removal of PAHs from soils.

analyzed further to obtain the transport characteristics.

Figure 6.2 shows the sketch of the laboratory EK reactor for the removal of PAHs organic compounds. Reactor is the same as that used in the chlorinated organics treatment. The contaminated soil was prepared by dissolving phenanthrene into hexane, then, mixing with soil samples. The soil-hexane mixture was put in the hood till hexane evaporates completely. The concentration of the contaminated soils is prepared ca. 100 μg/g. Then, contaminated soils were blended with 0.01M sodium acetate solution to reach 20% soil water content. These soil mixtures were carefully packed into the center unit and the membrane set was placed on each side. The surfactant solution at 10 times CMC was poured into both reservoirs of the EK system. Two types of surfactants, Triton X-100 and rhamnolipid, were selected to remove phenanthrene from soils.

At the end of a pre-selected time period, the soil sample in the cell were sliced into 10 equal sections. The extraction procedure for phenanthrene is the same as that for chlorinated organics. The phenanthrene concentration was measured by the high pressure liquid chromatography equipped with fluorescence (HPLC/FLD) (Hewlett-Packard, model 1100 series, DE, USA). The concentration profile of phenanthrene was plotted and data were analyzed further to gain insight into the transport characteristics of phenanthrene.

6.4. Results

6.4.1. Chlorinated Organic Compounds

During the EK remediation, the chemical properties of the pore fluid are closely related to the electrolysis reaction. When the chemical properties (e.g., pH) of the process fluid are not controlled (i.e., unenhanced EK treatment) and upon the application of a direct electric current, oxidation reaction takes place at the anode and creates an acid front. Likewise, reduction reaction occurs at the cathode and produces a base front according to the following reactions:

$$2H_2O - 4e^- \rightarrow O_2 + 4H^+ \quad \text{(anode)}$$

$$2H_2O + 2e^- \rightarrow H_2 + 2OH^- \quad \text{(cathode)}$$

Accordingly, the pH will usually drop to below 2 at the anode and it increases to above 12 at the cathode depending on the total current applied. The acid front will advance toward the cathode, which results in acidification of the soil (Acar and Alshawabkeh, 1993).

Under acidic pH, the electro-osmotic flow will decrease and facilitate the dissolution of Al(III) ions from the soil. The released Al(III) ions may have potential toxicity to plants and adversely affect nutrient uptake, in addition to groundwater acidification (Matzner and Prenzel, 1992). As a result, it is desirable to control the pH of the working solution within the neutral range.

Figure 6.3 shows that the change pH of the working solution and the applied current density as a function of operation time. Results show that the pH of solution reaches ca. 5.9

and the current density ranges from 0.26 to 0.37 mA/cm^2 in a 10-day run. This is attributed to the buffer capacity of sodium acetate and the circulation operation. A constant current indicates that the electrolyte concentration is almost constant as operation time increases. In addition, the soil pH and water content also remain constant during the treatment, as shown in Figure 6.4. The electro-osmotic flow rate maintains constant due to the constant pH, electric field intensity, and water content. Consequently, this system can be operated within a neutral pH range and produce a constant electro-osmotic flow.

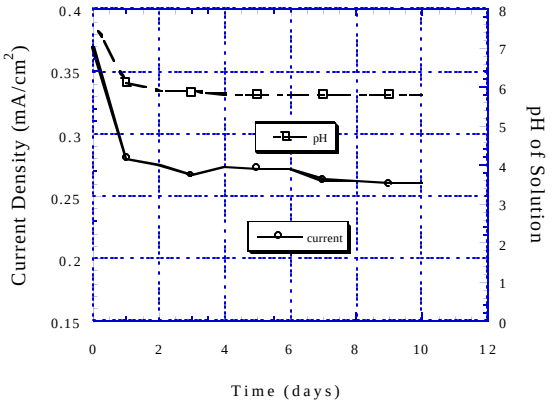

Figure 6.3. The solution pH and current as function of time. Experimental condition electrolyte concentration = 10^{-2} M CH_3COON water content = 20% (w/w); voltage = 12 V.

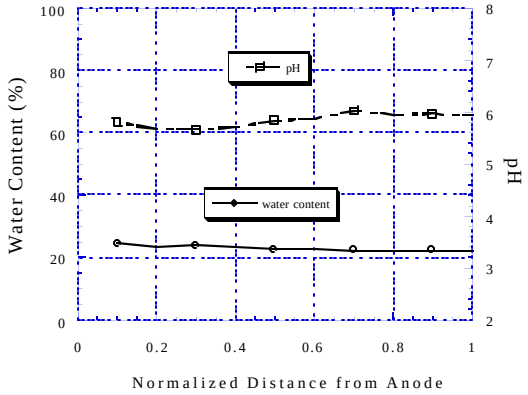

Figure 6.4. The average pH and water content profiles as a function of normalized distance from the anode. Experimental conditions: electrolyte concentration = 10^{-2} M CH_3COONa; water content = 20% (w/w); voltage = 12 V.

An electrical potential gradient of 1.2 V/cm was applied during all the tests. The water level of two reservoirs were kept the same, therefore, no hydraulic gradients were present. In order to determine the electro-osmotic flow rate of the circulation system, an EK system was controlled at the same situations such as pH value, water content, and intensity of electric field. Figure 6.5 shows the average pore volume and flow rate of electro-osmosis as a function of time. Results show that the elcetro-osmotic flow could be operated stable and the average flow rate was measured ca. 180 ml/day.

Figure 6.6 shows the removal efficiency of chlorinated organic compounds as a function of pore volume. Results show that chloroform can be removed at 98 % after a 2-pore volume treatment. TCE and carbon tetrachloride can be removed after a 3-pore volume treatment, at 85 % and 95 % respectively. PCE contaminated soils can be cleaned up to 90 % after a 5-pore volume treatment. In general, the organic compound with high water solubility is not preferably sorbable onto soils (Schwarzenbach et. al., 1993). Accordingly, TCE is relatively easier than PCE to be removed from the soil phase because the water solubility of PCE (110 mg/l) is much lower than that of TCE (1,100 mg/l). Likewise, chloroform having a water solubility of 8,000 mg/l can be better removed than all other selected organic contaminants. The removal efficiency of carbon tetrachloride is similar to that of TCE due to close water solubility.

In the EK system, the advection and sorption are the dominant processes governing the transport of nonionic organic contaminants. In this study, the advection effect is identical for all selected organics since the flow rate is identical in all tests. Accordingly, the removal efficiency is mainly controlled by the sorption effect. Based on experimental results, the

electrokinetics is effective in removing these chlorinated organics from the soil. It indicates that the binding between the soil and these organic compounds is insignificant.

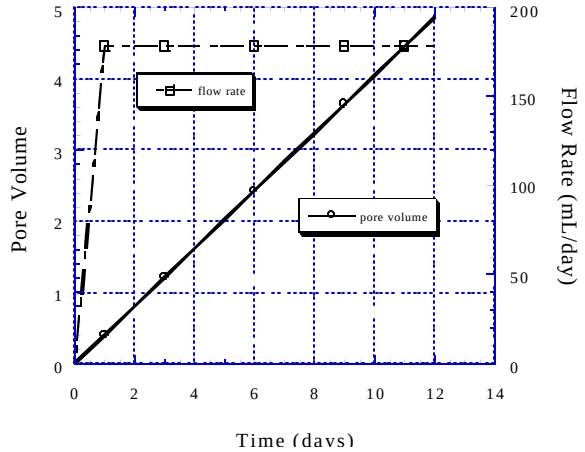

Figure 6.5. The average pore volume and flow rate of electro-osmosis as a function of time. Experimental conditions: electrolyte concentration = 10^{-2} M CH_3COONa; water content = 20% (w/w); voltage = 12 V.

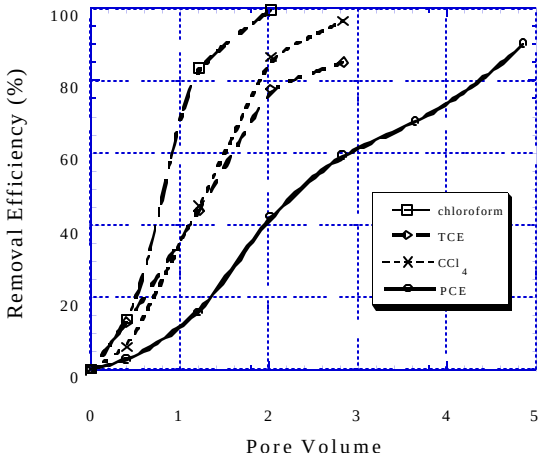

Figure 6.6. The removal efficiency of chlorinated organic compounds as a function of pore volume. Experimental conditions: electrolyte concentration = 10^{-2} M CH_3COONa; water content = 20% (w/w); voltage = 12 V.

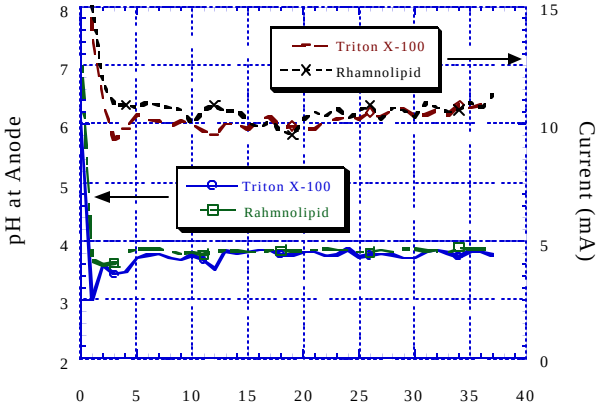

Figure 6.7. The solution pH at anode and current as a function of time. Experimental conditions: electrolyte concentration = 10^{-2} M CH_3COONa; water content = 20% (w/w);

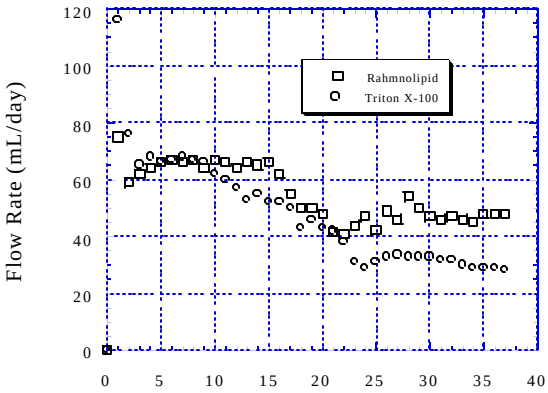

Figure 6.8. The electro-osmotic flow with surfactants as a function of time. Experimental conditions: electrolyte concentration = 10^{-2} M CH_3COONa; water content = 20% (w/w); voltage = 12 V.

6.4.2. Phenanthrene

In contrast to the chlorinated organic treatment, the EK system for phenanthrene was operated without the circulation and siphon operation. In addition, surfactant solutions were used in both electrode chambers. Figure 6.7 shows the pH at the anode and the applied current as a function of operation time for Triton X-100 and rhamnolipid system. Results show no significant difference of the pH and current between the use of Triton X-100 and rhamnolipid. For both systems, the pH at the anode maintains ca. 3.8 and the current ranges from 11 to 12 mA during the 37-day run. The constant pH can be attributed to the daily

addition of sodium acetate into the anode, which can buffer the solution pH. The electrolyte concentration increases with the addition of sodium acetate concurrently, which results in the electro-osmotic flow decreasing. Figure 6.8 show the electro-osmotic flow rate as a function time. Results demonstrate that the flow rate decreases with time. In addition, the electro-osmotic flow rate in rhamnolipid system is higher than that in Triton X-100. Triton X-100 is a nonionic surfactant but rhamnolipid is an anionic one. Rhamnolipid can form a complex with cations (Miller, 1995), which makes the electrolyte concentration in rhamnolipid system is lower than that in Triton X-100 system. Therefore, the use of rhamnolipid can has the higher electro-osmotic flow rate.

Figure 6.9 shows the residual concentration of phenanthrene as a function of normalized distance with two different surfactants. Results show that rhamnolipid has the better removal efficiency than Triton X-100. This may be attributed to the relatively high solubilization ability or the biodegration of rhamnolipid in the EK system. The solubilization indicator, β, obtained in PAHs dissolution tests is 0.44 for rhamnolipid and 0.4 for Triton X-100, respectively. The stronger solubilization of the rhamnolipid can facilitate the penanthrene desorption from the soil. In addition, the biodegradation may occur in the biosurfactant system since rhamnolipid can enhance the growth of bacteria in soils. The biodegradation makes the removal efficiency of phenanthrene become effectively. The total removal efficiency of phenanthrene with use of Triton X-100 is ca. 10% after of 8.5 pore volumes. The total removal efficiency of phenanthrene treated by rhamnolipid is ca. 20% and 30% for of 9.7 and 14.8 pore volumes, respectively.

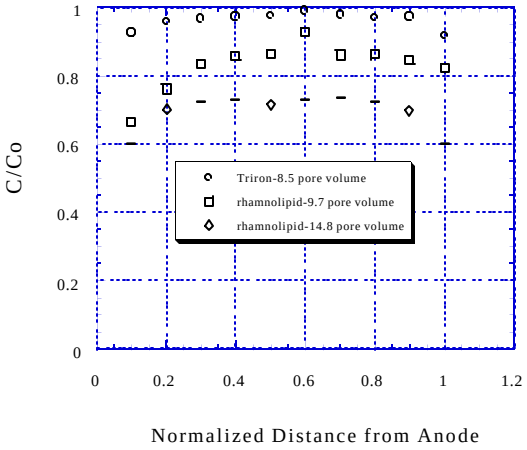

Figure 6.9. Phenanthrene concentration profile in the soil as a function of normalized distance. Experimental conditions: electrolyte concentration = 10^{-2} M CH_3COONa; water content = 20% (w/w); voltage = 12 V.

6.5. Discussion

6.5.1. Removal of Chlorinated Organics

A numirical solution for solving the DAS model was developed on the basis of linear sorption isotherms at equilibrium, i.e., $q = K_d C_i$. Figure 6.10 shows transport parameters of the DAS solution for chlorinated organic compounds under the EK influence. Parameters such as water content, contamination concentration, weight of soil-solution mixture, soil density, transport distance, and operation time obtained from the EK experiments are constants. Theta value, θ, was fixed at 0.5 in order to proceed a stable numerical computation. The diffusion coefficients of all target chlorinated organics can be calculated by Equation 6.2. Results were listed in Table 6.1. Since the electro-osmotic flow requires severally days to reach a stable state, the average EO flow rate varies with increasing operation time. According to the experimental results, the average value of EO flow rate for 1, 3, 5, and 7 days is 0.05, 0.1, 0.18, and 0.19 cm/hour, respectively. Only two parameters,

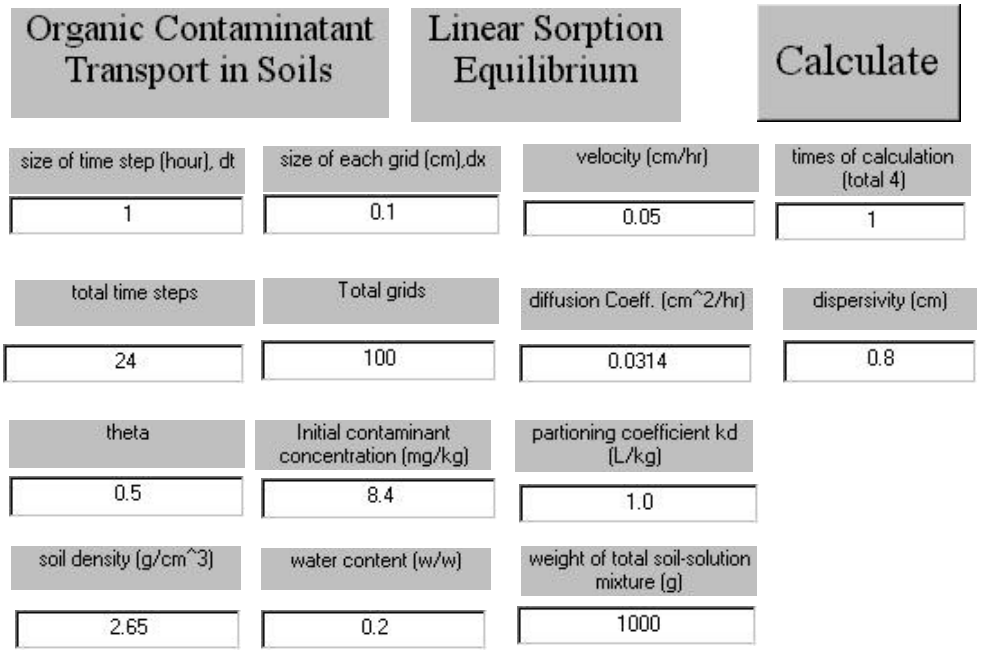

Figure 6.10. The parameters input menu of the diffusion-advection-sorption model for chlorinated organic compounds under EK influence.

partition coefficient and dispersivity, were not determined. Therefore, these two parameters were used to fit and analize experimental data.

Table 6.2 lists fitted values of partition and dispersion coefficient for chlorinated organic compounds under the EK treatment. The average partition coefficient of PCE, TCE, carbon tetrachloride, and chloroform is 1.2, 0.6, 0.4, and 0.15 L/Kg, individually. In contrast, the partition coefficient of chlorinated organics obtained by sorption experiments (see Chapter 3) is ca. 10, 3, 8, and 1 L/Kg for PCE, TCE, carbon tetrachloride, and chloroform, respectively. The one order of magnitude difference can be attributed to the effect of soil to solution ratio. According to this effect, the partition coefficient would decrease with increasing the soil concentration. Consequently, the partition coefficient of organic in the EK system (soil to solution at 5:1) is smaller than that in the over-saturated soil-water system (soil to solution at 1:5). Bruell (1992) reported that the partition coefficient of TCE was 0.85 L/Kg in the clay under electrokinetics. That is close to the partition ceofficient obtained in this study (0.6 L/Kg). The slight different is due to clay with high organic contents.

It is seen that the fitted values of partition coefficients for PCE and TCE increase with increasing time according to Table 6.2. The partition coefficient of PCE and TCE increases from 1.0 to 1.3 L/Kg and from 0.4 to 1.0 L/Kg, respectively. This can be attributed to the concentration effect on the organic sorption. The partition coefficient increases with decreasing organic concentration in the soil-water system. When proceeding the EK process, the contaminant is removed and its concentration decreases gradually. Therefore, the partition coefficient of organics in EK system increases with time. However, the concentration effect on the relative polar chlorinated compounds is insignificant. The partition coefficient of carbon tetrachloride varies with time slightly (from 0.3 to 0.4 L/Kg)

and that of chloroform maintains a constant value (0.15 L/Kg). This can be explained by the linear sorption isotherm of chloroform.

Table 6.2. Simulation parameters of the transport for chlorinated organic compounds under electrokinetics.

	Diffusion Coef. (cm^2/hr)	Partition Coef. (L/Kg)	EO Velocity (cm/hr)	Dispersion Coef. (cm^2/hr)
PCE				
24hours	0.0314	1.0	0.05	0.13
72hours	0.0314	1.2	0.10	0.26
120hours	0.0314	1.3	0.18	0.47
168hours	0.0314	1.3	0.19	0.49
TCE				
24hours	0.0347	0.4	0.05	0.13
72hours	0.0347	0.5	0.10	0.26
120hours	0.0347	0.5	0.18	0.47
168hours	0.0347	1.0	0.19	0.49
Carbon	Tetrachloride			
24hours	0.034	0.3	0.05	0.13
72hours	0.034	0.3	0.1	0.26
120hours	0.034	0.4	0.18	0.47
168hours	0.034	0.4	0.19	0.49
Chloroform				
24hours	0.038	0.15	0.05	0.13
72hours	0.038	0.15	0.10	0.26
120hours	0.038	0.15	0.18	0.47
168hours	0.038	0.15	0.19	0.49

Figures 6.11, 6.12, 6.13, and 6.14 show the movement profile of organics in the soil as a function of the travel distance for PCE, TCE, carbon tetrachloride, and chloroform, respectively. In these figures, the dot points represent experimental data and solid curves are the model simulation. It is seen that the errors between the simulation and experimental data occur relatively high in the beginning end (anode) of the travel distance. This can be attributed to the incomplete extraction of the hexane extractor. When the contaminants were washed out to the cathode chamber, the effluent was pumped through the hexane extractor and returned into the anode reservoir. After the extration process, the effluent may still contain few contaminants and enter the soil. This small amount of contaminants makes the experimental values higher than simulation ones. In addition, there are errors occuring near the cathode end. This results from the low organic concentration in the cathode reservoir. Due to this low organic concentration, the concentration gradient at the cathode boundary increases. The driving force of molecular diffusion is related to the gradient of concentration, therefore, the contaminants near the cathode is released faster than the simulation.

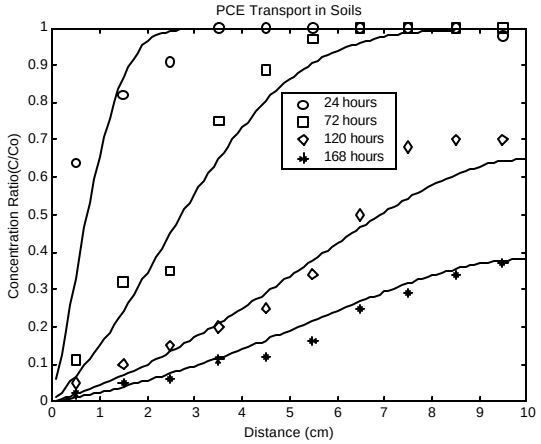

Figure 6.11. PCE concentration profile in the soil as a function of transport distance. Experimental conditions: electrolyte concentration = 10^{-2} M CH_3COONa; water content = 20% (w/w); voltage = 12 V.

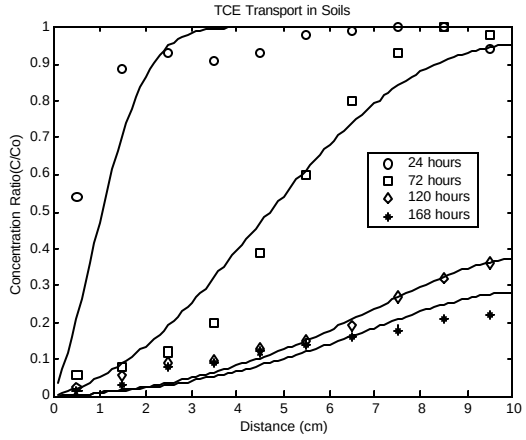

Figure 6.12. TCE concentration profile in the soil as a function of transport distance. Experimental conditions: electrolyte concentration = 10^{-2} M CH_3COONa; water content = 20% (w/w); voltage = 12 V.

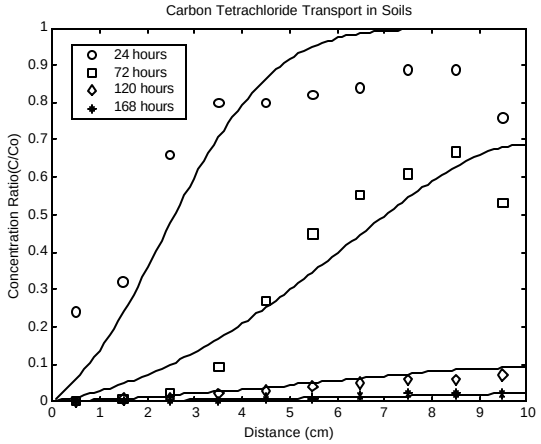

Figure 6.13. Carbon Tetrachloride concentration profile in the soil as a function of transport distance. Experimental conditions: electrolyte concentration = 10^{-2} M CH_3COONa; water content = 20% (w/w); voltage = 12 V.

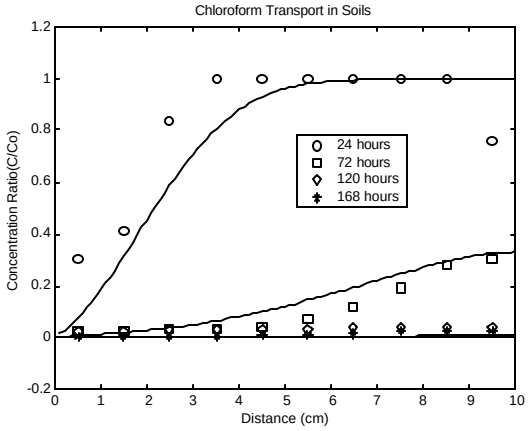

Figure 6.14. Chloroform concentration profile in the soil as a function of transport distance. Experimental conditions: electrolyte concentration = 10^{-2} M CH_3COONa; water content = 20% (w/w); voltage = 12 V.

6.5.2. Desorption Kinetics of Chlorinated Organics

The transport of organic compounds in the soil can be considered as a desorption reaction. The desorption reaction plays a key role in the transport of organic compounds in soils (Sabbah and Rebhun, 1997). Most research work on the desorption of organic from soils were conducted in batch or continuous mode (Kan et al., 1994; Pavlostathis and Jaglal, 1991). These desorption experiments were usually conducted under over-saturated conditions (i.e., soils mixed with a large amount of solution). These desorption data, thereby, may not reflect the desorption behavior of organic compounds in the vadoze zone (i.e., unsaturated

condition). To gain insight into the desorption of organic in the vadoze zone, electrokinetics provides an excellent tool.

From the EK experiments, the first slice of the contaminated soil in the EK cell can be considered as a unique reactor by itself. The organic concentration in the soil of the first slice as a function of time can be further analyzed for its desorption characteristics. By assuming that the desorption reaction can be described by the following equation:

$$\underline{S}\text{-}O \Rightarrow O + \underline{S} \qquad [6.10]$$

where $\underline{S}$-O is the organic sorbed in soil, O is the organic in the aqueous phase, $\underline{S}$ is the free soil surface. The desorption rate can be written as:

$$-d[\underline{S}\text{-}O]/dt = k[\underline{S}\text{-}O] \qquad [6.11]$$

Integration of Equation 6.11. One has:

$$[\underline{S}\text{-}O]/[\underline{S}\text{-}O]_0 = \exp(-kt) = C/C_o \qquad [6.12]$$

or

$$C = C_o e^{-kt} \qquad [6.13]$$

where k is the rate constant of the desorption reaction.

Figure 6.15 shows the plot of Equation 6.13 for the chlorinated organics studied. Results clearly indicate that desorption data can be fitted by a linear equation. This indicates that the desorption mechanism of the chlorinated organics in unsaturated soils is a first-order reaction. Table 6.3 summarizes the rate constant of desorption for the organic compounds studied. The rate constant for the desorption of PCE, TCE, carbon tetrachloride, and chloroform is 0.61, 0.70, 1.03, and 1.15 day^{-1}, respectively.

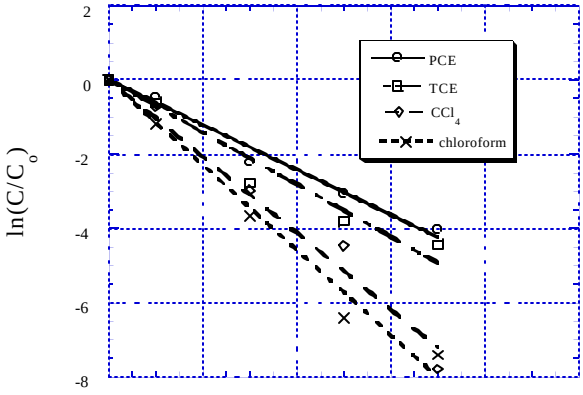

Figure 6.15. The organic concentration in first slice as a function of time. Experimental conditions: electrolyte concentration = 10^{-2} M CH_3COONa; water content = 20% (w/w); voltage = 12 V.

Table 6.3. Desorption rate constant for chlorinated organics.

	k value (day^{-1})	R value
PCE	0.60	0.99
TCE	0.70	0.97
Carbon tetrachloride	1.03	0.99
Chloroform	1.15	0.99

6.5.3. Removal of Phenanthrene in the Presence of Surfactants

A numerical solution for solving the DAS model was developed on the basis of the non-equilibrium condition. Moreover, the linear isotherm was assumed in the local region of soils (i.e., the interfact extremely close to the soil surface). Accordingly, Equation 6.7, $\partial q/\partial t = k_r(K_d C_i - q)$, was introduced to the DAS model. Figure 6.16 shows parameters of the solution for simulating phenanthrene transport under the EK treatment. In Figure 6.16, all constant parameters such as water content, contamination concentration, weight of soil-solution

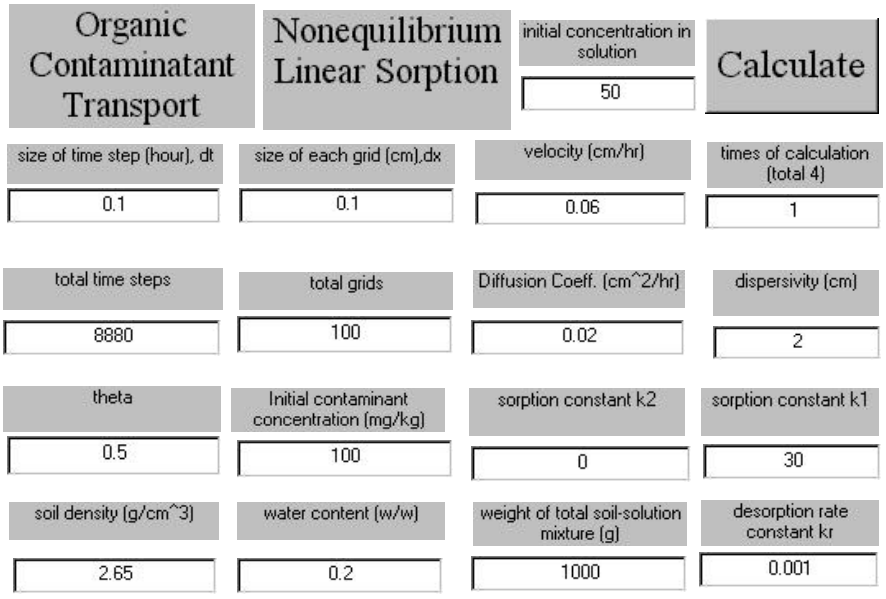

Figure 6.16. The parameters input menu of the diffusion-advection-sorption model for phenanthrene under electrokinetic influence.

mixture, soil density, transport distance, and operation time were obtained according to the experimental setup. The diffusion coefficient of phenanthrene, 0.02 cm^2/hour, can be calculated by Equation 6.2.

Table 6.4. Simulation parameters of phenanthrene transport under influence of electrokinetics.

	Diffusion Coef. (cm^2/hr)	Partition Coef. (L/Kg)	EO Velocity (cm/hr)
Triton X-100 -37 days	0.02	30	0.06
Rhamnolipid-37 days	0.02	400	0.10
Rhamnolipid-60 days	0.02	400	0.10
	Initial Solute Conc. (mg/L)	Dispersivity (cm)	Desorption Rate Const. (hr^{-1})
Triton X-100 -37 days	50	1.0	0.001
Rhamnolipid-37 days	400	1.6	0.001
Rhamnolipid-60 days	1500	1.6	0.001

Table 6.4 still lists other parameters for the simulation of phenanthrene movement. The electro-osmotic flow rate was determined from experimental results. The average EO flow rates for Triton X-100 and rhamnolipid are 0.06 and 0.1 cm/hr, respectively. The partition coefficient , $K_{d,cmc}$, measured from PAHs desorption tests was used to substitute the K_d in Equaiton 6.7. The measured $K_{d,cmc}$ values of phenanthrene for the Triton X-100 and rhamnolipid system are 30 and 400 L/Kg, respectively. The quantity of dispersivity, α = 2.6 cm, obtained from the transport simulation of the chlorinated compounds was used. The parameter, initial concentration in aqueous phase, was substituted by the solubility of phenanthrene in the surfactant solution. Based on the phenanthrene solubilization tests, the initial concentration of phenanthrene, 50 mg/L, was used for the Triton X-100 and 8 mg/L for

rhamnolipid system, respectively. Therefore, only one parameter, desorption rate constant, was used to fit and analize experimental data of phenanthrene movement.

Figure 6.17 shows the phenanthrene concentration profile as a function of the transport distance with use of various surfactants. Dot points represent experimental results and solid curves are the model simulation. Results indicate that the model simulation applied to the Triton X-100 system is close to experimental data. The desorption rate constant, 0.001 hr^{-1}, was determined when the model simulation matches experimental data. However, this model simulation failed to the rhamnolipid system. During the simulation for the rhamnolipid system, the desorption rate constant in Triton X-100 system was applied due to their similar solubilization abilities. Instead of the initial solute concentration, other parameters used in Triton X-100 system are the same as those in rhamnolipid system. In order to fit experimental data, the initial solute concentration must be ca. 400 and 1500 mg/L for 37 and 60-day run, respectively. In fact, the solubility of phenanthrene in rhamnolipid solution at 10 CMC is only 8 mg/L which is far less than the simulation values (400 and 1500 mg/L). The various solute concentration implies that phenanthrene may be degraded in addition to the removal by EK process. The biodegradation of phenanthrene may be significant due to the growth of bacteria enhanced by the biosurfactant (Tiehm et. Al., 1997).

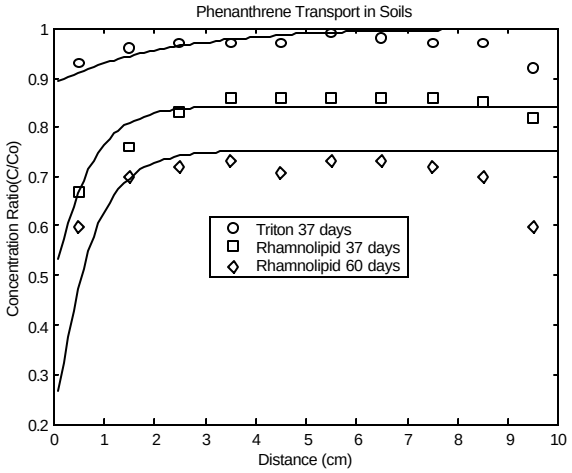

Figure 6.17. The phenanthrene concentration profile in the soil as a function of transport distance. Experimental conditions: electrolyte concentration = 10^{-2} M CH_3COONa; water content = 20% (w/w); voltage = 12 V; surfactant concentration = 10 CMC.

It is seen that errors between the simulation and experimental data occurs relatively high in the end of the tansport distance. This phenomenon was also found in the simulation of chlorinated organics transport. It can be attributed to the increase of diffusion force at the reactor boundary. The transport model based on the linear sorption isotherms at non-equilibrium condition is able to simulate the movement of phenanthrene under the EK treatment. This implies that the sorption behavior of phenanthrene is linear at non-equilibrium status during the EK process. Compared to the desorption rate constant of chlorinated organics (0.03~0.05 hr^{-1}), that of phenanthrene (0.001 hr^{-1}) is small.

6.6. Summary

Based on experimental results and model simulation for the nonionic organic compounds under the EK treatment, the following conclusions can be drawn. Buffer and circulation neutralization system can eliminate the acid front generated at the anode. A constant pH throughout the soil mass can be maintained to produce a stable electro-osmotic flow rate. The higher the water solubility of a chlorinated organic, the higher its transport rate in the soil. The EK process can effectively remove chlorinated organic compound such as PCE, TCE, chloroform, and carbon tetrachloride from the soil at an efficiency ranging from 85% to 98% in a matter of days. In addition, the desorption behavior of the organic in the unsaturated soil

can be obtained by EK experiments. The desorption of chlorinated organic compound follows a first-order kinetic reaction The rate constant is 0.61, 0.70, 1.15, and 1.03 day^{-1}, respectively, for PCE, TCE, chloroform, and carbon tetrachloride.

The DAS model based on the linear sorption isotherm at equilibrium can simulate the movement of chlorinated organic contaminants under the EK treatment. This indicates that the sorption behavior of PCE, TCE, carbon tetrachloride, and chloroform is at equilibrium status during the EK process. In this model, the partition coefficient is one of major factors controllin the organic transport. It is seen that the partition coefficient of organic in the EK system is higher than that obtained in over-saturated soil-water system. This can be attributed to the soil to solution effect on the organic sorption. In addition, the simulation value of partition coefficient increases with increasing time because of the concentration effect on the organic sorption.

In contrast, the DAS model based on the linear sorption isotherm at non-equilibrium condition is able to simulate the movement of phenanthrene during the EK treatment in the presence of Triton X-100. A desorption rate constant of 10^{-3} hr^{-1} was obtained. However, the DAS model does not predict well the distribution of phenanthrene in the presence of rhamnolipid. The presence of rhamnolipid apparently promotes microbial growth in the soil-water system which may bring about biodegradation of phenanthrene. As a result, the desorption behavior of phenanthrene is non-equilibrium.

6.7. References

1. Acar, Y. B., H. Li, and R. J. Gale (1992), Phenol Removal from Kaolinite by Electrokinetics, J. Geotech. Eng., Vol. 118, No. 11, 1837-1852.
2. Acar, Y. B. and A. N. Alshawabkeh (1993). Principles of Electrokinetic Remediation, Environ. Sci. and Technol., Vol. 27, No. 13, 2639 - 2646.
3. Acar, Y. B., J. T. Hamed, A. N. Alshawabkeh, and R. J. Gale (1994). Removal of Cadmium(II) from Saturated Kaolinite by the Application of Electrical Current, Geotechnique, Vol. 44, No. 2, 239 - 254.
4. Baraud, F, S. Tellier, and M. Astruc (1997), Ion Velocity in Soil Solution during Electrokinetic Remediation, J. Haz. Mat., Vol. 56, 315-332.
5. Bruell, C. J., B. A. Segall, and M. T. Walsh (1992), Electro-Osmosis Removal of Gasoline Hydrocarbons and TCE from Clay, J. Environ. Eng., Vol. 118, No. 1, 68-83.
6. Domenico, P. A. and F. W. Schwartz, Physical and Chemical Hydrogeology, John Wiley & Sons, Inc. New York, 1998.
7. Drew, T. B., G. R. Cokelet, J. W. Hoopes. JR., and T. Vermeulen (1981), Advances in Chemical Engineering, New York, Academic Press, Vol. 11, 30.
8. Fares, A., B. T. Kindt, P Lapuma, and G. P. Perram (1995), Desorption Kinetics of Trichloroethylene from Powdered Soils, Environ. Sci. and Technol., Vol. 29, No. 6, 1564-1568.
9. Fetter, C. W., Applied Hydrogeology, 2nd Ed., Merril Publishing, Columbus, Ohio, 1988.
10. Hsieh, K. H., A One-Dimensional Finite Difference Model for Transport of Solutes in Soil-Water System, Master Thesis, University of Delaware, 1988.
11. Kan, A. T., G. Fu, and M. B. Tomson (1994), Adsorption/Desorption Hysteresis in Organic Pollutant and Soil/Sediment In teraction, Environ. Sci. and Technol., Vol. 28, No. 5, 859 - 867.

12. Li, Z., J. W. Yu, and I. Neretnieks (1996), A New Approach to Electrokinetic Remediation of Soils Polluted by Heavy Metals, J. Contam. Hydrol., Vol. 22, 241-253.
13. Matzner, E. and J. Prenzel (1992), Acid Deposition in the German Soiling Area: Effects on Soil Solution Chemistry and Al Mobilization, Water, Air, and Soil Pollution, Vol. 61, No. 3/4, 221-226.
14. Miller R. M. (1995), Biosurfactant-Facilitated Remediation of Metal-Contaminated Soils, Environ. Health Perspect., Vol. 103(Suppl 1), 59-62.
15. Mitchell, J. K. and T. C. Yeung (1991), Electrokinetic Flow Barriers in Compacted Clay, Transportation Research Records, No. 1289, TRB, Washington, D.C., 53-64.
16. Pavlostathis, S. G. and K. Jaglal (1991), Desorption Behavior of Trichloroethylene in Contaminated Soil, Environ. Sci. and Technol., Vol. 25, No. 2, 274 - 279.
17. Probstein, R. F. and R. E. Hicks (1993), Removal of Contaminants from Soils by Electric Fields, Science, Vol. 260, No. 23, 498-503.
18. Reed, B. E., P. C. Carriere, J. C. Thompson and J. H. Hatfield (1996), Electronic (EK) Remediation of a Contaminated Soil at Several Pb Concentrations and Applied Voltages, J. Soil Contam., Vol. 5, No. 2, 95-120.
19. Renaud, P. C. and R. F. Probstein (1987), Electroosmotic Control of Hazardous Wastes, 6th Int. Conf, Dedicated to the Memory of Veniamin Levich Apr 6-8 1987 Vol. 9, No. 1-2, 345-360.
20. Sabbah, I. and M. Rebhun (1997), Adsorption-Desorption of Trichlorophenol in Water-Soil Systems, Wat. Environ. Res., Vol. 69, No. 5, 1032-1038.
21. Schwarzenbach, R. P., P. M. Gschwend, and D. M. Imboden, Environmental Organic Chemistry, New York, 1993.
22. Segall, B. A. and C. Bruell (1992), Electro-Osmotic Contaminant-Removal Process, J. Environ. Eng., ASCE, Vol. 118, No. 1, 84-100.
23. Shapiro A. P. and R. F. Probstein (1993), Removal of Contaminants from Saturated Clay by Electroosmosis, Environ. Sci. Technol., Vol. 27, No. 2, 283-291.
24. Smith, E. D., Numerical Solution of Partial Differential Equation, Oxford, Clarendon Press, 1978.
25. Sung, M. H., MATLAB GUI for Contaminant Transport with Different Adsorption Mechanism, Project for CIEG 667: Computer Application in Civil Engineering, University of Delaware, 1998.
26. Tiehm, A., M. Stieber, P. Werner, and F. H. Frimmel (1997), Surfactant-Enhanced Mobilization and Biodegradation of Polycyclic Aromatic Hydrocarbons in Manufactured Gas Plant Soil, Environ. Sci. and Technol., Vol. 31, No. 9, 2570-2576.
27. Van Genuchten, M Th. and R. W. (1982), Movement of Solutes in Soils: Computer Simulated and Laboratory Results, Soil Chemistry, ed. G. H. Bolt, 349-386. New York, N. Y.: Elsevier.
28. Werther,J. (1976), Powder Technology, Convective Solids Transport in Large Diameter gas Fluidized Beds, Vol. 15, 155-167.
29. Yeung, A. T. and J. K. Mitchell (1993), Coupled Fluid, Electrical and Chemical Flows in Soil, Geotechnique, Vol. 43, 121-134.

7. CONCLUSIONS AND RECOMMENDATIONS

7.1. Sorption of Nonionic Organics in the Soil-Water System

7.1.1. Chlorinated Organic Compounds

Both organic concentration and the soil to solution ratio have significant effects on the sorption behavior. This study used the fugacity corporated with the partition concept, $K_p = \gamma_w/\gamma_s$, to illustrate these sorption effects in the soil-water system. By analyzing the activity coefficients, γ_w and γ_s, on can gain insights into the nonionic organic sorption. The organic effect always results in the non-linear sorption isotherm. Accordingly, the Langmuir isotherm can describe the distribution of selected chlorinated organics such as PCE, TCE, carbon tetrachloride, and chloroform in this study. Experimental results show that the partition coefficient decreases with increasing the organic concentration. This can be attributed to the strong replusive interaction, i.e., high γ_s value, between the organic and the soil at the high organic concentraion. For the soil to solution ratio effect, it changes the sorption density of organics. The partition ceofficient decreases with increasing the soil to solution ratio. Since γ_w is related to TOC, the soil to solution effect can be attributed to the presence of the DOM in the liquid phase. It is seen that the relationship between the activity coefficients, γ_w, and TOC can be expressed: $\ln\gamma_w = m - n[TOC]$, where m is the $\ln\gamma_w$ value in the absence of TOC, n is an interaction coefficient. Based on experimental results, the n values of PCE, TCE, carbon tetrachloride, and chloroform are ca. 0.15, 0.04, 0.03, and 0.08, respcetively.

By introducing the Flory theory to the interpretation of activity coefficient, it is seen that the residual partial molar free energy, μ_1^R, are negative for the selected organics This indicates that the interaction energy between soil organic carbon and organic contaminants reaction is exothermic. In addition, the organic contaminant with higher hydrophobicity exhibits weaker interaction with soil organic carbon. According to experimental results, the order of the interaction is: PCE < carbon tetrachloride ≅ TCE < chloroform.

7.1.2. PAHs in the Presence of Surfactant

The PAHs distribution in the presnce of surfactant is controlled mainly by the PAHs sobubilization of surfactant and the surfactant sorption onto the soil. In this study, five PAHs were selected as target compounds including fluorene, phenantherne, anthracene, fluoranthene, and pyrene and two surfactnats, Triton X-100 (nonionic artificial surfactant) and rhamnolipid (anionic biosurfactant), were used to enhance the solubilization of PAHs. The solubility of PAHs can be effectively increased by surfactants, which can be expressed by: $K_m = \beta K_{ow}$. A high β value presents the high solubilization ability of the surfactant. According to experimental results, the β value for Triton X-100 and rhamnolipid is 0.4 and 0.44, respectively. An empirical equation, $\beta = (0.031y_1 - 0.0058y_2)$, can predict the β value both for Triton X-100 and rhamnolipid. The term, y_1, is the number of "hydrophobic" carbons and y_2 is the number of "hydrophilic" groups.

Both surfactants exhibit strong attraction to the soil phase. The Triton X-100 sorption on the soil can be described by the Langmuir isotherm and can be attributed to a partition process. However, the sorption of rhamnolipid is a linear isotherm and can be attributed to an interfacial interaction. It is seen that the sorption density of both surfactants decreases with increasing PAHs contamination in the soil. This is because the sorption competition between the PAHs and the surfactant onto the soil.

The apparent partition coefficient of PAHs, $K_{d,cmc}$, can be expressed by an equaiton, $K_{d,cmc} = \frac{\alpha K_{ow} f_{oc}^*}{(1+\beta K_{ow}[S])}$. In this equation, α is a constant for reflecting the affinity between the organic and the soil, β is a constant representing the PAHs solubilization capacity of the surfactant, K_{ow} is the octanol number of PAHs, f_{oc}^* represents the total soil organic carbon, and [S] is the surfactant concentration in the solution. Based on experimental results, the PAHs $K_{d,cmc}$ in Triton X-100 system can be related to the reciprocal of surfactant concentration proportionally, $K_{d,cmc} = K/[S]$, at a certain range of surfactant concentration (10~20 CMC). However, PAHs $K_{d,cmc}$ in the rhamnolipid system is constant, i.e, independent of the surfactant concentration.

7.2. Electrokinetic Remediaiton Process

7.2.1. Electro-Osmotic Flow

A semi-empirical equation, $Q = K\sigma_e(E_0/L)\omega^2$, for the Electro-Osmotic flow rate in an unsaturated soil-water system was established. The parameters such as Q, K, σ_e, E_0/L, and ω, are electro-osmotic flow rate, characterized coefficient, electrokinetic charge density, potential gradient, and soil water content, respectively. A finite plate model was used to derive the EO flow rate in unsaturated soils and the waterlayer on the soil surface was assumed as Newtonian fluid. The EO flow rate is theoretically proportional to the extent of electrokinetic charge density, the intensity of electric field, and square of the soil water content in the soil-solution systems. Experimental results were in agreement with these predictions. For the effect of electrolyte concentration, results imply that there is no significant effect on the EO flow rate as long as the electrolyte ions do not interact specifically with the soil. The characterized coefficient, K, reflects several physical properities of the soil-water system including the fluid density, the specific surface area, width of the water layer (on the basis of finite plate model) and fluid viscosity. The K value was 57 $cm^3 \bullet \mu C^{-1} \bullet V^{-1}$ for the soil tested in this work.

7.2.2. Electrokinetic Remediation for Nonionic Organics Contaminated Soils

Chlorinated organic contaminats and PAHs contaminated soils were treated with water and surfactant solution under the EK process, respectively. EK technique can effectively remove chlorinated organic compound such as PCE, TCE, chloroform, and carbon tetrachloride from the soil at an efficiency ranging from 85% to 98% in a matter of days. The higher the water solubility of a chlorinated organic, the higher its transport rate in the soil. The desorption behavior of the organic in the unsaturated soil can be obtained by treating the EK system as a contunuous desorption column. The desorption of chlorinated organic compound follows a first-order kinetics The rate constant is 0.61, 0.70, 1.15, and 1.03 day^{-1}, respectively, for PCE, TCE, chloroform, and carbon tetrachloride.

The diffusion-advection-sorption (DAS) model based on the linear sorption isotherm at equilibrium can simulate the movement of chlorinated organics under the EK treatement. Based on the model simulation, the fitted partition coefficient of organic in the EK system is higher than that in over-saturated soil-water system. This can be attributed to the soil to solution effect on the organic sorption behavior. In addition, the fitted partition coefficient increases with increasing the operation time due to the concentration effect on the organic sorption. The DAS model based on the linear sorption isotherm at non-equilibrium condition

is able to simulate the movement of phenanthrene during the EK treatment. The simulation of phenanthrene transport in the Triton X-100 system are close to experimental results. However, experimental results of phenanthrene flushed by rhamnolipid were not fitted by this model simulation. It implies that phenanthrene was degraded due to the growth of bacteria in the soil media.

7.3. Recommendations

Through the great amount of data collection and analysis about the sorption of nonionic organic compounds in the soil-water system. Generally, the partition process can be considered as the main driving force of the nonionic organic distribution in soil-water system. In addition to the hydrophbicity of orgnaics, SOM and DOM play key roles to the sorption of nonionic organics. The activity coefficient can illustrate the sorption affected by SOM and DOM. However, in order to develop a quantitive predication of the organic sorption, the fundamental reactions among various organic compounds, SOM and DOM must be studied. The content of SOM should be categorized into several groups which can be considered as the basic element of the SOM and posesses a specific sorption characterization. Then, the investigation of sorption reaction between the elemental group of SOM and various organic contaminants can serve as a database for estimating the organic sorption. In addition, the relationship between SOM and DOM also must be determined. By clarifying the reactions among SOM, DOM, and the organic, one might predict the distribution of nonionic organics in the soil-water system even the real site successfully.

The investigation of the EK remediation in this study provides a semi-emperical equaiton for estimating the electro-osmotic flow rate and demonstrates the effective removal of chlorinated organic contaminatnats. For the application to the real contaminanted site, the effect of soil heterogenity on the electro-osmotic flow rate and on the contaminant removal efficiency must be studied. In addition, the investigation of the organic electrolysis reaction and electricity efficiency become important when applying the high voltage electricity to the real site.

8. APPENDIX: NUMERICAL SOLUTION FOR TRANSPORT MODEL

8.1. Difference Scheme

The Finite Difference Method was used to solve the partial differential (i.e., Equation 8.1). Assume that a function of h = h(x,t) is defined in a one-dimensional space. Its value can be represented by the discrete values at a number of nodes. Its derivatives can be approximated by a truncated Taylor series. The central difference of the second derivative in x can be written as

$$(\frac{\partial^2 h}{\partial x^2})_i^l \approx \frac{h_{i+1}^l - 2h_i^l + h_{i-1}^l}{(\Delta x)^2} \qquad [8.1]$$

where i is discrete node of x axis, l is time steps and h_i^l is the value of h at mesh point (i,l) in x-t plane. The first derivative with respect to time can be approximately given by a forward difference scheme (Smith, 1978)

$$(\frac{\partial h}{\partial t})_i^l \approx \frac{h_i^{l+1} - h_i^l}{\Delta t} \qquad [8.2]$$

8.2. Difference Equation

Although the above difference scheme is computationally simple it has one serious drawback. The time step, Δt, is necessarily very small because the computational process is valid only for $0 < \Delta t/(\Delta x)^2 < 1/2$ and Δx must be kept small in order to attain reasonable accuracy. Crank and Nicolson (1947) proposed a method that reduces the total volume of calculation and is valid (i.e., convergent and stable) for the finite difference equations. According to this method, $\partial^2 C/\partial x^2$ can be replaced by the mean of its finite difference representations. The sorption term in Equation 8.1, $\partial q/\partial t$, can be referred as $K_d(\partial C/\partial t)$. Therefore, the Equation 8.1 can be written as follows:

$$\frac{C_i^{l+1} - C_i^l}{\Delta t} = \frac{\theta}{R_d}[D^*(\frac{C_{i+1}^{l+1} - 2C_i^{l+1} + C_{i-1}^{l+1}}{(\Delta x)^2}) - v(\frac{C_{i+1}^{l+1} - C_{i-1}^{l+1}}{2\Delta x})]$$
$$+ \frac{(1-\theta)}{R_d}[D^*(\frac{C_{i+1}^l - 2C_i^l + C_{i-1}^l}{(\Delta x)^2}) - v(\frac{C_{i+1}^l - C_{i-1}^l}{2\Delta x})] \qquad [8.3]$$

where $R_d = 1+\rho K_d/\phi$ based on the equilibrium linear sorption. Rearrange the equation, then we can obtain: $R_i C_{i-1}^{l+1} + S_i C_i^{l+1} + T_i C_{i+1}^{l+1} = U_i$ [8.4]

where $R_i = \frac{\theta D^*}{(\Delta x)^2} + \frac{\theta v}{2\Delta x}$

$$S_i = -\frac{R_d}{\Delta t} - \frac{2\theta D^*}{(\Delta x)^2}$$

$$T_i = \frac{\theta D^*}{(\Delta x)^2} - \frac{\theta v}{2\Delta x}$$

$$U_i = [\frac{(\theta-1)D^*}{(\Delta x)^2} + \frac{(\theta-1)v}{2\Delta x}]C_{i-1}^l + [-\frac{R_d}{\Delta t} - \frac{2(\theta-1)D^*}{(\Delta x)^2}]C_i^l + [\frac{(\theta-1)D^*}{(\Delta x)^2} - \frac{(\theta-1)v}{2\Delta x}]C_{i+1}^l$$

$1 \le i \le M-1$ and $1 \le l \le N$

where M = total distance steps, N= total time steps, R_i, S_i and T_i are constants. U_i are known at time level t_l. Hence, direct method can apply to solve for C_I^{l+1}.

8.3. Initial and Boundary Conditions

a. Initial Condition

At t=0, i.e. l=0, $C_i^0 = C_f$, (at $0 \le i \le 0$)

b. Boundary Conditions

1. At x = 0, i.e. i=0

   $C_0^{l+1} = 0$, (at l > 0)

2. At x = L, i.e. i = M,

   $$\frac{\partial C}{\partial x} = \frac{C_{M+1}^{l+1} - C_{M-1}^{l+1}}{2\Delta x} = 0\text{, then}$$

   $$C_{M+1}^{l+1} = C_{M-1}^{l+1}\text{, (at l > 0)}$$

The difference equation at i = M are

$$(R_M+T_M)c_{M-1}^{l+1}+S_M c_M^{l+1}=U_M \qquad [8.5]$$

Summarizing the difference equations shown in Equation 8.3 and 8.4 ($1 \le i \le M-1$) with boundary conditions at i = 0 and i = M, results in a set of algebraic equations in matrix form.

$$\begin{aligned}
&S_0C_0^{l+1}+T_0C_1^{l+1} &&= U_0\\
&R_1C_o^{l+1}+S_1C_1^{l+1}+T_1C_2^{l+1} &&= U_1\\
&\quad R_2C_1^{l+1}+S_2C_2^{l+1}+T_2C_3^{l+1} &&= U_2\\
&\quad \ldots\ldots\ldots\ldots\ldots\ldots\ldots\ldots\ldots\ldots\ldots\ldots\ldots\ldots\ldots\ldots\ldots\ldots &&\\
&\quad R_{M-1}C_{M-2}^{l+1}+S_{M-1}C_2^{l+1}+T_{M-1}C_M^{l+1} &&= U_{M-1}\\
&\qquad\qquad (R_M+T_M)C_{M-1}^{l+1}+S_MC_M^{l+1} &&= U_M
\end{aligned}$$

Each U_i is known quantity at previous time level t_l, while R, S, and T are constant. The matrix of coefficients R, S, and T is called a tridiagonal matrix. The matrix set can be solved by a Guassian elimination method. The solution process was programmed by MATLAB.

For the non-equilibrium linear sorption, the difference equation can be written as the same formation as follows:

$$R_iC_{i-1}^{l+1} + S_iC_i^{l+1} + T_iC_{i+1}^{l+1} = U_i \qquad [8.6]$$

where $R_i = \dfrac{\boldsymbol{q}D^*}{(\Delta x)^2} + \dfrac{\boldsymbol{q}v}{2\Delta x}$

$$S_i = -\frac{1}{\Delta t} - \frac{2\boldsymbol{q}D^*}{(\Delta x)^2} - \frac{\boldsymbol{r}}{\boldsymbol{f}\Delta t}\frac{k_r K_1 \boldsymbol{q}}{1/\Delta t + k_r\boldsymbol{q}}$$

$$T_i = \frac{\boldsymbol{q}D^*}{(\Delta x)^2} - \frac{\boldsymbol{q}v}{2\Delta x}$$

$$U_i = [\frac{(\boldsymbol{q}-1)D^*}{(\Delta x)^2} + \frac{(\boldsymbol{q}-1)v}{2\Delta x}]C_{i-1}^l + [-\frac{1}{\Delta t} - \frac{2(\boldsymbol{q}-1)D^*}{(\Delta x)^2} + \frac{\boldsymbol{r}}{\boldsymbol{f}\Delta t}\frac{k_r K_1(1-\boldsymbol{q})}{1/\Delta t + k_r\boldsymbol{q}}]C_i^l$$

$$+[\frac{(\boldsymbol{q}-1)D^*}{(\Delta x)^2} - \frac{(\boldsymbol{q}-1)v}{2\Delta x}]C_{i+1}^l + \frac{\boldsymbol{r}}{\boldsymbol{f}\Delta t}[-1+\frac{1/\Delta t + k_r(1-\boldsymbol{q})}{1/\Delta t + k_r\boldsymbol{q}}]q_i + \frac{\boldsymbol{r}}{\boldsymbol{f}\Delta t}\frac{k_r K_2}{1/\Delta t + k_r\boldsymbol{q}}$$

$1 \le i \le M-1$ and $1 \le l \le N$

C_i^{l+1} can be solved by using direct method, since R_i, S_i, T_i and U_i are allknown at time level t_l. The q_i^{l+1} can be obtained as:

$$q_i^{l+1} = [\frac{k_r K_1}{1/\Delta t + k_r \theta}] C_i^{l+1} + [\frac{1/\Delta t + k_r (1-\theta)}{1/\Delta t + k_r \theta}] q_i^l + [\frac{k_r K_1 (1-\theta)}{1/\Delta t + k_r \theta}] C_i^l + [\frac{k_r K_2}{1/\Delta t + k_r \theta}] \quad [8.7]$$

where K_1 and K_2 are the constant for linear sorption, k_r is the desorption rate constant.

The solution for the non-equilibrium linear model is similar to that for equilibrium except Equation 8.7. The matrix of coefficients R, S, and T can be solved by a Guassian elimination method and the solution process was also programmed by MATLAB.

8.4. MATLAB Program for Chlorinated Organic Compounds

```
%times of calculation
HH=findobj(gcf,'Tag','z');
z=str2num(get(HH,'String'));
%parameters
HH=findobj(gcf,'Tag','dt');
dt=str2num(get(HH,'String'));
HH=findobj(gcf,'Tag','n');
n=str2num(get(HH,'String'));
HH=findobj(gcf,'Tag','dx');
dx=str2num(get(HH,'String'));
HH=findobj(gcf,'Tag','m');
m=str2num(get(HH,'String'));
HH=findobj(gcf,'Tag','theta');
theta=str2num(get(HH,'String'));
HH=findobj(gcf,'Tag','Dh');
Dh=str2num(get(HH,'String'));
HH=findobj(gcf,'Tag','Ds');
Ds=str2num(get(HH,'String'));
HH=findobj(gcf,'Tag','lo');
lo=str2num(get(HH,'String'));
HH=findobj(gcf,'Tag','w');
w=str2num(get(HH,'String'));
HH=findobj(gcf,'Tag','M');
M=str2num(get(HH,'String'));
HH=findobj(gcf,'Tag','Vx');
Vx=str2num(get(HH,'String'));
HH=findobj(gcf,'Tag','cf');
cf=str2num(get(HH,'String'));
HH=findobj(gcf,'Tag','kd');
kd=str2num(get(HH,'String'));
Vx=Vx*659.5/M/w;
%stability criteria
Pe=(Vx*dx)/Dh
Cr=(Vx*dt)/dx
%calculate the initial concentration in water phase
cx=cf*M*(1-w);
```

```
cin=cx/((kd*(1-w)/w)+1);
c0=cin/(M*w);
Dh=Dh+Ds*Vx;
Rd=1+(kd*lo*(1-w)/w);
%definition of constants for finite difference calculation
s1=-Rd/dt-(2*theta*Dh)/(dx^2);
t1=(theta*Dh)/(dx^2)-(theta*Vx/(2*dx));
ri=(theta*Dh)/((dx)^2)+(theta*Vx)/(2*dx);
si=-Rd/dt-(2*theta*Dh)/(dx^2);
ti=(theta*Dh)/(dx^2)-(theta*Vx)/(2*dx);
s1j=-Rd/dt-(2*(theta-1)*Dh)/(dx^2);
t1j=((theta-1)*Dh)/(dx^2)-((theta-1)*Vx/(2*dx));
rj=((theta-1)*Dh)/(dx^2)+((theta-1)*Vx)/(2*dx);
sj=-Rd/dt-(2*(theta-1)*Dh)/(dx^2);
tj=((theta-1)*Dh)/(dx^2)-((theta-1)*Vx)/(2*dx);
% the distance of EK cell
for i=1:m
 d(i,1)=dx*i;
end
%arrange the "a matrix"
a=zeros(m);
a(1,1)=s1;a(1,2)=t1;
a(m,m-1)=ri+ti;a(m,m)=si;
for i=2:m-1
    a(i,i-1)=ri;
    a(i,i)=si;
    a(i,i+1)=ti;
end
%define the solution matrix and I.C.(contaminants)
c=zeros(m,1);
for k=1:m
   c(k,1)=c0;
end
% Boundary condition
u=zeros(m,1);
tt=zeros(n,1);
cc=zeros(n,1);
j=1;
   u(1,1)=s1j*c(1,1)+t1j*c(2,1)+(((theta-1)*Dh)/(dx^2)+((theta-1)*Vx)/(2*dx))*c0;
   for i=2:m-1
   u(i,1)=rj*c(i-1,1)+sj*c(i,1)+tj*c(i+1,1);
   end
      u(m,1)=(rj+tj)*c(m-1,1)+sj*c(m,1);
x=inv(a)*u;
c=x;
tt(1,1)=dt*j;
```

```
cc(1,1)=x(m,1);
%solve the equation
for j=2:n
      u(1,1)=s1j*c(1,1)+t1j*c(2,1);
   for i=2:m-1
   u(i,1)=rj*c(i-1,1)+sj*c(i,1)+tj*c(i+1,1);
   end
      u(m,1)=(rj+tj)*c(m-1,1)+sj*c(m,1);
x=inv(a)*u;
c=x;
tt(j,1)=dt*j;
cc(j,1)=x(m,1);
end
%calaulate the organic concentration ratio in mixed soils (soil+solution)
q=zeros(m,1);
s=zeros(m,1);
f=zeros(m,1);
for i=1:m
   q(i)=c(i)*kd;
   q(i)=q(i)*M*(1-w);
   s(i)=c(i)*M*w;
   f(i)=(q(i)+s(i))/cx;
end
if z==1
      y1=f;
      y11=cc;
      tt1=tt;
   end
if z==2
      y2=f;
      y22=cc;
      tt2=tt;
   end
if z==3
      y3=f;
      y33=cc;
      tt3=tt;
   end
if z==4
      y4=f;
      y44=cc;
      tt4=tt;
   end
if z==4
figure(6)
k=-0.5;
```

```
dd=zeros(10,1);
for i=1:10
   k=k+1;
   dd(i,1)=k;
end
yy1=[0.64 0.82 0.91 1.0 1.0 1.0 1.0 1.0 1.0 0.98];
yy2=[0.11 0.32 0.35 0.75 0.89 0.97 1.0 1.0 1.0 1.0];
yy3=[0.05 0.1 0.15 0.2 0.25 0.34 0.5 0.68 0.7 0.7];
yy4=[0.02 0.05 0.06 0.11 0.12 0.16 0.25 0.29 0.34 0.37];
plot(dd,yy1,'ko',dd,yy2,'ksquare',dd,yy3,'kdiamond',dd,yy4,'k*')
legend('24 hours','72 hours','120 hours','168 hours')
hold on
plot(d,y1,'k-',d,y2,'k-',d,y3,'k-',d,y4,'k-')
xlabel('Distance (cm)')
ylabel('Concentration Ratio(C/Co)')
title('PCE Transport in Soils')
hold off
else
   doelineargui
end
```

8.5. MATLAB Program for Phenanthrene

```
%times of calculation
HH=findobj(gcf,'Tag','z');
z=str2num(get(HH,'String'));
%parameters
HH=findobj(gcf,'Tag','dt');
dt=str2num(get(HH,'String'));
HH=findobj(gcf,'Tag','n');
n=str2num(get(HH,'String'));
HH=findobj(gcf,'Tag','dx');
dx=str2num(get(HH,'String'));
HH=findobj(gcf,'Tag','m');
m=str2num(get(HH,'String'));
HH=findobj(gcf,'Tag','theta');
theta=str2num(get(HH,'String'));
HH=findobj(gcf,'Tag','Dh');
Dh=str2num(get(HH,'String'));
HH=findobj(gcf,'Tag','Ds');
Ds=str2num(get(HH,'String'));
HH=findobj(gcf,'Tag','lo');
lo=str2num(get(HH,'String'));
HH=findobj(gcf,'Tag','w');
w=str2num(get(HH,'String'));
HH=findobj(gcf,'Tag','M');
M=str2num(get(HH,'String'));
```

```
HH=findobj(gcf,'Tag','Vx');
Vx=str2num(get(HH,'String'));
HH=findobj(gcf,'Tag','cf');
cf=str2num(get(HH,'String'));
HH=findobj(gcf,'Tag','cin');
cin=str2num(get(HH,'String'));
HH=findobj(gcf,'Tag','k1');
k1=str2num(get(HH,'String'));
HH=findobj(gcf,'Tag','k2');
k2=str2num(get(HH,'String'));
HH=findobj(gcf,'Tag','kr');
kr=str2num(get(HH,'String'));
Vx=Vx*659.5/M/w;
%stability criteria Pe<2 and Cr<1
Pe=(Vx*dx)/Dh
Cr=(Vx*dt)/dx
%calculate the initial concentration in water phase
cx=cf*M*(1-w)+cin*M*w;
c0=cin;
q0=cf;
Dh=Dh+Ds*Vx;
%definition of constants for finite difference calculation
s1=-1/dt-(2*theta*Dh)/(dx^2)-(lo/dt)*((1-w)/w)*(kr*k1*theta/((1/dt)+kr*theta));
t1=(theta*Dh)/(dx^2)-(theta*Vx/(2*dx));
ri=(theta*Dh)/((dx)^2)+(theta*Vx)/(2*dx);
si=-1/dt-(2*theta*Dh)/(dx^2)-lo*((1-w)/w)*(kr*k1*theta/((1/dt)+kr*theta));
ti=(theta*Dh)/(dx^2)-(theta*Vx)/(2*dx);
s1j=-1/dt-(2*(theta-1)*Dh)/(dx^2)+(lo/dt)*((1-w)/w)*(kr*k1*(1-theta)/((1/dt)+kr*theta));
t1j=((theta-1)*Dh)/(dx^2)-((theta-1)*Vx/(2*dx));
rj=((theta-1)*Dh)/(dx^2)+((theta-1)*Vx)/(2*dx);
sj=-1/dt-(2*(theta-1)*Dh)/(dx^2)+(lo/dt)*((1-w)/w)*(kr*k1*(1-theta)/((1/dt)+kr*theta));
tj=((theta-1)*Dh)/(dx^2)-((theta-1)*Vx)/(2*dx);
qj=(lo/dt)*((1-w)/w)*[-1+[(1/dt)+(kr*(1-theta))]/[(1/dt)+kr*theta]];
mj=(lo/dt)*((1-w)/w)*(kr*k2/((1/dt)+kr*theta));
% the distance of EK cell
for i=1:m
 d(i,1)=dx*i;
end
%arrange the "a matrix"
a=zeros(m);
a(1,1)=s1;a(1,2)=t1;
a(m,m-1)=ri+ti;a(m,m)=si;
for i=2:m-1
    a(i,i-1)=ri;
    a(i,i)=si;
    a(i,i+1)=ti;
```

```
end
%define the solution matrix and I.C.(contaminants)
c=zeros(m,1);
q=zeros(m,1);
for k=1:m
   c(k,1)=c0;
   q(k,1)=q0;
end
% Boundary condition
u=zeros(m,1);
tt=zeros(n,1);
cc=zeros(n,1);
j=1;
   u(1,1)=s1j*c(1,1)+t1j*c(2,1)+(((theta-1)*Dh)/(dx^2)+((theta-1)*Vx)/(2*dx))*c0+qj*q0+mj;
   for i=2:m-1
   u(i,1)=rj*c(i-1,1)+sj*c(i,1)+tj*c(i+1,1)+qj*q(i,1)+mj;
   end
      u(m,1)=(rj+tj)*c(m-1,1)+sj*c(m,1)+qj*q(m,1)+mj;
x=inv(a)*u;
c=x;
tt(1,1)=dt*j;
cc(1,1)=x(m,1);
%solve the equation
for j=2:n
   old=c;
   u(1,1)=s1j*c(1,1)+t1j*c(2,1)+qj*q(1,1)+mj;
   for i=2:m-1
   u(i,1)=rj*c(i-1,1)+sj*c(i,1)+tj*c(i+1,1)+qj*q(i,1)+mj;
   end
      u(m,1)=(rj+tj)*c(m-1,1)+sj*c(m,1)+qj*q(m,1)+mj;
x=inv(a)*u;
c=x;
tt(j,1)=dt*j;
cc(j,1)=x(m,1);
for k=1:m
   q(k,1)=(kr*k1/((1/dt)+kr*theta))*c(k,1)+[(1/dt)+(kr*(1-
theta))]/[(1/dt)+kr*theta]*q(k,1)+(kr*k1*(1-
theta)/((1/dt)+kr*theta))*old(k,1)+(kr*k2/((1/dt)+kr*theta));
  end
end
%calaulate the organic concentration ratio in mixed soils (soil+solution)
s=zeros(m,1);
f=zeros(m,1);
for i=1:m
   q(i)=q(i)*M*(1-w);
   s(i)=c(i)*M*w;
```

```
   f(i)=(q(i)+s(i))/cx;
end
if z==1
      y1=f;
      y11=cc;
      tt1=tt;
   end
if z==2
      y2=f;
      y22=cc;
      tt2=tt;
   end
if z==3
      y3=f;
      y33=cc;
      tt3=tt;
   end
if z==3
figure(5)
k=-0.5;
dd=zeros(10,1);
for i=1:10
   k=k+1;
   dd(i,1)=k;
end
yy1=[0.93 0.96 0.97 0.97 0.97 0.99 0.98 0.97 0.97 0.92];
yy2=[0.67 0.76 0.83 0.86 0.86 0.86 0.86 0.86 0.85 0.82];
yy3=[0.60 0.70 0.72 0.73 0.71 0.73 0.73 0.72 0.70 0.60];
plot(dd,yy1,'ko',dd,yy2,'ksquare',dd,yy3,'kdiamond')
legend('Triton 37 days','Rhamnolipid 37 days','Rhamnolipid 60 days')
hold on
plot(d,y1,'k-',d,y2,'k-',d,y3,'k-')
xlabel('Distance (cm)')
ylabel('Concentration Ratio(C/Co)')
title('Phenanthrene Transport in Soils')
hold off
else
  doeunlineargui
end
```

Part II

Removal of Selected Hazardous Organic Compounds by Electro-Fenton Oxidation Process

TABLES OF CONTENTS

ABSTRACT

This research investigates the removal of selected polycyclic aromatic compounds (PAHs) and chlorinated aliphatic hydrocarbons (CAHs) by the electro-Fenton oxidation process. It is divided into four parts: the electro-generation of H_2O_2, the electro-regeneration of Fe^{2+}, the removal of selected PAHs by conventional Fenton oxidation process, and the removal of selected CAHs by conventional Fenton process. After determining the optimal conditions and reaction kinetics of each experimental part, the electro-Fenton oxidation process is carried out to remove PCE and TCE.

Hydrogen peroxide (H_2O_2) was electro-generated in a parallel-plate electrolyzer by reduction of dissolved oxygen (DO) in acidic solutions containing dilute supporting electrolyte. Operational parameters such as cathodic potential, oxygen purity and mass flow rate, cathode surface area, pH, temperature, and inert supporting electrolyte concentration were systematically investigated as to improve the Faradic current efficiency of H_2O_2 generation. Results indicate that significant self-decomposition of H_2O_2 only occurs at high pH (>9) and elevated temperatures (>23^{o}C). Results also indicate that the optimal conditions for H_2O_2 generation are cathodic potential of –0.5V vs. saturated calomel electrode (SCE), oxygen mass flow rate of 8.2×10^{-2} mol/min, and pH 2. Under the optimal conditions, the average current density and average current efficiency are 6.4 A/m^2 and 81%, respectively. However, when air is applied at the optimal flow rate of oxygen, the average current density markedly decreases to 2.1 A/m^2, while the average current efficiency slightly increases to 90%. The limiting current density is 6.4 A/m^2, which is independent of cathode geometry and surface area. H_2O_2 generation is favored at low temperatures. In the concentration range studied (0.01~0.25M), the inert supporting electrolyte ($NaClO_4$) affects the total potential drop of the electrolyzer, but does not affect the net generation rate of H_2O_2.

The Fenton oxidation process, though efficient in degrading organic contaminants, is limited by the considerable amount of iron sludge generated. This research is to regenerate Fe(II) from ferric salt or iron sludge by electrochemical method as a means to minimize the iron sludge generation. Experiments were carried out in a parallel-plate electrolyzer using both constant potential and constant current modes. Results indicate that the optimal cathodic potential for the electro-regeneration of Fe(II) is –0.1V vs. the saturated calomel electrode (SCE). In the constant potential mode, the average current density obtained at –0.1V (vs. SCE) is approximately equal to the optimal current density applied in the constant current mode, provided an identical initial Fe(III) concentration ($[Fe^{3+}]_0$). The suitable pH range is determined by the hydrolysis of Fe(III) ions, which depends on Fe(III) concentration. Above the pH domain of Fe(III) hydrolysis, $Fe(OH)_3$(s) precipitates and significantly inhibits Fe(II) regeneration. As expected, increasing cathode surface area and solution temperature markedly accelerates Fe(II) regeneration rate. At the optimal cathodic potential (-0.1V vs. SCE), the average current density is in linear proportion to $[Fe^{3+}]_0$, showing a slope of 8.48×10^{-3} $(A/m^2)(mg/L)^{-1}$ (or 4.74×10^2 $(A/m^2)(M)^{-1}$). The average current efficiency varies with $[Fe^{3+}]_0$, i.e., 75% at $[Fe^{3+}]_0$ = 100 mg/L and 96~98% at $[Fe^{3+}]_0 \geq$ 500 mg/L, during the course of electrolysis for 3 hours . Once reaching 75% of the Fe(II) regeneration capacity (ca. 4 hours of extended electrolysis), further regeneration becomes difficult due to Fe(III) mass transfer limitation. Fe(II) can also be effectively regenerated from iron sludge, though a much lower pH (usually < 1) is required for sludge dissolution. Oxygenation of Fe(II) by pure

oxygen gas is kinetically negligible at pH < 4. The unit energy consumption is 2.0~3.0 kWh per kg Fe(II) regenerated.

The Fenton oxidation process can effectively degrade all selected PAHs, i.e., naphthalene, fluorene, phenanthrene, fluoranthene, pyrene and anthracene. The optimal pH value is pH 3. The extent of mineralization exemplified by naphthalene is around 85%. A "time-squared" kinetic model, $C = C_0 \exp(-k_{obs}t^2)$, can be used to describe the degradation kinetics of selected PAHs in the continuous dosing mode. This model assumes that the concentration of hydroxyl radicals increases linearly with reaction time. The observed rate constant, k_{obs}, follows the order: fluorene < phenanthrene < fluoranthene ≈ pyrene < anthracene, which reverses the order of water solubility. Methanol or ethanol significantly inhibits the degradation of PAHs by competing for hydroxyl radicals.

The oxidation of selected chlorinated aliphatic hydrocarbons, namely, tetrachloroethylene (PCE), trichloroethylene (TCE), 1,1-dichloroethylene (DCE) and chloroform by the conventional Fenton process was investigated. Results indicate PCE, TCE and DCE can be effectively removed by hydroxyl radicals, while the removal of chloroform is more difficult. The removal rate is primarily affected by the molecular structure of organic compound. The chlorinated ethenes can be readily oxidized by hydroxyl radicals due to their electron-rich double bond structure. On the contrary, chloroform is difficult to remove due to its highly chlorinated and saturated structure. The reaction rate of the chlorinated ethenes decreases as the chlorine substitution degree increases, i.e., DCE > TCE > PCE. The dosing mode of H_2O_2 and Fe^{2+} significantly affects the degradation of selected CAHs. Especially, the dosing mode of Fe^{2+} plays a more important role than that of H_2O_2. For the oxidation of PCE, TCE and DCE, the experimental data in the continuous dosing mode can be well fitted by the proposed "time-squared" kinetic model, i.e., $C = C_0 \exp(-k_{obs}t^2)$. A complete dechlorination can be readily achieved, and the minerailzation degree reaches about 65-70%. Since all chlorine is released from the molecular structure of the chlorinated ethenes, the residual TOC is only composed of low molecule (C_1 or C_2) carboxylic acids that are less toxic to the environment. For the oxidation of chloroform, the maximum removal efficiency achieved is about 90% by the continuous dosing mode. The dechlorination and mineralization degrees are both around 70%. The optimal pH range is 2~3, as exemplified by the oxidation of PCE and TCE.

The electro-Fenton process was used to generate H_2O_2 on site, and then degrade PCE and TCE after the external dose of Fe^{2+}. In the meantime, Fe^{2+} was continuously regenerated at the cathode once oxidized to Fe^{3+}. Results indicate that the electro-Fenton process yields a higher organic removal efficiency than the conventional Fenton process due to the effective regeneration of Fe^{2+} at the cathode of the electric cell. This demonstrates that the electro-Fenton oxidation process is an effective technology for the removal of hazardous organic contaminants.

1. INTRODUCTION

1.1. Significance of the Research

1.1.1. Sources of Hazardous Organic Contaminants in Soils

Soils at typical DOE (Department of Energy) waste sites are known to be contaminated by a host of hazardous organic chemicals. The major organic compounds can be classified into two groups: 1) chlorinated aliphatic hydrocarbons (CAHs), including tetrachloroethylene (PCE), trichloroethylene (TCE), dichloroethylene (DCE), chloroform; and 2) polycyclic aromatic hydrocarbons (PAHs), including naphthalene, fluorene, phenanthrene, fluoranthene, pyrene and anthracene. Arbitrary disposal of hazardous organic compounds, accidental petroleum spills, and leaking of underground petroleum storage tanks can seriously contaminate surrounding soils and groundwaters with toxic organic contaminants.

Chlorinated aliphatic hydrocarbons (CAHs) are commonly used as industrial solvents. They are considered as a significant category of hazardous organic compounds. Chlorination has become a widespread industrial practice because it yields compounds of lower flammability, higher density, high viscosity, and improved solvent properties compared to nonchlorinated solvents (Watts, 1998). Chlorinated solvents are mainly used for degreasing and cleaning a large range of products, from machine parts to computer chips. Although these compounds are highly volatile, they can also migrate through the subsurface. The properties of chlorinated solvents that make them mobile in groundwater systems include high density, relatively high water solubility, and low biodegradability (Watts, 1998). They also adsorb to soil surfaces, resulting in a high contamination level at some specific sites.

Polycyclic aromatic hydrocarbons (PAHs) are found in the heavier fractions of petroleum products (e.g., lubricating oils, asphalt, and tarlike materials) as well as automobile exhaust. The leaking of petroleum underground storage tanks may result in serious contamination of subsurface soils with PAHs, and eventual contamination of groundwater. Though these tanks are made of relatively durable materials, unfortunately, soil is a corrosive environment and, after a certain period of time, the tanks rust, corrode, and leak (Shwendeman and Wilcox, 1987). Another major source of PAHs contamination is gas plants, which produce gas from coal and oil. Soils around these gas plants are difficult to remediate because of high concentrations of PAHs, long chain aliphatics, and phenolics (Michelcic and Luthy, 1988). It is well known that PAHs chemically induce cancer.

Public concerns focus on health effects such as cancer and other chronic illnesses. The importance of minimizing the effects of these typical hazardous wastes is obvious: approximately 33% of the United States cities use groundwater, while 95% of the rural United States population relies on groundwater for domestic use (Patrick, 1983). That is why many CAHs and PAHs are listed among U.S. EPA priority pollutants.

1.1.2. Limitations of Current In-Situ Soil RemediationTechnologies

The removal of toxic organic chemicals from contaminated soils is a challenging task. The soil remediation processes are usually classified as in-situ and ex-situ applications. In-situ technologies are more attractive than ex-situ technologies. Soil in-situ remediation methods can be classified as physical, biological, and chemical processes based on different principles involved.

A number of physical methods such as in-situ heating, freezing and vitrification are currently being developed for soil remediation. In-situ heating uses steam injection (Hoogendon, 1984) or radio frequency (RF) (Brideg and Strestly, 1984) to heat the contaminated soil. At high temperatures, ranging from 300~400 ^{o}C, organic chemicals are decomposed. Artificial soil freezing involves the installation of freezing loops in the ground and a self-contained refrigeration system. Toxic chemicals are immobilized at low temperatures. In-situ vitrification is done by passing an electrical current through the soil to convert the soil into a glassy material. Though physical in-situ remediation processes appear effective, its implementation is difficult. Furthermore, method such as vitrification renders the affected aquifer useless.

Bioremediation has received much attention in the field. It is done by injecting appropriate nutrients to the contaminated zone to stimulate microbial growth and as a means to degrade the organic contaminants. However, bioremediation can only degrade those organic compounds which are amenable to microbes. Several factors can affect the operation of the bioremediation process: nutrient, oxygen content, redox potential, pH, water saturation, hydraulic conductivity, osmotic pressure, temperature, growth inhibitors, predators, and the type and concentration of the contaminants. Primary substrate must be provided if the organic contaminants are co-metabolized. Aerobes require oxygen, and anaerobes need nitrate or sulfate as electron acceptors. Optimum pH range for microbial activity is 6 to 8. The temperature is between 20 and 37 ^{o}C. Since subsurface temperature is generally around 10~15 ^{o}C, temperature is unfavorable for bioremediation. If the concentration of the target compound is low, the microbes may not be stimulated to utilize the organic compound in question. Moreover, if other "preferred" carbon sources are present, the microorganisms may by-pass the target pollutants as food source. The ecological structure of the underground can cause severe problems to bioremediation process. Competition between different microbial species and salt concentrations can have a severe influence on the microbes of interest. Extensive research has been conducted to use isolates from the soil-water system (Stief, 1984; Mckinnon and Dykesen, 1984; Strier, 1980; Macay and Shiu, 1981; Wood, 1980; Martinez, 1986; Chivers, 1971). However, the sustainability of these enriched isolates in the natural environment remains unknown. Another crucial factor is the hydraulic conductivity of the soil-water system. The hydraulic conductivity must be large enough and the residence time short enough so that the nutrients added will be effective. Recent development on bioremediation processes has been concentrated on the addition of oxidizing agents. Oxidizing agents such as H_2O_2, O_3 and air have been delivered to the soil-water system to enhance the microbial activity. However, due to the limited availability of oxygen in the subsurface system, the degradation of organics will be hindered.

Chemical in-situ treatment technology includes immobilization, extraction and detoxification. Precipitation, chelation and polymerization are major forms of immobilization. Extraction involves the flushing of contaminated soils with surfactants, dilute acids and bases, or water. Detoxification includes reduction, oxidation, neutralization (for heavy metals), and hydrolysis. Immobilization does not eliminate the contaminants permanently. Rather it releases the contaminants from their associated soil mass. Chemical oxidation and reduction change the oxidation state of the organic contaminants. Commonly used oxidizing agents include potassium permanganate, ozone, hydrogen peroxide and hypochlorite. Among these oxidants, ozone has received the greatest attention. However, the mechanism of ozonation was not fully understood until the last seventies when Hoigne and

Bader (1978, 1983) proposed that ozone can have two reaction modes: direct and indirect reactions. The direct ozone reaction is highly selective and slow with rate constants on the order of 1 to 10^3 (M^{-1} sec^{-1}). The indirect reaction is nonselective and fast with rate constants on the order of 10^7 to 10^{10} (M^{-1} sec^{-1}). Although ozone is a strong oxidant, ozonation is not feasible for the silt-laden or clay soils that have a low hydraulic conductivity, e.g., $< 10^{-5}$ cm/sec (Destephen and Benson, 1994).

1.1.3. Proposed Innovative Electro-chemical Technology for Soil Remediation

Due to above-mentioned limitations of current technologies, innovative in-situ remediation technologies for low permeability soils that are easy for application, dependable, and cost-effective are urgently needed. To be successful in in-situ remediation, one needs to address two basic engineering problems: (1) enhancing the release and subsequent transport of the contaminants from the soil surface to the solution phase, and (2) facilitating the detoxification of the released contaminants. This has prompted us to propose an integrated electro-chemical technology which couples the electro-kinetic (EK) process with the electro-Fenton (EF) oxidation process. The EK process releases hazardous contaminants from subsurface soils, and the EF process oxidatively decompose the released contaminants in aqueous solution. The EK process has been reported in Volume I. The Volume II introduces the decomposition of selected hazardous organic compounds, i.e., CAHs and PAHs, by the EF oxidation process.

1.2. Literature Review of Fenton Oxidation Process

1.2.1. Theoretical Consideration

(a) Advanced Oxidation Processes (AOPs)

The concept of "advanced chemical oxidation processes" (AOP) is defined as "the oxidation processes which generate hydroxyl radicals in sufficient quantity to affect water treatment" (Glaze *et al*., 1987). Due to its extremely high oxidation-reduction potential, hydroxyl radical can react with almost all organic compounds and some inorganic ions. Most of AOP systems use a combination of strong chemical oxidant, e.g. O_3 or H_2O_2, a catalyst, e.g. transition metal ions or photocatalyst, and with or without irradiation, e.g. ultraviolet (uv), ultrasound (us), or electron beam (eb). Huang *et al*. (1993) have discussed the merits and demerits of these various AOP processes and concluded that hydrogen peroxide-based AOPs such as conventional Fenton and electro-Fenton processes are the most promising technologies. These methods require no addition of obnoxious chemicals, easy for operation, effective, and economically attractive. Hydrogen peroxide-based processes are more efficient in mass transfer than ozone-based processes. The conventional Fenton process has been widely applied in industrial wastewater treatment and soil and goundwater remediation. The electro-Fenon process is a newly emerging technology. This inovative technology is more attractive than the conventional Fenton process because hydrogen peroxide can be on-site generated from dissolved oxygen and ferrous ions can be concurrently regenerated from ferric ions using an electrochemical method.

(b) Conventional Fenton (CF) Oxidation Process

Fenton's reagent consists of H_2O_2 and Fe^{2+} ion. Under an acidic condition, H_2O_2 decomposes to hydroxyl radical and hydroxide ion under the catalysis of Fe^{2+} ion. Hydroxyl radical is an intermediate species characterized by an unpaired electron. The one-electron

deficiency of hydroxyl radical results in its transient and highly oxidizing characteristics, with a redox potential being only next to elemental fluorine. Hydroxyl radical can nonselectively oxidize most of organic compounds as well as quite a few inorganic chemicals. This intermediate species can attack target organic contaminants, CO_3^{2-}, HCO_3^-, Cl^-, and even H_2O_2 and Fe^{2+}, as illustrated in Figure 1.1.

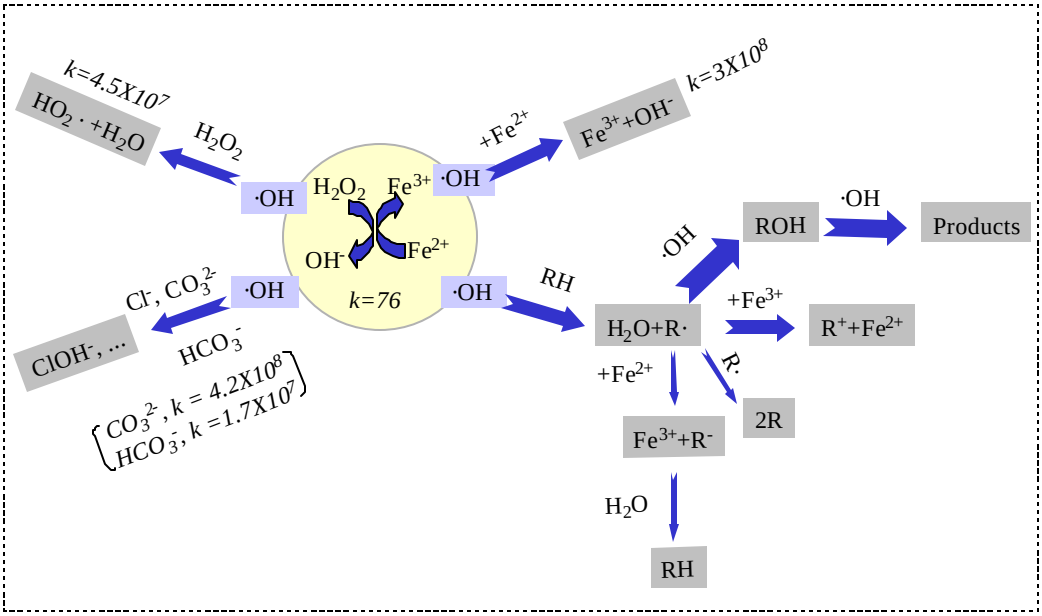

Figure 1.1. Illustration of proposed mechanisms of conventional Fenton oxidation process.

The reaction mechanisms of Fenton oxidation process are presented by a series of chain reactions (Walling, 1975):

$$H_2O_2 + Fe^{2+} \rightarrow Fe^{3+} + \cdot OH + OH^- \ , k_1 \qquad (1.1)$$

$$Fe^{2+} + \cdot OH \rightarrow Fe^{3+} + OH^- \ , k_2 \qquad (1.2)$$

$$RH + \cdot OH \rightarrow R\cdot + H_2O \ , k_3 \qquad (1.3)$$

$$R_1\cdot + Fe^{3+} \rightarrow R_1^+ + Fe^{2+} \ , k_{31} \qquad (1.4)$$

$$2R_2\cdot \rightarrow R_2 - R_2 \ , k_{32} \qquad (1.5)$$

$$R_3\cdot + Fe^{2+} \rightarrow Fe^{3+} + R_3^- \xrightarrow{H_2O} R_3H \ , k_{33} \qquad (1.6)$$

$$H_2O_2 + \cdot OH \rightarrow HO_2\cdot + H_2O \ , k_4 \qquad (1.7)$$

where, k_1 = 76 (M^{-1} Sec^{-1}),
k_2 = 3x10^8(M^{-1} Sec^{-1}),
k_4 = 2~4.5x10^7 (M^{-1} Sec^{-1}),
RH = target organic compound.

Reaction 1.1 is a chain initiation step which generates hydroxyl radicals. Hydroxyl radicals so produced will attack the organic compounds, producing organic radicals, as shown in reaction 1.3. These free organic radicals can be further transformed through three different pathways (Walling and Kato, 1970): $R_1\cdot$ radical is further oxidized by ferric ion, transforming

into an organic cation (Reaction 1.4); $R_2\cdot$ radical dimerizes(Reaction 1.5); $R_3\cdot$ radical is first reduced by ferrous ion, and then the resulting organic anion is reverted to the parent compound by hydroxylation (Reaction 1.6). Side reactions occur at the same time, for example, hydroxyl radicals can react with both H_2O_2 and Fe^{2+}. H_2O_2 is oxidized to superhydroxyl radical (Reaction 1.7), an intermediate species with a redox potential less than that of hydroxyl radical. Fe^{2+} is oxidized to Fe^{3+}, which accelerates the depletion of Fe^{2+} and eventually terminates the chain reactions (Reaction 1.2). Both H_2O_2 and Fe^{2+} compete for hydroxyl radicals at moderate rate constants. They are known as "scavengers" for hydroxyl radicals, and the two reactions are inevitable. Other common inorganic scavengers in aqueous solutions include bicarbonate, carbonate and chloride, as shown in Reactions 1.8~1.10:

$$HCO_3^- + \cdot OH \rightarrow HCO_3\cdot + OH^- \text{ or } CO_3\cdot^- + H_2O,\ k_5 \qquad (1.8)$$

$$CO_3^{2-} + \cdot OH \rightarrow CO_3\cdot^- + OH^-,\ k_6 \qquad (1.9)$$

$$Cl^- + \cdot OH \rightarrow HOCl\cdot^-,\ k_7 \qquad (1.10)$$

where, $k_5 = 3.6\text{x}10^7\ M^{-1}\cdot s^{-1}$ (Waltz *et al.*, 1973),
$k_6 = 3.65\text{x}10^8\ M^{-1}\cdot s^{-1}$ (Behar *et al.*, 1970),
$k_7 = 8.9\text{x}10^7\text{-}6.4\text{x}10^8\ M^{-1}\cdot s^{-1}$ (Anbar and Thomas, 1964).

Fortunately, most organic compounds react with hydroxyl radicals at a rate constant of $K_{OH} > 10^9 (M^{-1}\ Sec^{-1})$. Compared with the rate constants of H_2O_2, Fe^{2+} and other inorganic scavengers, the competition reactions are not significant unless the scavengers are present at a high concentration. The strong oxidizing ability of Fenton process is intrinsically expressed by the non-selective oxidation nature of hydroxyl radicals. The conventional Fenton oxidation process possesses the following advantages: 1) no chlorinated organic compounds formed as in chlorination or hypochlorination, 2) no mass transfer limitation due to its homogeneous catalytic nature, and 3) cheap and nontoxic ferrous sulfate and hydrogen peroxide (Huang *et al.*, 1993). The hydroxyl radicals combine with carbon in the organic compounds by attacking and substituting some functional groups (such as halogen elements, double bonds, and aromatic rings), converting organic compounds to harmless carbon dioxide and water in many cases.

(c) Mechanisms of Electro-Fenton (EF) Process

Compared to the conventional Fenton oxidation process, the electro-Fenton process has following major advantages: 1) H_2O_2 can be continuously generated on-site whenever needed, which avoids chemical purchase, shipment and storage; 2) A dilute H_2O_2 solution enhances safety during material handling; 3) The manufacturing process can be simply conducted at ambient pressure and temperature; 4) Ferrous ions can be electrochemically regenerated at the cathode, which minimizes the quantity of iron sludge; and 5) Oxygen or air sparging provides necessary mixing for the system. Figure 1.2 illustrates the proposed mechanisms of the electro-Fenton oxidation process. Major electro-chemical reactions involved are shown as follows:

At the cathode

(a) reduction of dissolved oxygen:

$$O_2 + 2H^+ + 2e^- \rightarrow H_2O_2, \qquad E^0 = 0.682\text{V} \qquad (1.11)$$

$$H_2O_2 + 2H^+ + 2e \rightarrow 2H_2O, \qquad E^0 = 1.770\text{V} \qquad (1.12)$$

$$O_2 + 4H^+ + 4e \rightarrow 2H_2O, \qquad E^0 = 1.229\text{V} \qquad (1.13)$$

(b) regeneration of Fe^{3+}:

$Fe^{3+} + e^- \rightarrow Fe^{2+}$, $E^0 = 0.771V$ (1.14)

(c) evolution of hydrogen gas

$2H^+ + 2e^- \rightarrow H_2$, $E^0 = 0V$ (1.15)

(d) electro-reduction of organic compounds

Organic compound + ne^- ® *Reduced products* (1.16)

At the anode

oxidation of water:

$2H_2O \rightarrow O_2 + 4H^+ + 4e^-$, $E^0 = 1.229V$ (1.17)

where, the redox potentials are versus normal hydrogen electrode (NHE).

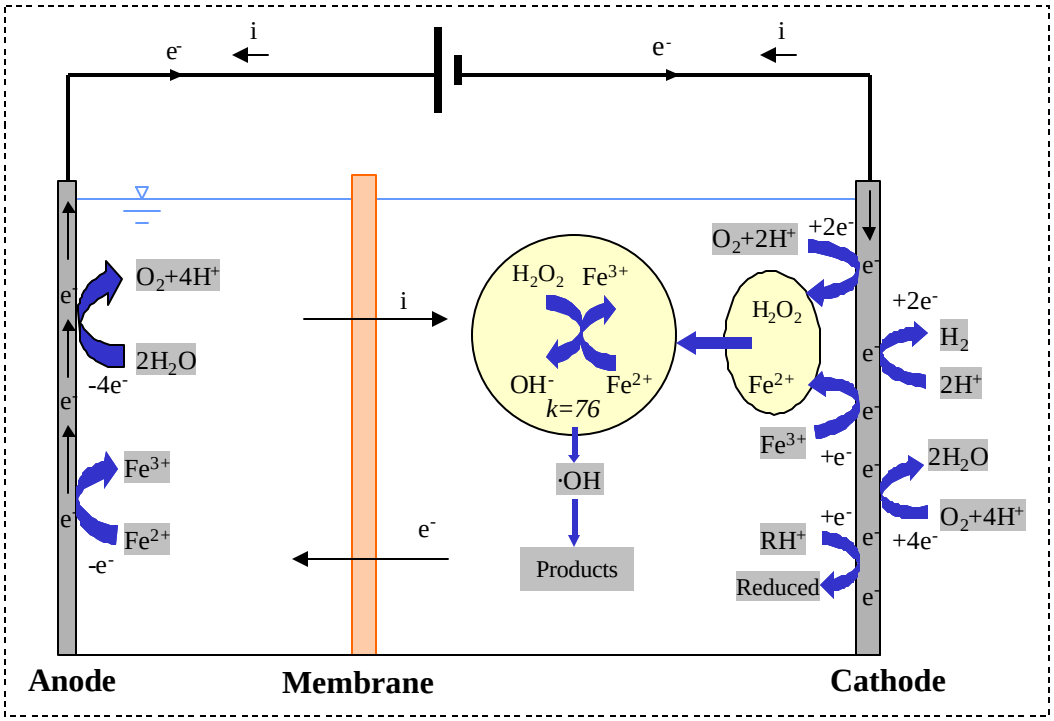

Figure 1.2. Illustration of proposed mechanisms of electro-Fenton oxidation process.

In this study, a two-compartmetn electrolyzer with parallel-plate electrodes was employed to generate hydrogen peroxide and regenerate ferrous ions. A cation exchange membrane is used to separate the anodic and cathodic compartments. In the cathodic compartment, pure oxygen gas or air is continuously sparged into the electrolyte solution and the dissolved oxygen is electrochemically reduced to hydrogen peroxide at the cathode (Reaction 1.11). This is a two-electron reaction. However, at an elevated cathodic potential (negative), hydrogen peroxide will be further reduced to water, as shown in Reaction 1.12. The overall reaction can be described by Reaction 1.13, which transfers 4 moles of electrons per mole of oxygen consumed. Reaction 1.12 decomposes hydrogen peroxide generated and reduces the current efficiency. Upon the external addition of ferrous ions into the cathodic compartment, hydrogen peroxide will be catalyzed to produce hydroxyl radicals. The organic contaminants

present in the aqueous solution are subjected to decomposition by the hydroxyl radicals. Ferrous ions are readily oxidized to ferric ions by both hydrogen peroxide and hydroxyl radicals, as shown in Reactions 1.1 and 1.2. In most Fenton oxidation processes, the rapid depletion of ferrous ions terminates the chain reactions. Though some organic radicals have the ability to regenerate ferrous ions (Reaction 1.4), the regeneration rate is kinetically insignificant. However, with externally applied electricity, ferrous ions can be effectively regenerated at the cathode by capturing one electron (Reaction 1.14). As a consequence, the hydroxyl radicals can be continuously generated. In an acidic solution, protons also compete for electrons to produce hydrogen gas, as shown in Reaction 1.15. The evolution of hydrogen gas will decrease the current efficiency of both hydrogen peroxide generation and ferrous ion regeneration. Therefore, the solution pH should be controlled. In addition, the organic compound may be directly decomposed by electrode-reduction (Reaction 1.16). Compared with the oxidative decomposition by hydroxyl radicals, this direct electrode-reduction is usually unimportant.

In the anodic compartment, the oxidation of water produces oxygen gas and protons (Reaction 1.17). Driven by the electric field, these anodic prontons will penetrate the cation exchange membrane and enter the cathodic compartment. The pH change of the catholyte is partially balanced by these protons. Furthermore, some portion of ferrous or ferric ions may enter the anodic compartment since the membrane tranfers cations. The ferrous ions will be oxidized at the anode, as shown in Reaction 1.18. Because the electric field resists the movement of ferrous ions from the cathode to the anode, the penetration of ferrous ions will not be significant.

From above-mentioned electrochemical reactions, it is obvious that the applied cathodic potential, current density, solution pH, solution temperature, oxygen mass flowrate, and inert electrolyte concnetration are important factors affecting the current efficiency of the electro-generation of hydrogen peroxide and electro-regeneration of ferrous ions.

1.2.2 Applications of Fenton Oxidation Process

Fenton's reagent has been extensively studied in the treatment of hazardous organic compounds. Sedlack and Andren (1991) reported that chlorophenols, chlorobenzene, and dichlorobiphenyls can be effectively degraded by Fenton's reagent. It is supposed that the most direct mechanism for the decomposition of chlorinated aromatic hydrocarbons (CAHs) proceeds through hydroxylation followed by ring cleavage and mineralization. Hayek and Dore (1990) studied the oxidation of phenolic compounds by hydrogen peroxide in an aqueous medium in the presence of various heterogeneous catalysts and in particular alumina supported iron. The catalytic oxidation of phenol depends on many different parameters, such as the preparation method of the catalyst, the nature of the supported metals, the reaction temperature and the presence of polyhydroxybenzenes at the beginning of the reaction. Catalyzed hydrogen peroxide has also been used as a pretreatment process for wastewater containing refractory organic compounds which are toxic to microorganisms by Spencer *et al.* (1992). Results show that stoichiometric ratios of compounds degraded to hydrogen peroxide consumed are related to both the iron concentration and the organic carbon content in the soil. Kuo (1992) applied Fenton's reagent to decolorize dye wastewater, and an average percent removal of chemical oxygen demand (COD) of approximately 88% was obtained. Recently, Fenton's reagent has been suggested as a means to oxidize entachlorophenol,

octachlorodibenzo-*p*-dioxin (OCDD) and hexachlorobenzene (Watts, 1991; Watts *et al.*, 1990, 1994) in silica sands or natural soils.

Electro-generated Fenton's reagent has been used to synthesize organic compounds (Matsue *et al.*, 1981; Fleszer *et al*., 1983; Hsiao and Nobe, 1993). For example, in Tzedakis *et al.*'s (1989) work, elctrochemically regenerated Fenton's reagent was applied to the hydroxylation of benzene into phenol. The EF process has also been used to detoxify wastewater containing hazardous organic compounds. Sudoh *et al*. (1986) investigated the feasibility of electro-Fenton oxidation of phenol using an H-type dual-compartment electrolyzer, and found that phenol was oxidatively degraded to oxalic acid and carbon dioxide. In the initial COD range of 260~2600 ppm, the complete degradation of phenol could be achieved. Two years later, Sudoh *et al*. (1988) employed an undivided bipolar electrolyzer to investigate the effect of anodic and cathodic reactions on the oxidative degradation of phenol. They reported that the current efficiency for producing hydrogen peroxide was 50~70% in the cathodic potential ranging from –2.0 V to –0.8 V at pH 2, and the COD current efficiency was highly related to the electrode potential difference. Oxidative reactions of phenol and chlorobenzene with electro-generated Fenton's reagent was investigated by Hsiao *et al*. (1993) using a three-compartment electrochemical cell. The reaction by-products of phenol included hydroquinone, catechol and resorcinol, and the major by-products of chlorobenzene were *p*-chlorophenol and phenol. Results also indicated that the electrochemical system provided an efficient way to regenerate ferrous ions.

1.3. Research Objectives

By all account, among the various remediation alternatives, in-situ remediation of contaminated soil is the most attractive approach. However, to be successful in in-situ remediation, one needs to consider two basic engineering problems: (1) enhancing the release and subsequent transport of the contaminants from the soil surface to the solution phase, and (2) facilitating the detoxification of the released contaminants.

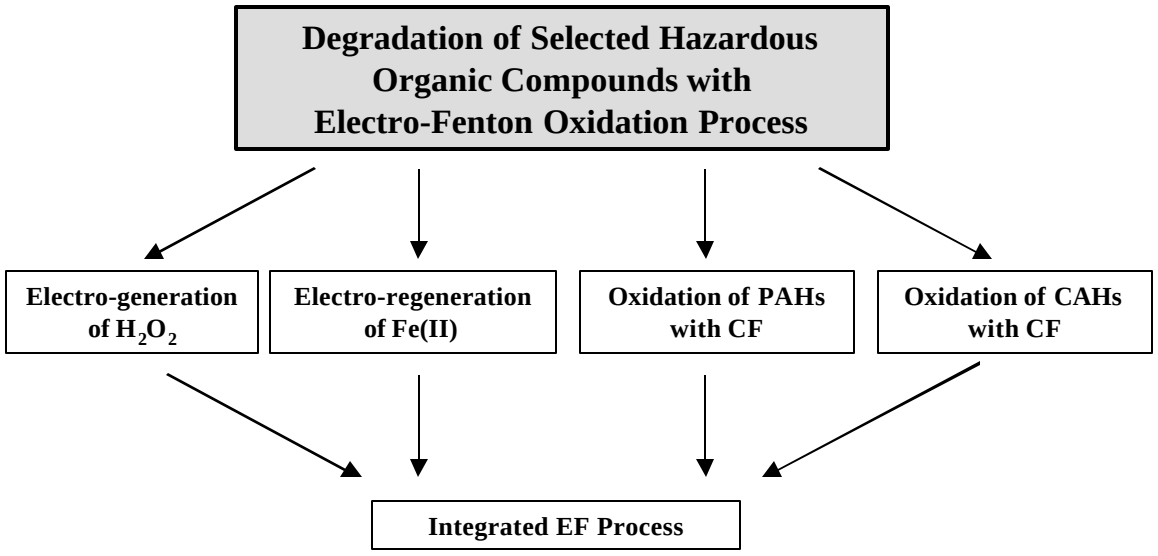

Figure 1.3. Illustrative presentation of research frame.

The proposed research is to develop electrochemical processes for the in-situ treatment of contaminated soils. It is composed of two parts, specifically, electrokinetic (EK) and electro-

Fenton (EF) processes. Electrokinetic process as a means to facilitate the removal of mixed contaminants, namely, organics and heavy metals, from soils. In order to effectively degrade the released organic contaminants, an advanced chemical oxidation process based on catalytic hydrogen peroxide is employed. Part II concentrates on the decomposition of selected hazardous organic compounds by the electro-Fenton oxidation process.

The research frame is illustratively presented in Figure 1.3. Correspondingly, this study is to achieve the following objectives:

(a) To investigate various parameters affecting the electro-generation of hydrogen peroxide in acidic solutions.
(b) To investigate various parameters affecting the electro-regeneration of ferrous ions.
(c) To investigate the decomposition of selected polycyclic aromatic hydrocarbons (PAHs) by conventional Fenton oxidation process.
(d) To investigate the decomposition of selected chlorinated aliphatic hydrocarbons (CAHs) by conventional Fenton oxidation process.
(e) To investigate the decomposition of selected organic compounds by intergrated electro-Fenton oxidation process.

1.4. References

43. Anbar M. and Thomas J. K. (1964) Pulse radiolysis studies of aqueous sodium chloride solutions. *J. Phys. Chem.*, **68** (12), 3829-3835.
44. Behar D., Czapski G. and Duchovny I. (1970) Carbonate radical in flash photolysis and pulse radiolysis of aqueous carbonate solutions. *J. Phys. Chem.*, **74** (10): 2206-2210.
45. Brideg J. E. and Strestly G. C. (1984) Decontamination of hazardous waste from spills and uncontrolled waste site by radio frequency in-situ heating. *Proceedings, Hazardous Material Spills Conference*: 9-65.
46. Chivers G. E. (1971) *Survey in Industrial Wastewater Treatment: Petroleum and Organic Industries, Volume 2*. Noyes Data Co.: Park Ridge, NJ.
47. Destephen R. A. and Benson C. P. (1994) *Hazardous and Industrial Wastes: Proceedings of the Twenty-sixth Mid-Atlantic Industrial Waste Conference,* Huang, C. P. Ed., p 20-27. Technomic Publishing Company, Inc.: Lancaster, PA.
48. Glaze W. H., Kang J. W. and Chapin D. H. (1987) The chemistry of water treatment involving ozone, hydrogen peroxide and ultraviolet radiation. *Ozone Sci. & Technol.*, **9** (4): 335-352.
49. Hayek N. A. and Dore M. (1990) Oxydation des phenols par le peroxyde d'hydrogene en milieu aqueux en presence de fer supporte sur alumine. *Wat. Res.*, **24** (8): 973-982.
50. Higgins T. E. (1989). *Hazardous Waste Minimization Handbook*. Lewis Publishers, Chelsea, MI.
51. Hoigne J. and Bader H. (1978) Ozone initiated oxidation of solutes in wastewater--a reaction kinetics approach. *Progress Water Technology*, **10**: 657-670.
52. Hoigne J. and Bader H. (1983) Rate constant of ozone with organic and inorganic compounds in water non-dissociating organic compounds. *Water Research*, **17** (2), 173-183.
53. Hoogendon D. (1984) Review of development of remediation action techniques for soil

contamination in netherlands. *Proceedings, Hazardous Material Spills Conference*: 9-65.
54. Hsiao Y. L. and Nobe K. (1993) Hydroxylation of chlorobenzene and phenol in a packed bed flow reactor with electrogenerated Fenton's reagent. *J. Appl. Electrochem.,* **23**: 943-946.
55. Huang C . P., Dong C. and Tang Z. (1993) Advanced chemical oxidation: its present role and potential future in hazardous waste treatment. *Waste Management*, **13**: 361-377.
56. Kuo W. G. (1992). Decolorizing dye wastewater with fenton's reagent. *Water Research,* 26 (7): 881-886.
57. Macay D. and Shiu W. Y. (1981) Evaluated kinetics data for high temperature reaction. *J. Phys. Chem. Ref. Data,* **10**: 1175.
58. Martinez D. (1986) *Chemical Waste: Handling and Treatment*. Springer-Verlag Inc.: Berlin.
59. Matsue T., Fujihira M. and Osa T. (1981) Oxidation of alkylbenzenes by electrogenerated hydroxyl radical. *J. Electrochem. Soc.: Electrochem. Sci. Tech.*, **128** (12): 2565-2569.
60. Mckinnon R. J. and Dykesen J. E. (1984) Removing organic from groundwater through aeration plus gac. *J. Am. Water Works Assoc.*, **76** (5): 42-47.
61. Michelcic J. R. and Luthy R. C. (1988) Degradation of polycyclic aromatic hydrocarbon compounds under various redox conditions in soil-water systems. *Applied Environmental Microbiology*, **54**: 1182-1187.
62. Patric R. (1983) *Groundwater Contamination in the United States*. National Academy Press: Washington, DC.
63. Sedlak D. L. and Andren A. W. (1991) Oxidation of chlorobenzene with fenton's reagent. *Environ. Sci. & Technol.*, **25** (4): 777-782.
64. Shwendeman T. D. and Wilcox H. K. (1987) *Underground Storage Systems: Leak Detection and Monitoring*. Lewis publishers, Chelsea, MI.
65. Spencer C. J., Stanton P. C. and Watts R. J. (1992) On-site treatment of contaminated soils and wastes from transportation maintenance activities using oxidative process. *Wat. Res.*, **26** (7): 976-978.
66. Stief K. (1984). Remedial action for groundwater protection. *Proceedings, Hazardous Material Spills Conference*: 9-65.
67. Strier M. P. (1980) Pollution treatability--molecular energineering approach. *Environ. Sci. & Technol.*, **14** (1): 28-31.
68. Sudoh M., Kodera T., Hino H. and Shimamura S. (1988) Effect of anodic and cathodic reactions on oxidative degradation of phenol in an undivided bipolar electrolyzer. *J. Chem. Eng. Japan*, **21** (2): 198-203.
69. Sudoh M., Kodera T., Sakai K., Zhang J. Q. and Koide K. (1986) Oxidative degradation of aqueous phenol effluent with electrogenerated fenton's reagent. *J. Chem. Eng. Japan,* **19** (6): 513-518.
70. Tzedakis T., Savall A. and Clifton M. J. (1989) The electrochemical regeneration of Fenton's reagent in the hydroxylation of aromatic substrates: batch and continuous processes. *J. Appl. Electrochem.*, **19**: 911-921.
71. Walling C. (1975) Fenton's reagent revisited. *Accounts Chem. Res.*, **8**: 125-131.
72. Walling C. and Kato S. (1970) The oxidation of alcohols by fenton's reagent: the effect of

copper ion[1]. *J. American Chemical Society*, **93** (17): 4275-4281.
73. Waltz W. L., Akhtar S. S. and Eager R. L. (1973) Oxidation of some transition-metal cyanide compounds by hydroxyl radical. *Can. J. Chem.*, **51** (15): 2525-2529.
74. Watts R. J. (1991) Catalyzed hydrogen peroxide treatment of octachlorodibenzo-p-dioxin (ocdd) in surface soils. *Chemosphere*, **23** (7): 949-955.
75. Watts R. J. (1998) *Hazardous Wastes: Sources, Pathways, Receptors*, p 69, 360. John Wiley & Sons, Inc.: New York, NY.
76. Watts R. J., Kong S., Dippre M. and Barnes W. T. (1994) Oxidation of sorbed hexachlorobenzene in soils using catalyzed hydrogen peroxide. *Journal of Hazardous Materials*, **39**: 33-47.
77. Watts R. J., Udell M. D., Rauch P. A. and Leung S. W. (1990) Treatment of entachlorophenol-contaminated soils using fenton's reagent. *Hazardous Waste & Hazardous Material*, **7**: 335-345.
78. Wood P. R. (1980) Removing potential organic precursors from drinking water. *EPA - 600/2-80-130a*.

2. ELECTROCHEMICAL GENERATION OF HYDROGEN PEROXIDE FROM DISSOLVED OXYGEN IN ACIDIC SOLUTIONS

2.1. Introduction

Hydrogen peroxide (H_2O_2) is an environmentally friendly chemical because it leaves no hazardous residuals but oxygen and water after reaction. It has been widely applied to the synthesis of organic compounds, bleaching of paper pulp, treatment of wastewater, and destruction of hazardous organic wastes. In the environmental field, H_2O_2 is used as a supplement of oxygen source to enhance the bioremediation of contaminated aquifers (Huling *et al.*, 1990; Wilson *et al.*, 1994). Moreover, H_2O_2 coupled with ozone or UV radiation can effectively decompose aqueous organic contaminants (Glaze and Kang, 1988; Aieta *et al.*, 1988; Lewis *et al.*, 1990; Bellamy *et al.*, 1991). The most common environmental application of H_2O_2 is the Fenton's reagent, an aqueous mixture of H_2O_2 and Fe^{2+}. Under an acidic condition, the reaction between H_2O_2 and Fe^{2+} generates hydroxyl radicals that are strong enough to non-selectively oxidize most organic as well as some inorganic compounds. The Fenton's reagent has recently been applied to in-situ remediation of contaminated soils and groundwaters (Ravikumar and Gurol, 1994; Watts *et al.*, 1994; Li *et al.*, 1997).

H_2O_2 is usually produced by electrochemical methods, such as electrolysis of inorganic chemicals ($H_2S_2O_8$, $KHSO_4$ and NH_4HSO_4) and autoxidation of organic compounds (alkylhydroanthraquinones and isopropyl alcohol) (Schumb *et al.*, 1955). The electrolysis of inorganics requires excessive energy and the autoxidation of organics requires non-aqueous solvents for catalyst cycle (Pletcher, 1999). H_2O_2 may also be directly generated from water, hydrogen, and oxygen using thermal, photochemical and electrical discharge processes. However, these processes require specific operational conditions such as high temperature, combustion, UV radiation plus mercury vapor, or high voltage. In recent years, small scale, on-site H_2O_2 production processes have gained increasing attention because of the cost and the hazards associated with the transport and handling of commercial concentrated H_2O_2 (Pletcher, 1999). If H_2O_2 can be generated on-site in an economic and safe way, its field application will be largely simplified. For example, it would be attractive to use the on-site generated H_2O_2, coupled with ozone, UV, or Fe^{2+}, for the detoxification of effluents from electro-kinetics, pump and treat, soil washing, and soil flushing processes.

Most electro-generation of H_2O_2 experiments are conducted in alkaline solutions with a high electrolyte concentration for the purpose of bleaching paper pulp (Oloman and Watkinson, 1975, 1976, 1979; Oloman, 1979; Sudoh *et al.*, 1985a, 1985b; Kalu and Oloman, 1990; Yamada *et al.*, 1999). In concentrated alkaline solutions, HO_2^- is formed ($pK_{a,\ H2O2}$=11.62 at 25 ^oC) which will be immediately repelled by the cathode upon its generation. Because the reduction of HO_2^- to OH^- is minimized, a high current efficiency (about 80~95%) can usually be achieved. However, if H_2O_2 is generated in alkaline solutions, a substantial amount of acid will be consumed for pH adjustment if an acidic condition is required. The Fenton's reagent, which is most commonly applied in organic synthesis and effluent treatment, has an optimal pH range of 2.5~3.5. Moreover, a high electrolyte concentration not only increases the treatment cost, but also introduces additional pollutants. Therefore, it is desirable to generate H_2O_2 in acidic solutions only containing dilute supporting electrolyte.

It has been reported that H_2O_2 can be electrochemically generated by reduction of dissolved oxygen (DO) in acidic solutions. The H_2O_2 so generated can be coupled with Fe^{2+}

to produce the Fenton's reagent for either degradation or synthesis of organic compounds (Matsue *et al.* 1981; Sudoh *et al.*, 1986, 1988; Tzedakis *et al.*, 1989; Do and Chen, 1993; Hsiao and Nobe, 1993a, 1993b; Chu, 1995; Huang *et al.*, 1999). In order to differentiate this process from conventional Fenton process that uses commercial H_2O_2, the term "electro-Fenton process" is applied. The major advantages of the electro-Fenton process include: 1) H_2O_2 can be continuously generated on-site whenever needed, which eliminates acquisition, shipment and storage; 2) A dilute H_2O_2 solution enhances safety during material handling; 3) The production process can be simply conducted at ambient pressure and temperature; 4) Fe^{2+} can be electrochemically regenerated at the cathode, which minimizes the quantity of iron sludge; and 5) Oxygen or air sparging enhances the mixing of reaction solution. The disadvantage is that H_2O_2 will accumulate at the cathode-solution interface and may be partially decomposed. Protons at a high concentration may also compete for electrons, leading to hydrogen gas evolution. Both effects will reduce the current efficiency of H_2O_2 production. Therefore, in acidic solutions, cathodic potential and solution pH are two essential factors controlling the current efficiency.

Though the electro-generation of H_2O_2 in acidic solutions has been studied by a few researchers, there exist conflicting results. Sudoh *et al.* (1986) investigated the decomposition of aqueous phenol by electro-generated Fenton's reagent. They found that the highest current efficiency (85%) was obtained at a cathodic potential of –0.6V vs. a saturated Ag/AgCl electrode (SSE) and pH 3. Tzedakis *et al.* (1989) reported that the electrolysis of an oxygen-saturated H_2SO_4 solution (0.6M) using a stirred mercury pool electrode yielded a current efficiency of 55% at a cathodic potential of –0.30V vs. SCE. Chu (1995) used the electro-Fenton process to remove aqueous chlorophenols at a cathodic potential of –0.6V vs. SCE, and reported that the current efficiency increased with decreasing pH. Hsiao and Nobe (1993a) investigated the oxidative hydroxylation of phenol and chlorobenzene using electro-generated Fenton's reagent. They reported that the optimal cathodic potential was –0.55V vs. SCE, and the generation of H_2O_2 was favored at low pH values.

The primary objective of the present study is to improve the Faradic current efficiency of H_2O_2 generation in acidic solutions. It is also expected that the results will clarify existing discrepancies among various studies of its kind. Influential parameters such as cathodic potential, oxygen purity and mass flow rate, cathode surface area, solution pH, temperature, and inert supporting electrolyte concentration were systematically examined. Considering that a high electrolyte concentration is usually not feasible for effluent treatment by the electro-generated H_2O_2, the inert supporting electrolyte, i.e., $NaClO_4$, was used only at a low concentration.

2.2 Theoretical

2.2.1. Electrochemical Reaction Mechanisms

Figure 2.1 illustrates the electrochemical reaction mechanisms of the electro-generation of H_2O_2 by reduction of dissolved oxygen in acidic and alkaline solutions. In acidic solutions, dissolved oxygen (DO) is electrochemically reduced to H_2O_2 at the cathode:

$$O_2 + 2H^+ + 2e \rightarrow H_2O_2 \qquad (2.1)$$

Two side reactions simultaneously occur at the cathode: 1) the reduction of H_2O_2 to H_2O due to the accumulation of H_2O_2 at the cathode-solution interface, and 2) the hydrogen gas (H_2) evolution:

$$H_2O_2 + 2H^+ + 2e \rightarrow 2H_2O \quad (2.2)$$

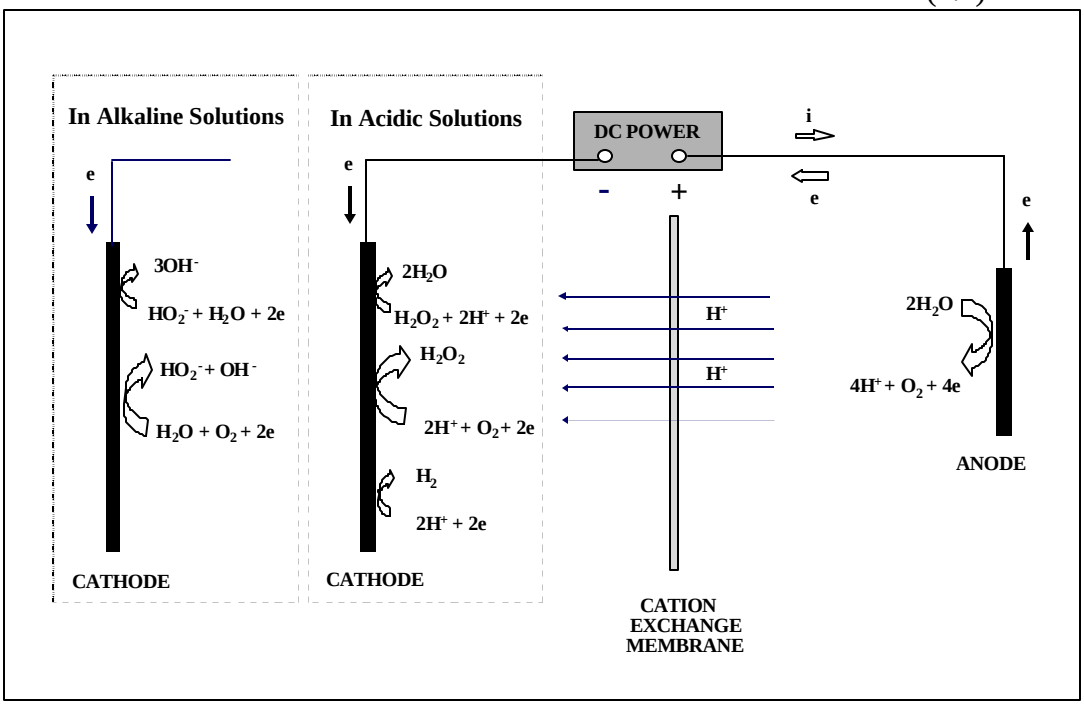

Figure 2.1. Schematic presentation of reaction mechanisms of electro-generation of H_2O_2 in acidic and alkaline solutions.

$$2H^+ + 2e \rightarrow H_2 \quad (2.3)$$

At the anode, the oxidation of H_2O leads to oxygen gas (O_2) evolution and proton release:

$$H_2O \rightarrow 2H^+ + \frac{1}{2}O_2 + 2e \quad (2.4)$$

The protons so generated will be driven to the catholyte electro-statically and partially supplementing the protons consumption during the synthesis of H_2O_2.

In alkaline solutions, dissolved oxygen is electrochemically reduced to HO_2^- anions at the cathode:

$$O_2 + H_2O + 2e \rightarrow HO_2^- + OH^- \quad (2.5)$$

Simultaneously, a side reaction competing for cathode electrons may further reduce HO_2^- to OH^-:

$$HO_2^- + H_2O + 2e \rightarrow 3OH^- \quad (2.6)$$

Due to the electro-static repulsion from the negatively charged cathode, the HO_2^- will be immediately driven away from the cathode-solution interface upon its generation. As a result, this side reaction will not play an important role. Therefore, the current efficiency with respect to H_2O_2 generation is usually higher in alkaline solutions than in acidic solutions.

2.2.2. Overpotential

Overpotential (E_{over}) is defined as the difference between the applied potential (E_c) and the conditional equilibrium potential (E_0):

$$E_{over} = E_c - E_0 \quad (2.7)$$

The overpotential primarily controls the rate of charge transfer of an electrochemical reaction. However, when the mass transfer of reactant predominates, the overpotential varies little in the region of limiting current.

2.2.3. Limiting Current

In the limiting current region, H_2O_2 generation is controlled by the mass transfer of DO through the cathode-solution diffusion layer, rather than by the electron transfer between DO and cathode. Since the DO concentration at the cathode surface rapidly approaches zero after electrolysis starts, the limiting current under a steady-state condition can be expressed by the following equation for macroscopic electrodes (Wendt and Kreysa, 1999):

$$I = k_m nFA_e(C^* - C_s) \tag{2.8}$$

where, I represents the current (A), k_m is the mass transfer coefficient (m/s), n is the stoichiometric number of electron transferred, F is the Farady's constant (96490 C/mol), A_e is the effective surface area of working electrode, C* is the concentration of reactant in bulk solution, and C_s is the concentration of reactant at working electrode surface.

The mass transfer coefficient, k_m, can be expressed by Equation 2.9:

$$k_m = D/\delta \tag{2.9}$$

where, D represents the diffusion coefficient of reactant (m^2/s) and δ is the thickness of the diffusion layer (m).

When the charge transfer rate exceeds the upper limit of the mass transfer rate, C_s rapidly approaches zero and the current reaches the maximum value, i.e., the limiting current (I_L). Thus, Equation 2.8 can be simplified as follows:

$$I_L = k_m nFA_e C^* \tag{2.10}$$

Since the limiting current (I_L) and the reactant concentration (C*) can be experimentally determined, the mass transfer coefficient (k_m) can be readily calculated using Equation 2.10.

2.2.4. Current Efficiency

Current efficiency (η), defined as the ratio of the electricity consumed by the electrode reaction of interest (Q_{eff}) over the total electricity passed through the circuit (Q_{tot}), can be calculated by Equation 2.11:

$$\eta = \frac{Q_{eff}}{Q_{tot}} \times 100\% \tag{2.11}$$

By definition, the η actually represents an overall current efficiency during a certain period of electrolysis time. By on-line monitoring the current, the amount of the total electricity (Q_{tot}) can be calculated using the following equation:

$$Q_{tot} = \int_0^t Idt \tag{2.12}$$

The amount of the effective electricity (Q_{eff}) can be calculated by measuring the H_2O_2 concentration generated during the same time period:

$$Q_{eff} = nFCV \tag{2.13}$$

where, C represents the H_2O_2 concentration (M) and V the rector volume (L). The overall equation for calculating the current efficiency of H_2O_2 generation is generalized as follows:

$$\eta = \frac{nFCV}{\int_0^t Idt} \times 100\% \qquad (2.14)$$

2.3. Experimental

2.3.1. Reaction System

Figure 2.2 shows the schematic diagram of the reaction system. An acrylic parallel-plate electrolyzer was employed for the electro-generation of H_2O_2. The cathodic and anodic compartments had a volume of 4.50L and 3.15L, respectively. In experiments, 4.0L of catholyte and 3.0L of anolyte were used and completely mixed by a magnetic stir plate. Sodium perchlorate ($NaClO_4$) was utilized as inert supporting electrolyte for conducting electricity.

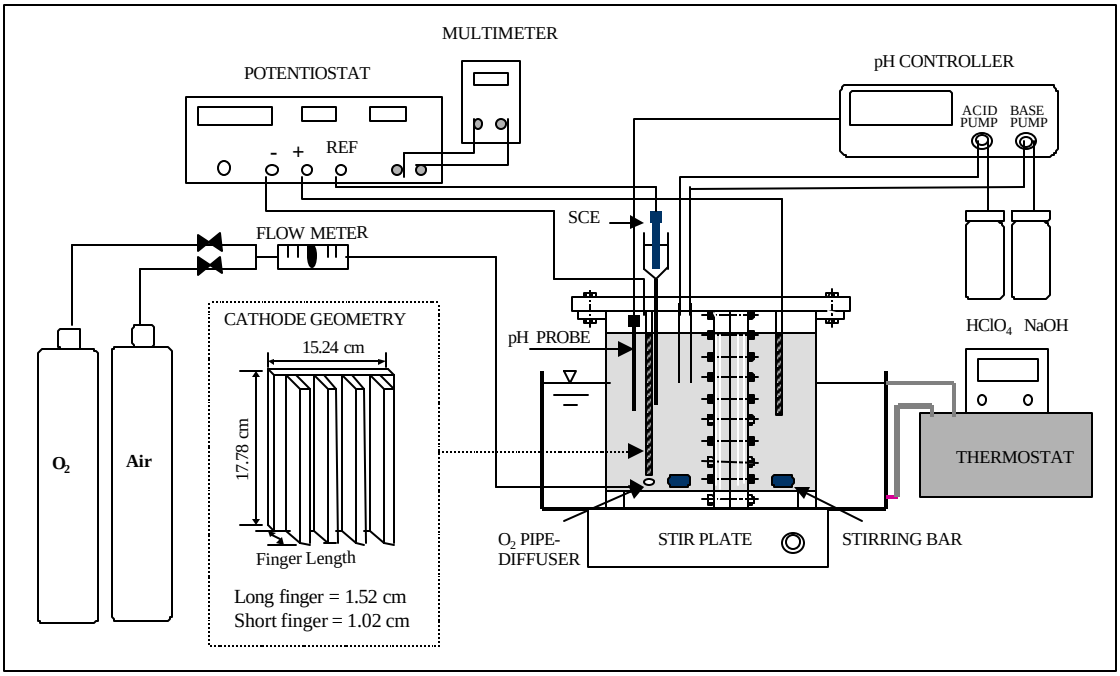

Figure 2.2. Schematic diagram of reaction system.

Both cathode and anode were made of corrosion-resistant graphite (Grade 2020, Carbon of America, Bay City, MI). The properties of this graphite are shown in Table 2.1. Sudoh *et al.* (1985a) reported that graphite was the best cathode material for the electro-generation of H_2O_2 in alkaline solutions, while metal cathodes such as copper, stainless steel, lead and nickel were likely to decompose H_2O_2. Three cathode geometries (Figure 2.2), i.e., plain plate (17.78cm x 15.24cm, or 7in x 6in), plate with protruded short "fingers" (17.78 cm x 15.24 cm x 1.02 cm, or 7 in x 6 in x 0.4 in) and plate with protruded long "fingers" (17.78 cm x 15.24 cm x 1.52 cm, or 7 in x 6 in x 0.6 in) were employed to investigate the effect of cathode surface area. The thickness of the plate and the fingers was 0.25cm (or 0.1 inch). A graphite conductive epoxy glue, EP75 (Master Bond, Inc., Hackensack, NJ), was used to connect the fingers with the plain plate. Unless otherwise stated, all experiments were conducted using the long-finger plate. A graphite plain plate (8.89cm x 15.24cm, or 3.5in x

6in) was used as the anode. Copper wires were connected to both electrodes through Teflon screws. The connections were carefully sealed with silicon to prevent copper electro-corrosion.

Table 2.1. Properties of graphite 2020 (from Manual of Carbon of America Co.)

Properties	Values
Density (g/cm^3)	1.76
Porosity (%)	9
Electric resistance (ohm-m)	$1.78x10^{-5}$
Grain size (μm)	43
Flexural strength (MPa)	38
Thermal conductivity ($W/m-^oC$)	70
Thermal expansion coefficient ($m/^oC$)	$9.1x10^{-8}$

A cation exchange membrane, Neosepta CMX (Electrosynthesis Co., Lancaster, NY), was chosen to separate the cathodic and anodic compartments. Ion exchange membranes are usually made of organic polymers that possess a hydrophobic backbone and a hydrophilic head group---a chemical structure similar to that of surfactant. A cation exchange membrane possesses hydrophilic groups such as sulfonic acids ($-SO_3H$) or carboxylic acids (-COOH). These groups allow cations to freely penetrate by electro-static adsorption and subsequent ion exchange in aqueous solutions, but prohibit the penetration of anions. An anion exchange membrane possesses hydrophilic groups such as ammonium hydroxides ($-NR_3OH$) which function oppositely. Figure 2.3 depicts the phase separation of a cation exchange membrane swollen by water (from Wendt and Kreysa, 1999). The organic polymers of this membrane have a perflourinated backbone and a sulfonic head. The perfluorinated backbone assures the mechanical strength while the sulfonic group allows the transport of cations. In general, both cations and anions are solvated with a certain number of water molecules. The solvated water moves together with the ions and thus changes the volume of the catholyte or the anolyte. However, in a solution only containing dilute supporting electrolyte the effect of water migration can be neglected. An ideal ion exchange membrane should have such properties as high permselectivity, large exchange capacity, high resistance to chemically

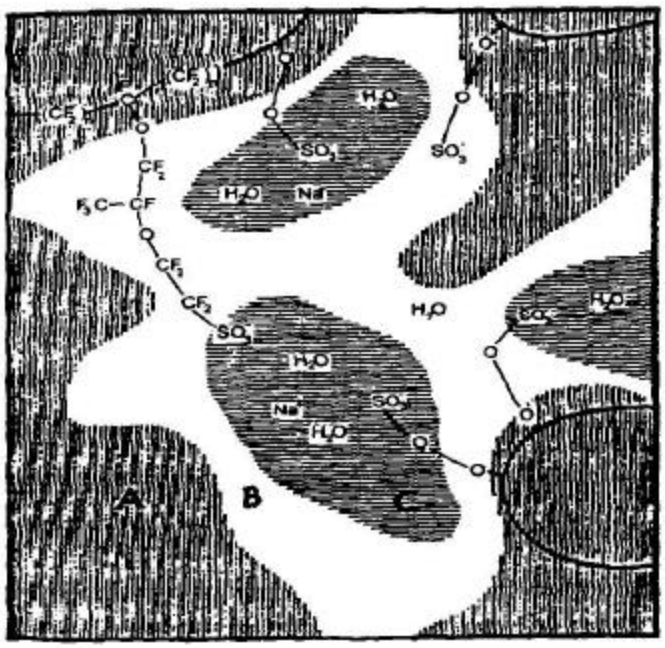

Figure 2.3. Schematic diagram of phase separation of a cation exchange membrane swollen by water: A. hydrophobic area; B. solvated sulfonic acid groups; C. aqueous phase (from Wendt and Kreysa, 1999).

aggressive environments, high physical and mechanical strength and low electric resistance. The properties of the selected Neosepta CMX membrane are listed in Table 2.2. This Na-form membrane is strongly acidic, cation permeable and mechanically reinforced. The transport numbers of total cations and anions are approximately 0.98 and 0.02, respectively, which shows an excellent permselectivity. In experiments, the CMX membrane prohibits the penetration of anions (ClO_4^-) and H_2O_2 molecules, but allows cations (Na^+ and H^+) to freely penetrate. Therefore, H_2O_2 generated at the cathode will be confined in the catholyte, avoiding its decomposition at the anode. Moreover, protons generated at the anode will be electrically driven into the catholyte, partially supplementing the protons consumed at the cathode.

Table 2.2. Properties of NEOSEPTA CMX membrane (from Manual of Ion Exchange Membranes of Electrosynthesis Co.).

Properties	CMX
Type	Strongly acidic, cation permeable, high mechanical strength, Na-form
Electric resistance (ohm-cm^2)	2.5-3.5
Transport number	-
Total cations or anions	< 0.98
$Na^+ + K^+$	0.70
$Ca^{2+} + Mg^{2+}$	0.28
$Cl^- + SO_4^{2-}$	> 0.02
Water content (g H_2O/g dry mem)	25-30
Exchange capacity (meq/g dry mem)	1.5-1.8
Thickness (mm)	0.17-0.19
Reinforcing	yes

Measurement basis:
Electric resistance: Equilibrated with 0.5N NaCl solution at 25 ^oC;
Transport number: Measured by electrophoresis with salt water at 25 ^oC;
Water content: Equilibrated with 0.5N NaCl solution.

Compressed gas (pure oxygen or air) was used as the sources of dissolved oxygen. The gas was sparged into the catholyte through a porous pipe-diffuser which was placed right under the cathode (Figure 2.2). The catholyte was pre-saturated with oxygen by sparging pure oxygen gas or air for 15 minutes. The pH of catholyte was controlled by a pH-stat (Model pH-40, New Brunswick Scientific Co., Edison, NJ), $HClO_4$ (1.0 M) and NaOH (1.0 M) solutions. A high performance combination pH probe (Cat. No. 376490, Corning Inc., Corning, NY) was placed behind the cathode to avoid the interference from the electrical field. The solution temperature was controlled by a thermostat (Model EX-200, Brookfield Engineering Laboratories, Inc., Stoughton, MA) and a water bath.

2.3.2. Electrolysis Control Modes

The electro-generation of H_2O_2 experiments were carried out under either constant potentia1 or constant current mode. Usually, constant potential mode is used to derive

fundamental electrochemical information in laboratory scale experiments, while constant current mode is commonly used in industrial electrolysis because it is technically much easier to control the current than the potential (Wendt and Kreysa, 1999). In general, electrochemical study is first carried out using the constant potential mode because most electrode redox reactions occur in a narrow potential range of –1.5 to +1.5V. On the contrary, the electrical current depends largely on reagent concentration, electrode surface area and solution temperature. It may vary from milli-amperes to hecto-amperes. Therefore, the constant current mode is usually employed after obtaining an approximate value of the current density using the constant potential mode.

Polarization curves were obtained by cyclic voltammetry using a three-electrode bi-potentiostat (Model AFRDE4, Pine Instrument Co., Grove City, PA). A saturated calomel electrode (SCE) was used as the reference electrode. The SCE was inserted into a Luggin capillary filled with saturated KCl solution. The schematic diagram of the lab-made Luggin capillary electrode is presented in Figure 2.4. A porous glass tip (3.2 mm x 3 mm, 50Å pores) purchased from Bioanalytical Systems Inc. (West Lafayette, IN) was connected to the end of a glass pipette through a heat shrinkable Teflon tube. By placing the tip of the Luggin capillary in contact with the cathode surface, the cathodic potential can be accurately controlled against the SCE. The cathodic potential of the parallel-plate electrolyzer was swept from 0 to –0.8V (vs. SCE) at a linear rate of 33.3 mV/s. Transient current response was recorded by a Hewlett Packard X-Y recorder (Model 7001A, Moseley Division, Pasadena, CA).

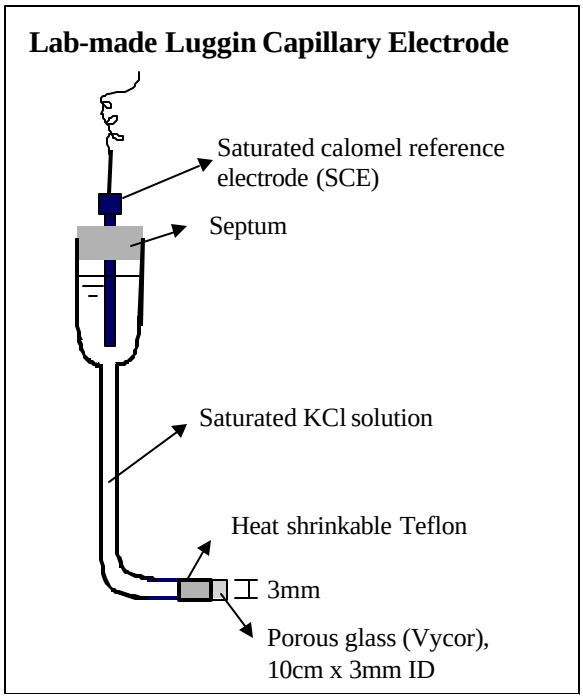

Figure 2.4. Schematic diagram of the lab-made Luggin capillary electrode.

In this study, the factors significantly affecting the limiting current of H_2O_2 generation, including cathodic potential, oxygen purity and mass flow rate, and cathode surface area, were investigated using the constant potential mode. Under this mode, the electrical current was monitored on-line by a digital multimeter (Model 22-183A, Tanday Co., Fort Worth, Texas). The effect of pH was studied using both constant potential and constant current modes. The effects of temperature and inert supporting electrolyte concentration were investigated by the constant current mode. A regulated DC power supply (Model WP-705B, Vector-Vid Inc., Horsham, PA) was employed to provide constant current.

2.3.3. Chemical Analysis

The concentration of H_2O_2 was determined by the titanic sulfate [$Ti(SO_4)_2$] method (Sudoh *et al.*, 1985a). A diode array spectrophotometer (Model 8452A, Hewlett Packard) was used to measure the light absorbance of the Ti^{4+}-H_2O_2 orange complex at 410 nm. The concentration of DO was determined using an oxygen electrode (Model 97-08-99, Orion Research, Inc., Beverly, MA). A pH meter was used to record the DO concentration in the

range of 0~14 mg/L. When the concentration exceeded the upper response limit, dilution was made with deoxygenated distilled water.

2.4. RESULTS AND DISCUSSION

2.4.1. Stability of Hydrogen Peroxide

In a thoroughly clean container without the presence of any catalysts, H_2O_2 is very stable at any concentration. However, the presence of a trace amount of metal ions in the solution or on the container surface will lead to the decomposition of H_2O_2. In practice, stabilizing agents such as sodium stannate, 8-hydroxyquinoline and sodium pyrophosphate are commonly used to stabilize H_2O_2 for long-term storage (Schumb *et al.*, 1955). The self-decomposition rate of H_2O_2 is primarily influenced by pH and temperature. Sudoh *et al.* (1985a) attributed the low current efficiency (6.88%) of H_2O_2 generation in alkaline solutions at 30°C to a high self-decomposition rate of H_2O_2. Solution pH influences the chemical speciation of both H_2O_2 and trace metals. The trace metals that can catalytically initiate the self-decomposition of H_2O_2 may be introduced from acid and base used for pH adjustment, from container surfaces, and even from distilled water. At low pH, H_2O_2 and free metal ions predominate. At high pH, HO_2^- and metal-hydroxo complexes are the major species. Therefore, it is necessary to investigate the effects of pH and temperature on the self-decomposition of H_2O_2.

The H_2O_2 solution with an initial concentration of 150 mg/L was prepared by diluting a commercial grade H_2O_2 solution (31.5% by weight) with distilled water. A series of plastic bottles (250mL) were washed with 1M $HClO_4$ solution, and then filled with the H_2O_2 solution. The pH was adjusted by reagent grade $HClO_4$ or NaOH to cover the range of 1 to 13. The effect of temperature was investigated at 10, 23 and 50 °C. At selected time intervals, the concentration of H_2O_2 was determined. Figure 2.5 shows the self-decomposition of H_2O_2 at various pH values, temperatures and reaction times. Results indicate that H_2O_2 is relatively stable at pH < 9. However, above pH 9, H_2O_2 decomposes markedly with increasing pH, temperature and reaction time. There is complete H_2O_2 decomposition at pH 13 and temperature 50°C after 96 hours. According to Schumb *et al.* (1955), even with the puriest H_2O_2 and at elevated temperatures, the decomposition of H_2O_2 in the liquid phase is not a homogeneous autodecomposition process of the H_2O_2 itself. Generally, increasing temperature increases the reaction rate. The self-decomposition of H_2O_2 at high pH and elevated temperatures are attributed in part to the catalytic effect of

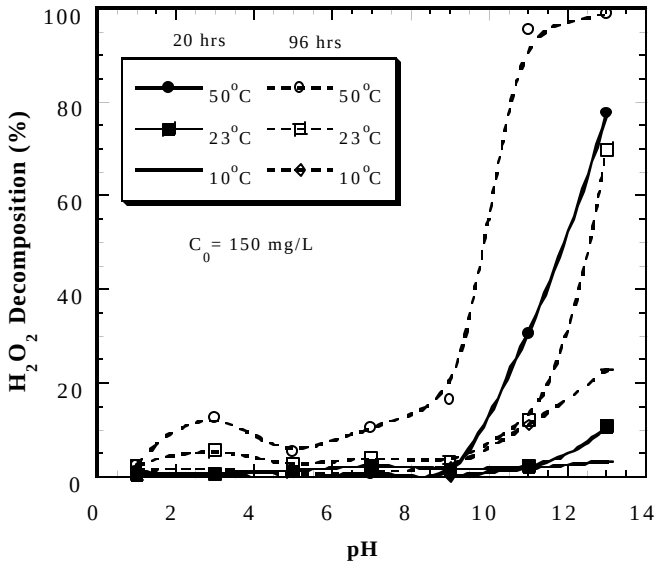

Figure 2.5. Stability of hydrogen peroxide.

the container walls and the reagent impurities. Another aspect is the anion, HO_2^-. The role of HO_2^- in the base catalyzed H_2O_2 decomposition was suggested by Abel (1952) following the reaction:

$$H_2O_2 + HO_2^- \rightarrow H_2O + O_2 + OH^- \qquad (1)$$

However, a low temperature (e.g., 10 ^oC) suppresses H_2O_2 self-decomposition, even at high pH. It is also noted that in the acidic region, the highest self-decomposition rate appears at pH 3. It is known that pH 3 is the optimal value for the Fenton's reagent. The possible presence of trace metals in the solution or on the bottle surfaces may catalytically stress the decomposition of H_2O_2 at pH 3.

It is noted that the electrolysis was conducted in acidic conditions, i.e., pH $\leq$ 4.0, and the electrolysis time was 2 hr. Therefore, based on the results shown in Figure 2, it is clear that the self-decomposition of H_2O_2 would be insignificant.

2.4.2. Optimal Cathodic Potential

Polarization curves reflect transient current response with respect to cathodic potential (E_c) applied. Results in Figure 2.6 indicate that at $-E_c$ < 0.15V, the current density (i) increases rapidly with increasing $-E_c$. However, a "plateau" appears in the range of 0.15 to 0.5V. This "plateau" represents the limiting current region for the electro-generation of H_2O_2 (Reaction 2.1). When the $-E_c$ continues to increase above 0.5V, the i quickly rises again. It implies a significant reduction of H_2O_2 to H_2O (Reaction 2.2) and an enhanced H_2 evolution (Reaction 2.3). Pure oxygen gas provides a higher DO concentration than air, thereby yielding a higher i. Figure 2.6 also shows that the initial equilibrium potential, E_0, is –0.075V at i = 0. If a constant potential of -0.5V is applied, the initial overpotential is calculated as –0.425V. As electrolysis proceeds, the overpotential becomes more negative since the E_0 continuously increases with increasing H_2O_2 concentration. Figure 2.6 shows that the maximum limiting current is approximately located in the range of 0.4~0.5V of $-E_c$.

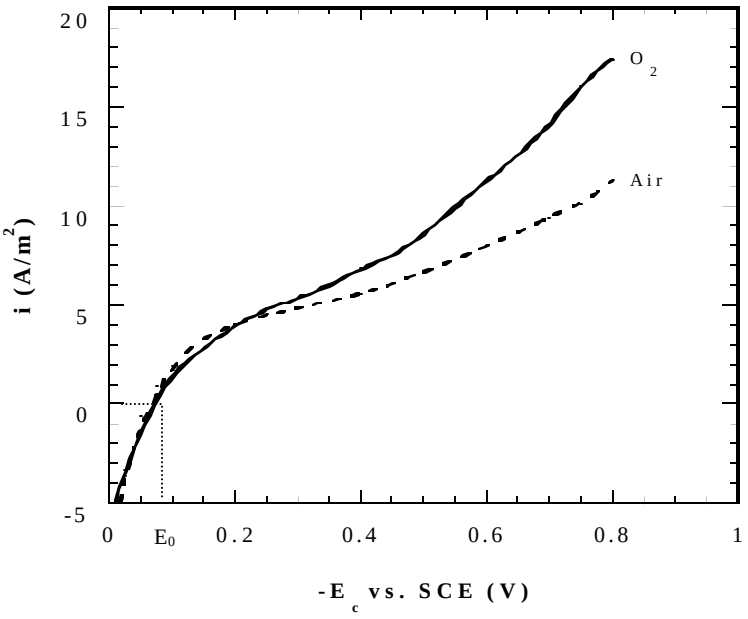

Figure 2.6. Polarization curves of pure oxygen and air sparging. Experimental conditions: completely mixing, sweeping rate = 33.3 mV/s, pH = 2, T = 23 ^oC, Q_{O2} = 8.2x10^{-2} mol/min, Q_{air} = 8.2x10^{-2} mol/min, ionic strength = 0.05M $NaClO_4$, long-finger plate cathode.

The effect of cathodic potential was investigated from 0.2 to 0.9V ($-E_c$). Figures 2.7, 2.8 and 2.9 show the time-dependent changes of H_2O_2 concentration, current density and current

efficiency at various applied potentials, respectively. Results indicate that at $0.2 \leq -E_c \leq 0.5V$, the H_2O_2 concentration increases linearly with reaction time (Figure 2.7). The slope represents a constant net generation rate of H_2O_2 (γ_n) throughout the whole electrolysis course. Correspondingly, Figure 2.8 shows that i stabilizes quickly after the electrolysis is initiated. A steady-state condition is rapidly reached because a constant DO concentration is maintained in the solution. Figure 2.9 indicates a slight decrease of η during electrolysis because the reduction of H_2O_2 to H_2O is gradually promoted by the accumulation of H_2O_2. Results further indicate that at $-E_c > 0.5V$, both γ_n and η decrease notably with reaction time (Figures 2.7 and 2.9). It implies that a high $-E_c$ stresses the reduction of H_2O_2 as well as the evolution of H_2. Figure 2.8 shows that at 0.6V, the i exhibits a slight increase with reaction time. Meanwhile, a remarkable increase of i is observed at 0.8 and 0.9V. Though more electricity is consumed at high $-E_c$, a higher fraction of which is wasted by side reactions. The maximum H_2O_2 concentration is obtained at 0.6V, i.e., 79 mg/L after electrolysis for 2 hours. However, based on η, a constant potential of -0.5V (vs. SCE) is the optimal cathodic potential.

It is noted that there exists a high initial i at all applied potentials (Fiugre 2.8). This is caused by the pre-saturated DO concentration on the cathode surface. Once the surface DO concentration approaches zero and the mass transfer of oxygen through the cathode-solution diffusion layer starts to control the generation of H_2O_2, the i stabilizes rapidly. The study of current density reveals that the mass transfer of protons through the diffusion layer may also become a limiting step at high $-E_c$. For example, at $-E_c = 0.9V$ (vs. SCE) and t = 20 min, the current density and current efficiency for H_2O_2 generation are 15.4 A/m^2 and 48%, respectively (Figures 2.8 and 2.9). Assuming that during the early stage of electrolysis the decomposition of H_2O_2 is insignificant due to its low concentration, the current densities used for H_2O_2 generation and H_2 evolution are 7.4 A/m^2 and 8 A/m^2, respectively. At t = 120 minutes, the net generation rate of H_2O_2 is zero, which means that the formation rate of H_2O_2 equals its decomposition rate. So the current density for the H_2O_2 part is doubled (now it is a 4-electron reaction compared to the previous 2-electron reaction), i.e., 14.8 A/m^2. Adding current density for the part of H_2 evolution, i.e., 8 A/m^2, the total current density is 22.8 A/m^2. Figure 2.7b shows that the correspondingly measured current density is 19.5 A/m^2, which is 3.3 A/m^2 less than the theoretical maximum. Since at t = 120 min, the rapid reduction of H_2O_2 to H_2O consumes two additional protons (Reaction 2.2), the mass transfer limitation of protons may suppress both H_2O_2 generation and H_2 evolution. This suppression results in the decrease of current density, i.e., by 3.3 A/m^2.

Figure 2.10 shows the plot of the average i and average η vs. $-E_c$. It is clear that the optimal cathodic potential is –0.5V vs. SCE, and the corresponding i and η are 6.4 A/m^2 and 81%, respectively. The i obtained at the optimal potential, i.e., 6.4 A/m^2, is called "the limiting current density".

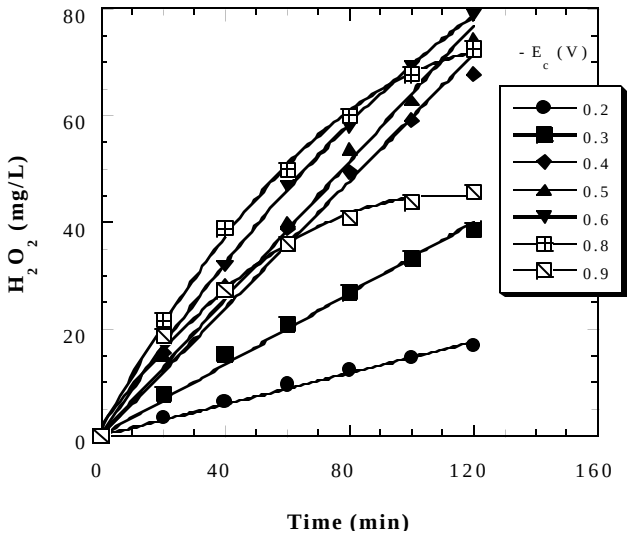

Figure 2.7. Generation of H_2O_2 at various applied cathodic potentials: accumulated concentration. Experimental conditions: pH = 2, T = 23 ^oC, Q_{O2} = $8.2x10^{-2}$ mol/min, ionic strength = 0.05M $NaClO_4$, long-finger plate cathode.

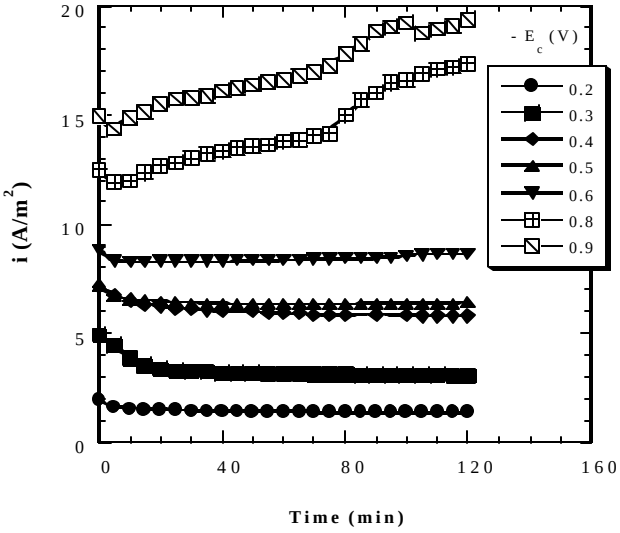

Figure 2.8. Generation of H_2O_2 at various applied cathodic potentials: current density. Experimental conditions: pH = 2, T = 23 ^oC, Q_{O2} = $8.2x10^{-2}$ mol/min, ionic strength = 0.05M $NaClO_4$, long-finger plate cathode.

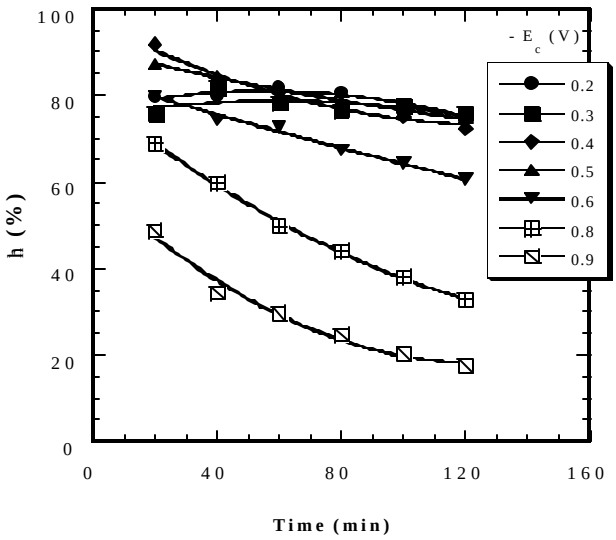

Figure 2.9. Generation of H_2O_2 at various applied cathodic potentials: current efficiency. Experimental conditions: pH = 2, T = 23 ^oC, Q_{O2} = $8.2x10^{-2}$ mol/min, ionic strength = 0.05M $NaClO_4$, long-finger plate cathode.

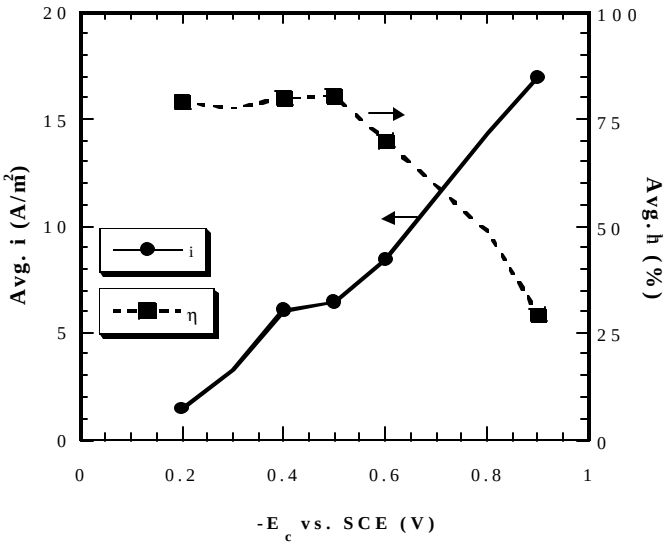

Figure 2.10. Generation of H_2O_2 at various applied cathodic potentials: average current density and average current efficiency. Experimental conditions: pH = 2, T = 23 ^oC, Q_{O2} = $8.2x10^{-2}$ mol/min, ionic strength = 0.05M $NaClO_4$, long-finger plate cathode.

2.4.3. Effect of Oxygen Quality and Mass Flow Rate

Pure oxygen gas (99.6 %) and air were used as the sources of DO. Both oxygen purity and mass flow rate affect the limiting current of H_2O_2 generation. The equilibrium DO concentration is proportional to the partial pressure of oxygen in the supply gas. For example, the equilibrium DO concentrations were measured as 8.3 mg/L and 39.3 mg/L when sparging air and pure oxygen at pH 2 and 0.05M $NaClO_4$, respectively (Figure 2.11). Figures 2.12, 13, 14 show the time-dependent changes of H_2O_2 concentration, average current density and average current efficiency at various oxygen purities and mass flow rates under the constant potential mode. Results in Figure 2.12 indicate that γ_n increases with increasing oxygen mass flow rate until a rate of $8.2x10^{-2}$ mol/min is achieved. Further increasing the flow rate does not change γ_n. Moreover, the γ_n is much smaller when air is applied. The variation of i in Figure 2.13 shows a good agreement with that of γ_n in Figure 2.12. Figure 2.14 indicates that the η slightly decreases as the electrolysis proceeds due to the accumulation of H_2O_2. The effect of oxygen mass flow rate on the average i and average η is shown in Figure 2.15. In accordance with Figures 2.12 and 13, the average i reaches the maximum value of 6.4 A/m^2 at the flow rate of $8.2x10^{-2}$ mol/min. Doubling oxygen flow rate will not increase the i any more. It is clearly seen that a rate of $8.2x10^{-2}$ mol/min is adequate to maintain the highest steady-state DO concentration during electrolysis. Since the optimal potential was applied ($-E_c$ = 0.5V vs. SCE), a high average η could be achieved for all flow rates, i.e., 80~90%. Figure 2.16 shows the effect of air mass flow rate on the average i and average η. Results indicate that the maximum i is achieved at the flow rate of $8.2x10^{-2}$ mol air/min (or $1.7x10^{-2}$ mol O_2/min). At this flow rate, the average i decreases to 2.1 A/m^2, while the average η slightly increases to 90% (Figure 2.16). Sparging air yields a higher η than sparging oxygen. It is mainly due to the low i in the air mode that brings down the reduction of H_2O_2 to H_2O.

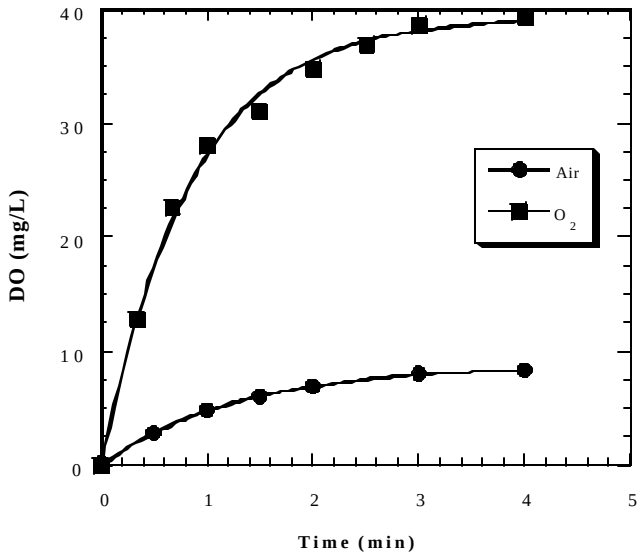

Figure 2.11. Aeration of reaction solution by pure oxygen and air. Experimental conditions: pH = 2, T = 23 °C, ionic strength = 0.05M $NaClO_4$.

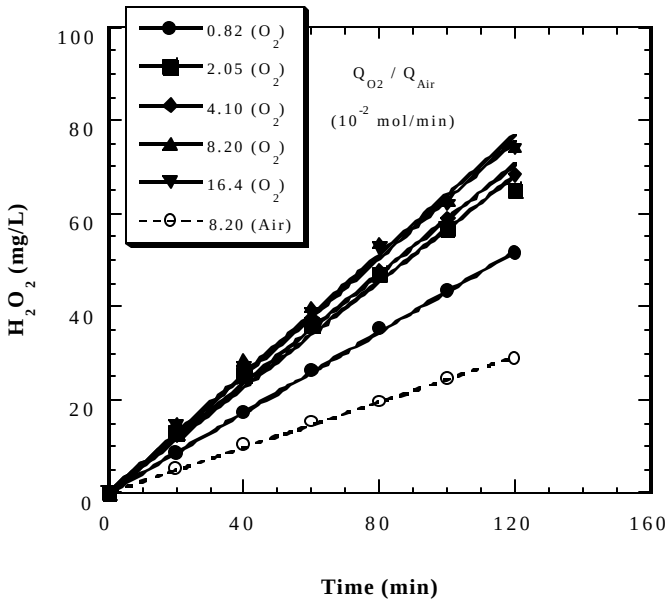

Figure 2.12. Generation of H_2O_2 at various oxygen purities and mass flow rates: accumulated concentration. Experimental conditions: $-E_c$ = 0.5V vs. SCE, pH = 2, T = 23 °C, ionic strength = 0.05M $NaClO_4$, long-finger plate cathode.

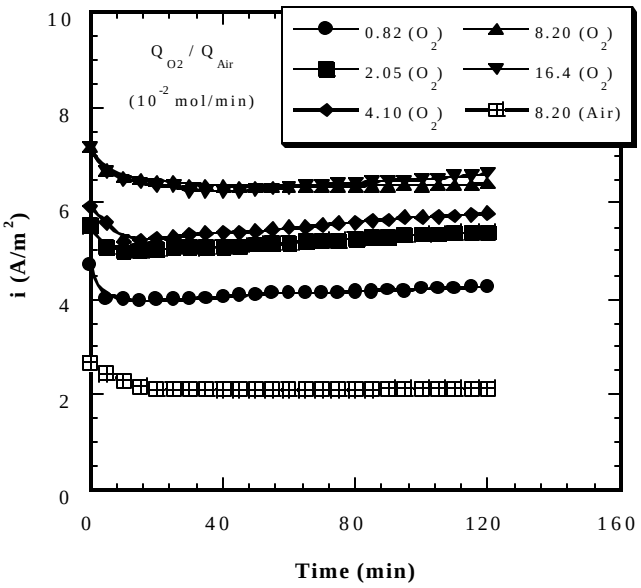

Figure 2.13. Generation of H_2O_2 at various oxygen purities and mass flow rates: current density. Experimental conditions: $-E_c$ = 0.5V vs. SCE, pH = 2, T = 23 °C, ionic strength = 0.05M $NaClO_4$, long-finger plate cathode.

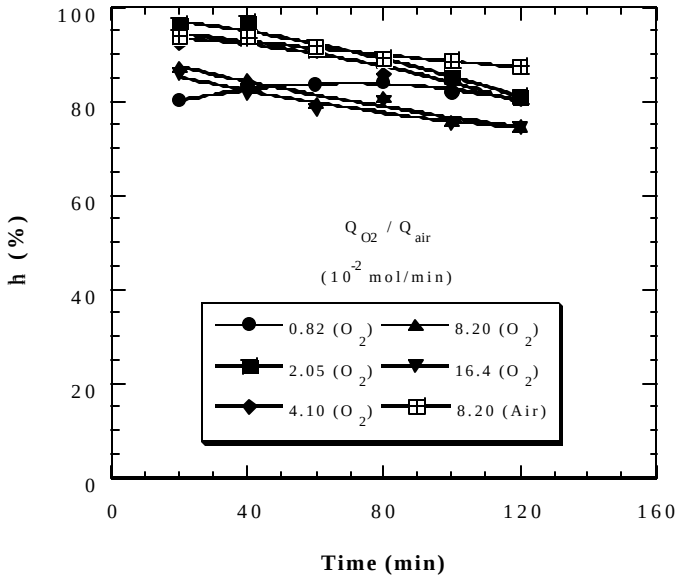

Figure 2.14. Generation of H_2O_2 at various oxygen purities and mass flow rates: current efficiency. Experimental conditions: $-E_c$ = 0.5V vs. SCE, pH = 2, T = 23 °C, ionic strength = 0.05M $NaClO_4$, long-finger plate cathode.

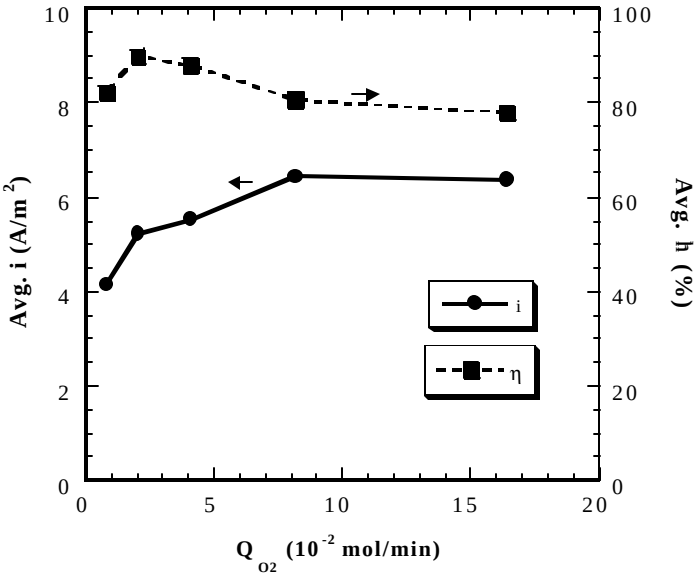

Figure 2.15. Generation of H_2O_2 at various oxygen purities and mass flow rates: average current density and average current efficiency vs. oxygen mass flow rate. Experimental conditions: $-E_c$ = 0.5V vs. SCE, pH = 2, T = 23 °C, ionic strength = 0.05M $NaClO_4$, long-finger plate cathode.

2.4.4. Effect of Cathode Surface Area

Three graphite electrode configurations, i.e., plain plate, short-finger plate and long-finger plate were used to investigate the effect of cathode geometry and surface area. It should be pointed out that H_2O_2 was only generated at one side of the cathode that faces the applied electrical field. The effective surface areas were 271, 415 and 488 cm^2 for the plain plate, short-finger plate and long-finger plate, respectively. The potential was controlled at -0.5V vs. SCE, and the oxygen mass flow rate was $8.2x10^{-2}$ mol/min. The electrical current was measured after the electrolysis reached the steady-state condition (ca. 20 min). Figure 2.17 shows that a linear relationship is achieved between the limiting current and the effective surface area. The slope of 6.4 A/m^2 is just the limiting current density. Results clearly indicate that the limiting current density is independent of the cathode geometry and surface area applied. It is obvious that increasing the surface area is a convenient way to raise the limiting current, and consequently, the net generation rate of H_2O_2. The mass transfer coefficient, k_m, is calculated as $2.70x10^{-5}$ m/s using Equation 2.10 and taking C* as 39.3 mg/L. Moreover, by assuming the oxygen diffusion coefficient (D) as $2.0x10^{-9}$ m^2/s (Kinoshita, 1992), the thickness of the diffusion layer (δ) is calculated as about 74 μm using Equation 2.9. Both k_m and δ provide a detailed microscopic insight into the electrolytic synthesis of H_2O_2.

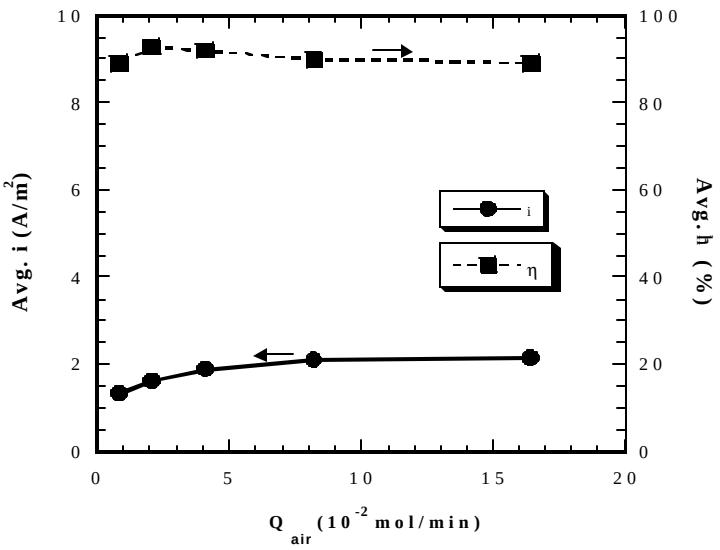

Figure 2.16. Generation of H_2O_2 at various oxygen purities and mass flow rates: average current density and average current efficiency vs. air mass flow rate. Experimental conditions: $-E_c$ = 0.5V vs. SCE, pH = 2, T = 23 °C, ionic strength = 0.05M $NaClO_4$, long-finger plate cathode.

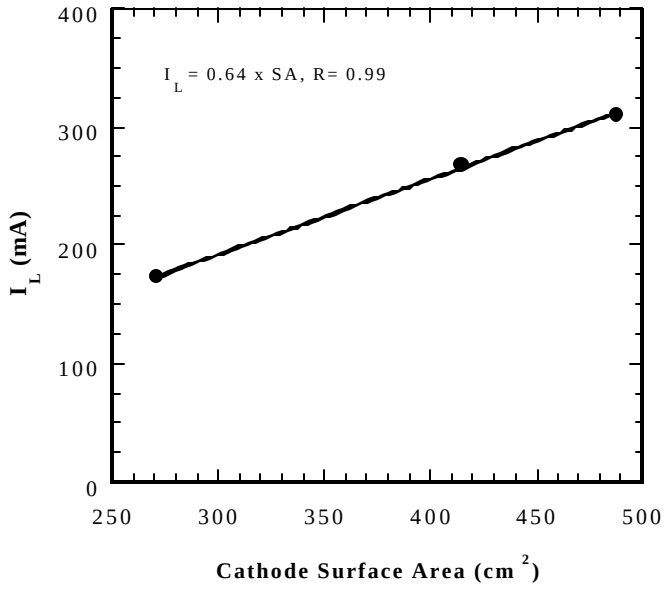

Figure 2.17. Effect of cathode surface area on limiting current. Experimental conditions: $-E_c$ = 0.5V vs. SCE, pH = 2, T = 23 °C, Q_{O2} = $8.2x10^{-2}$ mol/min, ionic strength = 0.05M $NaClO_4$.

2.4.5. Effect of pH

From Equation 2.2, it seems that a low pH is favorable for the electro-generation of H_2O_2 in acidic solutions since its synthesis consumes protons. However, a high proton concentration may promote H_2 evolution and reduce the current efficiency. Figure 2.18 shows the effect of pH on γ_n and average η in the constant current mode (i = 6.4 A/m^2). Results indicate that pH 2 is the optimal condition. Above pH 2, γ_n decreases due to insufficient protons. Below pH 2, γ_n decreases again due to enhanced H_2 evolution. Because pH 3 may stress the decomposition of H_2O_2 by trace metals as previously mentioned, the γ_n at pH 3 is a little smaller than at other pH values. Since the current was holding constant, the average η curve exhibits a similar trend as the γ_n curve. The highest η is 84% at pH 2, and the lowest is 69% at pH 3.

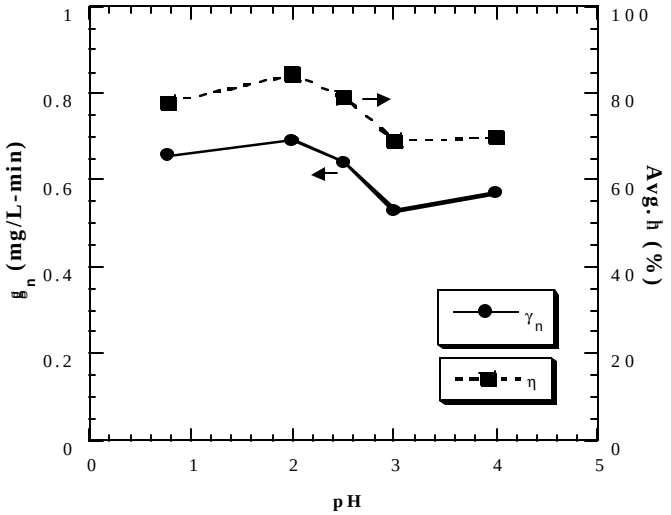

Figure 2.18. Generation of H_2O_2 as a function of pH: net generation rate and average current efficiency in acidic region under constant current mode. Experimental conditions: i = 6.4 A/m^2, T = 23 ^oC, Q_{O2} = $8.2x10^{-2}$ mol/min, ionic strength = 0.05M $NaClO_4$, long-finger plate cathode.

The effect of pH was also investigated using the constant potential mode at $-E_c$ = 0.5V vs. SCE. Results in Figure 2.19 indicate that the γ_n increases with decreasing pH. The γ_n reaches the maximum at pH 1, i.e., 0.72 mg/L-min vs. 0.64 mg/L-min at pH 2. However, the value of η at pH 2 (81%) is slightly higher than that at pH 1 (79%). Furthermore, pH 1 requires a considerable amount of acid for pH adjustment. Therefore, it is concluded that pH 2 is the optimal value for H_2O_2 generation in acidic solutions.

For the purpose of comparison, the electro-generation of H_2O_2 was investigated in alkaline region from pH 10 to 13 using the constant current mode (i = 6.4 A/m^2). Figure 2.20 shows the plot of γ_n and average η vs. pH. Results indicate that both γ_n and η increase with increasing pH. The γ_n increases from 0.69 mg/L-min at pH 10 to 0.82 mg/L-min at pH 13, and the η increases from 87% to 100% correspondingly. It demonstrates that H_2O_2 is generated more efficiently in alkaline solutions than in acidic solutions. Alkaline condition minimizes the reduction of HO_2^- to OH^- and prevents the evolution of H_2 as well.

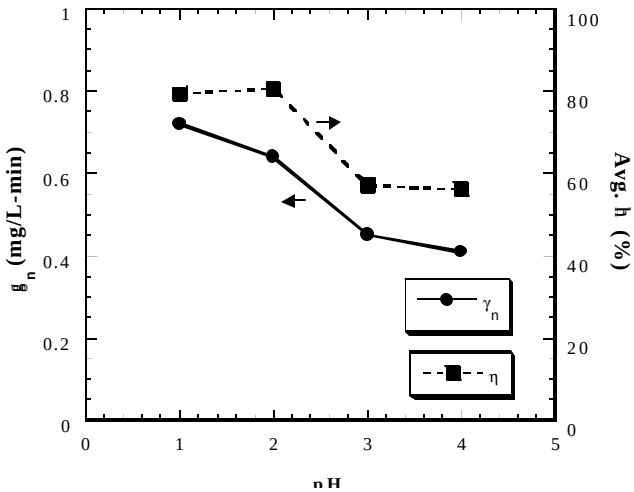

Figure 2.19. Generation of H_2O_2 as a function of pH: average current density and average current efficiency in acidic region under constant potential mode. Experimental conditions: $-E_c$ = 0.5V vs. SCE, T = 23 °C, Q_{O2} = $8.2x10^{-2}$ mol/min, ionic strength = 0.05M $NaClO_4$, long-finger plate cathode.

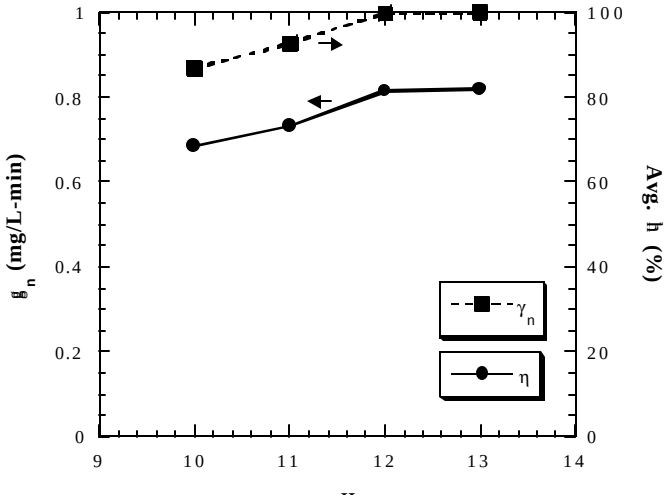

Figure 2.20. Generation of H_2O_2 as a function of pH: net generation rate and average current efficiency in alkaline region under constant current mode. Experimental conditions: i = 6.4 A/m^2, T = 23 °C, Q_{O2} = $8.2x10^{-2}$ mol/min, ionic strength = 0.05M $NaClO_4$, long-finger plate cathode.

2.4.6. Effect of Solution Temperature

Temperature exerts conflicting effects on H_2O_2 generation. As temperature rises, the oxygen diffusion coefficient will increase, resulting in an increase of γ_n. However, increasing temperature will decrease the DO solubility and increase the H_2O_2 decomposition rate, thereby decreasing γ_n. If the current is held constant, the formation rate of H_2O_2 will not change appreciably, but the decomposition rate of H_2O_2 will increase as temperature rises. The effect of temperature was investigated from 13 to 33°C using the constant current mode (i = 6.4 A/m^2). Figure 2.21 demonstrates that γ_n slightly decreases with increasing temperature. The average η shows a similar trend, decreasing from 92% at 13 °C to 81% at 33 °C. It is seen that the H_2O_2 generation is favored at low temperatures.

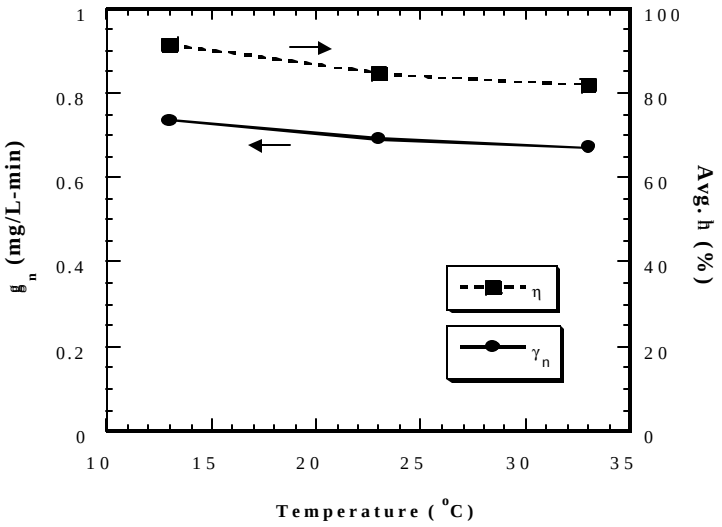

Figure 2.21. Effect of temperature on net generation rate and average current efficiency. Experimental conditions: i = 6.4 A/m^2, pH = 2, Q_{O2} = $8.2x10^{-2}$ mol/min, ionic strength = 0.05M $NaClO_4$, long-finger plate cathode.

2.4.7. Effect of Inert Supporting Electrolyte Concentration

The effect of inert supporting electrolyte concentration was investigated using the constant current mode. Figure 2.22 shows that in the region of $NaClO_4$ concentration less than 0.1M, the total potential drop between cathode and anode (ΔE) decreases notably with increasing $NaClO_4$ concentration. In the >0.1M region, the ΔE drops slowly because the decrease of ion activity coefficients slows down the increase of solution conductance. Since $NaClO_4$ does not participate in electrochemical reactions, the γ_n remains almost constant in the concentration range studied. Do and Chen (1993) investigated the oxidative degradation of formaldehyde with electro-generated H_2O_2 and reported that the formaldehyde degradation was not affected by the concentration of supporting electrolyte, Na_2SO_4, in the range of 0 to 0.5M. The results indicate that the background ionic strength in wastewater may be directly used as supporting electrolyte for on-site H_2O_2 generation.

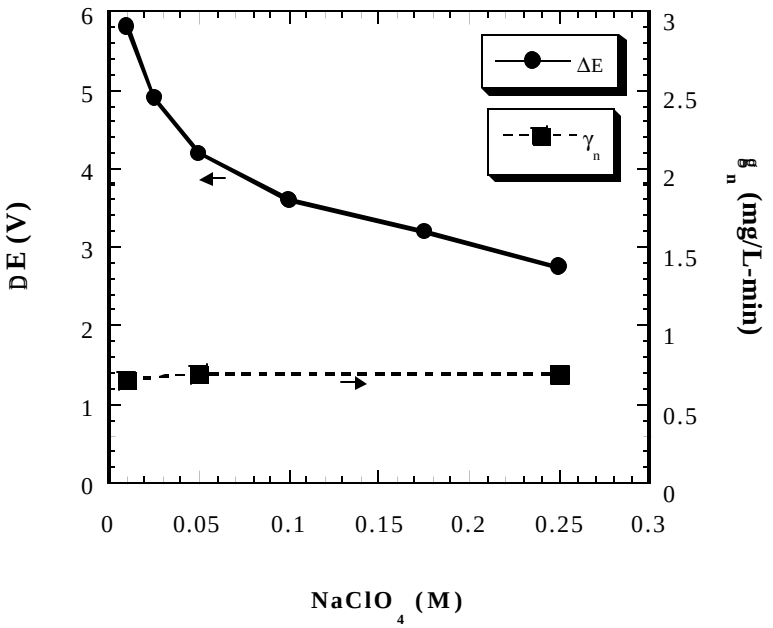

Figure 2.22. Effect of $NaClO_4$ concentration on total potential drop and net generation rate. Experimental conditions: i = 6.4 A/m^2, pH = 2, T = 23 ^{o}C, Q_{O2} = 8.2x10^{-2} mol/min, long-finger plate cathode.

It should be pointed out that chloride or bromide can promote H_2O_2 generation (Gosser and Schwartz, 1989; Berzins and Gosser, 1992). Since the SCE reference was filled with saturated KCl solution, the diffusion of chloride from the SCE into catholyte might enhance H_2O_2 generation and skew the experimental data. Therefore, the experimental results from the constant potential mode ($-E_c$ = 0.5V vs. SCE, with SCE inserted in the catholyte) and from the constant current mode (i = 6.4 A/M^2, without SCE) are compared with other operational conditions identical. During 2 hours of electrolysis, the electricities consumed are very close, i.e., 2257 coulombs for the constant potential mode and 2232 coulombs for the constant current mode. The γ_n and η are 0.64 mg/L-min and 81% (Figures 2.7 and 2.10), and 0.68 mg/L-min and 84% (Figure 2.18), correspondingly. It is seen that the presence of the SCE in the catholyte does not promote H_2O_2 generation. The diffusion of chloride is negligible, mainly due to a large reactor volume and a relatively short electrolysis time.

2.4.7. Potential Profile and Energy Consumption

Figure 2.23 shows the potential profile in the electrolyzer at $-E_c$ = 0.5V vs. SCE. Results indicate that the ΔE is composed of three parts, i.e., the potential drops at the electrode-solution interfaces caused by activation polarization and concentration polarization of DO,

and the IR drop in the electrolyte solution. In the solution, Ohm's law is well obeyed since the electrolyte concentration remains almost constant. The electrical resistance of the cation exchange membrane is negligible, which means a prompt migration of protons from anolyte to catholyte. A constant anolyte pH was observed during the course of electrolysis although protons were being continuously generated at the anode.

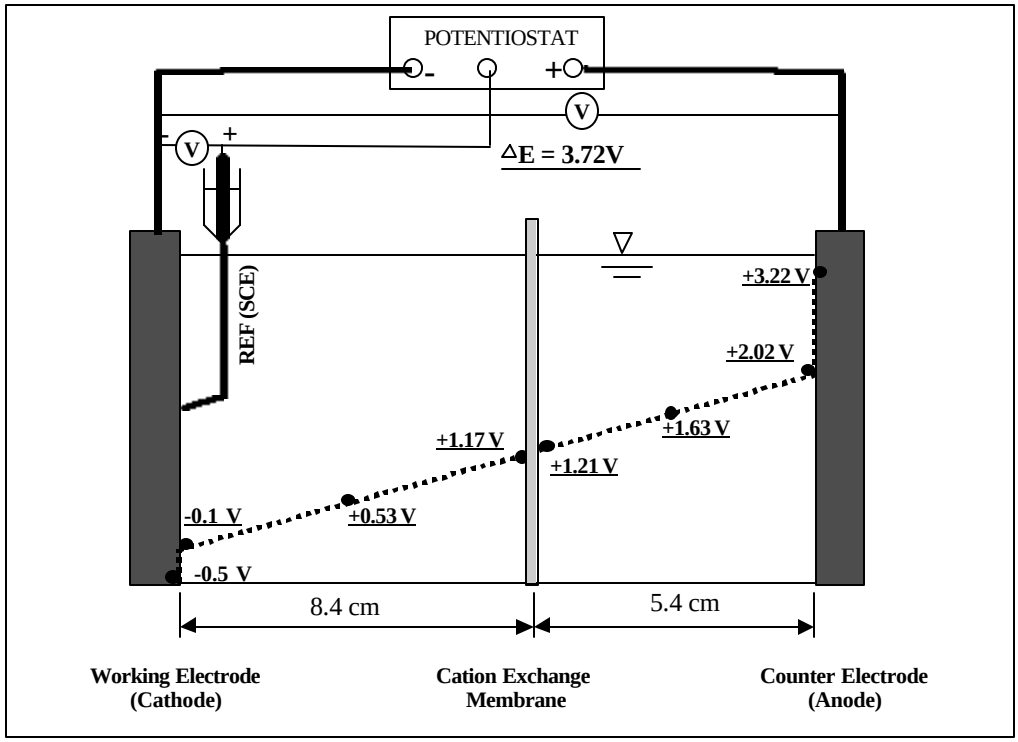

Figure 2.23. Potential profile of electrolyzer under constant potenital mode. Experimental conditions: $-E_c$ = 0.5V vs. SCE, pH = 2, T = 23 ^oC, Q_{O2}= $8.2x10^{-2}$ mol/min, ionic strength = 0.05M $NaClO_4$, long-finger plate cathode, reaction time = 2 hr.

Under the experimental conditions stated in Figure 2.23, the unit energy consumption for H_2O_2 generation is calculated as 7.8 kWh / kg H_2O_2.

2.5. Conclusions

This study is to improve the Faradic current efficiency of H_2O_2 generation in acidic solutions containing dilute supporting electrolyte by optimizing the operational parameters. Based on the experimental results presented above, the following conclusions are drawn:

- Significant self-decomposition of H_2O_2 is observed only at high pH (>9) and elevated temperatures (>23 ^oC).
- The optimal conditions for H_2O_2 generation are cathodic potential of –0.5V (vs. SCE), oxygen mass flow rate of $8.2x10^{-2}$ mol/min, and pH 2. Under the optimal conditions, the average current density and average current efficiency are 6.4 A/m^2 and 81%, respectively.

- The optimal mass flow rate of air is also $8.2x10^{-2}$ mol/min. At the optimal flow rate, the average current density decreases to 2.1 A/m^2, while the average current efficiency slightly increases to 90%.
- The limiting current density, i.e., 6.4 A/m^2, is independent of the cathode geometry and surface area applied.
- H_2O_2 generation is favored at low temperatures.
- In the concentration range studied, the supporting electrolyte affects the total potential drop of the electrolyzer, but does not affect the net generation rate of H_2O_2.

2.6. References

1. Abel E. (1952) Uber die selbstzersetzung von wasserstoffsuperoxyd. *Monatshefte fur Chemie*, **83** (2): 422-439.
2. Aieta E. M., Reagan K. M., Lang J. S., McReynolds L., Kang J. W. and Glaze W. H. (1988) Advanced oxidation processes for treating groundwater contaminated with TCE and PCE: pilot-scale evaluations. *Journal AWWA*, May: 64-72.
3. Bellamy W. D., Hickman G. T., Mueller P. A. and Ziemba N. (1991) Treatment of VOC-contaminted groundwater by hydrogen peroxide and ozone oxidation. *Res. J. Water Pollut. Control Fed.*, **63** (2): 120-128.
4. Berzins T. and Gosser L. W. (1992) *US patent*, US5112702.
5. Brillas E., Mur E. and Casado J. (1996) Iron (II) catalysis of the mineralization of aniline using a carbon-PTFE O_2-Fed cathode. *J. Electrochem. Soc.*, **143** (3): L49-L53.
6. Chu C. H. (1995) *The electrochemical oxidation of recalcitrant organic compounds*. Ph.D. dissertation, University of Delaware, Newark, DE.
7. Do J. S. and Chen C. P. (1993) In situ oxidative degradation of formaldehyde with electrogenerated hydrogen peroxide. *J. Electrochem. Soc.*, **140** (6): 1632-1637.
8. Glaze W. H. and Kang J. W. (1988) Advanced oxidation processes for treating groundwater contaminated with TCE and PCE: laboratory studies. *Journal AWWA*, May: 57-63.
9. Gosser L. W. and Schwartz J. T. (1989) *US Patent*, US4832938.
10. Hsiao Y. L. and Nobe K. (1993a) Oxidative reactions of phenol and chlorobenzene with in situ electrogenerated Fenton's reagent. *Chem. Eng. Comm.*, **126**: 97-110.
11. Hsiao Y. L. and Nobe K. (1993b) Hydroxylation of chlorobezene and phenol in a packed bed flow reactor with electrogenerated Fenton's reagent. *J. Appl. Electrochem.*, **23**: 943-946.
12. Huang Y. H., Chou S., Perng M. G., Huang G. H. and Cheng S. S. (1999) Case study on the bioeffluent of petrochemical wastewater by electro-Fenton method. *Wat. Sci. Tech.*, **39** (10-11): 145-149.
13. Huling S. G., Bledsoe B. E. and White M. V. (1990) Enhanced bioremediation utilizing hydrogen peroxide as a supplemental source of oxygen: a laboratory and field study. *Bioremediation*, EPA/600/S2-90/006.
14. Kalu E. E. and Oloman C. (1990) Simultaneous electrosynthesis of alkaline hydrogen-peroxide and sodium chlorate. *J. Appl. Electrochem.*, **20**: 932-940.
15. Kinoshita K. (1992) *Electrochemical Oxygen Technology*, p.8. John Wiley & Sons, Inc.: Newark, N.Y.

16. Lewis N., Topudurti K., Welshans G. and Foster R. (1990) A field demonstration of the UV/oxidation technology to treat ground water contaminated with VOCs. *J. Air Waste Manage, Assoc.*, **40** (4): 540-547.
17. Li Z. M., Shea P. J. and Comfort S. D. (1997) Fenton oxidation of 2,4,6-trinitrotoluene in contaminated soil slurries. *Environ. Eng. Sci*., **14** (1): 55-66.
18. Matsue T., Fujihira M. and Osa T. (1981) Oxidation of alkylbenzenes by electrogenerated hydroxyl radical. *J. Electrochem. Soc.: Electrochem. Sci. Tech.*, **128** (12): 2565-2569.
19. Oloman C. and Watkinson A. P. (1975) The electroreduction of oxygen to hydrogen peroxide on fluidized cathodes. *Can. J. Chem. Eng*., **53** (3): 268-273.
20. Oloman C. and Watkinson A. P. (1976) The electroreduction of oxygen to hydrogen-peroxide on fixed-bed cathodes. *Can. J. Chem. Eng*., **54** (4): 312-318.
21. Oloman C. (1979) Trickle bed electrochemical reactors. *J. Electrochem. Soc*., **126** (11): 1885-1892.
22. Oloman C. and Watkinson A. P. (1979) Hydrogen-peroxide production in trickle-bed electrochemical reactors. *J. Appl. Electrochem.*, **9** (1): 117-123.
23. Pletcher D. (1999) Electrogenerated hydrogen peroxide-from history to new opportunities. *http://www.electrosynthesis.com, Watts New*, **4** (1): 1-7,
24. Ravikumar J. X. and Gurol M. D. (1994) Chemical oxidation of chlorinated organics by hydrogen peroxide in the presence of sand. *Environ. Sci. Technol.*, **28**: 394-400.
25. Schumb W. C., Satterfield C. N. and Wentworth R. L. (1955) *Hydrogen Peroxide*, p. 392, 515, 535-546. Reinhold Publishing Co.: New York, N.Y.
26. Sudoh M., Kitaguchi H. and Koide K. (1985a) Electrochemical production of hydrogen peroxide by reduction of oxygen. *J. Chem. Eng. Japan*, **18** (5): 409-414.
27. Sudoh M., Kitaguchi H. and Koide K. (1985b) Polarization characteristics of packed bed electrode reactor for electroreduction of oxygen to hydrogen peroxide. *J. Chem. Eng. Japan*, **18** (4): 364-371.
28. Sudoh M., Kodera T., Sakai K., Zhang J. Q. and Koide K. (1986) Oxidative degradation of aqueous phenol effluent with electrogenerated Fenton's Reagent. *J. Chem. Eng. Japan*, **19** (6): 513-518.
29. Sudoh M., Kodera T., Sakai K., Hino H. and Shimamura H. (1988) Oxidative degradation rate of phenol in an undivided bipolar electrolyzer. *J. Chem. Eng. Japan*, **21** (5): 536-538.
30. Tzedakis T., Savall A. and Clifton M. J. (1989) The electrochemical regeneration of Fenton's reagent in the hydroxylation of aromatic substrates: batch and continuous processes. *J. Appl. Electrochem.*, **19**: 911-921.
31. Watts R. J., Kong S., Dippre M. and Barnes W. T. (1994) Oxidation of sorbed hexachlorobenzene in soils using catalyzed hydrogen peroxide. *J. Hazard. Mater.*, **39**: 33-47.
32. Wendt H. and Kreysa G. (1999) *Electrochemical Engineering: Science and Technology in Chemical and Other Industries*, p. 53. Springer-Verlag: Berlin, Germany.
33. Wilson J. T., Armstrong J. M. and Rifai H. S. (1994) A full-scale field demonstration on the use of hydrogen peroxide for in situ bioremediation of an aviation gasoline contaminated aquifer. *Bioremediation: field experiences*, EPA/600/A-94/019/ PB94-146396.
34. Yamada N., Yaguchi T., Otsuka H. and Sudoh M. (1999) Development of Trickle-Bed Electrolyzer for on-site electrochemical production of hydrogen peroxide. *J. Electochem. Soc.*, **146** (7): 2587-2591.

3. ELECTRO-REGENERATION OF FERROUS IONS FOR FENTON'S OXIDATION PROCESSES

3.1. Introduction

Though the Fenton's reagent is effective in decomposing hazardous organic compounds, its practical application is largely limited by the cost and handling of concentrated H_2O_2 as well as the considerable amount of iron sludge generated. Therefore, electrochemical modifications are under development in an attempt to generate H_2O_2 and Fe(II) on site, either separately or concurrently. H_2O_2 can be electro-generated by reduction of dissolved oxygen, and Fe(II) by electro-reduction of Fe(III) or electro-oxidation of a sacrificial Fe anode. Involved electrochemical reactions are shown as follows:

$$O_2 + 2H^+ + 2e \rightarrow H_2O_2 \qquad (3.1)$$

$$Fe^{3+} + e \rightarrow Fe^{2+} \qquad (3.2)$$

$$Fe \rightarrow Fe^{2+} + 2e \qquad (3.3)$$

These electrochemical modifications are termed "electro-Fenton" (EF) processes.

Table 3.1 classifies various Fenton oxidation and related processes, including conventional Fenton (CF), electro-Fenton (EF), UV-assisted Fenton (Photo-CF or Photo-EF), electro-generation of H_2O_2 and electro-regeneration of Fe(II). The illustrative presentation of Fenton oxidation processes is shown in Figure 3.1. Based on different sources of H_2O_2 and Fe(II), the EF process can be further divided into four types: FeRe, FeOx, H_2O_2-FeRe, H_2O_2-FeOx. The feature and application of each process are briefly introduced below.

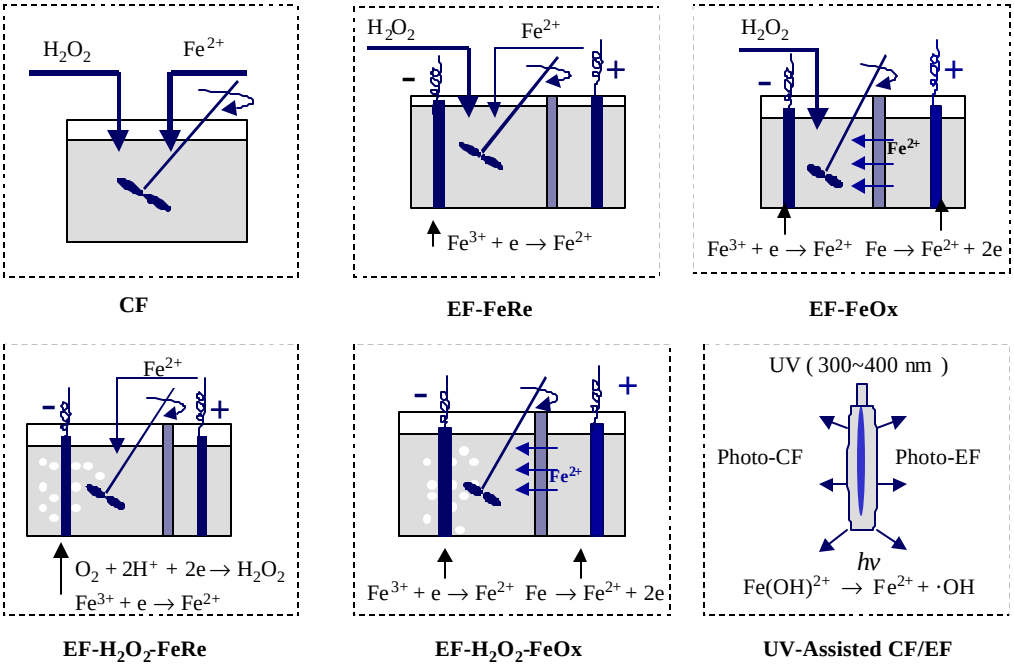

Figure 3.1. Illustrative presentation of various Fenton oxidation processes.

Table 3.1. Classification of Fenton oxidation and related processes.

Type	H_2O_2		Fe^{2+}			References
	EG	ED	EG		ED	
			RC	OA		
CF		✔			✔	Sedlak and Andren, 1991; Kuo, 1992; Mohanty and Wei, 1993; Lou and Lee, 1995; Tang and Huang, 1997; Kim and Huh, 1997; Qiang *et al.*, 2000.
EF-FeRe		✔	✔		✔	Tzedakis *et al.*, 1989; Chou *et al.*, 1999.
EF-FeOx		✔		✔		Pratap and Lemley, 1994; Huang *et al.*, 1999.
EF-H_2O_2-FeRe	✔		✔		✔	Matsue *et al.*, 1981; Sudoh *et al.*, 1986; Tzedakis *et al.*, 1989; Hsiao and Nobe, 1993; Chu, 1995; Brillas *et al.*, 1996, 1997, 1998, 1998; Oturan *et al.*, 1999, 1999.
EF-H_2O_2-FeOx	✔			✔		Brillas *et al.*, 1997, 1998.
Electro-H_2O_2	✔					Oloman and Watkinson, 1975, 1976, 1979; Tzedakis *et al.*, 1989; Sudoh *et al.*, 1985, 1986, 1991; Do and Chen, 1993; Chu, 1995; DeLeon and Pletcher, 1995; Brillas *et al.*, 1996, 1997, 1998, 1998; Yamada *et al.*, 1999; Alvarez-Gallegos and Pletcher, 1999; Qiang *et al.*, 2000.
Electro-Fe^{2+}		✔				Gnann *et al.*, 1993; Chou *et al.*, 1999.
Photo-CF	CF + UV					Pignatello, 1992; Ruppert and Bauer, 1994; Pignatello and Sun, 1995; Huston and Pignatello, 1996; Cermenati *et al.*, 1997; Nadtochenko and Kiwi, 1998.
Photo-EF	EF (any type) + UV					Brillas *et al.*, 1996, 1997, 1998, 1998.

Notation: CF — Conventional Fenton; EF — Electro-Fenton; EG — Electro-generated; ED — Externally dosed; RC — Electro-reduced at cathode; OA — Electro-oxidized at anode

The conventional Fenton (CF) process is the most commonly used one where both H_2O_2 and Fe(II) are externally dosed. It has been used to decontaminate the organic wastewaters containing polychlorinated-biphenyls (PCBs) (Sedlak and Andren, 1991), dyes (Kuo, 1992), dinitrotoluene (Mohanty and Wei, 1993), benzene, tuloene, xylene (BTX) (Lou and Lee, 1995), chlorinated aliphatic hydrocarbons (CAHs) (Tang and Huang, 1997), polycyclic aromatic hydrocarbons (PAHs) (Qiang *et al.*, 2000), and landfill leachates (Kim and Huh, 1997). In this process, concentrated H_2O_2 has to be purchased, transported and stored. In addition, a considerable amount of iron sludge will be generated which requires further disposal.

The electro-Fenton (EF) process is developed from the CF process. In the EF process, either H_2O_2 or Fe(II), or both of them, is generated on site by electrochemical technology. Based on the sources of H_2O_2 and Fe(II), the EF processes can be further divided into four types, as shown in Figure 31. In the EF-FeRe process, both H_2O_2 and Fe(II) are externally applied but Fe(II) is continuously regenerated at the cathode once oxidized to Fe(III). Tzedakis *et al.* (1989) used this process to synthesize phenol by oxidation of benzene at a mercury pool cathode. Chou *et al.* (1999) reported that the EF-FeRe process was more efficient than the CF process in treating high-strength hexamine wastewater. In the EF-FeOx process, H_2O_2 is externally applied but a sacrificial Fe anode is used as the Fe(II) source. Additionally, Fe(II) can be continuously regenerated at the cathode. This process has been applied to detoxifying herbicides-containing wastewater (Pratap and Lemley, 1994), and polishing biological effluent of a petrochemical wastewater (Huang *et al.*, 1997). The third type, EF-H_2O_2-FeRe, is most extensively investigated among all EF processes. This process concurrently generates H_2O_2 and regenerates Fe(II). It has been employed not only for organic synthesis, such as oxidation of alkylbenzene (Matsue *et al.*, 1981), benzene and fluorobenzene (Tzedakis *et al.*, 1989), phenol and chlorobenzene (Hsiao and Nobe, 1993), and Riluzole [2-amino-5-(trifluoromethoxy)benzothiazole] (Oturan *et al.*, 1999); but also for wastewater decontamination, such as the decomposition of phenol (Sudoh *et al.*, 1986), chlorophenols (Chu, 1995), aniline and 4-chlorophenol (Brillas *et al.*, 1996, 1997, 1998, 1998), and chlorophenoxyacid herbicides (Oturan *et al.*, 1999). The forth type, EF-H_2O_2-FeOx, combines electro-generated H_2O_2 with a sacrificial Fe anode. Brillas *et al.* (1997, 1998) applied this process to treat aniline and 4-chlorophenol-containing wastewaters. However, they reported that most of TOC was removed by the $Fe(OH)_3$(s) precipitates instead of organic mineralization. We found that it is due to the oversupply of the current denisty.

When UV radiation is applied, the Fenton process is termed "photo-CF" or "photo-EF". Photolysis of an acidic Fe(III) solution by blacklight UV (300~400 nm) simultaneously generates Fe(II) and ·OH. The reaction is shown as follows:

$$Fe(OH)^{2+} \xrightarrow{h\nu} Fe^{2+} + \cdot OH \qquad (3.4)$$

The reaction efficiency is enhanced by both Fe(II) and ·OH generated. The photo-CF process has been applied to treating organic wastewaters containing chlorophenoxy herbicides (Pignatello, 1992), 4-chlorophenol and dyes (Ruppert and Bauer, 1994), metolachlor and methyl parathion (Pignatello and Sun, 1995), reduction products of perchloroalkanes (Huston and Pignatello, 1996), quinoline (Cermenati *et al.*, 1997) and xylidine (Nadtochenko and Kiwi, 1998). The photo-EF process significantly regenerates Fe(II) by both photolysis and electrolysis. Brillas *et al.* (1996) reported that a higher residual Fe(II) concentration was obtained in the photo-EF process and consequently, a higher TOC removal than those in the EF process. The treatment of aniline and 4-chlorophenol wastwaters with the photo-EF

process were also investigated by the same authors (Brillas *et al.*, 1997, 1998, 1998). Among all Fenton oxidation processes, the photo-EF appears to be the most effective one. However, the photo-assisted processes are not feasible for turbid or colored wastewater because particles or colors tend to shorten the penetration of the UV light.

H_2O_2 or Fe(II) can also be individually generated in an electrolytic cell, and thus termed "electro-H_2O_2" or "electro-Fe(II)", respectively. Most electro-H_2O_2 experiments were conducted in concentrated alkaline solutions by the reduction of dissolved oxygen for the purpose of bleaching paper pulp (Oloman and Watkinson, 1975, 1976, 1979; Sudoh *et al.*, 1985; Yamada *et al.*, 1999). More recently, H_2O_2 has been electro-generated in an acidic solution by either constant potential or constant current mode for the purpose of direct application of the Fenton oxidation process (Sudoh, *et al.*, 1986; Tzedakis *et al.*, 1989; Do and Chen, 1993; DeLeon and Pletcher, 1995; Chu, 1995; Brillas *et al.*, 1996, 1997, 1998a, 1998b; Alvarez-Gallegos and Pletcher, 1999; Qiang *et al.*, 2000). Moreover, a novel technology that generates HO_2^- in an alkaline solution but synthesizes H_2O_2 in an acidic solution has been developed by Sudoh *et al*. (1991). The electro-Fe(II) process regenerates Fe(II) from ferric salts or iron sludge. Chou *et al*. (1999) used a cylindrical steel cathode to regenerate Fe(II) from ferric sulfate. Gnann *et al*. (1993) regenerated Fe(II) from iron sludge in an electrolytic cell at pH < 1, which is specially termed "Fenton sludge recycling system" (FSRS).

In the Fenton oxidation processes, the propagation of chain reactions which generates hydroxyl radicals is usually terminated by the rapid depletion of Fe(II). It is because that Fe(II) reacts with the hydroxyl radical at a second-order rate constant of 3.2×10^8 $M^{-1}s^{-1}$, which is approximately 10 times the rate constant of H_2O_2 toward the hydroxyl radical (3.3×10^7 $M^{-1}s^{-1}$) (DeLatt *et al*., 1999). Therefore, the prompt regeneration of Fe(II) is a key point for enhancing the reaction efficiency of the Fenton's reagent. Although H_2O_2 and Fe(II) may be concurrently generated in the EF-H_2O_2-FeRe process, the applied potential or current density usually satisfies the generation of H_2O_2. Chou *et al*. (1999) studied the regeneration of Fe(II) using the constant current mode, and reported that the initial current efficiency was 85~87% at $[Fe^{3+}]_0 \geq 3000$ mg/L, but dropped to 39% at $[Fe^{3+}]_0 = 1000$ mg/L. They applied an identical current density for various $[Fe^{3+}]_0$ values, failing to realize that the current density is dependent on $[Fe^{3+}]_0$. In fact, the overall regeneration rate is governed by the mass transfer of Fe(III) ions. A current density higher than required will undoubtedly lead to the occurrence of side reactions and consequently, decrease the current efficiency. In addition, iron sludge will eventually be produced in any Fenton oxidation process, though the application of UV and electricity will reduce its quantity. If the FSRS is employed to regenerate and recycle Fe(II) from iron sludge, there is almost no sludge discharge during wastewater treatment. This meets the goal of "design for environment" (DFE). Therefore, it is necessary to specifically investigate the electro-regeneration of Fe(II) from ferric salt or iron sludge.

The objective of the present study is to improve the current efficiency and clarify the optimal conditions for the electro-regeneration of Fe(II) for the purpose of minimizing iron sludge generated in the Fenton oxidation processes. The effects of operational parameters, such as cathodic potential, current density, solution pH, cathode surface area, solution temperature, and initial Fe(III) concentration on the current efficiency of Fe(II) regeneration were systematically investigated. Both constant potential and constant current modes were employed, and their results were compared and bridged. At the optimal cathodic potential, the relationship between the average current density and the $[Fe^{3+}]_0$ was established. The regeneration of Fe(II) from iron sludge was also investigated to evaluate the feasibility of iron

sludge recycling and reuse. Finally, the economic assessment of this process was conducted.

3.2. Experimental

3.2.1. Electrochemical Reaction Mecahnisms

The schematic diagram of electrochemical reaction mechanisms of Fe(II) regeneration is presented in Figure 3.2. At the cathode, Fe(III) is electrochemically reduced to Fe(II) in acidic solutions. Simultaneously, the side reaction of hydrogen gas evolution occurs, which competes for electrons and reduces the current efficiency. At the anode, the oxidation of H_2O leads to oxygen gas evolution and proton release.

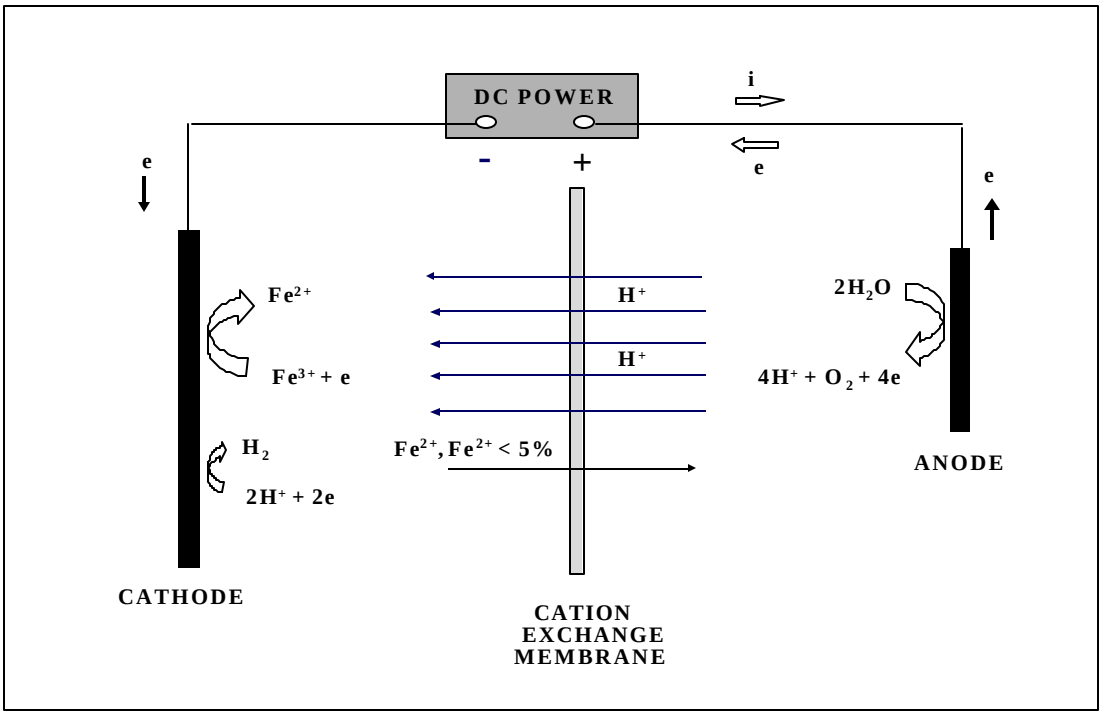

Figure 3.2. Schematic diagram of reaction mechanisms of electro-regeneration of Fe(II).

3.2.2. Reaction System

The schematic diagram of the reaction system is shown in Figure 3.3. The reaction system was similar to that employed for the electro-generation of H_2O_2 except that there is no pH control in this study. Sodium perchlorate was still used as the inert supporting electrolyte. The cathodic and anodic compartments contained 4.0 L of ferric solution and 3.0 L of distilled water, respectively, both with identical $NaClO_4$ concentration and initial pH value. Under the influence of electric field, most of iron was confined in the cathodic compartment, while the protons generated at the anode were driven to the catholyte.

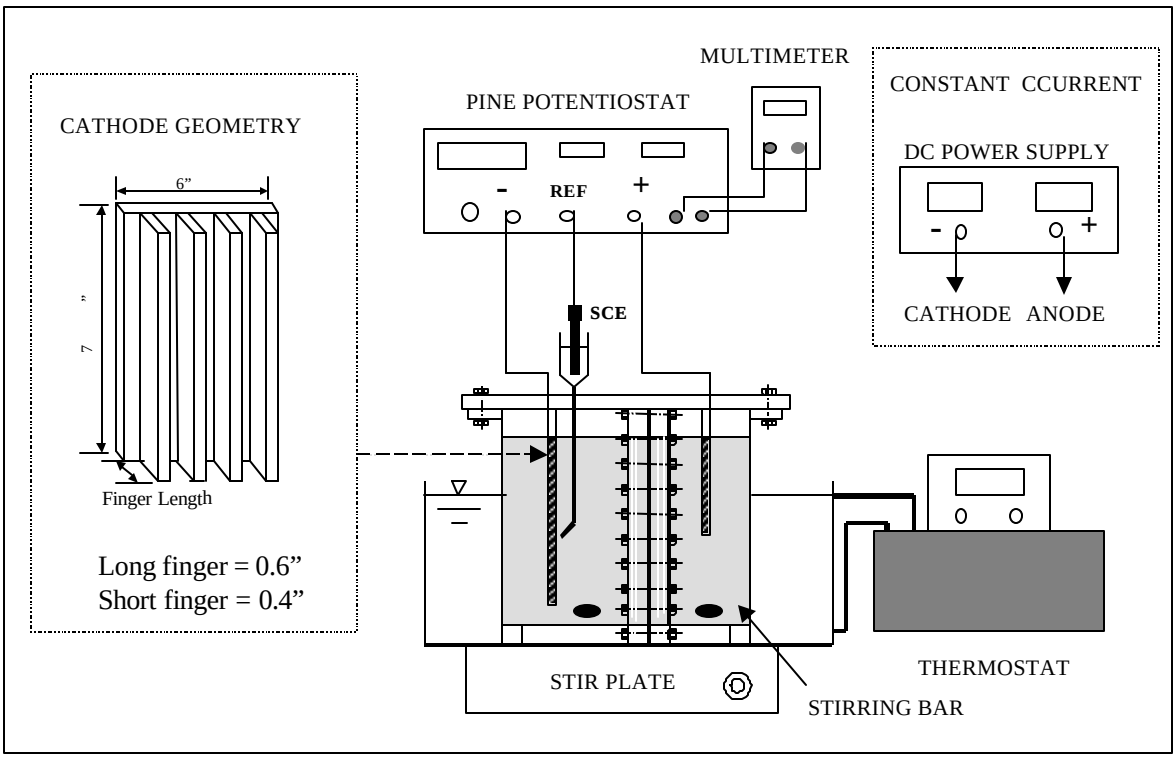

Figure 3.3. Schematic diagram of reaction system for electro-regeneration of Fe(II).

Ferric nitrate or Fenton's sludge was first dissolved in distilled water by pH adjustment. After the addition of supporting electrolyte, experiment was initiated. During electrolysis, solution pH was no longer adjusted. The experimental conditions are generalized in Table 3.2.

Table 3.2. Experimental conditions.

Experimental conditions	Unit	Range
Cathodic potential (vs. SCE)	[V]	-0.1 ~ -0.9
Current density	[A/m^2]	2.05 ~ 8.20
Solution pH	[-]	1.0 ~ 3.0
Cathodic surface area	[cm^2]	271 ~ 488
Solution temperature	[^oC]	10 ~ 46
Initial ferric concentration	[mg/L]	100 ~ 5000
Ferric source	[-]	$Fe(NO_3)_3$, Fenton's sludge

3.2.3. Chemical Analysis

All chemicals used were of ACS reagent grade. Ferric nitrate nonahydrate (98+%), sodium perchlorate (99%) and ammonium fluoride (98+%) were purchased from the Aldrich Chemical; ferrous ammonium sulfate hexahydrate (99+%), ammonium acetate (97.3%) and 1,10-phenanthroline monohydrate from the Sigma Chemical; and hydroxylamine hydrochloride (100.1%), perchloric acid (70%), sulfate acid (96.1%) and sodium hydroxide from the Fisher Scientific. All solutions were prepared by distilled water.

Ferrous iron concentration was determined by measuring the light absorbance at 510 nm after complexing with 1,10-phenanthroline. To avoid the interference from ferric iron, ammonium fluoride was chosen as a masking agent (Tamura *et al.*, 1973). One-milliliter samples were first diluted by 4 mL distilled water, and then the analyzing reagents were added in the following order: 1mL of 3.6 M sulfuric acid, 1 mL of 2 M ammonium fluoride, 2 mL of 3.2 M ammonium acetate and 1 mL of 1% 1,10-phenanthroline. The solution was shaken up after the addition of each reagent. A diode array spectrophotometer (Hewlett Packard, model 8452A) was used with a one-centimeter cell. Figure 3.4 shows the calibration curves of Fe(II) in the presence or absence of Fe(III) using the standard and modified analysis methods. Results clearly indicate that the interference of Fe(III) can be well prevented using F^- as a masking agent of Fe(III) in the modified method. The calibration curve of Fe(II) shows a molar absorptivity of 2.78×10^6 M^{-1} cm^{-1}, with Fe(II) concentration up to 100 mg/L and Fe(III) background concentration up to 2500 mg/L. Dilution was made when Fe(II) concentration exceeded 100 mg/L. For measuring total iron concentration, Fe(III) was first reduced to Fe(II) by hydroxylamine hydrochloride under acidic and boiling conditions, and then the total Fe(II) concentration was determined by the method above-mentioned.

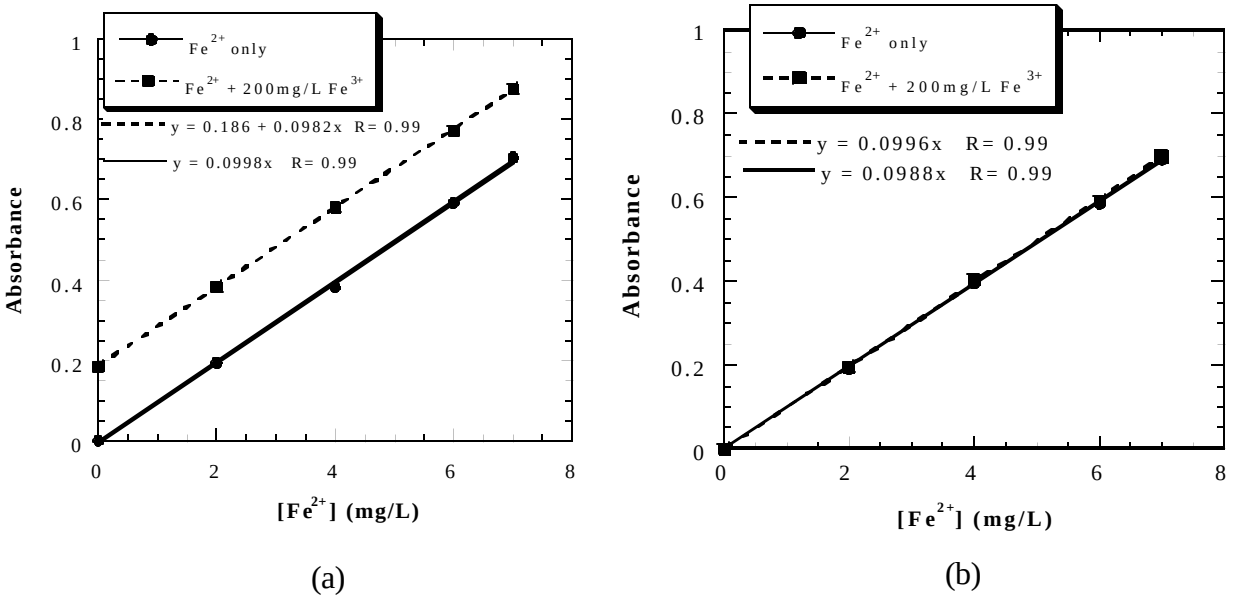

Figure 3.4. Calibrauon curves of Fe(II) in the presence of 200mg/L Fe(III): (a) standard method; (b) modified method.

3.3. Results And Discussion

3.3.1. Optimal Cathodic potential

The polarization curve of the elecro-regeneration of Fe(II) is shown in Figure 3.5. Results indicate that at $-E_c < 0.1V$, the current density (i) increases rapidly with increasing $-E_c$. In this region, the electron transfer between Fe(III) and cathode controls the regeneration rate of Fe(II). However, a "plateau" appears in the potential range of 0.1 to 0.8V. This "plateau" represents the limiting current region for the electro-regeneration of Fe(II). In this region, the Fe(II) regeneration is dominated by the mass transfer of Fe(III) ions across the cathode-

solution diffusion layer. As $-E_c$ continues to increase above 0.8V, the current density rapidly rises again, implying a significant H_2 evolution.

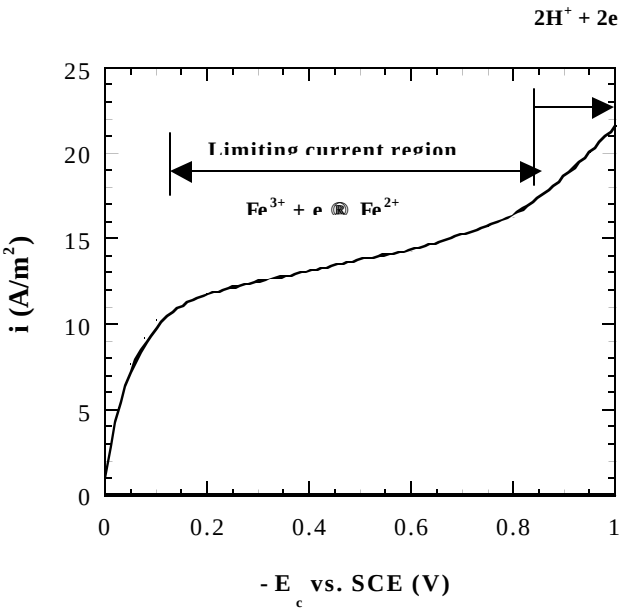

Figure 3.5. Polarization curve of electro-regeneration of Fe(II). Experimental conditions: completely mixing, linear sweeping rate = 33.3 mV/sec, $[Fe^{3+}]_0$ = 500 mg/L, pH_0 = 2, T = 23 ^oC, ionic strength = 0.05M $NaClO_4$, long-finger plate cathode.

From the information reflected in the polarization curve, the effect of cathodic potential was investigated from -0.1 to -0.9V. Figures 3.6, 3.7 and 3.8 show the time-dependent changes of accumulated regeneration percentage of Fe(II), current density (i) and current efficiency (η) at various cathodic potentials, respectively. Figure 3.6 shows that there is little difference in Fe(II) regeneration percentage from 0.1 to 0.7V ($-E_c$). After the electrolysis for 3 hours, about 60% of Fe(II) is regenerated from Fe(III). However, a slightly higher regeneration percentage is observed at $-E_c$ = 0.9V. Figure 3.7 shows that i only slightly increases with increasing potential from 0.1 to 0.7V. At 0.9V, a notably higher i is observed because this high potential stresses Fe(II) regeneration as well as H_2 evolution. Results further indicate that at all potentials applied, the i drops dramatically in the first 5 minutes, and then decreases slowly with proceeding electrolysis. The initial rapid drop of i is due to the pre-saturation of Fe(III) at the cathode surface. After the electrolysis starts, the surface concentration of Fe(III) immediately approaches zero, and the reduction of Fe(III) becomes mass-transfer controlled. As the Fe(III) concentration in the bulk solution continuously decreases with reaction time, the i shows a corresponding decrease. Figure 3.8 shows that η decreases with increasing $-E_c$, dropping from 96% at 0.1V to 55% at 0.9V. However, at a certain potential, η almost remains constant during the course of electrolysis. It is seen that although the highest regeneration percentage is obtained at 0.9V (Figure 3.6), its current efficiency is the lowest. A considerable amount of electricity is wasted for H_2 evolution.

Figure 3.9 shows the plot of the average i and average η vs. $-E_c$. It is clearly seen that the optimal cathodic potential is –0.1 vs. SCE, and the corresponding averaged i and average η are 4.3 A/m^2 and 96%, respectively. The average i curve is in good agreement with the polarization curve except that the polarization i is much higher due to a higher initial Fe(III) concentration. The accumulation of Fe(II) regeneration percentage with electricity consumed is shown in Figure 3.10. Results indicate that the electricity consumption increases with increasing $-E_c$. The smaller the slope of regeneration curve, the lower the current efficiency. Matsue *et al*. (1981) reported a distinguished peak at $-E_c$ = 0.1V vs. SCE using a glassy carbon cathode for the electro-reduction of Fe(III). Tzedakis *et al*. (1989) also observed a notable peak at the same potential using a mercury pool cathode (32 cm^2), but this peak was

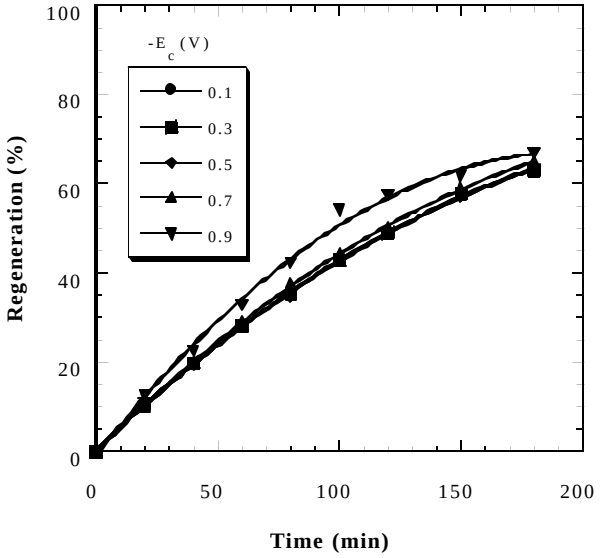

Figure 3.6. Regeneration of Fe(II) at various applied cathodic potentials: regeneration percentage. Experimental conditions: $[Fe^{3+}]_0$ = 500 mg/L, pH_0 = 2, T = 23 °C, ionic strength = 0.05M $NaClO_4$, long-finger plate cathode..

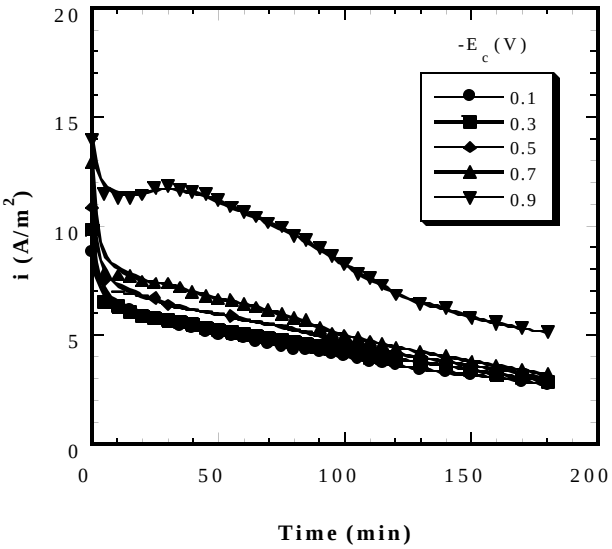

Figure 3.7. Regeneration of Fe(II) at various applied cathodic potentials: current density. Experimental conditions: $[Fe^{3+}]_0$ = 500 mg/L, pH_0 = 2, T = 23 °C, ionic strength = 0.05M $NaClO_4$, long-finger plate cathode.

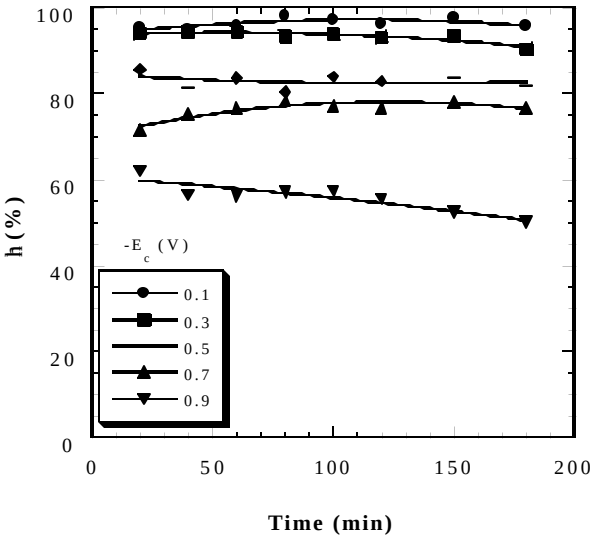

Figure 3.8. Regeneration of Fe(II) at various applied cathodic potentials: current efficiency. Experimental conditions: $[Fe^{3+}]_0$ = 500 mg/L, pH_0 = 2, T = 23 °C, ionic strength = 0.05M $NaClO_4$, long-finger plate cathode.

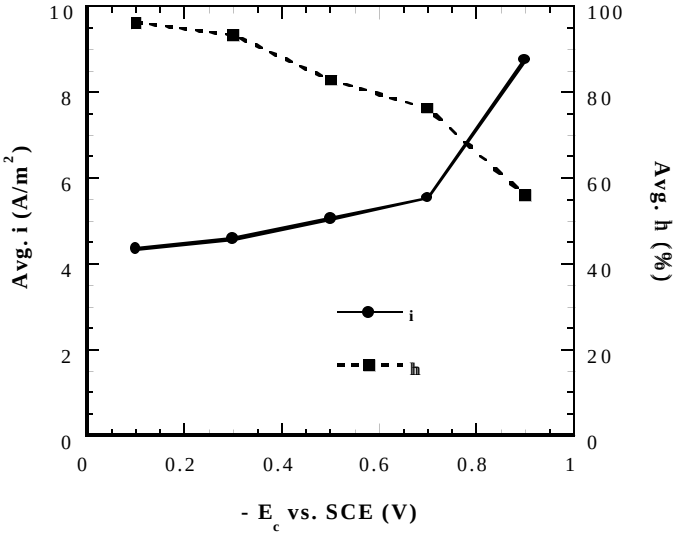

Figure 3.9. Regeneration of Fe(II) at various applied cathodic potentials: average current density and average current efficiency vs. cathodic potential applied. Experimental conditions: $[Fe^{3+}]_0$ = 500 mg/L, pH_0 = 2, T = 23 °C, ionic strength = 0.05M $NaClO_4$, long-finger plate cathode.

unfortunately misinterpreted. In this study, a large graphite cathode with an effective surface area of 488 cm^2 was employed. The large surface area makes the cathode not very sensitive to potential sweeping. As a result, a long plateau instead of a distinguished peak is observed.

Though the solution pH was no longer controlled after the initial pH adjustment, it only changed slightly during electrolysis (< 0.2 units). At the end of electrolysis, the total iron concentrations in both cathodic and anodic compartments were measured. Results also indicate that some Fe(II)/Fe(III) ions do migrate from catholyte to anolyte, but the penetration percentage never exceeds 5%. Therefore, it is cleared that most of Fe(II)/Fe(III) ions were successfully confined in the catholyte by the electric force in spite that a cation exchange membrane was used.

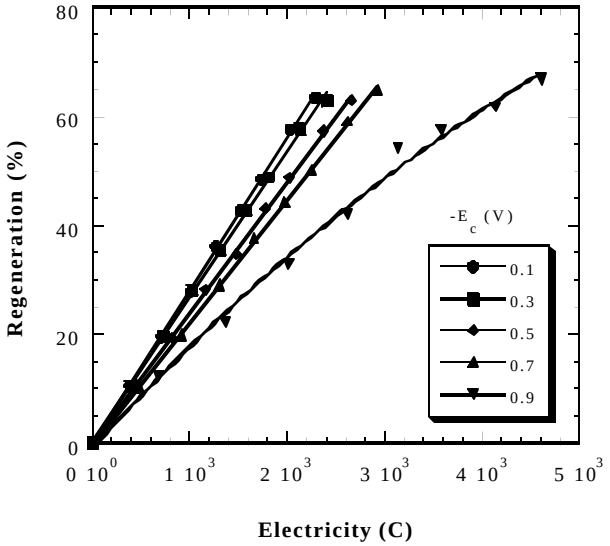

Figure 3.10. Regeneration of Fe(II) at various applied cathodic potentials: regeneration percentage vs. electricity consumed. Experimental conditions: $[Fe^{3+}]_0$ = 500 mg/L, pH_0 = 2, T = 23 °C, ionic strength = 0.05M $NaClO_4$, long-finger plate cathode.

3.3.2. Optimal Current Density

In the constant potential mode mentioned above, the current density automatically changes in accordance with the cahnge of instantaneous Fe(III) concentration in the bulk solution (Figure 3.7). However, the current density is held constant in the constant current method during the whole course of electrolysis. Under this circumstance, the electro-reduction rate of Fe(III) is primarily controlled by the current density applied.

The effect of current density was investigated at $[Fe^{3+}]_0$ = 500 mg/L from 2.05 to 8.20 A/m^2. This current density range was selected because the optimal average current density was determined as 4.3 A/m^2 in the constant potential mode ($-E_c$ = 0.1V) under identical experimental conditions. Figures 3.11, 3.12 and 3.13 show the changes of Fe(II) regeneration percentage, total potential drop and current efficiency with reaction time at various current densities applied. Figure 3.11 indicates that the Fe(II) regeneration percentage increases with increasing current density. Furthermore, at $i \leq 4.10$ A/m^2 the regeneration percentage is in linear proportion to the electrolysis time. It assures a constant current efficiency throughout the whole course of electrolysis. However, at higher current densities, i.e., 6.15 and 8.20 A/m^2, the concave regeneration curves imply a gradual decrease of current efficiency with proceeding electrolysis. Figure 3.12 shows that the total potential drop (ΔE) increases with increasing current density. Additionally, at a certain current density, the ΔE exhibits a slight increase with electrolysis time. The reduction of Fe(III) to Fe(II) at the cathode decreases the solution conductance, while the generation of protons at the anode exerts an opposite influence. Overall, the electrode reactions result in a slight decrease of solution conductance and consequently, a slight increase of ΔE. Figure 3.13

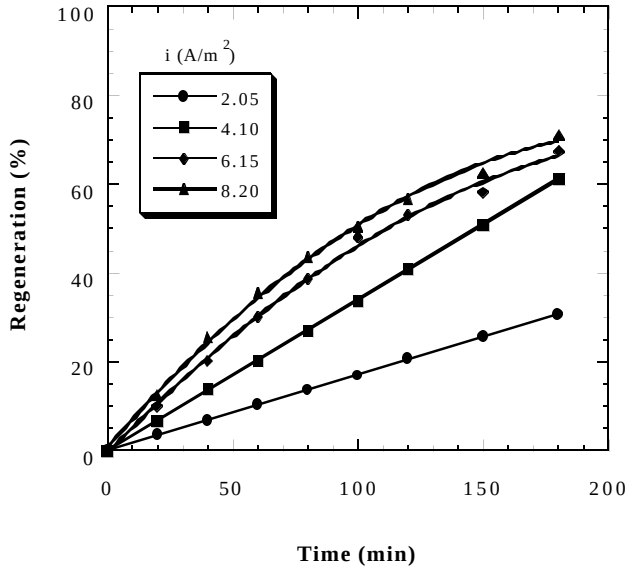

Figure 3.11. Regeneration of Fe(II) at various current densities: regeneration percentage. Experimental conditions: $[Fe^{3+}]_0$ = 500 mg/L, pH_0 = 2, T = 23 °C, ionic strength = 0.05M $NaClO_4$, long-finger plate cathode.

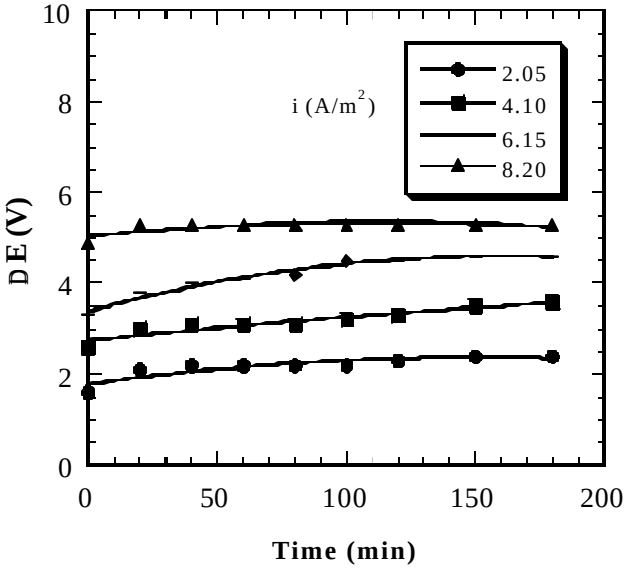

Figure 3.12. Regeneration of Fe(II) at various current densities: current efficiency. Experimental conditions: $[Fe^{3+}]_0$ = 500 mg/L, pH_0 = 2, T = 23 °C, ionic strength = 0.05M $NaClO_4$, long-finger plate cathode.

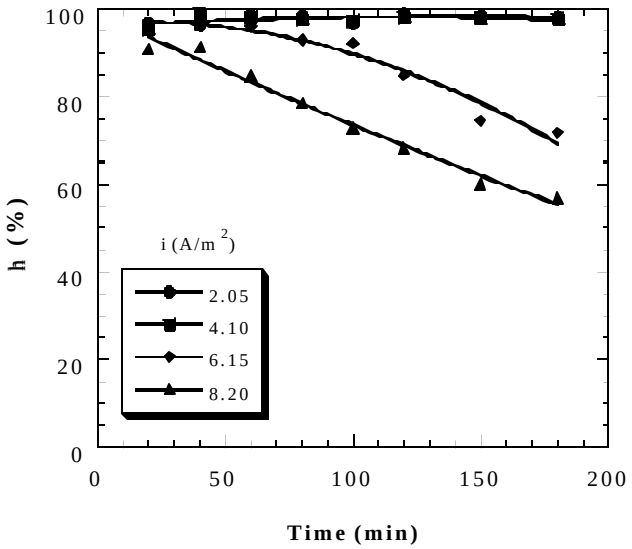

Figure 3.13. Regeneration of Fe(II) at various current densities: current efficiency. Experimental conditions: $[Fe^{3+}]_0$ = 500 mg/L, pH_0 = 2, T = 23 °C, ionic strength = 0.05M $NaClO_4$, long-finger plate cathode.

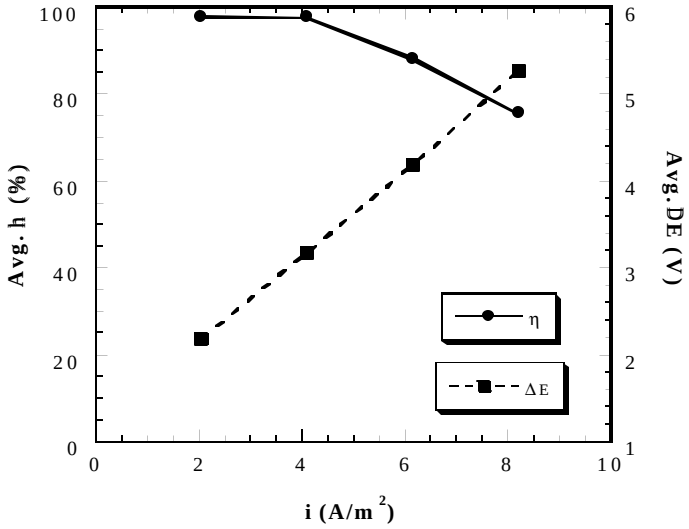

Figure 3.14. Regeneration of Fe(II) at various current densities: average current efficiency and average potential drop vs. current density applied. Experimental conditions: $[Fe^{3+}]_0$ = 500 mg/L, pH_0 = 2, T = 23 °C, ionic strength = 0.05M $NaClO_4$, long-finger plate cathode.

shows that at $i \leq 4.10$ A/m^2, the current efficiency remains unchanged during the electrolysis. A high current efficiency can be readily achieved. However, above 4.10 A/m^2 the current efficiency decreases with both electrolysis time and increasing current density. It indicates a significant occurrence of H_2 evolution.

Figure 3.14 shows the plot of average η and average ΔE vs. current density. It is clearly seen that the ΔE increases proportionally to the current density. Moreover, a current efficiency of 98% is achieved at $i \leq 4.10$ A/m^2. At 6.15 and 8.20 A/m^2, the average current efficiency drops to 88% and 75%, respectively. Taking both Fe(II) regeneration rate and current efficiency into consideration, the current density of 4.10 A/m^2 is the optimal value for $[Fe^{3+}]_0$ = 500 mg/L. As mentioned previously (Figure 3.9), the average current density obtained at the optimal potential ($-E_c$ = 0.1V) is 4.30 A/m^2. It is seen that the average current density yielded at the optimal potential is approximately equal to the optimal current density applied in the constant current mode. This relationship bridges the constant potential mode with the constant current mode. It should be mentioned that the optimal current density depends on initial Fe(III) concentration ($[Fe^{3+}]_0$) since the overall Fe(II) regeneration rate is controlled by the mass transfer of Fe(III). The relationship between the optimal current density and $[Fe^{3+}]_0$ is a crucial factor which determines the applied value of current density for any given $[Fe^{3+}]_0$. It will be discussed later.

3.3.3. Effect of pH

In a homogeneous Fe(III) solution, the following hydrolysis equilibria exist: (Stumm and Morgan, 1981):

$$Fe^{3+} + H_2O = FeOH^{2+} + H^+, \log K_1 = -2.19 \qquad (3.5)$$

$$Fe^{3+} + 2H_2O = Fe(OH)_2^+ + 2H^+, \log \beta_2 = -5.67 \qquad (3.6)$$

$$2Fe^{3+} + 2H_2O = Fe_2(OH)_2^{4+} + 2H^+, \log \beta_{22} = -2.95 \qquad (3.7)$$

$$Fe^{3+} + 4H_2O = Fe(OH)_4^- + 4H^+, \log \beta_4 = -21.6 \qquad (3.8)$$

Figure 15 depicts the dependence of hydrolysis pH on total Fe(III) concentration ($\log Fe_T$) for both experimentally measured and theoretically calculated data. Experimental results (solid curve) indicate that the hydrolysis pH is in linear proportion to $-\log Fe_T$ in the range of Fe_T studied, i.e., 1.8~89.5 mM (or 100~5000 mg/L), exhibiting a slope of 0.75. The theoretical calculation (dashed curve) using Equations 3.5~3.8 shows an identical slope. The difference in the intercept is due to different background ionic strengths, i.e., 0.05 M $NaClO_4$ for the experimental curve and zero for the theoretical curve. Several ferric-hydroxo species co-exist in the solution, including Fe^{3+}, $FeOH^{2+}$, $Fe_2(OH)_2^{4+}$, $Fe(OH)^{2+}$ and $Fe(OH)_4^-$. At $Fe_T = 1x10^{-3}$ M, $Fe(OH)^{2+}$ predominates. At $Fe_T = 1x10^{-1}$ M, free Fe^{3+} ion becomes the major component. $Fe(OH)_4^-$ is always negligible in the Fe_T range studied.

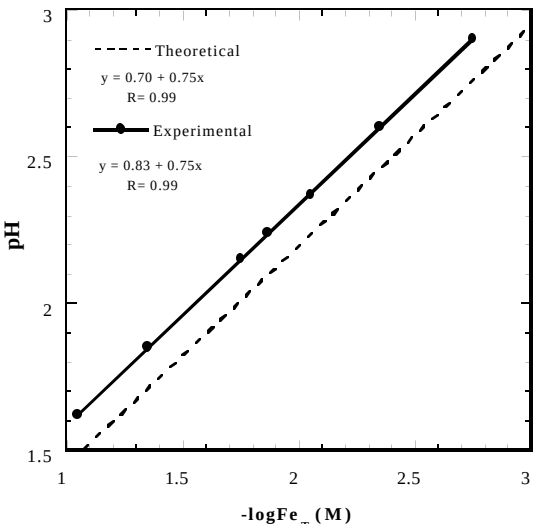

Figure 3.15. Plot of pH vs. $-\log Fe_T$ in Fe(III) hydrolysis.

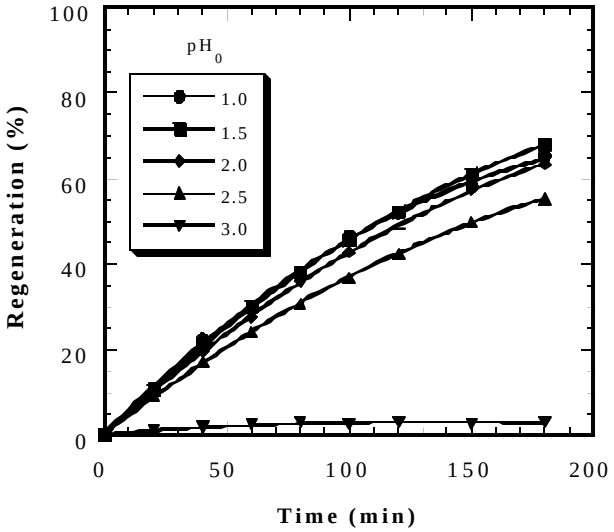

Figure 3.16. Regeneration of Fe(II) at various pH values using the constant potential mode: regeneration percentage. Experimental conditions: $-E_c$ = 0.1 V vs. SCE; $[Fe^{3+}]_0$ = 500 mg/L, pH_0 = 2, T = 23 ^oC, ionic strength = 0.05M $NaClO_4$, long-finger plate cathode.

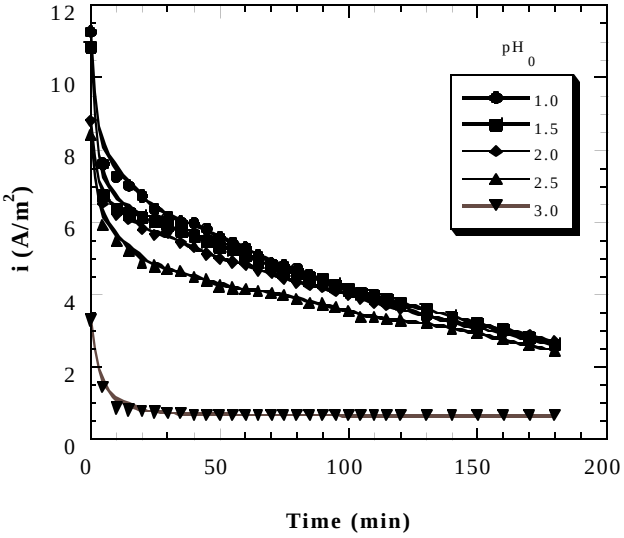

Figure 3.17. Regeneration of Fe(II) at various pH values using the constant potential mode: current density. Experimental conditions: $-E_c$ = 0.1 V vs. SCE; $[Fe^{3+}]_0$ = 500 mg/L, T = 23 ^oC, ionic strength = 0.05M $NaClO_4$, long-finger plate cathode.

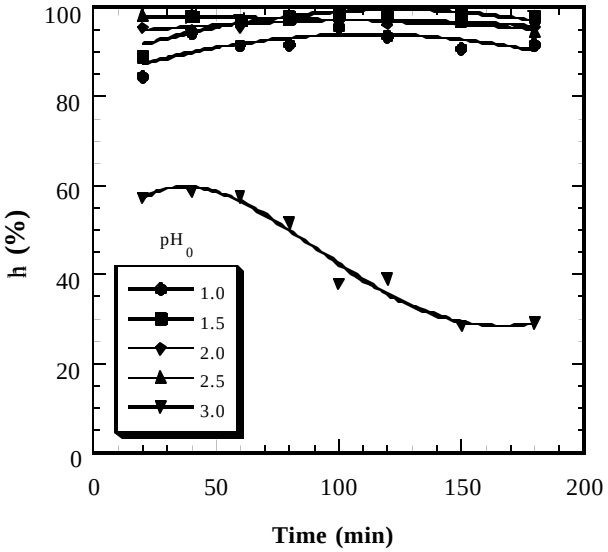

Figure 3.18. Regeneration of Fe(II) at various pH values using the constant potential mode: current efficiency. Experimental conditions: $-E_c$ = 0.1 V vs. SCE; $[Fe^{3+}]_0$ = 500 mg/L, T = 23 ^oC, ionic strength = 0.05M $NaClO_4$, long-finger plate cathode..

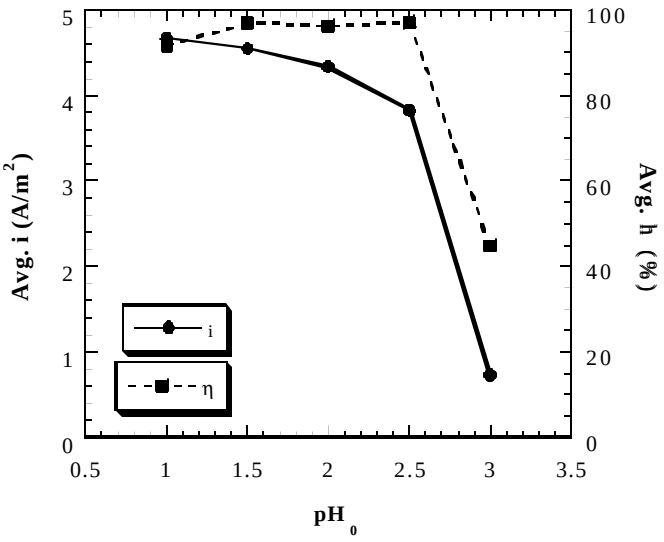

Figure 3.19. Regeneration of Fe(II) at various pH values using the constant potential mode: average current density and average current efficiency vs. initial pH. Experimental conditions: $-E_c$ = 0.1 V vs. SCE; $[Fe^{3+}]_0$ = 500 mg/L, T = 23 ^oC, ionic strength = 0.05M $NaClO_4$, long-finger plate cathode.

The effect of initial pH on Fe(II) regeneration was investigated from pH_0 1 to 3 at $[Fe^{3+}]_0$ = 500 mg/L, using both constant potential and constant current modes. Figures 16, 17 and 18 show the time-dependent changes of regeneration percentage, current density and current efficiency with electrolysis time at various adjusted initial pH values under the constant potential mode. The applied cathodic potential was -0.1V vs. SCE. Figure 16 indicates that the Fe^{2+} regeneration percentage reaches the maximum at pH_0 1.0 and 1.5, and then decreases with increasing pH. At pH_0 3.0, little Fe^{2+} is regenerated. The changes of current density (Figure 3.17) and current efficiency (Figure 3.18) show a good agreement with the results indicated in Figure 3.16. Figure 3.19 plots the average current density and average current efficiency vs. initial pH. Results indicate that the average i slightly decreases with increasing pH_0 from 1 to 2.5. It drops remarkably at pH_0 = 3 where only a small i of 0.7 A/m^2 can be achieved. As indicated in Figure 3.15, the hydrolysis of 500 mg/L Fe(III) ions corresponds to a solution pH of 2.37. Above this pH, Fe(III) starts to precipitate as solid amorphous $Fe(OH)_3(s)$. It was observed that a small amount of $Fe(OH)_3(s)$ was formed at pH 2.5, while most Fe(III) precipitated at pH 3. The formation of $Fe(OH)_3(s)$ undoubtedly accounts for the decrease of current density. The $Fe(OH)_3(s)$ not only decreases the concentration of dissolved Fe(III), but also inhibits the Fe(II) regeneration by partially coating the cathode surface. The average current efficiency curve shows that the highest efficiency is achieved between pH_0 1.5 and 2.5. A slight efficiency decrease occurs at pH_0 1, which is due to hydrogen gas evolution at a high proton concentration. At pH_0 3, the low current efficiency is mainly ascribed to the coating of $Fe(OH)_3(s)$ on the cathode surface, as previously mentioned.

The effect of pH_0 was also investigated using the constant current mode. The current density applied was 4.10 A/m^2. Figure 3.20 shows that the Fe^{2+} regeneration percentage increases linearly with electrolysis time. There is little difference in regeneration rate from

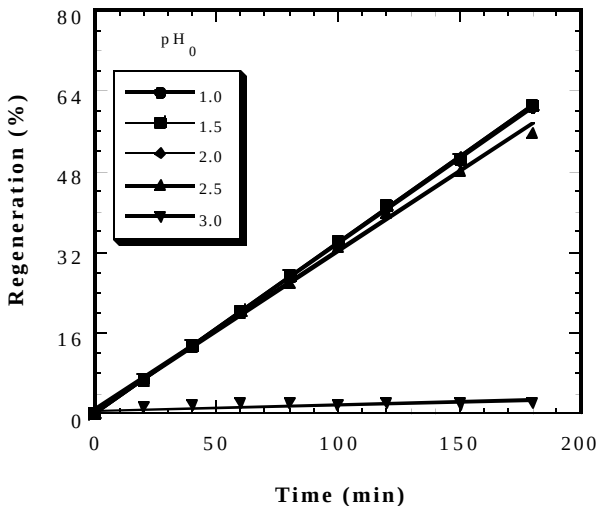

Figure 3.20. Regeneration of Fe(II) at various pH values using the constant current mode: regeneration percentage. Experimental conditions: i = 4.10 A/m^2; $[Fe^{3+}]_0$ = 500 mg/L, T = 23 ^oC, ionic strength = 0.05M $NaClO_4$, long-finger plate cathode.

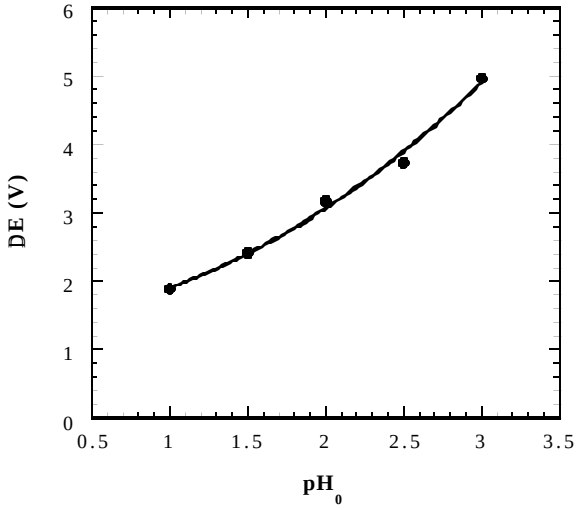

Figure 3.21. Regeneration of Fe(II) at various pH values using the constant current mode: change of total potential drop. Experimental conditions: i = 4.10 A/m^2; $[Fe^{3+}]_0$ = 500 mg/L, T = 23 ^oC, ionic strength = 0.05M $NaClO_4$, long-finger plate cathode.

pH_0 1.0 to 2.5, but the rate drops significantly at pH_0 3.0 because of the $Fe(OH)_3(s)$ precipitation as mentioned before. Figure 3.21 shows that the total potential drop of the cell increases with increasing pH_0 due to the decrease of the solution conductance. Figure 3.22 plots the average current efficiency vs. pH_0. This curve shows a similar trend as the average η curve obtained in the constant potential mode (Figure 3.19).

Therefore, it is concluded that as long as Fe(III) is totally dissolved, it can be effectively reduced to Fe(II). The suitable pH range is below the pH value controlled by Fe(III) hydrolysis. It should be noted that this critical pH value is Fe(III) concentration dependent, as demonstrated in Figure 3.15.

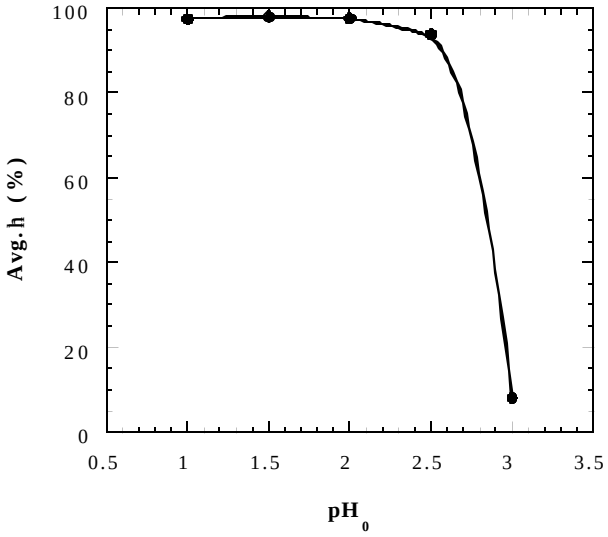

Figure 3.22. Regeneration of Fe(II) at various pH values using the constant current mode: average current efficiency. Experimental conditions: i = 4.10 A/m^2; [Fe^{3+}]$_0$ = 500 mg/L, T = 23 ^{o}C, ionic strength = 0.05M $NaClO_4$, long-finger plate cathode.

3.3.4. Effects of Cathode Surface Area

Three cathode geometries were used to investigate the effect of cathode surface area, including the plain, short-finger and long-finger plates that have an effective surface area of 271, 415 and 488 cm^2, respectively. Since the electric current is a function of the cathode surface area, the constant potential method was employed. The cathodic potential was controlled at –0.1V vs. SCE. Figures 23, 24 and 25 show the time-dependent changes of regeneration percentage, current density and current efficiency. Results indicate that as the cathode surface area increases, both regeneration percentage and current density increase correspondingly. Since the electrolysis is conducted at the optimal potential, the current efficiency is not significantly affected by the change of cathode surface area. Figure 3.26 plots regeneration percentage and average current efficiency vs. cathode surface area. Results indicate that after three hours of electrolysis, the regeneration percentage reaches 41%, 59% and 63% for the plain, short-finger and long-finger plates, respectively. The current efficiency is independent of the surface area. At the optimal cathodic potential, a high current efficiency of 94~96% is achieved for all cathode geometries. Therefore, the regeneration rate of Fe(II) can be easily enhanced by increasing cathode surface area without sacrifice of the current efficiency.

3.3.5. Effect of Solution Temperature

Solution temperature influences Fe(II) regeneration rate mainly because that it changes the mass transfer rate of Fe(III). Under constant potential mode, a high temperature leads to a fast mass transfer of Fe(III) through the cathode-solution diffusion layer. Consequently, the rate of Fe(II) regeneration will be raised. The effect of temperature was investigated

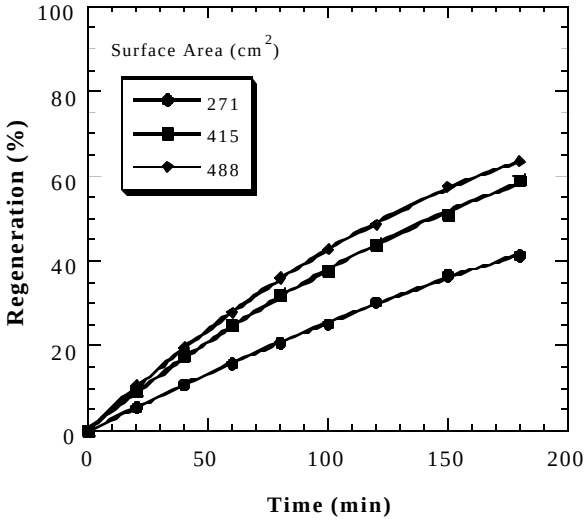

Figure 3.23. Regeneration of Fe(II) at various cathode surface areas using the constant potential mode: regeneration percentage. Experimental conditions: $-E_c$ = 0.1V vs. SCE, $[Fe^{3+}]_0$ = 500 mg/L, pH_0 = 2, T = 23 ^oC, ionic strength = 0.05M $NaClO_4$.

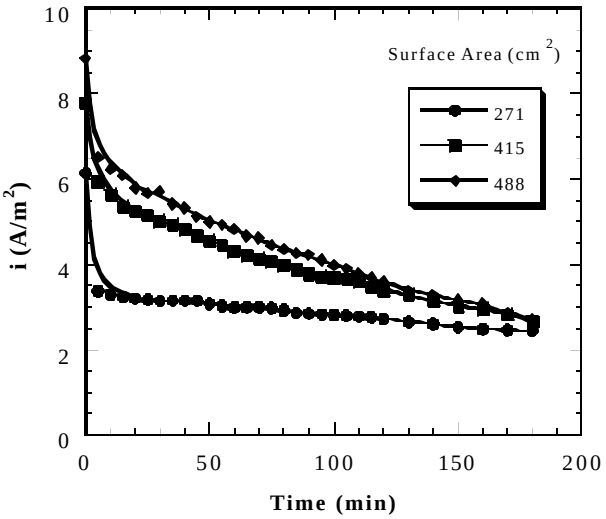

Figure 3.24. Regeneration of Fe(II) at various cathode surface areas using the constant potential mode: current density. Experimental conditions: $-E_c$ = 0.1V vs. SCE, $[Fe^{3+}]_0$ = 500 mg/L, pH_0 = 2, T = 23 ^oC, ionic strength = 0.05M $NaClO_4$.

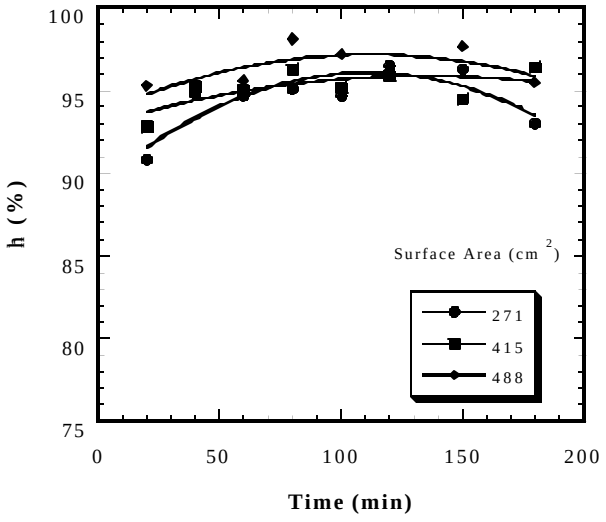

Figure 3.25. Regeneration of Fe(II) at various cathode surface areas using the constant potential mode: current efficiency. Experimental conditions: $-E_c$ = 0.1V vs. SCE, $[Fe^{3+}]_0$ = 500 mg/L, pH_0 = 2, T = 23 ^oC, ionic strength = 0.05M $NaClO_4$.

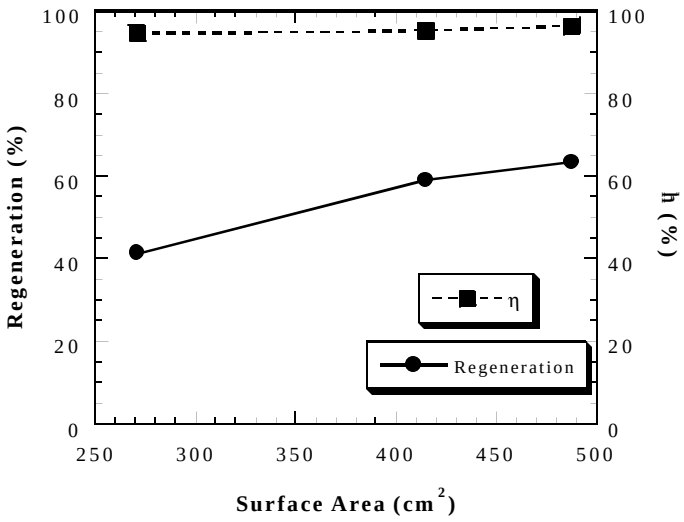

Figure 3.26. Regeneration of Fe(II) at various cathode surface areas using the constant potential mode: average current density and average current efficiency vs. cathode surface area. Experimental conditions: $-E_c$ = 0.1V vs. SCE, $[Fe^{3+}]_0$ = 500 mg/L, pH_0 = 2, T = 23 ^oC, ionic strength = 0.05M $NaClO_4$.

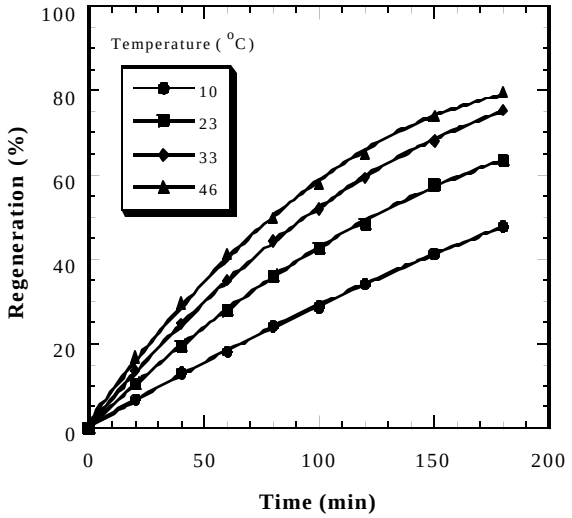

Figure 3.27. Regeneration of Fe(II) at various temperatures using the constant potential mode: regeneration percentage. Experimental conditions: $-E_c$ = 0.1V vs. SCE, $[Fe^{3+}]_0$ = 500 mg/L, pH_0 = 2, ionic strength = 0.05M $NaClO_4$, long-finger plate cathode.

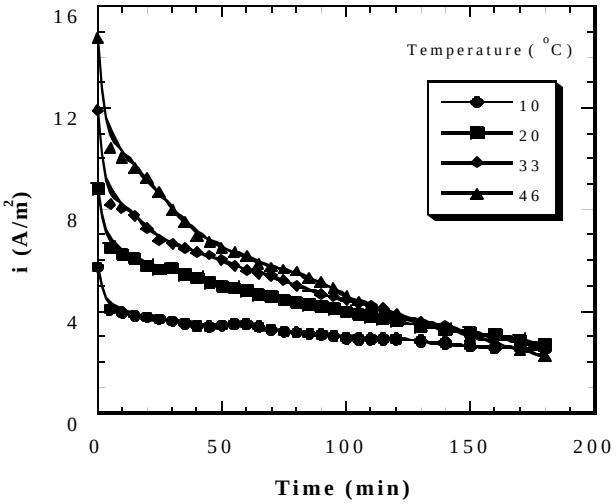

Figure 3.28. Regeneration of Fe(II) at various temperatures using the constant potential mode: current density. Experimental conditions: $-E_c$ = 0.1V vs. SCE, $[Fe^{3+}]_0$ = 500 mg/L, pH_0 = 2, ionic strength = 0.05M $NaClO_4$, long-finger plate cathode.

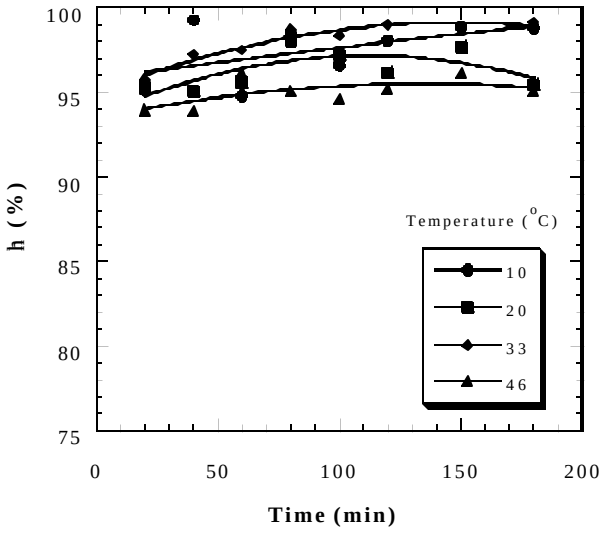

Figure 3.29. Regeneration of Fe(II) at various temperatures using the constant potential mode: current efficiency. Experimental conditions: $-E_c$ = 0.1V vs. SCE, $[Fe^{3+}]_0$ = 500 mg/L, pH_0 = 2, ionic strength = 0.05M $NaClO_4$, long-finger plate cathode.

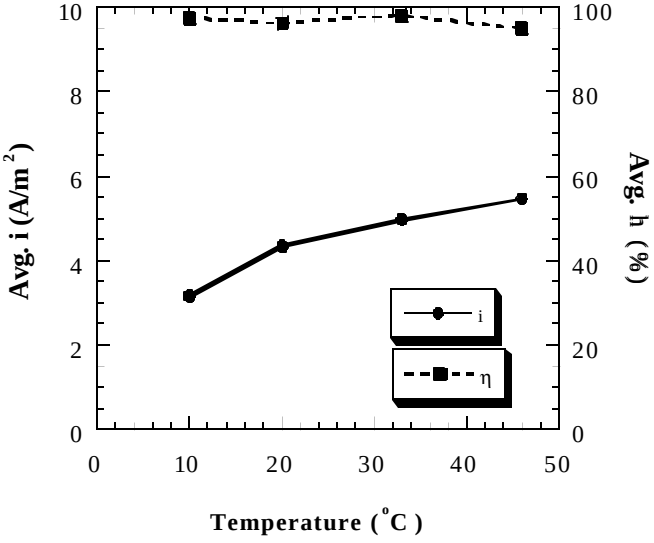

Figure 3.30. Regeneration of Fe(II) at various temperatures using the constant potential mode: regeneration percentage and average current efficiency vs. temperature. Experimental conditions: $-E_c$ = 0.1V vs. SCE, $[Fe^{3+}]_0$ = 500 mg/L, pH_0 = 2, ionic strength = 0.05M $NaClO_4$, long-finger plate cathode..

using the constant potential method ($-E_c$ = 0.1 V vs. SCE) at 10, 23, 33 and 46 ^oC. Figures 3.27, 3.28 and 3.29 show the changes of regeneration percentage, current density and current efficiency with electrolysis time. Results indicate that both regeneration percentage and current density increase significantly with increasing temperature. At the end of electrolysis, the regeneration percentage is only 48% at 10 ^oC, but reaches 80% at 46 ^oC. The current efficiency is almost independent of temperature under the constant potential mode. A high current efficiency (ca. 95~98%) can be readily achieved in the temperature range studied. The effect of temperature on the average current density and average current efficiency is summarized in Figure 3.30. It is concluded that the Fe(II) regeneration is favored at high temperatures, while the current efficiency is independent of temperature.

3.3.6. Effect of Initial Ferric Concentration

The instantaneous current (I_L) is a linear function of Fe(III) concentration in the bulk solution if the mass transfer of Fe(III) controls the reaction rate. As electrolysis proceeds, the current density gradually decreases with decreasing Fe(III) concentration in the constant potential method. Previous results have clarified that the average current density obtained at the optimal constant potential is approximately equal to the optimal current density in the constant current method. If a current density less than the optimal value is applied, the regeneration rate of Fe(II) is decreased though the current efficiency remains high. On the other hand, if a current density greater than the optimal value is applied, the regeneration rate of Fe(II) is increased, but the current density drops substantially due to the occurrence of side reaction. Therefore, it is necessary to clarify the relationship between average current density and initial ferric concentration.

The effect of initial ferric concentration ($[Fe^{3+}]_0$) was investigated in the range of 100 to 1000 mg/L by the constant potential method ($-E_c$ = 0.1 V vs. SCE). Figures 3.31, 3.32 and 3.33 show the changes of regeneration percentage, current density and current efficiency with electrolysis time. Results indicate that the regeneration percentage is similar for various $[Fe^{3+}]_0$ applied. The current density exhibits a positive proportion to $[Fe^{3+}]_0$. Above 500 mg/L, the current efficiency is almost independent of $[Fe^{3+}]_0$. However, below 500 mg/L, the current density decreases with decreasing $[Fe^{3+}]_0$.

Figure 3.34 shows the average current density and average current efficiency at various initial ferric concentrations. Results clearly indicate that the average current density increases linearly with increasing $[Fe^{3+}]_0$, exhibiting a slope of 8.48 x 10^{-3} $(A/m^2)(mg/L)^{-1}$, or 4.74 x 10^2 $(A/m^2)(M)^{-1}$ if molarity is used. This slope is a crucial factor to determine the value of applied current density for a given $[Fe^{3+}]_0$. Chou *et al*. (1999) reported that the initial current efficiency was around 85-87% for an initial ferric concentration between 3000 and 10000 mg/L, but dropped to 39% at 1000 mg/L, in the electro-regeneration of Fe(II) by the constant current method. They applied a constant current density of 98 A/m^2 for all ferric concentrations studied. However, it is calculated from the slope of 8.48 x 10^{-3} $(A/m^2)(mg/L)^{-1}$ that the optimal current densities should be 8.48, 25.4 and 84.8 A/m^2 for an initial ferric concentration of 1000, 3000 and 10000 mg/L, respectively. Undoubtedly, the applied current density of 98 A/m^2 is too high for all ferric concentrations investigated in their study. It stresses the side reaction of hydrogen gas evolution, especially at low ferric concentrations. Even at $[Fe^{3+}]_0$ = 10000 mg/L, the current efficiency they obtained (87%) is less than that achieved in this study (ca. 96% at $[Fe^{3+}]_0$ = 500 mg/L). Therefore, to achieve a high current efficiency, the current density applied should be adjusted in accordance with the initial ferric

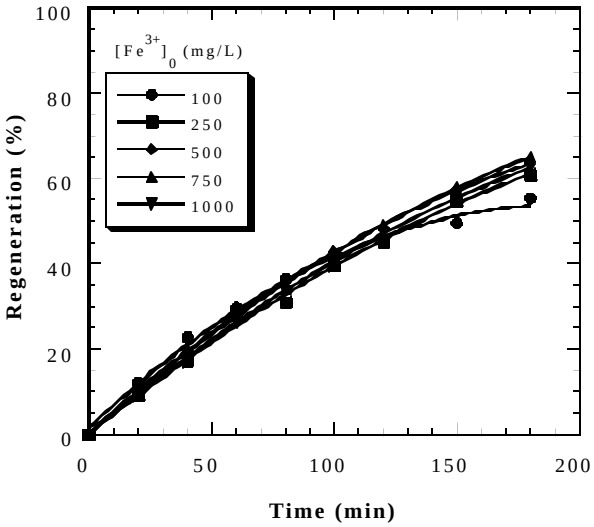

Figure 3.31. Regeneration of Fe(II) at various initial Fe(III) concentrations using the constant potential mode: regeneration percentage. Experimental conditions: $-E_c$ = 0.1V vs. SCE, pH_0 = 2, T = 30 ^oC, ionic strength = 0.05M $NaClO_4$, long-finger plate cathode.

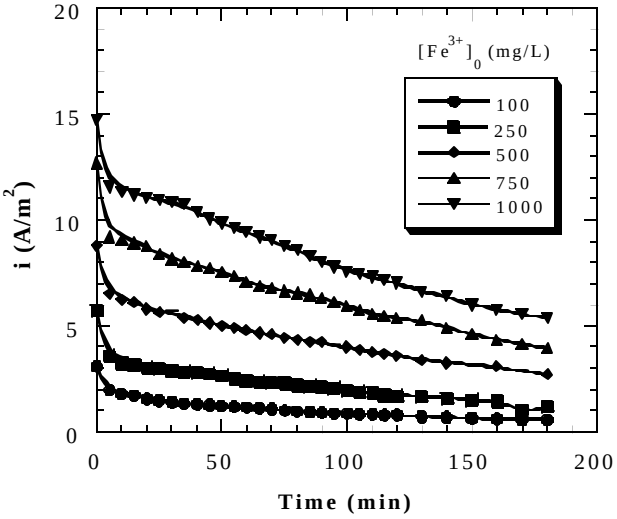

Figure 3.32. Regeneration of Fe(II) at various initial Fe(III) concentrations using the constant potential mode: current density. Experimental conditions: $-E_c$ = 0.1V vs. SCE, pH_0 = 2, T = 30 ^oC, ionic strength = 0.05M $NaClO_4$, long-finger plate cathode.

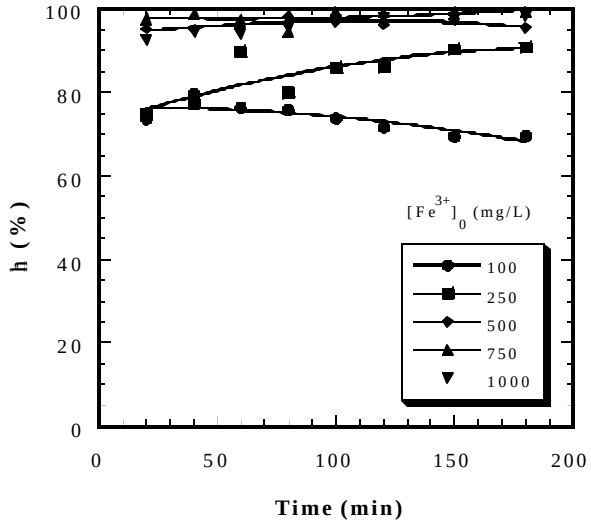

Figure 3.33. Regeneration of Fe(II) at various initial Fe(III) concentrations using the constant potential mode: current efficiency. Experimental conditions: $-E_c$ = 0.1V vs. SCE, pH_0 = 2, T = 30 ^oC, ionic strength = 0.05M $NaClO_4$, long-finger plate cathode.

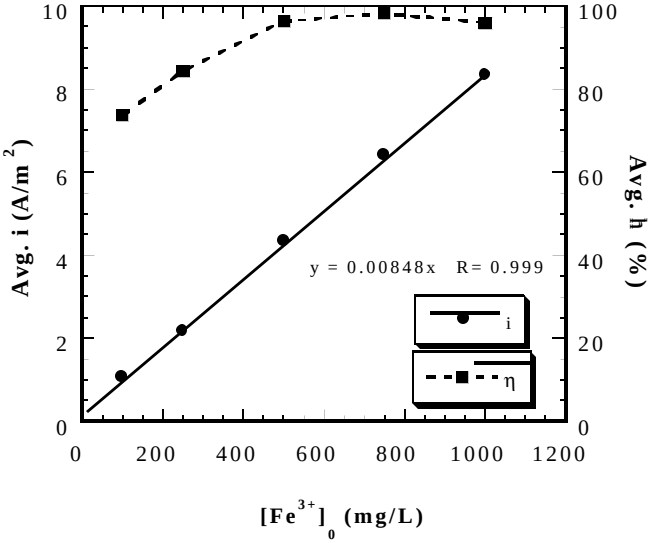

Figure 3.34. Regeneration of Fe(II) at various initial Fe(III) concentrations using the constant potential mode: average current density and average current efficiency vs. concentration. Experimental conditions: $-E_c$ = 0.1V vs. SCE, pH_0 = 2, T = 30 ^oC, ionic strength = 0.05M $NaClO_4$, long-finger plate cathode.

concentration. Figure 3.34 also shows that the average current efficiency gradually drops as the initial ferric concentration becomes less than 500 mg/L. The relative significance of hydrogen gas evolution depends on the molar ratio of $[H^+]/[Fe^{3+}]$. For example, the molar ratio ($[H^+]/[Fe^{3+}]$) is 5.6 for $[Fe^{3+}]_0$ = 100 mg/L at pH 2. The corresponding average current efficiency is only 74%, much lower than 96% at $[Fe^{3+}]_0$ = 500 mg/L ($[H^+]/[Fe^{3+}]$) = 1.1). However, above 500 mg/L, the interference from the side reaction is negligible. The average current efficiency remains unchanged from 500 to 1000 mg/L of $[Fe^{3+}]_0$.

Figure 3.35 shows the Fe(II) regeneration percentage vs. the electricity consumed. Results indicate that at a fixed cathodic potential, the current density automatically increases with increasing ferric concentration. More electricity is consumed at a higher ferric concentration. The linear relationship between the regeneration percentage and the electricity consumed assures a constant current efficiency during the whole course of electrolysis at $[Fe^{3+}]_0 \geq 250$ mg/L. At $[Fe^{3+}]_0$ = 100 mg/L, the regeneration curve implies a slight decrease of current efficiency with reaction time.

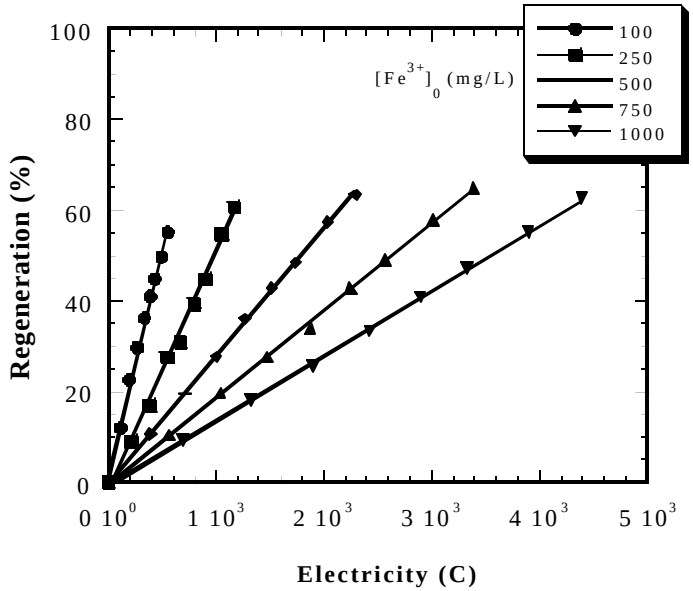

Figure 3.35. Regeneration of Fe(II) at various initial Fe(III) concentrations using the constant potential mode: regeneration percentage vs. electricity consumed. Experimental conditions: $-E_c$ = 0.1V vs. SCE, pH_0 = 2, T = 30 ^oC, ionic strength = 0.05M $NaClO_4$, long-finger plate cathode.

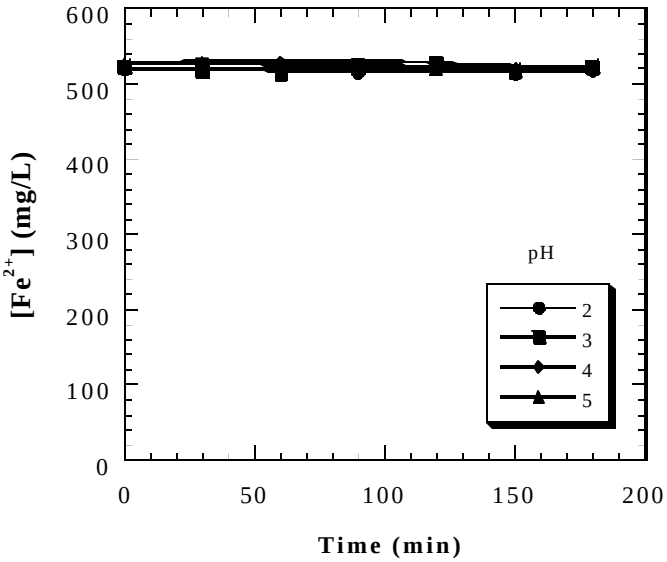

Figure 3.36. Oxygenation of Fe(II) at various pH various.

3.3.7. Oxygenation of Fe(II)

It is stated that Fe(II) ion is easily converted to Fe(III) by the oxidation of molecular oxygen in acidic solution (Silver, 1993). In the EF processes where H_2O_2 and Fe(II) are simultaneously generated, it is necessary to investigate the oxidation of Fe(II) by pure oxygen gas. The oxygenation of a Fe(II) solution

([Fe^{2+}] = 500 mg/L) was carried out from pH 2 to 4 by bubbling pure oxygen gas. Results in Figure 3.36 indicate that the Fe(II) concentration does not change within hours, however. It is reported by Stumm and Morgan (1981) that the half life of oxygenation of Fe(II) is about 10^8 seconds at pH < 4, and significant oxygenation only occur above pH 5. This is in consistence with our results. Silver (1993) overestimated the kinetics of Fe(II) oxygenation. As a conclusion, the oxygenation of Fe(II) by pure oxygen gas is negligible in the pH range suitable for the Fenton's reagent.

3.3.8. Long-term Regeneration of Fe(II)

Previous results indicate that in the constant potential mode, Fe(II) regeneration rate decreases as electrolysis proceeds due to the continuous decrease of Fe(III) concentration in the bulk solution (Figure 3.6). Though in the constant current mode, this phenomenon was not observed at i = 4.10 A/m^2 during three hours of electrolysis (Figure 3.11), it is readily inferred that the current efficiency will eventually drop at extended electrolysis time. The long-term regeneration of Fe(II) was investigated at $[Fe^{3+}]_0$ = 500 mg/L using both constant potential and constant current modes.

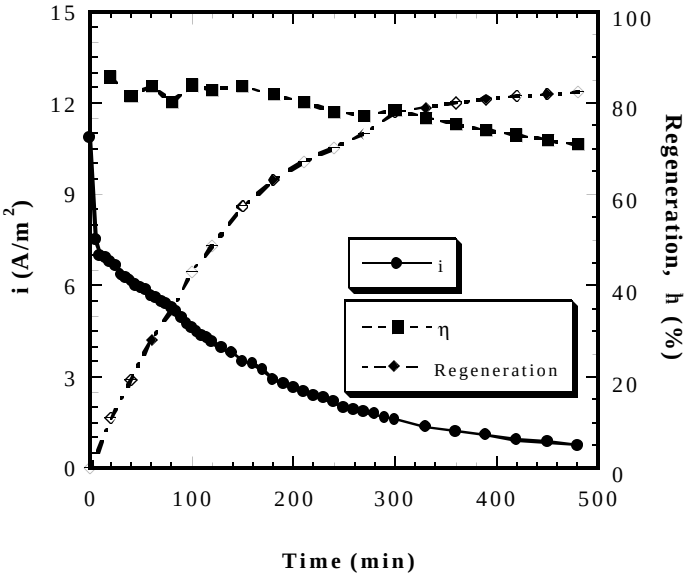

Figure 3.37. Long-term regeneration of Fe(II) using constant potential mode. Experimental conditions: - E_c = 0.1V vs. SCE, $[Fe^{3+}]_0$ = 500 mg/L, pH_0 = 2, T = 30 ^oC, ionic strength = 0.05M $NaClO_4$, long-finger plate cathode.

Figure 3.37 shows the time-dependent changes of current density, regeneration percentage and current efficiency at $-E_c$ = 0.5V (vs. SCE) for an extended electrolysis of eight hours. The potential was chosen because it is optimal for electro-generation of H_2O_2 in acidic solutions (Matsue *et al.*, 1981; Oturan *et al.*, 1999; Qiang *et al.*, 2000). Results indicate that the current density continuously decreases with electrolysis time, and consequently, the regeneration of Fe(II) gradually slows down. After 75% of Fe(II) has been regenerated, further regeneration becomes more difficult. The current efficiency changes only a little, i.e., from the initial 85% to the final 70%.

Figure 3.38 shows the time-dependent changes of total potential drop of the cell, regeneration percentage and current efficiency at the optimal current density of 4.10 A/m^2 for an extended electrolysis. Results indicate that the current efficiency markedly drops after three hours of electrolysis, and correspondingly, the regeneration rate of Fe(II) decreases. The total potential drop exhibits a slight increase with time because the reduction of Fe(III) to Fe(II) decreases the solution conductance.

Comparing the results obtained in both modes, it is seen that the decrease of Fe(II) regeneration rate is mainly due to the automatic decrease of current density in the constant

potential method; while in the constant current method, the decrease of Fe(II) regeneration rate is due to the drop of current efficiency. Before reaching the 75% of regeneration capacity, Fe(II) can be effectively regenerated. In the EF processes, the dissolved iron is mainly composed of Fe(III) due to the presence of H_2O_2. This will lead to a fast Fe(II) regeneration at a high current efficiency. In the Fenton's sludge recycling system, a 75% of Fe(II) regeneration percentage is also acceptable for field application.

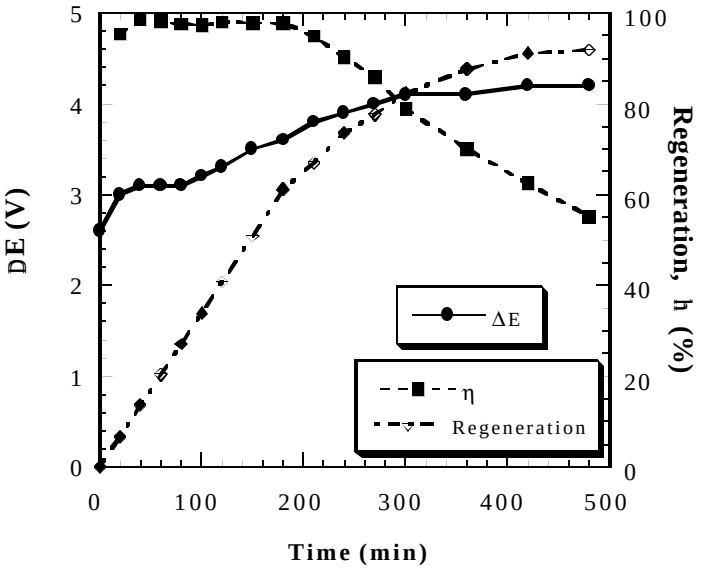

Figure 3.38. Long-term regeneration of Fe(II) using constant current mode. Experimental conditions: i = 4.10 A/m^2, [Fe^{3+}]$_0$ = 500 mg/L, pH$_0$ = 2, T = 30 ^{o}C, ionic strength = 0.05M NaClO$_4$, long-finger plate cathode.

3.3.9. Comparison of Fe(II) Regeneration from Ferric Salt and Fenton's Sludge

The Fenton's sludge was prepared by reaction between H_2O_2 and Fe^{2+} at a molar ratio of 1:1 at pH 3, precipitation by adjusting pH to 8~9, and phase separation. The sludge was then dissolved in distilled water containing 0.05 M $NaClO_4$ as background ionic strength by pH adjustment to obtain a certain ferric concentration. It was observed that a much lower pH was required for sludge dissolution than the hydrolysis-determined pH value at an idnetical ferric concentration. For example, the hydrolysis of 2500 and 5000 mg/L of Fe^{3+} from ferric nitrate gave a solution pH value of 1.85 and 1.61, respectively. However, to dissolve identical amounts of Fenton's sludge, the pH values were approximately 1.02 and 0.81. According to Stumm

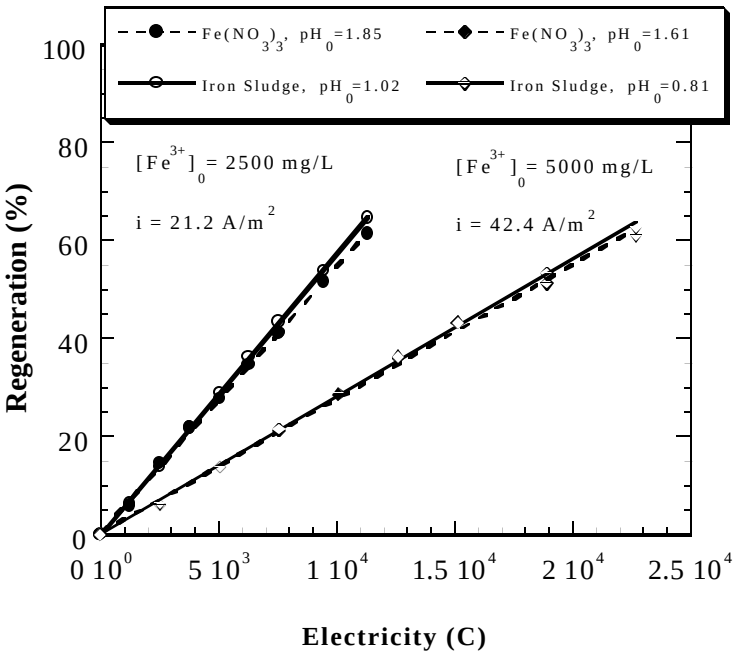

Figure 3.39. Regeneration of Fe(II) from Fe(NO$_3$)$_3$ and Fenton's sludge using constant current mode. Experimental conditions: i = 4.10 A/m^2, T = 30 ^{o}C, ionic strength = 0.05M NaClO$_4$, long-finger plate cathode.

and Morgan (1981), in the hydrolysis of a ferric salt, the hydrolysis species are in a condition of metastable oversaturation. Only after standing for days or weeks, solid $Fe(OH)_3(s)$ will precipitate. However, in the dissolution of the Fenton's sludge, the heterogeneous equilibria exist between $Fe(OH)_3(s)$ and dissolved ferric hydroxo species. Furthermore, the "aging" process will convert active amorphous $Fe(OH)_3(s)$ to more stable solid modifications, such as α-FeOOH and α-Fe_2O_3. Therefore, a lower pH is required for Fenton's sludge dissolution. This is consistent with that reported by Gnann *et al.* (1993) who reported that the dissolution of Fenton's sludge was only obtained at pH < 1.

Figure 3.39 shows the comparison of Fe(II) regeneration from ferric nitrate and Fenton's sludge at ferric concentrations of 2500 and 5000 mg/L, using the constant current mode. The current densities applied were calculated by multiplying the ferric concentration by the previously determined slope of 8.48×10^{-3} $(A/m^2)(mg/L)^{-1}$, i.e., 21.2 and 42.4 A/m^2 for ferric concentrations of 2500 and 5000 mg/L, respectively. Results indicate that there is little difference in Fe(II) regeneration between the two ferric sources, except different initial pH values. As long as Fe(III) is totally dissolved, Fe(II) can be effectively regenerated. Results also imply that the i-$[Fe^{3+}]_0$ slope determined in Figure 3.34 is well obeyed, at least up to $[Fe^{3+}]_0$ = 5000 mg/L. The effective regeneration of Fe(II) from Fenton's sludge proves that the FRS is a feasible process for recycling Fe(II). Though the regenerated Fe(II) solution has a very low pH value (< 1), it can be used to adjust the pH of influent wastewater for Fenton's oxidation.

3.3.10. Energy consumption

The energy consumption was assessed at the initial Fe(III) concentrations of 2,500 and 5,000 mg/L, as summarized in Table 3.3. As the applied current density increases linearly with increasing $[Fe^{3+}]_0$, the average total potential drop (ΔE) does not increase proportionally because of the increase of solution conductance. Results indicate that the unit energy consumption is 2.05 and 2.96 kWh per kg Fe(II) regenerated for $[Fe^{3+}]_0$ = 2,500 and 5,000 mg/L, respectively. Obviously, this energy consumption is considerably low.

Table 3.3. Assessment of energy consumption.

Initial Fe(III) concentration (mg/L)	2,500	5,000
Current density applied (A/m^2)	21.2	42.4
Average total potential drop (V)	4.3	6.0
Regeneration percentage (%)	65	63
Unit energy consumption (kWh/kg Fe(II))	2.05	2.96

Notation: effective cathode surface area = 4.88×10^{-2} m^2,
electrolysis time = 3 hours.

3.4. Conclusions

This paper classified various types of Fenton's oxidation processes based on different sources of H_2O_2 and Fe(II), and the processes for individual electro-generation of H_2O_2 or Fe(II). It is seen that the application of Fenton's oxidation processes is mainly limited by the generation of iron sludge. The present study investigated the regeneration of Fe(II) from ferric salt or Fenton's sludge by electro-reduction of Fe(III) ions for the purpose of both dose

reduction of ferrous salt and reuse of Fenton's sludge. The effects of operational parameters, such as cathodic potential, current density, solution pH, cathode surface area, solution temperature and initial ferric concentration, were systematically investigated. Based on the experimental results presented above, following conclusions can be drawn:

- The optimal cathodic potential for Fe(II) regeneration is –0.1 V vs. SCE, and the average current density at this potential is approximately equal to the optimal current density in the constant current mode.
- The suitable pH range is below the pH value controlled by ferric hydrolysis.
- Increasing cathode surface area and solution temperature markedly increases Fe(II) regeneration rate.
- At the optimal potential, the average current density increases linearly with initial ferric concentration, exhibiting a slope of 8.48×10^{-3} $(A/m^2)(mg/L)^{-1}$.
- The maximum current efficiency achieved is 96~98%.
- Fe(II) can also be effectively regenerated from Fenton's sludge though the sludge dissolution requires pH < 1.
- Oxygenation of Fe(II) by pure oxygen gas is kinetically negligible at pH < 4.
- The energy consumption is about 1.6 kWh per kg Fe(II) regenerated.

3.5. References

1. Alvarez-Gallegos A. and Pletcher D. (1999) The removal of low level organics via hydrogen peroxide formed in a reticulated vitreous carbon cathode cell. Part 2: The removal of phenols and related compounds from aqueous effluents. *Electrochim. Acta*, **44** (14): 2483-2492.
2. Brillas E., Mur E. and Casado J. (1996) Iron (II) catalysis of the mineralization of aniline using a carbon-PTFE O2-fed cathode. *J. Electrochem. Soc.*, **143** (3): L49-53.
3. Brillas E., Sauleda R. and Casado J. (1997) Peroxi-coagulation of aniline in acidic medium using an oxygen diffusion cathode. *J. Electrochem. Soc.*, **144** (7): 2374-2379.
4. Brillas E., Sauleda R. and Casado J. (1998) Degradation of 4-chlorophenol by anodic oxidation, electro-Fenton, photoelectro-Fenton, and peroxi-coagulation processes. *J. Electrochem. Soc.*, **145** (3): 759-765.
5. Brillas E., Mur E., Sauleda R., Sanchez L., Peral J., Domenech X. and Casado J. (1998) Degradation of 4-chlorophenol by anodic oxidation, electro-Fenton, photoelectro-Fenton, and peroxi-coagulation processes. *Appl. Cata. B: Environ.*, **16**: 31-42.
6. Cermenati L., Pichat P., Guillard C. and Albini A. (1997) Probing the TiO_2 photocatalytic mechanisms in water purification by use of quinoline, photo-Fenton generated $OH\cdot$ radicals and superoxide dismutase. *J. Phys. Chem. B*, **101**: 2650-2658.
7. Choi H. J. (1998) *Evaluation of Fenton's process for the treatment of landfill leachate.* Ph.D. dissertation, University of Delaware, Newark, DE.
8. Chou S., Huang Y. H., Lee S. N., Huang G. H. and Huang C. P. (1999) Treatment of high strength hexamine-containing wastewater by electro-Fenton method. *Wat. Sci. Tech.*, **33** (3): 751-759.
9. Chu C. H. (1995) *The electrochemical oxidation of recalcitrant organic compounds*. Ph.D. dissertation, University of Delaware, Newark, DE.
10. Delatt J. and Gallard H. (1999) Catalytic decomposition of hydrogen peroxide by Fe(III) in homogeneous aqueous solution: mechanism and kinetic modeling. *Environ. Sci. Technol.*, **33**: 2726-2732.

11. DeLeon C. P. and Pletcher D. (1995) Removal of formaldehyde from aqueous-solutions via oxygen reduction using a reticulated vitreous carbon cathode cell. *J. Appl. Electrochem.*, **25** (4): 307-314.
12. Do J. S. and Chen C. P. (1993) In situ oxidative degradation of formaldehyde with electrogenerated hydrogen peroxide. *J. Electrochem. Soc.*, **140** (6): 1632-1637.
13. Gnann M., Gregor C. H. and Schelle S. (1993) Chemical oxidative process for purifying highly contaminated wastewater. *WO patent 93/08/29*, Peroxide-Chemie GmbH, Germany.
14. Hsiao Y. L. and Nobe K. (1993) Hydroxylation of chlorobenzene and phenol in a packed bed flow reactor with electrogenerated Fenton's reagent. *J. Appl. Electrochem.*, **23**: 943-946.
15. Hsiao Y. L. and Nobe K. (1993) Oxidative reactions of phenol and chlorobenzene with in situ electrogenerated Fenton's reagent. *Chem. Eng. Comm.*, **126**: 97-110.
16. Huang Y. H., Chou S., Perng M. G., Huang G. H. and Cheng S. S. (1999) Case study on the bioeffluent of petrochemical wastewater by electro-Fenton method. *Wat. Sci. Tech.*, **39** (10-11): 145-149.
17. Huston P. L. and Pignatello J. J. (1996) Reduction of perchloroalkanes by ferrioxalate-generated carboxylate radical preceding mineralization by the photo-Fenton reaction. *Environ. Sci. Technol.*, **30** (12): 3457-3463.
18. Kim Y. K. and Huh I. R. (1997) Enhancing biological treatability of landfill leachate by chemical oxidation. *Environ. Eng. Sci.*, **14** (1): 73-79.
19. Kuo W. G. (1992) Decolorizing dye wastewater with Fenton's reagent. *Wat. Res.*, **21** (2): 187-191.
20. Lindsey M. E. and Tarr M. A. (2000) Inhibition of hydroxyl radical with aromatics by dissolved natural organic matter. *Environ. Sci. Technol.*, **34** (3): 444-449.
21. Lou J. C. and Lee S. S. (1995) Chemical oxidation of BTX using Fenton's reagent. *Haz. Waste & Haz. Mater.*, **12** (2): 185-193.
22. Matsue T., Fujihira M. and Osa T. (1981) Oxidation of alkylbenzenes by electrogenerated hydroxyl radical. *J. Electrochem. Soc.: Electrochem. Sci. Tech.*, **128** (12): 2565-2569.
23. Mohanty N. R. and Wei I. W. (1993) Oxidation of 2,4-dinitrotoluene using Fenton's reagent: reaction mechanisms and their practical applications. *Haz. Waste & Haz. Mater.*, **10** (2): 171-183.
24. Nadtochenko V. and Kiwi J. (1998) Primary photochemical reactions in the photo-Fenton system with ferric chloride. 1. A case study of xylidine oxidation as a model compound. *Environ. Sci. Technol.*, **32**: 3273-3281.
25. Oloman C. and Watkinson A. P. (1975) Electroreduction of oxygen to hydrogen-peroxide on fluidized cathodes. *Can. J. Chem. Eng.*, **53** (3): 268-273.
26. Oloman C. and Watkinson A. P. (1976) Electroreduction of oxygen to hydrogen-peroxide on fixed-bed cathodes. *Can. J. Chem. Eng.*, **54** (4): 312-318.
27. Oloman C. and Watkinson A. P. (1979) Hydrogen-peroxide generation in trickle-bed electrochemical reactors. *J. Appl. Electrochem.*, **9** (1): 117-123.
28. Oturan M. A., Aaron J. J., Oturan N. and Pinson J. (1999) Degradation of chlorophenoxyacid herbicides in aqueous media, using a novel electrochemical method. *Pestic. Sci.*, **55**: 558-562.

29. Oturan M. A., Pinson J., Traikia M. and Deprez D. (1999) The electrochemical oxidation of Riluzole, a neuroprotective drug: comparison with the reaction with oxygen derived radicals. *J. Chem. Soc.: Perkin Trans.*, **2**: 619-622.
30. Oturan M. A., Pinson J., Oturan N. and Deprez D. (1999) Hydroxylation of aromatic drugs by the electro-Fenton method: formation and identification of the metabolites of Riluzole. *New J. Chem.*, **23**: 793-794.
31. Pignatello J. J. and Sun Y. F. (1995) Complete oxidation of metolachlor and methyl parathion in water by the photoassisted Fenton Reaction. *Wat. Res.*, **29** (8): 1837-1844.
32. Pignatello J. J. (1992) Dark and photoassisted Fe^{3+}-catalyzed degradation of chlorophenoxy herbicides by hydrogen peroxide. *Environ. Sci. Technol.*, **26**: 944-951.
33. Pletcher D. (1999) Indirect oxidations using electrogenerated hydrogen peroxide. *Acta Chemica Scandinavica*, **53**: 745-750.
34. Qiang Z., Chang J. H. and Huang C. P. (2001) Electrochemical generation of hydrogen peroxide from dissolved oxygen in acidic solutions. *Wat. Res.* (Submitted).
35. Qiang Z., Chang J. H., Huang C. P. and Cha D. (2001) Oxidation of selected polycyclic aromatic hydrocarbons by the Fenton's reagent: effect of major factors including organic solvent. *ACS/EMSP symposium proceedings book*, 218th ACS National Meeting and Exposition Program, New Orleans, LA.
36. Ruppert G. and Bauer R. (1993) Mineralization of cyclic organic water contaminants by the photo-Fenton reaction-influence of structure and substituents. *Chemosphere*, **27** (8): 1339-1347.
37. Ruppert G. and Bauer R. (1994) UV-O_3, UV-H_2O_2, UV-TiO_2 and the photo-Fenton reaction – comparison of advanced oxidation processes for wastewater treatment. *Chemosphere*, **28** (8): 1447-1454.
38. Sedlak D. L. and Andren A.W. (1991) Aqueous-phase oxidation of polychlorinated-biphenyls by hydroxyl radicals. *Environ. Sci. Technol.*, **25** (8): 1419-1427.
39. Silver J. (1993) *Chemistry of Iron*, p12. Blackie Academic & Professional: Glasgow G64 2NZ, UK.
40. Stumm W. and Morgan J. J. (1981) *Aquatic Chemistry: An Introduction Emphasizing Chemical Equilibria in Natural Waters, 2nd edition*, p113, 236, 338, 467. John Wiley & Sons, Inc.: New York, NY.
41. Sudoh M., Kitaguchi H. and Koide K. (1985) Electrochemical generation of hydrogen peroxide by reduction of oxygen. *J. Chem. Eng. Japan*, **18** (5): 409-414.
42. Sudoh M., Kodera T., Sakai K., Zhang J. Q. and Koide K. (1986) Oxidative degradation of aqueous phenol effluent with electrogenerated Fenton's reagent. *J. Chem. Eng. Japan*, **19** (6): 513-518.
43. Sudoh M., Kodera T., Hino H. and Shimamura S. (1988) Effect of anodic and cathodic reactions on oxidative degradation of phenol in an undivided bipolar electrolyzer. *J. Chem. Eng. Japan*, **21** (2): 198-203.
44. Sudoh M., Kodera T., Hino H. and Shimamura S. (1991) Transport properties of anion-exchange membrane prepared for producing hydrogen peroxide in acidic solutions by electrodialysis of peroxide ions. *J. Chem. Eng. Japan*, **25** (2): 170-176.
45. Tamura H., Goto K., Yotsuyanagi T. and Nagayama M. (1974) Spectrophotometric determination of iron(II) with 1,10-phenanthroline in the presence of large amounts of iron(III). *Talanta*, **21**: 314-318.

46. Tang W. Z. and Huang C. P. (1997) Stoichiometry of Fenton's reagent in the oxidation of chlorinated aliphatic organic pollutants. *Environ. Tech.*, **18**: 13-23.
47. Tzedakis T., Savall A. and Clifton M. J. (1989) The electrochemical regeneration of Fenton's reagent in the hydroxylation of aromatic substrates: batch and continuous processes. *J. Appl. Electrochem.*, **19**: 911-921.
48. Wendt H. and Kreysa G. (1999) *Electrochemical Engineering: Science and Technology in Chemical and Other Industries*, p53. Springer-Verlag: Berlin, Germany.
49. Yamada N., Yaguchi T., Otsuka H. and Sudoh M. (1999) Development of trickle-bed electrolyzer for on-site electrochemical generation of hydrogen peroxide. *J. Electochem. Soc.*, **146** (7): 2587-2591.

4. REMOVAL OF SELECTED POLYCYCLIC AROMATIC HYDROCARBONS (PAHS) BY CONVENTIONAL FENTON OXIDATION PROCESS

4.1. Introduction

Polycyclic aromatic hydrocarbons (PAHs) belong to a typical group of hazardous organic contaminants commonly found at waste sites. They are major byproducts of incomplete thermal combustion of fossil fuels. Automobile exhausts, power plants, chemical, coke and oil-shale industries, urban sewage (Trapido et al., 1995), cigarette smoke and charcoal grilled foods (Watts, 1998) are the major emission sources of environmental PAHs. PAHs are also found in the heavier fractions of petroleum products, e.g., lubricating oils, asphalt, and tarlike materials (Watts, 1998). Accidental petroleum spills and leaking of underground petroleum storage tanks can seriously contaminate surrounding soils and groundwater with PAHs. It is estimated that the U.S. Air Force alone needs to remediate more than 2000 petroleum contaminated sites (Miller, 1994). Many PAHs are known to be carcinogenic or potentially carcinogenic to animals and probably to humans (Menzie et al., 1992). Sixteen PAHs are listed as the U.S. EPA priority pollutants (Keith and Telliard, 1979). The U.S. EPA has imposed a maximum contaminant level (MCL) for total PAHs in drinking water at 0.2μg/L (Sayre, 1988).

Fenton's reagent is a reaction system consisting of H_2O_2 and Fe^{2+} ion. Under acidic conditions and in the presence of Fe^{2+}, H_2O_2 is decomposed to hydroxyl radical. The hydroxyl radical (·OH) is an intermediate species characterized by an unpaired electron. The one-electron deficiency of the hydroxyl radical results in its transient and highly oxidizing characteristics, with a redox potential being only next to elemental fluorine (Huang et al., 1993). The hydroxyl radical can nonselectively oxidize most organic compounds as well as inorganic chemicals through a chain reaction mechanism. The oxidation mechanism of the hydroxyl radical was first proposed Haber and Weiss (1934), and further clarified by Walling and co-researchers (1970, 1975) using competitive reaction theory. Major reactions taking place in the system are shown as follows (Walling, 1975):

$$Fe^{2+} + H_2O_2 \rightarrow Fe^{3+} + \cdot OH + OH^-, \; k_1 \qquad (4.1)$$

$$H_2O_2 + \cdot OH \rightarrow HO_2 \cdot + H_2O, \; k_2 \qquad (4.2)$$

$$Fe^{2+} + \cdot OH \rightarrow Fe^{3+} + OH^-, \; k_3 \qquad (4.3)$$

$$RH + \cdot OH \rightarrow R\cdot + H_2O, \; k_4 \qquad (4.4)$$

$$R\cdot + Fe^{3+} \rightarrow Fe^{2+} + product \qquad (4.5)$$

$$R\cdot + Fe^{2+} \rightarrow Fe^{3+} + R^- \xrightarrow{H^+} RH \qquad (4.6)$$

$$R\cdot + R\cdot \rightarrow product \;\; \text{(dimer)} \qquad (4.7)$$

where, $k_1 = 76\ M^{-1}\cdot s^{-1}$ (Walling, 1975),
$k_2 = 3\times10^8\ M^{-1}\cdot s^{-1}$ (Walling, 1975),
$k_3 = 2.7\times10^7\ M^{-1}\cdot s^{-1}$ (Buxton et al., 1988),
$k_4 = 10^7\text{-}10^{10}\ M^{-1}\cdot s^{-1}$ (Dorfman and Adams, 1973).

Reaction 4.1 produces hydroxyl radicals, initiating a series of chain reactions. Compared with the reactivity of hydroxyl radical toward most organic compounds (k_4), ferrous ion (k_2) and hydrogen peroxide (k_3), the production rate of hydroxyl radical (k_1) is very small. Therefore, the overall reaction rate is dominated by Reaction 4.1. Both H_2O_2 and Fe^{2+} compete for hydroxyl radicals at a moderate rate constant. They are known as "scavengers" for hydroxyl radicals. Other common inorganic scavengers in aqueous solution include bicarbonate, carbonate, and chloride. The organic radical produced in Reaction 4.4 may be oxidized by Fe^{3+} to regenerate Fe^{2+}, or be reduced by Fe^{2+} to reform the parent compound under acid catalysis, or dimerize at a high initial organic concentration.

Generally, most organic compounds react with hydroxyl radicals at a rate constant of 10^9~10^{10} $M^{-1}\cdot s^{-1}$ (Watts, 1998). The high rate constant allows target organic contaminant to be preferably oxidized in the competitive environment. Due to the unselective oxidation nature of the hydroxyl radical, Fenton's reagent has been extensively studied as a technology of advanced oxidation processes (AOP) for the treatment of various hazardous organic compounds. These include but not inclusively, chlorinated aromatic hydrocarbons (Sedlack and Andren, 1991), phenolic compounds (Hayek and Dore, 1990), microorganism-refractory organics in wastewater (Spencer et al., 1992), and dye wastewater (Kuo, 1992). Watts and co-researchers (1990, 1991, 1994) have used Fenton's reagent to oxidize pentachlorophenol, octachlorodibenzo-p-dioxin and hexachlorobenzene in silica sands or natural soils.

Extensive research effort has been made to study the oxidation of PAHs with ozone (Sturrock et al., 1963; Bailey et al., 1964; Legube et al., 1984, 1986). Most of their experiments were conducted in organic solvents and at high PAHs concentrations. The extremely low water solubility of PAHs makes the study of PAHs ozonation in water considerably difficult. Therefore, methanol, acetone and octane were frequently used as participating solvents to increase the solubility of PAHs. However, the influence of organic solvent on the degradation of PAHs has not been investigated. The rate constants so obtained may not totally reflect the oxidation behavior of PAHs in the aqueous solution. Many byproducts by the ozonation of naphthalene and phenanthrene have been identified (Legube et al., 1984, 1986; Sturrock et al., 1963). The degree of mineralization of PAHs is considerably low. Fenton's reagent is a more attractive oxidation agent than ozone. It is stronger and it does not have mass transfer limitation. Therefore, it is expected that a higher degree of mineralization may be obtained.

Some specific DOE sites are significantly contaminated by PAHs. Current in-situ remediation technologies include hydrodynamic or physical barrier, solidification or stabilization, soil vapor extraction (soil venting) and bioventing. Clearly, only the bioventing process can destroy the contaminants. Other processes provide only temporary solutions, i.e., either containment or phase transfer. However, the bioventing process is not suitable for the silt-laden or clay soils that have a low hydraulic conductivity, e.g., $< 10^{-5}$ cm/sec (Destephen et al., 1994). Under such circumstance, the transport of chemical species, i.e., gas, water and nutrients, in the subsurface is significantly limited. Therefore, innovative technologies are urgently needed for in-situ remediation of low permeability soils. This has prompted us to study an electro-chemical technology for in-situ applications. The total project integrates the electro-kinetic process with the electro-Fenton oxidation process. The electro-kinetic process removes hazardous contaminants from subsurface soils, and the followed electro-Fenton process decomposes the released contaminants in the aqueous solution. Additionally, the electro-Fenton process can also be coupled with pump and treat, soil washing and soil

flushing processes for the treatment of hazardous organic contaminants on-site or off-site. In this study, we only focus on the degradation of selected PAHs by conventional Fenton process. The optimal conditions and the reaction kinetics of the degradation of selected PAHs, namely, naphthalene, fluorene, phenanthrene, fluoranthene, pyrene and anthracene using Fenton oxidation process were investigated. Several media-assisted dissolution methods for the preparation of reaction solutions were developed. Furthermore, the effect of organic solvent, exemplified by methanol and ethanol, on the degradation of PAHs was also studied.

4.2. Materials and Methods

4.2.1. Chemicals

All selected PAHs, namely, naphthalene (99.5%), fluorene (98%), phenanthrene (98%), fluoranthene (98%), pyrene (98%) and anthracene (97%) were purchased from the Aldrich Chemical Company (Milwaukee, WI). They were used without further purification. Hydrogen peroxide and ferrous sulfate were purchased from the Fisher Scientific Company with a content of 31.5% and 98%, respectively. H_2O_2 and $FeSO_4$ solutions were stored in acidic conditions in a refrigerator (4 ^oC) after preparation. At low pH and temperature, H_2O_2 and $FeSO_4$ can be sufficiently preserved for several weeks.

Table 4.1 lists the important physical-chemical properties of selected PAHs. Naphthalene is bicyclic; fluorene, phenanthrene and anthracene are tricyclic; and fluoranthrene and pyrene are tetracyclic. Furthermore, phenanthrene and anthracene are isomers. Based on water solubility and octanol/water partition coefficient, it is seen that all selected PAHs are hydrophobic. Naphthalene has a relatively large water solubility, around 32 ppm, while all other PAHs have a water solubility of less than 2 ppm. The negative Henry's constants (log) indicate that the volatilization of PAHs is negligible. Naphthalene is semi-volatile, whereas other PAHs are non-volatile. Experimental conditions such as vigorous stirring may facilitate the volatilization of the semi-volatile compound, i. e., naphthalene. We have discovered that by stirring the naphthalene solution with an initial concentration of 27 ppm in an open beaker, will volatize all naphthalene into air within 20 minutes. Therefore, a closed reactor without headspace is necessary for naphthalene oxidation experiments. For other non-volatile PAHs, volatilization is negligible even under vigorously stirring conditions.

Table 4.1. Major physical-chemical properties of selected PAHs (Schwarzenbach et al., 1993).

Compound	*Chem. Struct.*	*Wat. Solub. @ 25 ^oC (mg/L)*	*LogK_H @25 ^oC (atm$\cdot M^{-1}$)*	*Log K_{ow} @ 25 ^oC*
Naphthalene		31.9	-0.37	3.36
Fluorene		1.84	-1.14	4.18
Phenanthrene		1.09	-1.59	4.57
Anthracene		0.06	-1.64	4.54
Fluoranthene	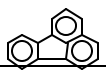	0.23	-1.98	5.22

Pyrene		0.13	-2.05	5.13

4.2.2. Reaction System

Figure 4.1 illustrates the laboratory setup of the reaction system. A closed, double-jacketed glass reactor with a total volume of 600 mL was used to conduct oxidation experiments. The reactor was completely stirred. A pH controller was used to maintain constant solution pH through intermittent additions of NaOH (1M) or $HClO_4$ (1M) solutions. Since Cl^- is a known hydroxyl radical scavenger, $HClO_4$ was used instead of HCl for pH adjustment. Default experimental conditions were ambient room temperature (23^oC), 0.05M $NaClO_4$ ionic strength and pH 3, unless otherwise stated.

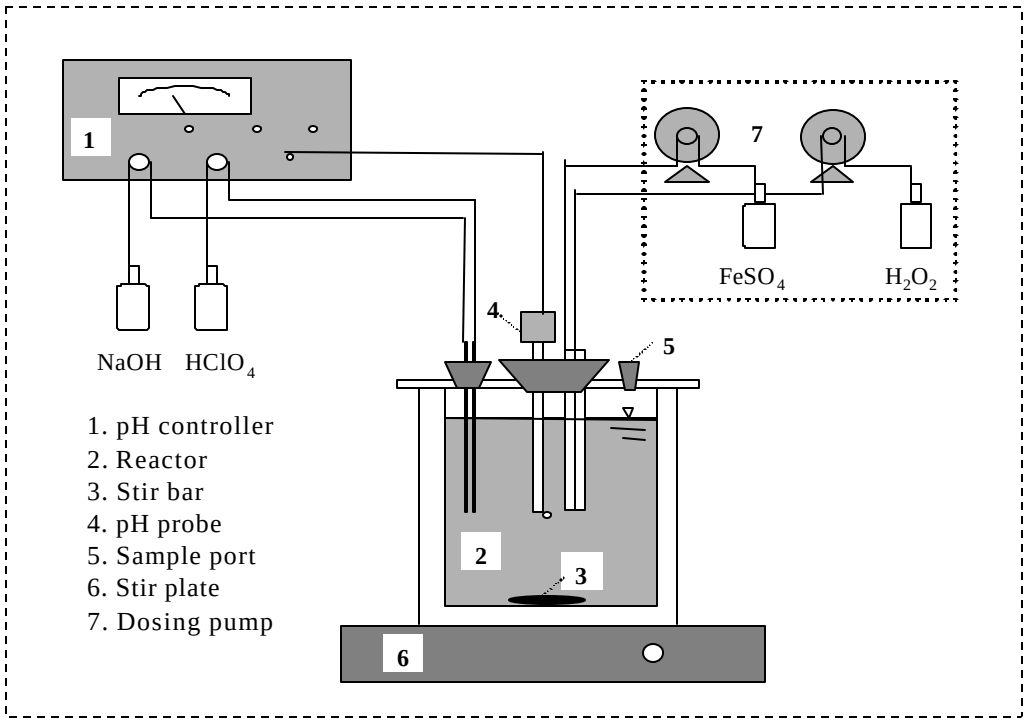

Figure 4.1. Schematic diagram of Fenton oxidation system.

In order to evaluate the effect of dosing mode on the oxidation of PAHs, three different dosing modes, namely, batch, pseudo-continuous and continuous modes were employed to deliver the Fenton's reagent into the reactor. In the batch mode, both H_2O_2 and Fe^{2+} were singly added at the beginning of reaction. In the pseudo-continuous mode, either H_2O_2 or Fe^{2+} was singly added at the beginning of reaction, whereas the other reagent was continuously delivered using a fine-flowrate dosing pump. In the continuous mode, both H_2O_2 and Fe^{2+} were continuously delivered using two separate dosing pumps. Since the Fenton process consists of a series of competitive reactions, it is expected that the concentrations of H_2O_2 and Fe^{2+} will affect their ability to compete for hydroxyl radicals. As a result, the reaction kinetics of PAHs will be changed. Another consideration is the volatility of PAHs. Naphthalene is considerably volatile under the experimental conditions. In order to minimize its evaporation, 600 mL solution was used with zero initial headspace. It is noted

that the headspace would vary a little during the reaction period caused by sample withdraws and chemical additions. However, the volume fluctuation is negligible compared to the relatively large volume of the original solution. All rubber stoppers were wrapped in Teflon tape to avoid loss of organic due to adsorption onto the rubber surface. For other non-volatile PAHs such as fluorene, phenanthrene, fluoranthene, pyrene and anthracene, 500 mL solution was used with 100 mL reactor headspace.

4.2.3. Chemical Analysis

The selected PAHs were first extracted by hexane and then analyzed by gas chromatograph with mass spectrometry (GC/MS, Hewlett Packard; GC model 5890, MS model 5972). A HP-1MS capillary column (cross-linked 5% Ph Me silicon, 30m x 0.25mm x 0.25μm) was used to separate organic compounds. The extremely low water solubility of all selected PAHs makes chemical analysis difficult. However, PAHs can produce very stable molecular ions under EI ionization mode in the MS detector due to their stable fused-ring structures. This characteristic makes GC/MS considerably sensitive for detecting PAHs compounds, with a detection limit of about 100 ppb. The concentrating factor of hexane extraction is compound specific, i.e., depends on water solubility. Naphthalene, fluorene, phenanthrene, fluoranthene, pyrene and anthracene were concentrated by 1, 2.5, 2.5, 5, 20 and 20 times, respectively. Preliminary experiments show that the recovery efficiency of hexane extraction is greater than 95% for all PAHs studied. Chemical oxygen demand (COD) was determined using a Hach spectrometer (Hach DR/2000, Loveland, CO) at an absorbance wavelength of 420 nm. The concentrations of H_2O_2 and Fe^{2+} were determined by measuring the light absorbance after chelating with certain reagents using a HP diode array spectrophotometer (8452A) at 410nm and 510nm, respectively. H_2O_2 chelates with titanic ion, forming an orange complex. Fe^{2+} chelates with 1,10-phenanthroline, forming an orange-red complex (Standard Methods for the Examination of Water and Wastewater, 3500-Fe D, 1995).

4.2.4. Media-assisted Dissolution Methods

In order to accelerate the dissolution process of selected PAHs, three media-assisted dissolution methods were investigated and compared. Phenanthrene was selected as a model compound for dissolution study. Methanol, glass-beads, and hexane were separately used to enhance phenanthrene dissolution. Methanol, miscible with water, can easily dissolve hydrophobic organic compounds. Hexane is an organic solvent, but immiscible with water. Glass beads (No. 50 sieve size) provide large surface area for the partitioning of phenanthrene, thus accelerate phenanthrene dissolution.

In the methanol method, 1mL phenanthrene/methanol solution (1.5mg phenanthrene /mL methanol) was spiked to 1L distilled water. After vigorously stirring for 1 hour, followed by vacuum filtration to remove solid phenanthrene residue, the reaction solution was obtained. All methanol remained in the solution with a volume fraction of 0.1% (about 790 ppm). In the glass beads method, 3mL phenanthrene/methanol solution was spiked to 10g glass beads. After methanol completely evaporated, the glass beads with fine phenanthrene crystals adsorbing on the surface were transferred into 1L distilled water. The reaction solution was obtained by vigorously stirring and vacuum filtration. No methanol was detected by GC/FID in the final solution. In the hexane method, 1mL phenanthrene/hexane solution (4.5mg phenanthrene /mL hexane) was spiked to 1L distilled water which was preheated to 75~80 ^{o}C.

Preheating can not only increase the evaporation rate of hexane but also increase the initial dissolution rate of phenanthrene. After vigorously stirring for 20 minutes in an open flask, all hexane evaporated into air. By determining the aqueous concentration of phenanthrene at different times, the dissolution kinetics could be obtained. For the purpose of comparison, the blank experiment without any media assistance was also conducted. Figure 4.2 shows the kinetics of phenanthrene dissolution with or without media assistance. Results indicate that the dissolution of phenanthrene in the blank experiment is considerably slow. It may take weeks to obtain a nearly saturated solution. However, both glass beads and hexane can significantly enhance the dissolution rate of phenanthrene. After 2 hours, a relative concentration of 85% can be obtained in both methods. In the hexane method the successive vacuum filtration is very fast, while in the glass-beads method the filtration is very difficult because the broken glass fragments severely clog up the filter paper (0.45 μm).

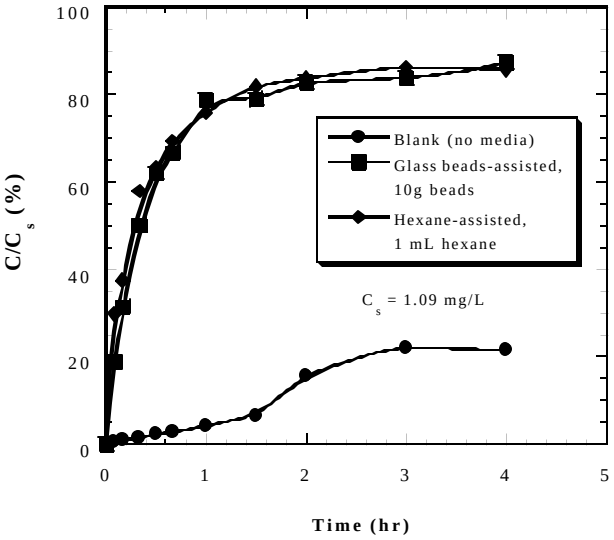

Figure 4.2. Phenanthrene dissolution as a function of time by different methods.

Based on above results, hexane is a better medium for preparing PAHs solutions than glass beads. In our experiments, all PAHs solutions without organic solvent were prepared by the hexane method. Meanwhile, the methanol method is suitable for preparing PAHs/methanol (analogously PAHs/ethanol) solutions when investigating the influence of organic solvent.

4.3. Results and Discussion

4.3.1. Effect of pH

The effect of pH on the oxidation of naphthalene was evaluated at pH 2, 3, 5, 9 and 12 with continuous dosing mode. Results in Figure 4.3 show that the optimal pH value is around 3. In basic conditions, the oxidation efficiency decreases dramatically. It is well known that the solubility of both Fe^{2+} and Fe^{3+} ions decreases markedly as pH increases. Moreover, at high pH values Fe^{2+} may be readily oxidized to Fe^{3+} by dissolved oxygen and loses its catalytic ability. Another possibility is that H_2O_2 may be unstable at alkaline pH values. However, our previous

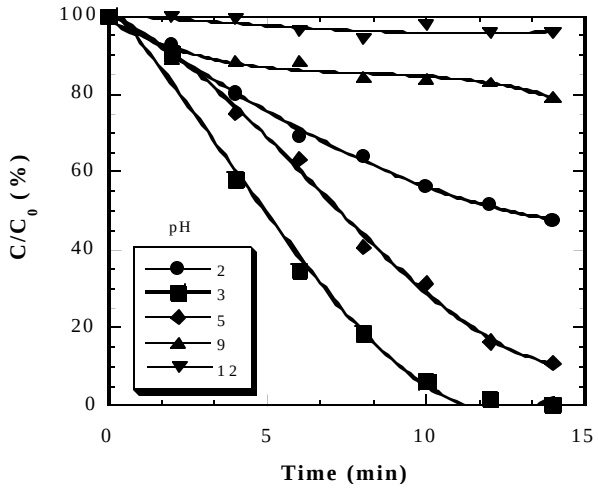

Figure 4.3. Effect of pH on oxidation of naphthalene. Experimental conditions: continuous dosing mode, H_2O_2 dosing rate = 1.16×10^{-4} M/min, Fe^{2+} dosing rate = 5.78×10^{-5} M/min, $C_{0,naph}$ = 0.18~0.20 mM, ionic strength = 0.05M $NaClO_4$.

results (Figure 2.5) show that H_2O_2 self-decomposition can be ruled out as a possible reaction step in such a short reaction time (15 min). Therefore, the low efficiency of Fenton's reagent at alkaline pH values can only be attributed to insufficient soluble iron(II) in the solution. It is also noted that the oxidation efficiency decreases again at pH 2. In highly acidic conditions, the aromatic radicals generated by the hydroxyl radical (Reaction 4.4) may be reduced by Fe^{2+}, and then under acid catalysis reform the parent compound (Reaction 4.6). Therefore, less substrate is decomposed.

Schumb (1949) reported that the decomposition rate of H_2O_2 reaches the maximum at pH 3.5. With the progressive hydrolysis of ferric ions, the hydrolysis product provides a relatively large catalytically active surface for contact with H_2O_2. Therefore, the decomposition of H_2O_2 is accelerated, and more hydroxyl radicals are produced. Watts *et al.* (1990) also pointed out that the Fenton's reaction proceeds most effectively at pH 2-4. The acidic condition maintains iron stability and lowers the redox potential of the system, which promotes the most efficient generation of hydroxyl radicals (Watts *et al.*, 1990). Latt *et al.* (1999) investigated the effect of pH on the pseudo-first-order rate constant (k_{obs}) for the initial rate of decomposition of H_2O_2 by Fe (III). His results indicate that k_{obs} reaches the maximum at pH 3.2, which is approximately 100 times that at pH 1, and 5 times that at pH 2. Therefore, the optimal pH value for the Fenton's reagent oxidation is generally around pH 3.

4.3.2. Degree of Mineralization

The chemical oxygen demand (COD) is used as an indicator for the degree of mineralization. The COD removal efficiency versus naphthalene degradation is shown in Figure 4.4. It should be mentioned that both H_2O_2 and Fe^{2+} can be oxidized by potassium dichromate, thus exerting a certain amount of COD. The corresponding COD equivalence is 0.471 mg O_2 / mg H_2O_2 and 0.143 mg O_2 / mg Fe^{2+}. The COD removal efficiencies in Figure 4.4 have been corrected by subtracting the contributions from H_2O_2 and Fe^{2+}. Results indicate that most of naphthalene can be oxidized to carbon dioxide and water. The COD removal rate lags behind the naphthalene degradation rate due to the formation of reaction intermediates. It also means that the intermediates are less reactive and possibly refractory toward hydroxyl radicals. When naphthalene is completely oxidized, only 50% COD is removed. The COD removal efficiency increases further when additional Fenton's reagent is added. The final degree of mineralization is around 85%. There is still 15% COD remaining in the solution that can not be further decomposed under the current experimental conditions.

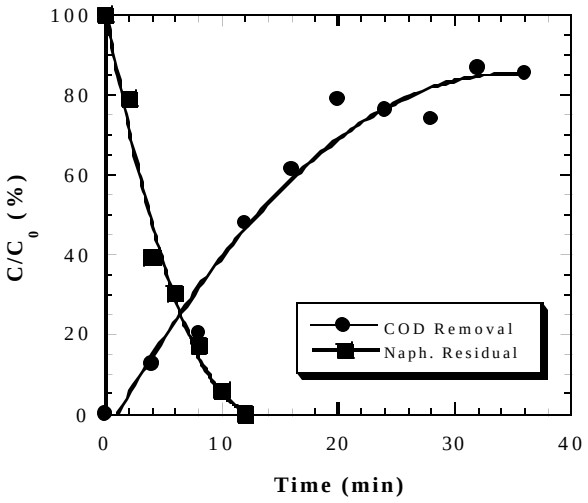

Figure 4.4. COD removal vs. naphthalene degradation. Experimental conditions: continuous dosing mode, H_2O_2 dosing rate = 1.16×10^{-4} M/min, Fe^{2+} dosing rate = 1.16×10^{-4} M/min, $C_{0,naph}$ = 0.20 mM, ionic strength = 0.05M $NaClO_4$,

4.3.3. Effect of Dosing Mode

The Fenton oxidation process is a competitive reaction system. Target organic contaminant, H_2O_2 and Fe^{2+} all compete for hydroxyl radicals. The dosing mode determines the time-dependent concentrations of H_2O_2 and Fe^{2+}, thus affecting the oxidation kinetics of the target organic compound. If H_2O_2 is singly added, there is an excess amount of H_2O_2 initially which will significantly compete for hydroxyl radicals. Likewise, if Fe^{2+} is singly added, the excessive Fe^{2+} will significantly compete for hydroxyl radicals during the initial phase of reaction. By comparing the second-order rate constants of H_2O_2 ($2.7x10^7$ $M^{-1}\cdot s^{-1}$) and Fe^{2+} ($3x10^8$ $M^{-1}\cdot s^{-1}$) toward hydroxyl radicals, it is seen that Fe^{2+} scavenges hydroxyl radicals approximately 10 times faster than H_2O_2.

Figures 4.5a, b, c show the oxidation of naphthalene with reaction time at various dosages of H_2O_2 and Fe^{2+} in the batch dosing mode. Results indicate that the degradation rate of naphthalene increases as either H_2O_2 or Fe^{2+} dosage increases. The reaction is so fast that it is completed within one min. Extended reaction time has no significant effect on the further degradation of naphthalene. Figure 4.5d plots the removal efficiency of naphthalene vs. H_2O_2 dosage. It is seen that all naphthalene can be removed at H_2O_2 dosage of $2x10^{-3}$ M and Fe^{2+} dosage of $1x10^{-3}$ M.

Figure 4.6 summaries the oxidation kinetics of fluorene using various dosing modes, i.e., batch, pseudo-continuous and continuous modes. The total dosages of hydrogen peroxide and ferrous ion were maintained constant in all modes, i.e., $7.92x10^{-4}$ M and $9.9x10^{-6}$ M ($[H_2O_2]/[Fe^{2+}]$=8:1), respectively. Results clearly indicate that the oxidation kinetics varies significantly with different dosing modes.

In the batch mode, the largest initial oxidation rate of fluorene is observed. Since both H_2O_2 and Fe^{2+} were singly added at the beginning of reaction, most of hydroxyl radicals were generated during the initial reaction period. This results in about 90% of fluorene removal within the first minute. The solution became cloudy brown immediately, suggesting the rapid oxidation of ferrous to ferric ion by both hydrogen peroxide and hydroxyl radicals. As ferrous ion disappears quickly, the production of hydroxyl radicals dramatically decreases. Only additional 10% naphthalene is oxidized in the next 5 minutes. So, the batch mode is characterized by a rapid initial organic removal followed by a much slower successive removal. This characteristic is also displayed in the oxidation of naphthalene as above mentioned.

In the pseudo-continuous mode, either H_2O_2 or Fe^{2+} was batch dosed while the other was continuously dosed. Results show that the oxidation kinetics differs markedly. When H_2O_2 is batch dosed, the oxidation rate lags behind when Fe^{2+} is batch dosed. The rate then reverses as reaction proceeds. The excessive Fe^{2+} initially present in the batch Fe^{2+} dosing mode effectively produces hydroxyl radicals; then as Fe^{2+} becomes rapidly depleted, the reaction rate is slowed down. In contrast, in the batch H_2O_2 dosing mode, hydroxyl radicals are gradually produced and consumed. The slower reaction rate of H_2O_2 toward hydroxyl radicals makes significant amount of residual H_2O_2 available throughout the course of reaction. Therefore, the latter system exhibits a better organic removal efficiency.

In the continuous mode, the production rate of hydroxyl radicals was the slowest since both H_2O_2 and Fe^{2+} were continuously added. The competition from the Fenton's reagents is minimized. H_2O_2 and Fe^{2+} are available throughout the course of reaction with hydroxyl radicals being continuously produced. The relatively slow reaction is compensated by its high removal efficiency.

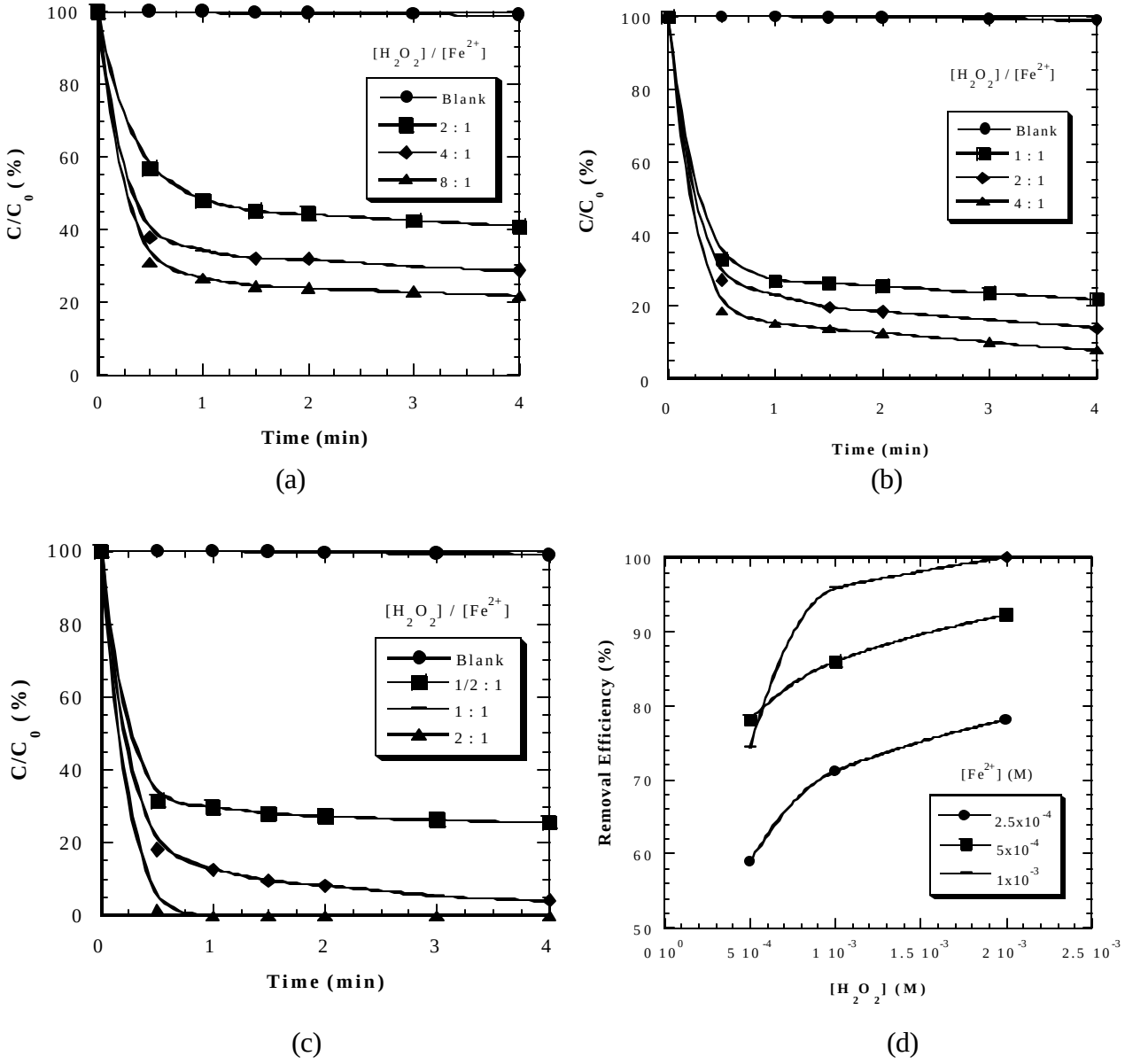

Figure 4.5. Oxidation of naphthalene in batch dosing mode: (a) $[Fe^{2+}]$ = 2.5x10^{-4} M; (b) $[Fe^{2+}]$ = 5x10^{-4} M; (c) $[Fe^{2+}]$ = 1x10^{-3} M; (d) removal efficiency vs. H_2O_2 dosage. Experimental conditions: $C_{0,naph}$ = 0.17~0.22 mM, pH = 3, ionic strength = 0.05M $NaClO_4$.

It should be mentioned that most researchers preferred to using the pseudo-continuous mode, specifically, batch Fe^{2+} dosing and continuous H_2O_2 dosing. Results of this study, however, have demonstrated that this dosing mode yields the lowest removal efficiency of organic compounds. In the following experiments, the continuous dosing mode was employed for all selected PAHs.

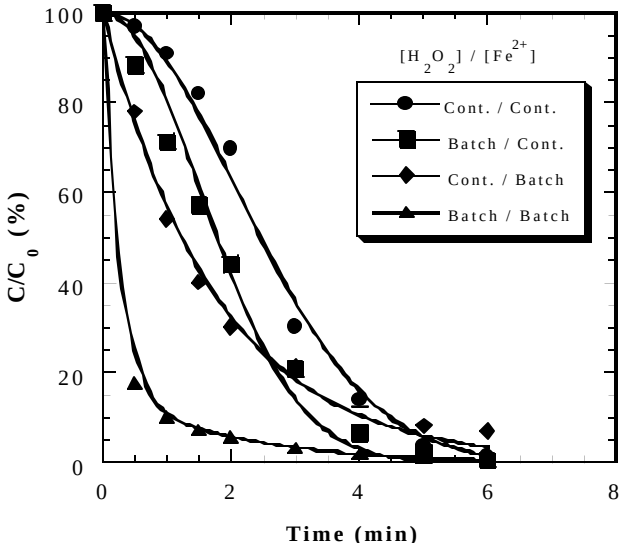

Figure 4.6. Effect of dosing mode on the oxidation of fluorene. Experimental conditions: H_2O_2 = 7.92x10^{-4} M, Fe^{2+} = 9.9x10^{-5} M, $C_{0,flr}$ = 7.5~9.0 mM, ionic strength = 0.05M $NaClO_4$.

4.3.4. Kinetics of PAHs Oxidation

The intrinsic reaction kinetics of organic substrate toward hydroxyl radicals can be described by a second-order expression:

$$-\frac{d[RH]}{dt} = k_{\text{int}}[RH][\cdot OH] \qquad (4.8)$$

where, RH represents organic substrate and k_{int} is the second-order intrinsic rate constant. Most k_{int} data have been supplied by radiation chemists (Walling, 1975). In contrast to most other oxidants, reactions of hydroxyl radicals with organic compounds containing unsaturated structures, such as double bonds and aromatic rings, generally proceed with rate constants approaching the diffusion-controlled limit (~$10^{10}M^{-1}\cdot s^{-1}$). Many researchers (Sedlak and Andren, 1991; Dong, 1993; Huang *et al.*, 1993) observed pseudo-first-order reaction kinetics for the oxidation of organic substrates by the Fenton's reagent, with batch Fe^{2+} dosing and continuous H_2O_2 dosing. In those cases, a steady-state assumption for hydroxyl radicals can be applied to the reaction system. Since the concentration of hydroxyl radicals remains constant during the course of reaction, one can obtain a pseudo-first-order kinetic expression (Equation 4.9) by transforming Equation 4.8:

$$-\frac{d[RH]}{dt} = k_{obs}[RH] \qquad (4.9)$$

$$k_{obs} = k_{\text{int}}[\cdot OH] \qquad (4.10)$$

From Equation 4.10, it is clear that the observed rate constant, k_{obs} depends on both k_{int} and the concentration of hydroxyl radicals. Though k_{int} is very large, k_{obs} is relatively small due to the extremely low concentration of hydroxyl radicals in the reaction system. In natural water systems, hydroxyl radical is produced by photolysis of nitrate ions (Schwarzenbach et al., 1993). Its concentration usually ranges from 10^{-18} to 10^{-16} M. From the viewpoint of engineering application, k_{obs} is more meaningful than k_{int} since hydroxyl radical concentration varies markedly with different reaction systems.

However, the concentration of hydroxyl radicals is no longer constant in the continuous dosing mode since both H_2O_2 and Fe^{2+} are continuously supplied to the reactor. Either H_2O_2 or Fe^{2+} must accumulate in the solution, thus increasing the generation rate of hydroxyl radicals. This in turn increases the concentration of hydroxyl radicals in the reaction solution.

According to Reaction 4.1, the generation of hydroxyl radicals follows first-order with respect to H_2O_2 and Fe^{2+}, individually. By simultaneously measuring the concentrations of H_2O_2 and Fe^{2+} at different reaction times in the fluorene oxidation experiments, we can achieve useful kinetic information. Figure 4.7 indicates that at a molar ratio ($[H_2O_2]/[Fe^{2+}]$) of 4:1, the concentration of Fe^{2+} remains constantly low ($3.0\sim3.5\times10^{-5}$M) during the course of reaction, while the concentration of H_2O_2 increases linearly with the reaction time (Figure 4.7 insert: $C_{H_2O_2} = 1.19\times10^{-4}\times t$, R = 0.989). The linear increment of H_2O_2 concentration will have the effect of increasing the generation rate of hydroxyl radicals. Therefore, we approximate that the concentration of hydroxyl radicals increases as a linear function of reaction time, i.e., $[\cdot OH] = at$. After substituting this equation into Equation 4.8, one gets:

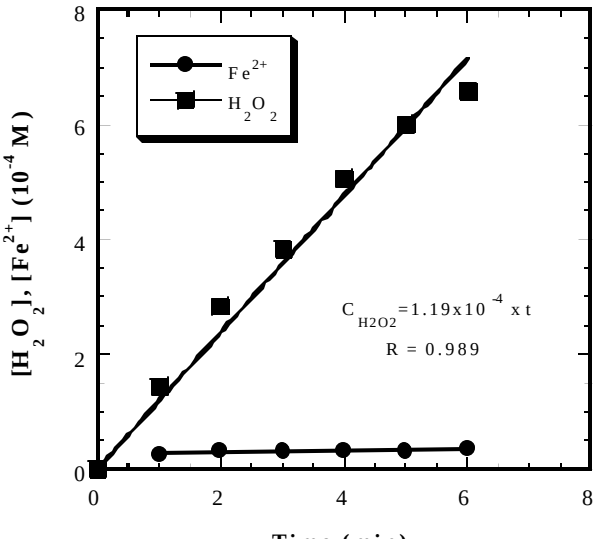

Figure 4.6. Concentration change of H_2O_2 and Fe^{2+} as a function of reaction time in the oxidation of fluorene. Experimental conditions: H_2O_2 dosing rate = 1.32×10^{-4} M/min, Fe^{2+} dosing rate = 3.3×10^{-5} M/min, C_0 = 9.5 mM, ionic strength = 0.05M $NaClO_4$.

$$-\frac{d[RH]}{dt} = ak_{\text{int}}t[RH] \qquad (4.11)$$

By merging a and k_{int}, and integrating Equation 4.11, one obtains:

$$[RH] = [RH]_0 \exp(-k_{obs}t^2) \qquad (4.12)$$

$$a = 2k_{obs}/k_{\text{int}} \qquad (4.13)$$

where, a is the slope of the concentration increment of hydroxyl radicals ($M\cdot min^{-1}$), k_{obs} is the observed rate constant (min^{-2}), and $[RH]_0$ is the initial concentration of organic substrate (M). The value of k_{obs} can be computed by model fitting of experimental data, and k_{int} is available in literatures. Thus, the slope a can be calculated from Equation 4.13. Consequently, the concentration of hydroxyl radicals can be calculated at any reaction time. Equation 4.12 can be rewritten in a more common form, i.e., $C = C_0 \exp(-k_{obs}t^2)$. This "time-squared" kinetic expression is used to fit our experimental data.

The results of naphthalene, fluorene, phenanthrene, fluoranthene, pyrene and anthracene oxidation at various $[H_2O_2]/[Fe^{2+}]$ molar ratios are shown in Figures 4.7~4.12. For the oxidation of naphthalene (Figure 4.7), 600mL solution was used without initial headspace. The dosage rate of H_2O_2 was constant at 1.16×10^{-4} M/min. The dosage rate of Fe^{2+} was adjusted accordingly as to obtain the desired $[H_2O_2]/[Fe^{2+}]$ molar ratios ranging from 1:1 to 1:1/16. For the oxidation of fluorene (Figure 4.8), phenanthrene (Figure 4.9), fluoranthene (Figure 4.10), pyrene (Figure 4.11) and anthracene (Figure 4.12), 500 mL solution was used

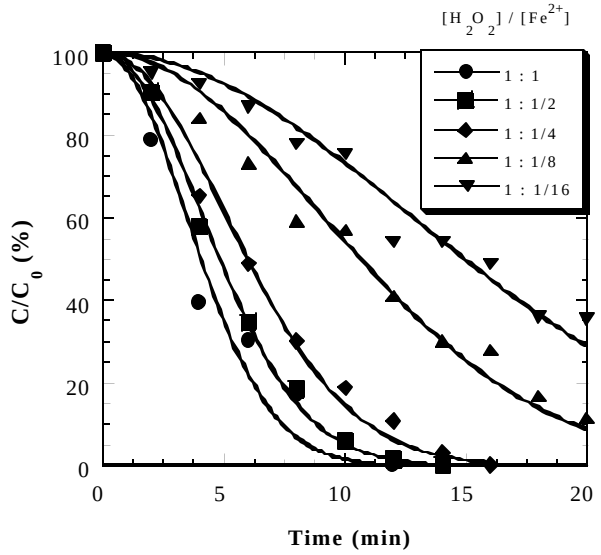

Figure 4.7. Oxidation of naphthalene in continuous dosing mode. Experimental conditions: H_2O_2 dosing rate = $1.16x10^{-4}$ M/min, Fe^{2+} dosing rate = varying, ionic strength = 0.05M $NaClO_4$, pH = 3, 600mL solution, $C_{0,naph}$ = 190~230 mM. Symbols: experimental data; lines: "time-squared" model fitting.

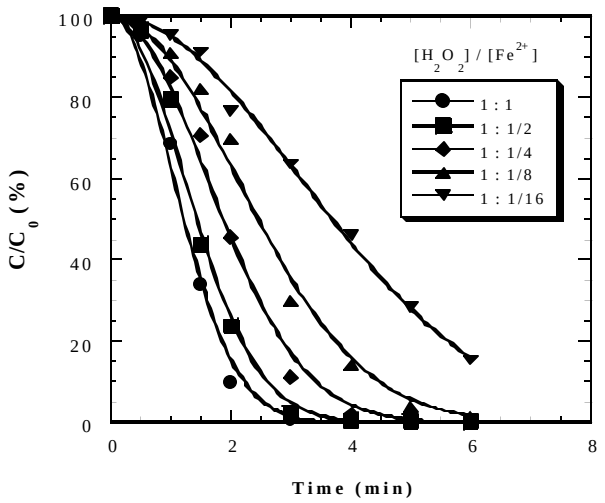

Figure 4.8. Oxidation of fluorene in continuous dosing mode. Experimental conditions: H_2O_2 dosing rate = $1.32x10^{-4}$ M/min, Fe^{2+} dosing rate = varying, ionic strength = 0.05M $NaClO_4$, pH = 3, 500mL solution, $C_{0,flr}$ = 8.3~10.2 mM. Symbols: experimental data; lines: "time-squared" model fitting.

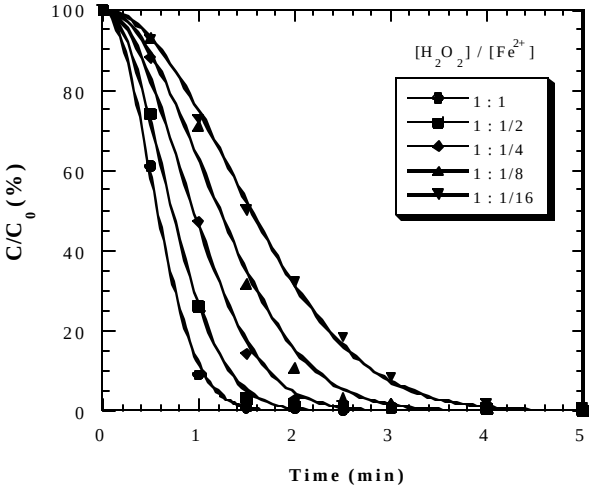

Figure 4.9. Oxidation of phenanthrene in continuous dosing mode. Experimental conditions: H_2O_2 dosing rate = $1.32x10^{-4}$ M/min, Fe^{2+} dosing rate = varying, ionic strength = 0.05M $NaClO_4$, pH = 3, 500mL solution, $C_{0,phen}$ = 4.3~5.2 mM. Symbols: experimental data; lines: "time-squared" model fitting.

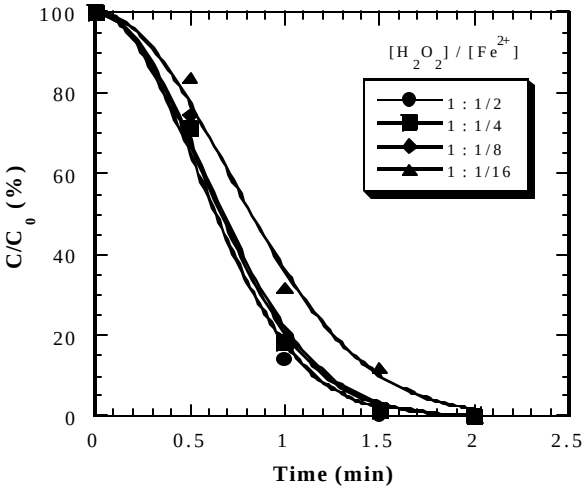

Figure 4.10. Oxidation of fluoranthene in continuous dosing mode. Experimental conditions: H_2O_2 dosing rate = $1.32x10^{-4}$ M/min, Fe^{2+} dosing rate = varying, ionic strength = 0.05M $NaClO_4$, pH = 3, 500mL solution, $C_{0,fluoran}$ = 0.86~0.96 mM. Symbols: experimental data; lines: "time-squared" model fitting.

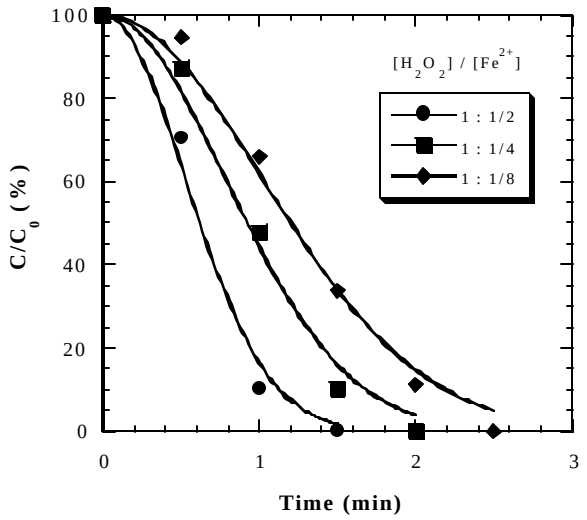

Figure 4.11. Oxidation of phenanthrene in continuous dosing mode. Experimental conditions: H_2O_2 dosing rate = $1.32x10^{-4}$ M/min, Fe^{2+} dosing rate = varying, ionic strength = 0.05M $NaClO_4$, pH = 3, 500mL solution, $C_{0,\ pyr}$ = 0.64~0.69 mM. Symbols: experimental data; lines: "time-squared" model fitting.

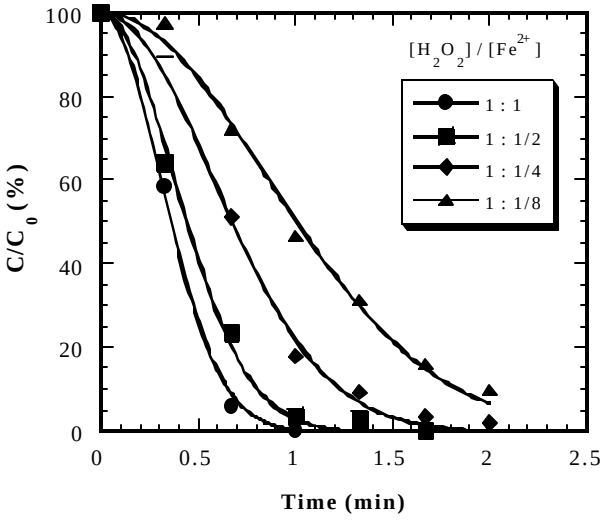

Figure 4.12. Oxidation of fluoranthene in continuous dosing mode. Experimental conditions: H_2O_2 dosing rate = $1.32x10^{-4}$ M/min, Fe^{2+} dosing rate = varying, ionic strength = 0.05M $NaClO_4$, pH = 3, 500mL solution, $C_{0,\ anth}$ = 0.20~0.34 mM. Symbols: experimental data; lines: "time-squared" model fitting.

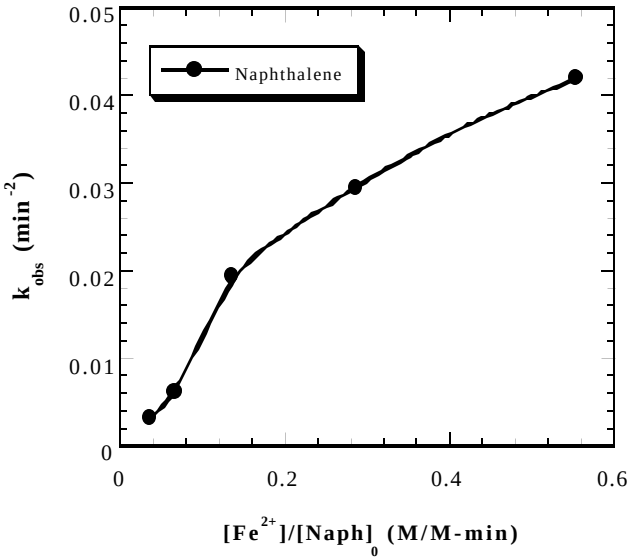

Figure 4.13. Plot of k_{obs} versus $[Fe^{2+}]/[RH]_o$ for oxidation of naphthalene.

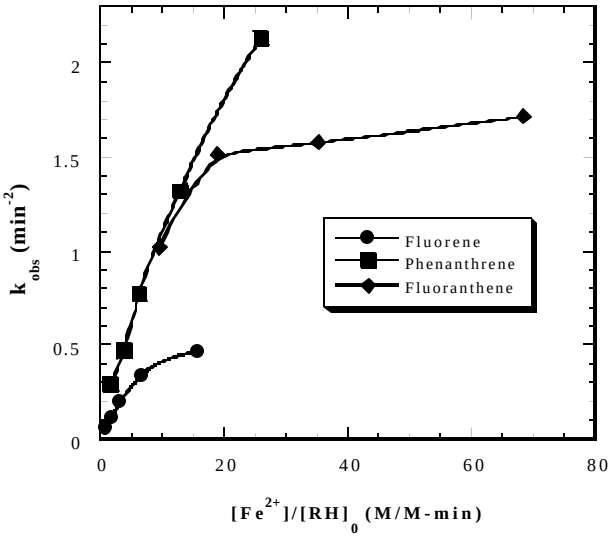

Figure 4.14. Plot of k_{obs} versus $[Fe^{2+}]/[RH]_o$ for oxidation of fluorene, phenanthrene and fluoranthene.

with 100mL headspace. H_2O_2 dosage was maintained at $1.32x10^{-4}$M/min. Results indicate that as H_2O_2 dosage remains constant, the reaction rate increases with increasing dosage of Fe^{2+}. In these figures , the symbols represent experimental data points, while the lines indicate the model fitting results using the "time-squared" kinetic equation. All experimental data in the continuous mode can be well fitted by the "time-squared" model, especially at high Fe^{2+} dosages.

Figures 4.13, 4.14 and 4.15 summarize the k_{obs} values of oxidation of selected PAHs at various Fe^{2+} dosages. Due to the high hydrophobicity of selected PAHs, the initial concentration of each reaction solution varied a little which would somewhat affect the k_{obs} values. Therefore, a plot of k_{obs} against $[Fe^{2+}]/[RH]_0$, is preferred to $[Fe^{2+}]$. Results indicate that the k_{obs} increases with increasing ratios of $[Fe^{2+}]/[RH]_0$. As the dosage of Fe^{2+} increases, more hydroxyl radicals are competitively consumed by Fe^{2+}. As a consequence, the increment of k_{obs} slows down at high ratios of $[Fe^{2+}]/[RH]_0$. The intrinsic rate constant of PAHs toward hydroxyl radicals is about 10^{10} $M^{-1}\cdot s^{-1}$ (Watts, 1998). From the k_{obs}, one can calculate the *a* values via Equation 4.13, and then the time-dependent concentration of hydroxyl radicals using the linear equation, $[\cdot OH] = at$. For example, in the naphthalene oxidation experiments the concentration of hydroxyl radicals ranges from $2.1x10^{-13}$ to $2.8x10^{-12}$ M at the end of the reaction. Compared with natural water systems (10^{-18} to 10^{-16}M), it is clear that the Fenton oxidation system generates hydroxyl radicals more effectively by a factor of 4 to 5 orders of magnitude.

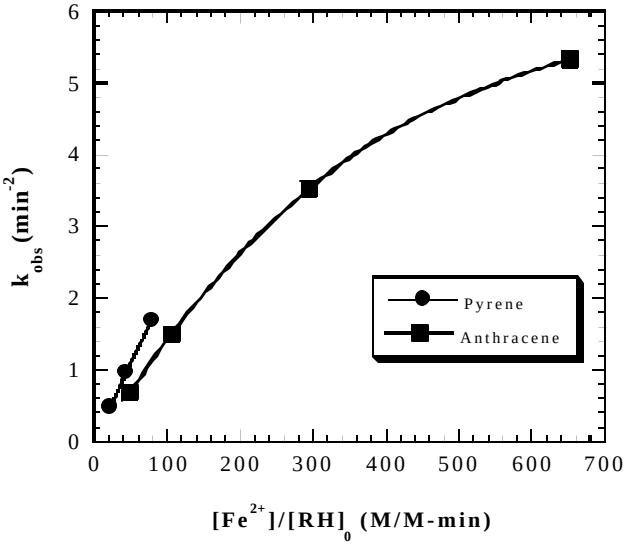

Figure 4.15. Plot of k_{obs} versus $[Fe^{2+}]/[RH]_o$ for oxidation of pyrene and anthracene.

In order to compare the reaction rate constants of selected PAHs, the solution containing fluorene (C_0 = 0.24μM), phenanthrene (C_0 = 0.30μM), fluoranthene (C_0 = 0.26μM), pyrene (C_0 = 0.29μM) and anthracene (C_0 = 0.31μM) was prepared with a nearly identical concentration for each compound. Figure 4.16 shows the degradation of selected PAHs with reaction time. Experimental data are fitted by the "time-squared" kinetic model. The k_{obs} values obtained by model fitting are compared in Figure 4.17. Results indicate that anthracene exhibits the largest k_{obs} value, which is about 4.5 times that of fluorene. The observed rate constants differ from different PAHs and follow the order: fluorene < phenanthrene < fluoranthene ≈ pyrene < anthracene. It is noted that the order of rate constant reverses the order of water solubility. It has been reported that various PAHs compounds vary considerably in their reactivity toward ozone (Bailey, 1988). For example, the order of reaction rate of some PAHs compounds with ozone follows: anthracene > pyrene > phenanthrene (Razumovskii and Zaikov, 1971). This is in agreement with our results. Since both ozonation and Fenton oxidation are among AOP processes that in principle use hydroxyl

radicals as the major oxidant, these results are comparable.

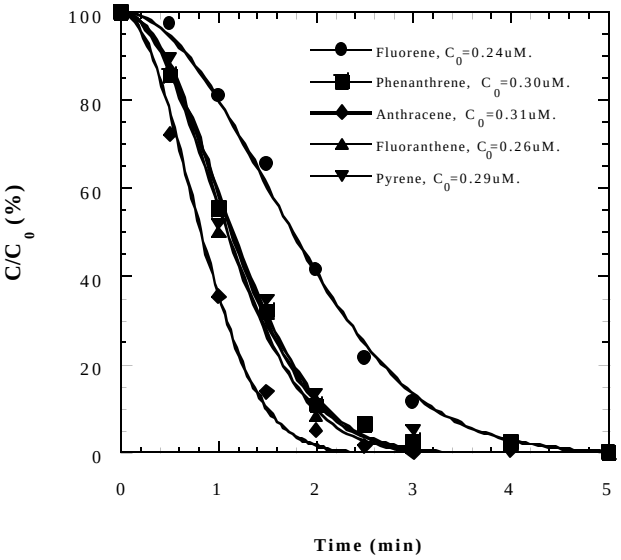

Figure 4.16. Degradation of selected PAHs with reaction time in one solution.

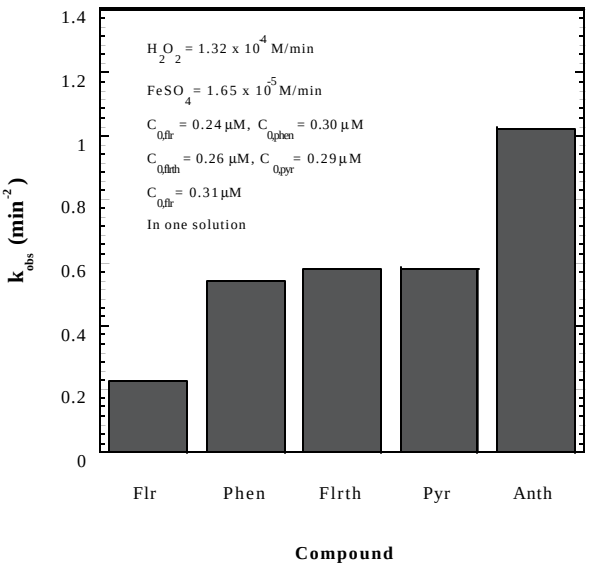

Figure 4.17. Comparison of k_{obs} for degradation of selected PAHs.

4.3.5. Effect of Organic Solvent

As described above, the majority of PAHs oxidation experiments were carried out in organic solvent or in water/organic solvent mixture. However, the effect of organic solvent on the oxidation of PAHs has not been reported. Moreover, organic solvents are frequently employed to enhance the desorption of hydrophobic organic compounds, e.g., PAHs and PCBs, from soil particles in pump and treat, soil flushing and electro-kinetic processes (Khodadoust *et al.*, 1999; Raghavan *et al.*, 1991; Walker *et al.*, 1998; Atalay *et al.*, 1996). Since the Fenton oxidation process can be integrated with any of the above processes as a means to destroy hazardous organic contaminants on-site or off-site, the effect of organic solvent should be investigated. Oxidation of selected PAHs experiments were carried out either in the presence or in the absence of methanol (0.1% volume fraction).

Figure 4.18a shows the degradation of fluorene at various dosages of Fe^{2+} in the presence of methanol. H_2O_2 dosage rate is maintained constant, i.e., $1.32x10^{-4}$ M/min. Results indicate that Fe^{2+} dosage does not exert notable effect on the degradation rate of fluorene. At the end of reaction, the normalized concentrations of residual fluorene are all in the range of 66~74%, though Fe^{2+} dosage changes by 16 times. The optimum molar ratio of $[H_2O_2]/[Fe^{2+}]$ is about 8:1. Figure 4.18b shows the oxidation of fluorene at various H_2O_2 dosage rate, while Fe^{2+} dosage rate is maintained constant, i.e., $6.6x10^{-5}$ M/min. The degradation rate is substantially enhanced as H_2O_2 dosage increases. The maximum removal efficiency achieved is about 25% at the molar ratio of 8:1. Similar to Figure 4.18a, the degradation rate of fluorene decreases when the molar ratio exceeds the optimum value. It is seen that in order to achieve a high degradation rate, it is necessary to simultaneously increase both H_2O_2 and Fe^{2+} dosages while maintaining the optimal molar ratio. Figure 4.18c shows that at the optimum molar ratio of 8:1, the degradation rate increases significantly with increasing H_2O_2 dosage. At the

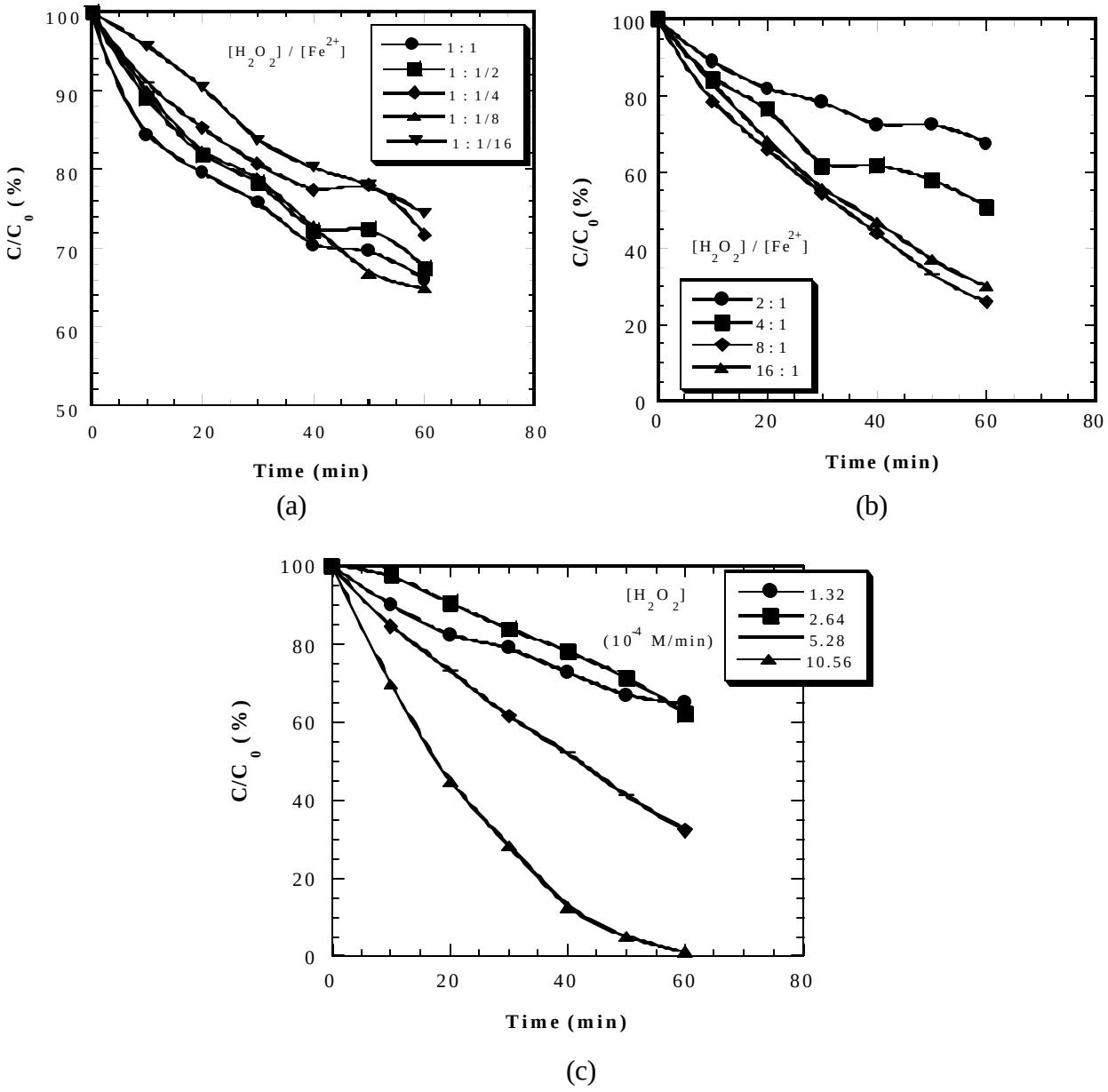

Figure 4.18. Oxidation of fluorene in the presence of methanol: (a) H_2O_2 dosing rate = $1.32x10^{-4}$ M/min, Fe^{2+} dosing rate = varying, $C_{0,flr}$ = 12.2~13.3 mM; (b) H_2O_2 dosing rate = varying, Fe^{2+} dosing rate = $6.6x10^{-5}$ M/min, $C_{0,flr}$ = 10.8~12.7 mM; (c) $[H_2O_2]/[Fe^{2+}]$ = 8:1, $C_{0,flr}$ = 9.6~12.7 mM. Experimental conditions: $C_{0,methanol}$ = 24.7 mM, pH = 3, ionic strength = 0.05M $NaClO_4$.

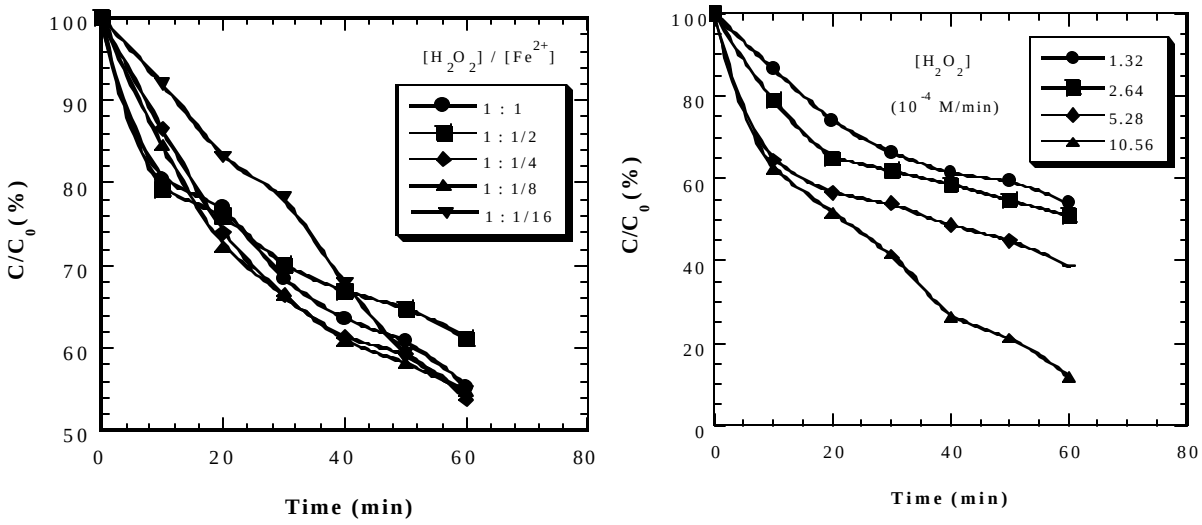

(a) (b)

Figure 4.19. Oxidation of phenanthrene in the presence of methanol: (a) H_2O_2 dosing rate = $1.32x10^{-4}$ M/min, Fe^{2+} dosing rate = varying, $C_{0,phen}$ = 5.08~6.66 mM; (b) $[H_2O_2]/[Fe^{2+}]$ = 4:1, $C_{0,phen}$ = 5.08~5.54 mM. Experimental conditions: $C_{0,methanol}$ = 24.7 mM, pH = 3, ionic strength = 0.05M $NaClO_4$.

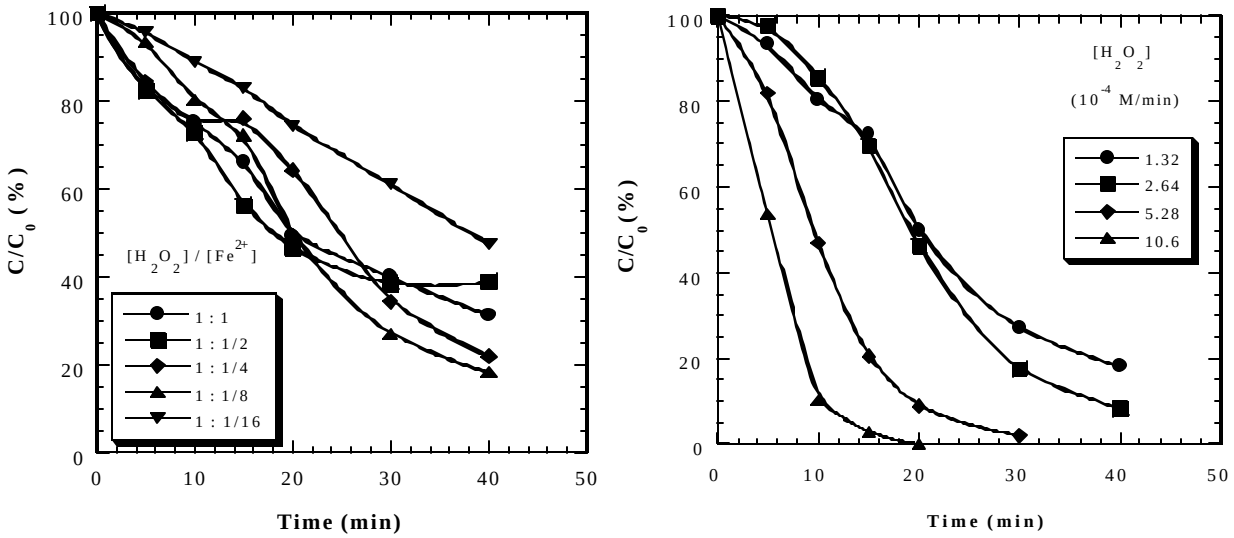

(a) (b)

Figure 4.20. Oxidation of fluoranthene in the presence of methanol: (a) H_2O_2 dosing rate = $1.32x10^{-4}$ M/min, Fe^{2+} dosing rate = varying, $C_{0,fluoran}$ = 1.13~1.47 mM; (b) $[H_2O_2]/[Fe^{2+}]$ = 8:1, $C_{0,fluoran}$ = 1.16~1.45 mM. Experimental conditions: $C_{0,methanol}$ = 24.7 mM, pH = 3, ionic strength = 0.05M $NaClO_4$.

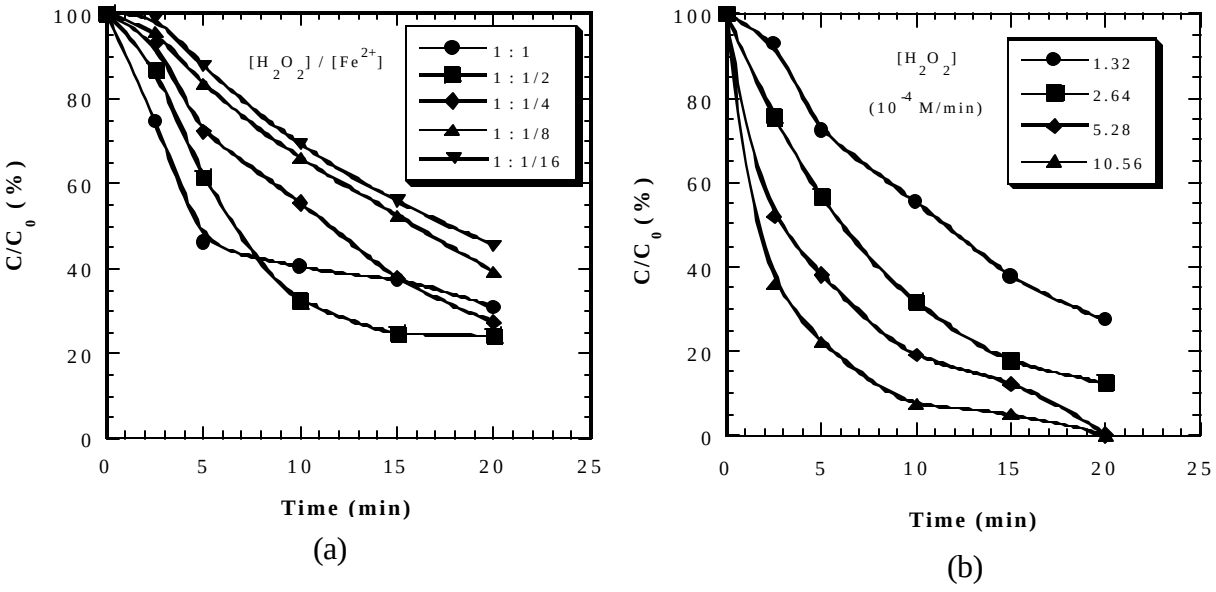

Figure 4.21. Oxidation of pyrene in the presence of methanol: (a) H_2O_2 dosing rate = $1.32x10^{-4}$ M/min, Fe^{2+} dosing rate = varying, $C_{0,pyr}$ = 0.56~0.69 mM; (b) $[H_2O_2]/[Fe^{2+}]$ = 4:1, $C_{0,pyr}$ = 0.69~0.73 mM. Experimental conditions: $C_{0,methanol}$ = 24.7 mM, pH = 3, ionic strength = 0.05M $NaClO_4$

H_2O_2 dosage of $10.56x10^{-4}$ M/min, all fluorene can be degraded. Figures 4.19, 4.20, 4.21 and 4.22 show the degradation of phenanthrene, fluoranthene, pyrene and anthracene at various dosages of H_2O_2 and Fe^{2+} in the presence of methanol, respectively. The results are similar to those obtained in the oxidation of fluorene.

Figure 4.23 compare the degradation efficiencies of fluorene in three different media: water, water/methanol and water/ethanol. In the water medium, fluorene can be effectively oxidized. All fluorene is removed within 6 minutes. However, in the presence of methanol or ethanol, the removal efficiencies decrease to 30% and 35%, respectively, even after 1 hour of reaction. It is obvious that methanol or ethanol significantly inhibits fluorene oxidation due to their strong competition for hydroxyl radicals. Walling et al. (1970) investigated the oxidation of alcohols (methyl, ethyl, isopropyl alcohols) by the Fenton's reagent, and found that all the selected alcohols can be oxidized by hydroxyl radicals. They reported that the rate constants

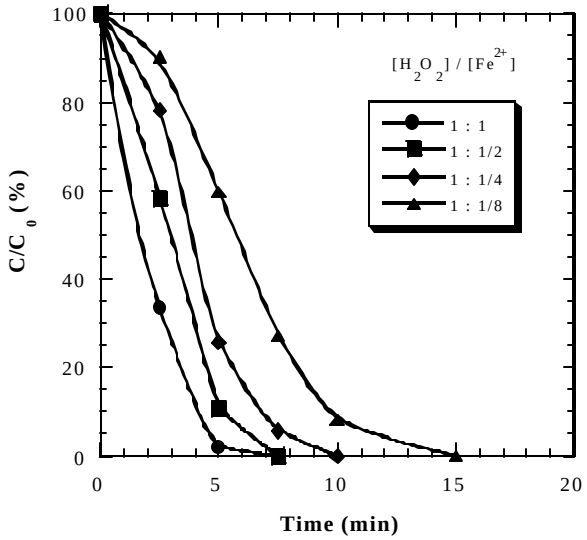

Figure 4.22. Oxidation of anthracene in the presence of methanol: (a) H_2O_2 dosing rate = $1.32x10^{-4}$ M/min, Fe^{2+} dosing rate = varying, $C_{0,anth}$ = 0.22~0.27 mM. Experimental conditions: $C_{0,methanol}$ = 24.7 mM, pH = 3, ionic strength = 0.05M $NaClO_4$.

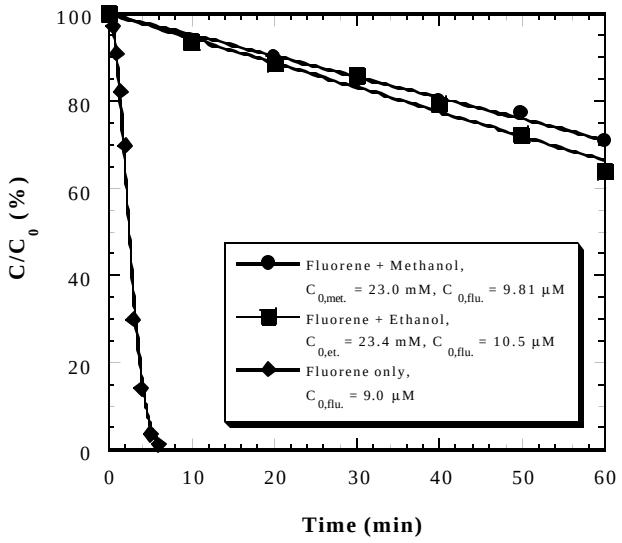

Figure 4.23. Effect of alcohol on the oxidation of fluorene; (b) effect of fluorene on the oxidation of alcohol. Experimental conditions: H_2O_2 dosing rate = 1.32×10^{-4} M/min, Fe^{2+} dosing rater = 1.65×10^{-5} M/min, pH = 3, ionic strength = 0.05M $NaClO_4$.

of methanol and ethanol are 1.2×10^9 and 2.1×10^9 $M^{-1} \cdot s^{-1}$, respectively (Walling, 1970). In this study, the initial concentration ratios of methanol/fluorene and ethanol/ fluorene range from 2,000 to 2,500. Though methanol and ethanol are less reactive than fluorene, they are able to capture most of hydroxyl radials due to their high concentrations. Figure 4.23 also indicates that methanol is a stronger hydroxyl radical scavenger compared with ethanol. Therefore, the oxidation of fluorene is inhibited more severely in the water/methanol media than in the water/ethanol media. The effect of fluorene on the oxidation of methanol or ethanol was also evaluated. Figure 4.24 shows that fluorene exerts very little effect on the oxidation of methanol or ethanol. At the reaction time of 60 minutes, 87% methanol and 91% ethanol, respectively, remain in the reaction solution. The low oxidation efficiency can be attributed to the low molar ratio of $[H_2O_2]/[CH_3OH]$ or $[H_2O_2]/[CH_3CH_2OH]$, which is only about 1:3. In order to oxidize methanol and ethanol more efficiently, a higher molar ratio of H_2O_2 to methanol or ethanol is needed, usually greater than 10:1.

Since organic solvent exerts significant influence on the degradation of PAHs, the rate constants obtained in the presence of organic solvent must be much smaller than those obtained in the water medium only.

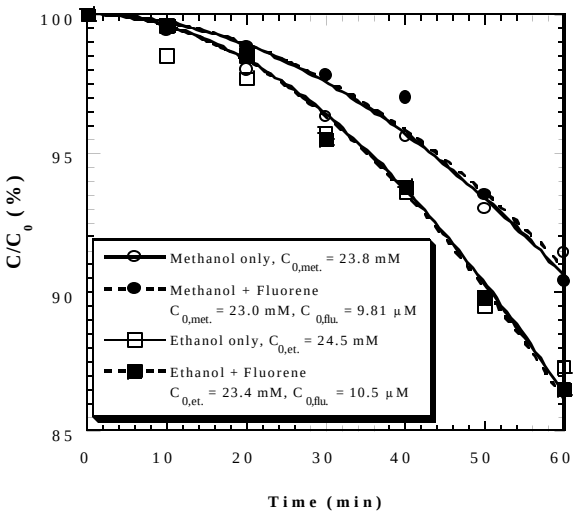

Figure 4.24. Effect of fluorene on the oxidation of alcohol. Experimental conditions: H_2O_2 dosing rate = 1.32×10^{-4} M/min, Fe^{2+} dosing rater = 1.65×10^{-5} M/min, pH = 3, ionic strength = 0.05M $NaClO_4$.

4.4. Conclusions

Fenton's reagent can effectively degrade all selected PAHs, i.e., naphthalene, fluorene, phenanthrene, fluoranthene, pyrene and anthracene. The optimal pH value is pH 3. The extent of mineralization exemplified by naphthalene is around 85%. A "time-squared" kinetic model, $C = C_0 \exp(-k_{obs} t^2)$, can be used to describe the degradation kinetics of selected

PAHs in the continuous dosing mode. This model assumes that the concentration of hydroxyl radicals increases linearly with reaction time. The observed rate constant, k_{obs}, follows the order: fluorene < phenanthrene < fluoranthene ≈ pyrene < anthracene, which reverses the order of water solubility. Methanol or ethanol significantly inhibits the degradation of PAHs by competing for hydroxyl radicals.

4.5. References

1. Atalay A. and Hwang K. J. (1996) *Water Air and Soil Pollution*, **90** (3-4): 451-468.
2. Bailey P. S., Kolsaker P., Sinha B., Ashton J. B., Dobinson, F. and Batterbee J. E. (1964) *J. Org. Chem.*, **29**: 1400-1409.
3. Bailey P. S. (1982) *Ozonation in Organic Chemistry (Vol. II)*, p. 46. Academic Press, Inc.: New York, NY.
4. Buxton G. V., Greenstock C. L., Helman W. P. and Ross A. B. (1988) *J. Phys. Chem. Ref. Data*, **17** (2): 513-886.
5. Destephen R. A. and Benson C. P. (1994) *Hazardous and Industrial Wastes: Proceedings of the Twenty-sixth Mid-Atlantic Industrial Waste Conference*, Huang, C. P. Ed., p 20-27. Technomic Publishing Company, Inc.: Lancaster, PA.
6. Dong C. (1993) Ph. D. Dissertation, University of Delaware, Newark, DE.
7. Dorfman L. M. and Adams G. E. (1973) *National Bureau of Standards Report No. NSRDS-NBS-46*, p 59. U. S. Government Printing Office, Washington D.C.
8. Haber F. and Weiss J. J. (1934) *Proc. R. Soc. London*, **A147**: 332-336.
9. Hayek N. A. and Dore M. (1990) *Wat. Res.*, **24** (8): 973-982.
10. Huang C. P., Dong C., Tang Z. (1993) *Waste Management*, **13**: 361-377.
11. Keith L. H., and Telliard W. A. (1979) *Environ. Sci. Technol.*, **13** (4): 416-423.
12. Khodadoust A. P., Sorial G. A., Wilson G. J., Suidan M. T., Griffiths R. A. and Brenner R. C. (1999) *J. of Environ. Eng.-ASCE*, **125** (11): 1033-1041.
13. Khodadoust A. P., Suidan M. T., Acheson C. M. and Brenner R. C. (1999) *J. of Hazardous Materials*, **64** (2): 167-179.
14. Kuo W. G. (1992) *Wat. Res.*, **26** (7): 881-886.
15. Latt J. D. and Gallard H. (1999) *Environ. Sci. Technol.*, **33** (16): 2726-2732.
16. Legube B., Guyon S., Sugimitsu H. and Dore M. (1983) *Ozone: Sci. & Eng.*, **5** (3): 151-170.
17. Legube B., Guyon S., Sugimitsu H., Dore M. (1986) *Wat. Res.*, **20** (2): 197-208.
18. Menzie C. A., Potocki B. B., Santodonato J. (1992) *Environ. Sci. Technol.*, **26** (7): 1278-1284.
19. Miller R. (1994) *Bioventing, Performance and Cost Summary*, U. S. Air Force Center for Environmental Excellence, Brooks AFB, TX.
20. Raghavan R., Coles E. and Dietz D. (1991) *J. of Hazardous Materials*, **26** (1): 81-87.
21. Razumovskii S. D. and Zaikov G. E. (1971) *Bull. Acad. Sci. USSR, Div. Chem. Sci. (Engl. Transl.)*, 2524.
22. Sayre I. M. (1988) *J. Am. Water Works Assoc.*, **80** (1): 53-60.
23. Schumb W. C. (1949) *Ind. Eng. Chem.*, **41**: 992.
24. Schwarzenbach R. P., Gschwend P. M. and Imboden D. M. (1993) *Environmental Organic Chemistry*, p 480-481, 621. John Wiley & Sons, Inc.: New York, NY.
25. Sedlak D. L. and Andren A. W. (1991) *Environ. Sci. & Technol.*, **25** (4): 777-782.
26. Spencer C. J., Stanton P. C. and Watts R. J. (1992) *Wat. Res.*, **26** (7): 976-978.

27. Eaton A. D, Clesceri L. S. and Greenberg A. E., Eds (1995) *Standard Methods for the Examination of Water and Wastewater (19th edition*), p 3-68~70. American Public Health Association: Washington D.C.
28. Stumm W and Morgan J. J. (1981) *Aquatic Chemistry: An Introduction Emphasizing Chemical Equilibria in Natural Waters (2nd Edition),* p 266. John Wiley & Sons, Inc.: New York, NY.
29. Sturrock M. G., Cline E. L. and Robinson K. L. (1963) *J. Org. Chem.*, **28** (9): 2340-2343.
30. Trapido M., Veressinina Y. and Munter R. (1995) *Environ. Technol.*, **16** (8): 729-740.
31. Walker R. C., Hofstee C., Dane J. H. and Hill W. E. (1998) *J. of Contaminant Hydrology,* **34**(1-2): 17-30.
32. Walling C. and Kato S. (1970) *J. Am. Chem. Soc.*, **93** (17): 4275-4281.
33. Walling C. (1975) *Acc. Chem. Res.*, **8** (4): 125-131.
34. Watts R. J., Udell M. D., Rauch P. A. and Leung S. W. (1990) *Hazardous Waste & Hazardous Materials*, **7** (4): 335-345.
35. Watts R. J. (1991) *Chemosphere*, **23** (7): 949-955.
36. Watts R. J., Kong S., Dippre M. and Barnes W. T. (1994) *Journal of Hazardous Materials*, **39** (1): 33-47.
37. Watts R. J. (1998) *Hazardous Wastes: Sources, Pathways, Receptors*, p 69, 360. John Wiley & Sons, Inc.: New York, NY.

5. REMOVAL OF SELECTED CHLORINATED ALIPHATIC HYDROCARBONS BY CONVENTIONAL AND ELECTRO-FENTON OXIDATION PROCESSES

5.1. Introduction

Chlorinated aliphatic hydrocarbons (CAHs), commonly used as industrial solvents, are a significant category of hazardous organic compounds. Chlorination has become a widespread industrial practice because it yields compounds of lower flammability, higher density, high viscosity, and improved solvent properties compared to non-chlorinated solvents (Watts, 1998). In the 1970s, 46.5% chlorine gas was used for the production of chlorinated organic compounds in the United States (Higgins, 1989). Chlorinated solvents are mainly used for degreasing and cleaning a large range of products, from machine parts to computer chips. Tetrachloroethylene is one of the most stable species of the chlorinated aliphatic solvents due to its total chlorination status. Its primary application has been in dry cleaning. About 80% of the cleaning industry uses tetrachloroethylene. Trichloroethylene is an excellent solvent for a large number of natural and industrial materials. It is moderately toxic, nonflammable, and slowly oxidized. Trichloroethylene has greatest use in the vapor degreasing of fabricated metal parts (Higgins, 1989). Chloroform has been used most frequently as a dry cleaning spot remover and for cleaning and degreasing machine and engine parts. Other applications include industrial intermediates, insecticides, and the purification of vitamins. Although these compounds are highly volatile, they can also migrate through the subsurface. The properties of chlorinated solvents that make them mobile in groundwater systems include high density, relatively high water solubility, and low biodegradability (Watts, 1998). A survey of 7000 wells conducted in California from 1984 to 1988 showed that approximately 1500 of which had detectable concentrations of organic chemicals present. The most common chemicals detected were chlorinated hydrocarbons such as tetrachloroethylene, trichloroethylene, chloroform, 1,1,1-trichloroethane, and carbon tetrachloride (Mackay, 1990). In addition, at National Priorities List (NPL) sites the contaminants that are most frequently found include trichloroethylene (42%) and tetrachloroethylene (28%) (ATSDR, 1989). As a result, chlorinated aliphatic hydrocarbons such as TCE are listed among the eight major classes of priority pollutants by the U.S. EPA (Keith and Telliard, 1979).

This study investigated the degradation of four CAHs, namely, tetrachloroethylene (PCE), trichloroethylene (TCE), 1,1-dichlorowthylene (DCE) and chloroform by Fenton oxidation process. The conventional Fenton process was first employed to determine the optimal conditions and reaction kinetics. Since we have already clarified the optimal operational conditions for the electro-generation of H_2O_2 and electro-regeneration of Fe^{2+}, the electro-Fenton oxidation process was used to degrade PCE and TCE in aqueous solutions.

5.2. Materials and Methods

5.2.1. Chemicals

PCE (ACS reagent grade, 99%), TCE (spectrophotometric grade, 99.5+%), DCE (ACS reagent grade, 99%) and chloroform (HPLC grade, 99+%) were bought from Aldrich Chemical Company. Hydrogen peroxide (ACS reagent grade, 31.5% w/w solution) and ferrous sulfate (ACS reagent grade, 98%) were bought from Fisher Scientific Company.

Table 1 summarizes the major physical-chemical properties of selected CAHs. It is seen that PCE, TCE and DCE have an unsaturated double-bond structure, and both the water solubility and the vapor pressure increase with descending degree of chlorination. Chloroform has a saturated and highly chlorinated structure. Its water solubility is the highest, while its vapor pressure is between those of TCE and DCE.

Table 5.1. Major physical-chemical properties of selected CAHs (Schwarzenbach et al., 1993).

Properties	PCE	TCE	1,1-DCE	Chloroform
Molecular Structure	$CCl_2=CCl_2$	$CHCl=CCl_2$	$CH_2=CCl_2$	$CHCl_3$
Molecular weight	165.8	131.5	97.0	119.4
Water soluility @ 25°C (mg/L)	150	1,100	2,500	9300
Vapor pressure @ 20°C (mm)	14	60	500	160
$LogK_{ow}$ @ 25°C	2.88	2.42	2.02	1.93

The CAHs were dissolved by distilled water in a glass flask. The flask was sealed by parafilm to prevent the leaking of organic vapor since all selected CAHs are highly volatile. The stock solutions of H_2O_2 and $FeSO_4$ were prepared weekly and stored in refrigerator. Sulfuric acid was added into these stock solutions because an acid condition retards the decomposition of H_2O_2 and the oxidation of Fe^{2+} to Fe^{3+}.

5.2.2. Reaction System

The reaction system was same as used for the oxidation of PAHs (Figure 4.1). Since the selected CAHs are highly volatile, 600mL of reaction solution was used for experiments so that there was no headspace left in the reactor. Default experimental conditions were ambient room temperature of 23°C, 0.05M $NaClO_4$ of ionic strength and pH 3, unless otherwise stated. It should be pointed out that perchloric acid ($HClO_4$) was used for pH adjustment instead of chloric acid (HCl). There are two considerations: (a) chloride ion is a hydroxyl radical scavenger, and (b) HCl interferes with the analysis of chloride ion which is released from the dechlorination of selected CAHs. Three dosing modes, i.e., batch, pseudo-continuous and continuous modes were evaluated for the oxidation efficiency of selected CAHs.

5.2.3. Chemical Analysis

All selected CAHs were analyzed by GC/ECD (Hewlett Packard, 5890, Series II) with nitrogen carrier gas (grade 5). An HP-5MS capillary column (crosslinked 5% Ph Me Silicone, 30m x 0.25mm x 0.25μm film thickness, HP part No. 19091S-433) was used for organic separation. Oven temperature was held at 50 °C for 5 minutes for each sample analysis. A constant temperature reduces the analysis time. Other instrumental conditions

were GC injector temperature of 250 ^{o}C, ECD detector temperature of 300^{o}C, column head pressure of 18 psi, and a total flow rate of 80 mL/min.

The concentrations of H_2O_2 and Fe^{2+} were determined with a diode array spectrophotometer (Model 8452A, Hewlett Packard). Their analysis methods were described previously (Sudoh *et al.*, 1985; Tamura *et al.* 1974). Chloride concentration was determined using a chloride-selective electrode (Model 94-17B) coupled with a reference electrode (Model 90-02) from Orion Research Inc. The two electrodes were connected to a pH meter (Corning Company, Model 125), and the potentials were recorded.

5.3. Results and Discussion

5.3.1. Conventional Fenton Oxidation Process

5.3.1.1. Effect of Dosing Mode

(a) Batch Dosing Mode

In practice, batch reactors are usually employed for wastewater treatment by Fenton oxidation process. Wastewater compositions vary greatly, and reaction time in batch mode can be easily extended to meet the requirements of discharge regulations. Batch systems have such advantages as very tolerant, easy to manage, and simple to model. In the batch mode, both H_2O_2 and Fe^{2+} stock solutions were singly delivered into the reactor.

PCE was chosen as the model compound to evaluate the reaction efficiency of batch dosing mode. Figure 5.1 shows the oxidation of PCE in the batch mode at various dosages of Fe^{2+} while H_2O_2 dosage is maintained constant. Figure 5.1a plots the normalized concentration of residual PCE vs. reaction time. Results indicate that the reaction proceeds rapidly, i.e., within 0.5 minutes. Extended reaction time has little effect on the further degradation of PCE. At a constant H_2O_2 dosage, the degradation rate increases significantly with increasing dosage of Fe^{2+}. A complete removal is achieved at the H_2O_2 dosage of 4.24 mM and the Fe^{2+} dosage of 2.12 mM. The molar ratio of H_2O_2 to PCE for a complete removal is approximately 10:1. Figure 5.1b shows PCE removal efficiency vs. Fe^{2+} dosage. Results indicate that above the molar ratio (Fe^{2+}/PCE) of about 5:1, all PCE is removed. Figure 5.1c shows the change of H_2O_2 concentration as a function of reaction time. In accordance with Figure 5.1a, it is seen that the decomposition of H_2O_2 stops immediately after the reaction is initiated. Extended reaction time will no longer decompose H_2O_2 notably. The decomposition rate of H_2O_2 increases with increasing dosage of Fe^{2+} as expected. The change of Fe^{2+} concentration with reaction time is shown in Figure 5.1d. Results indicate that all Fe^{2+} is oxidized to Fe^{3+} below the Fe^{2+} dosage of 4.24 mM. It is obvious that the rapid depletion of Fe^{2+} terminates the chain reactions of hydroxyl radical, and as a consequence, no further decomposition of PCE and H_2O_2 can be achieved after the Fe^{2+} is used up. Though Fe^{2+} is commonly considered as a catalyst for the Fenton oxidation process, its catalytic ability is negligible if it can not be effectively regenerated. Results also indicate that at the Fe^{2+} dosage of 8.48mM, there is about 1.3 mM Fe^{2+} left in the reaction solution. If Fe^{2+} solely reacts with H_2O_2 on a stoichiometry of 1:1, there should be 4.24 mM of Fe^{2+} residual at the H_2O_2 dosage of 4.24 mM. This result shows that about 3 mM of Fe^{2+} is consumed by hydroxyl radicals. An overdose of Fe^{2+} not only reduces the reaction efficiency by competing for hydroxyl radicals, but also produces more iron sludge that requires further disposal.

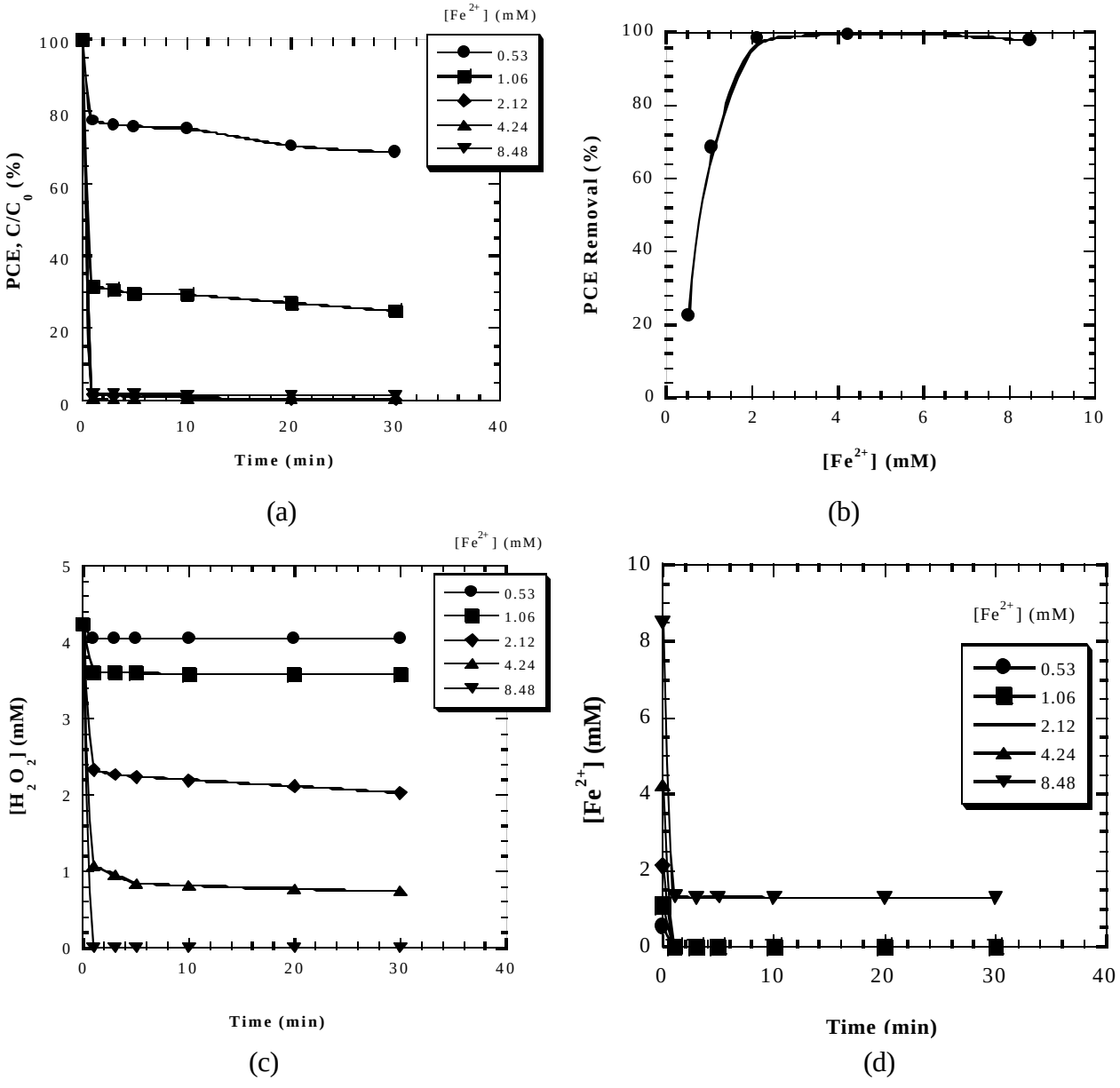

Figure 5.1. Oxidation of PCE--H_2O_2 batch, Fe^{2+} batch: (a) PCE, (b) removal efficiency, (c) H_2O_2, (d) Fe^{2+}. Experimental conditions: $C_{0,PCE}$ = 0.43~0.46mM, $[H_2O_2]$ = 4.24mM, $[Fe^{2+}]$ = varying, pH = 3, ionic strength = 0.05M $NaClO_4$.

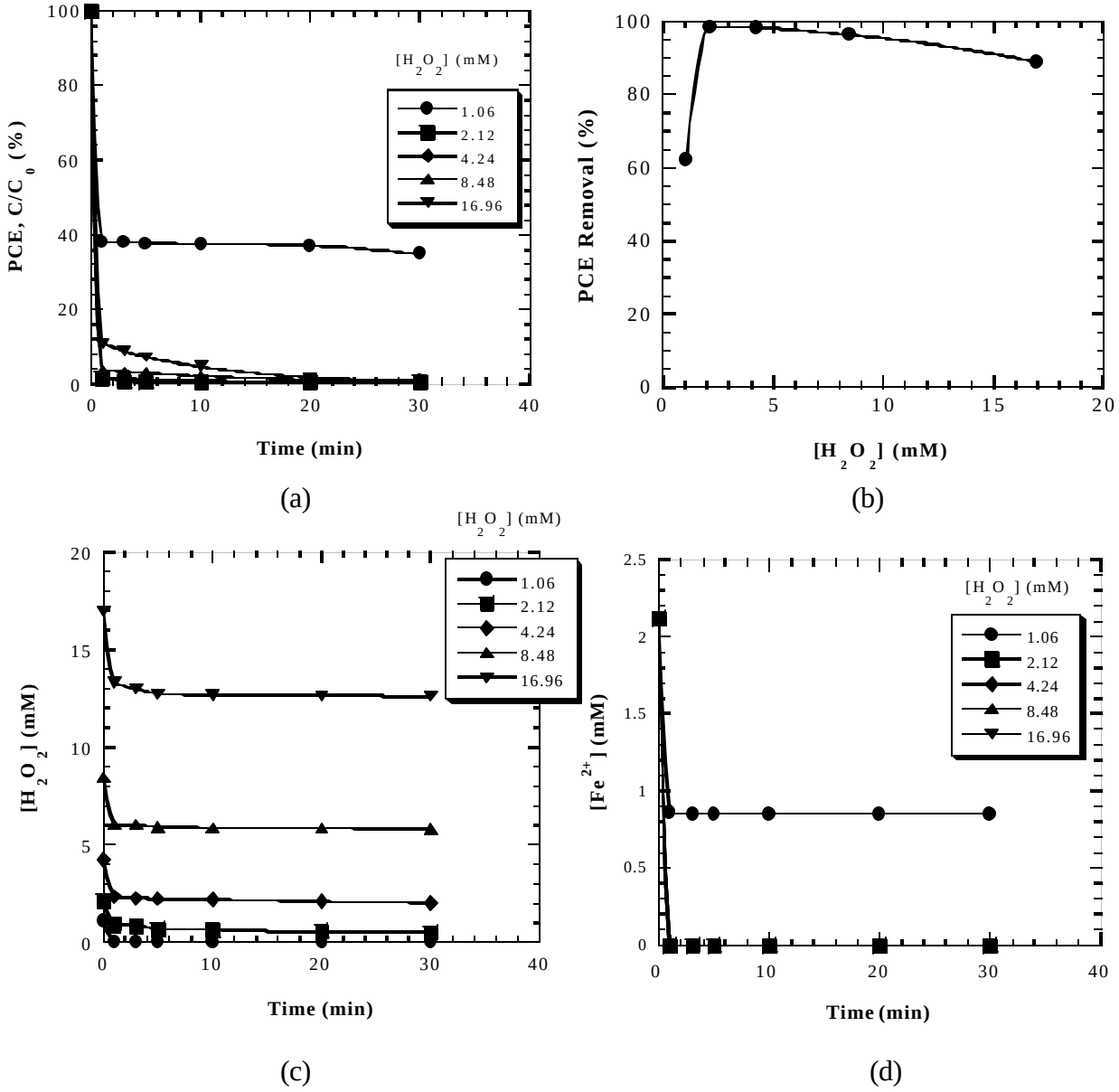

Figure 5.2. Oxidation of --H_2O_2 batch, Fe^{2+} batch: (a) PCE, (b) removal efficiency, (c) H_2O_2, (d) Fe^{2+}. Experimental conditions: $C_{0,PCE}$ = 0.43~0.46mM, $[H_2O_2]$ = varying, $[Fe^{2+}]$ = 2.12mM, pH = 3, ionic strength = 0.05M $NaClO_4$.

Figure 5.2 shows the oxidation of PCE in the batch mode at various dosages of H_2O_2 while Fe^{2+} dosage is maintained constant. Figures 5.2a, c and d show the concentration change of residual PCE, H_2O_2 and Fe^{2+} as a function of reaction time at Fe^{2+} dosage of 2.12 mM. Again, results indicate that the rapid depletion of Fe^{2+} terminates the further decomposition of PCE and H_2O_2. At the H_2O_2 dosage of 2.12 mM, there is about 0.6 mM H_2O_2 left in the solution but no Fe^{2+} is left (Figures 5.1c and d). This demonstrates that Fe^{2+} reacts with hydroxyl radicals much faster than H_2O_2. The competition of H_2O_2 for hydroxyl radicals is presented in Figure 5.2b. Results imply that an overdose of H_2O_2 reduces the removal efficiency of PCE.

As a generalization, the batch mode is characterized by a fast initial organic degradation and little further degradation with extended reaction time. Lou and Lee (1995) investigated the oxidation of benzene, toluene and xylene using the Fenton's reagent. Saxe *et al.* (2000) investigated the oxidation of polycyclic aromatic hydrocarbons by the Fenton's reagent after surfactant-enhanced soil washing. They reported similar reaction phenomena.

(b) Pseudo-continuous Dosing Mode

The pseudo-continuous dosing mode can be divided into two cases: one is H_2O_2 batch but Fe^{2+} continuous, and the other is H_2O_2 continuous but Fe^{2+} batch. Since H_2O_2 and Fe^{2+} compete for hydroxyl radicals at different rates, the reaction efficiency of the two cases is expected to be different.

The results of oxidation of PCE using the pseudo-continuous mode are shown in Figures 5.3 and 5.4. In Figure 5.3, H_2O_2 is batch dosed at the beginning of reaction, while Fe^{2+} is continuously delivered using a fine flowrate dosing pump. Figures 5.3a, c and d show the concentration change of PCE, H_2O_2 and Fe^{2+} with reaction time, respectively. The data of PCE degradation are fitted by the "time-squared" model, i.e., $C = C_0 \exp(-k_{obs} t^2)$. Results indicate that the degradation rate of PCE increases with increasing dosage of Fe^{2+}, and the experimental are well fitted by the proposed model at the molar ratio of H_2O_2 to Fe^{2+} larger than 4:1. All H_2O_2 is decomposed if Fe^{2+} dosage is greater than 2.12 mM at the end of reaction. It is seen that H_2O_2 is notably decomposed by hydroxyl radicals due to its high concentration. In other words, the high concentration of H_2O_2 enhances its ability for capturing hydroxyl radicals. Correspondingly, Fe^{2+} concentration starts to accumulate after all H_2O_2 is used up. H_2O_2 and Fe^{2+} can not coexist in the reaction solution since the reaction between the two species occurs very fast. The observed rate constant, k_{obs}, depends on Fe^{2+} dosage, as summarized in Figure 5.3b. Approximately, k_{obs} increases as a linear function of Fe^{2+} dosage (Figure 5.3b insert, $k_{obs} = -0.032 + 0.040[Fe^{2+}]$). Figure 5.4 shows the oxidation of PCE with continuous dosing H_2O_2 and batch dosing Fe^{2+}. In this dosing mode, the data of PCE degradation can not be fitted by the proposed "time-squared" model. Instead, a pseudo-first-order kinetic expression is suitable to fit the experimental data at the Fe^{2+} dosage larger than 2.12 mM. Many researchers (Sedlak and Andren, 1991; Dong, 1993; Huang *et al.*, 1993) reported that the oxidation kinetics of organic compounds by the Fenton's reagent in the same dosing mode could be described by the pseudo-first-order model. Compared to Figure 5.3a, the reaction efficiency is significantly reduced because the high concentration of Fe^{2+} scavenges hydroxyl radicals more quickly than H_2O_2. Figure 5.4b and c show the increase of H_2O_2 concentration and the decrease of Fe^{2+} concentration, respectively. When all Fe^{2+} disappears, H_2O_2 starts to accumulate.

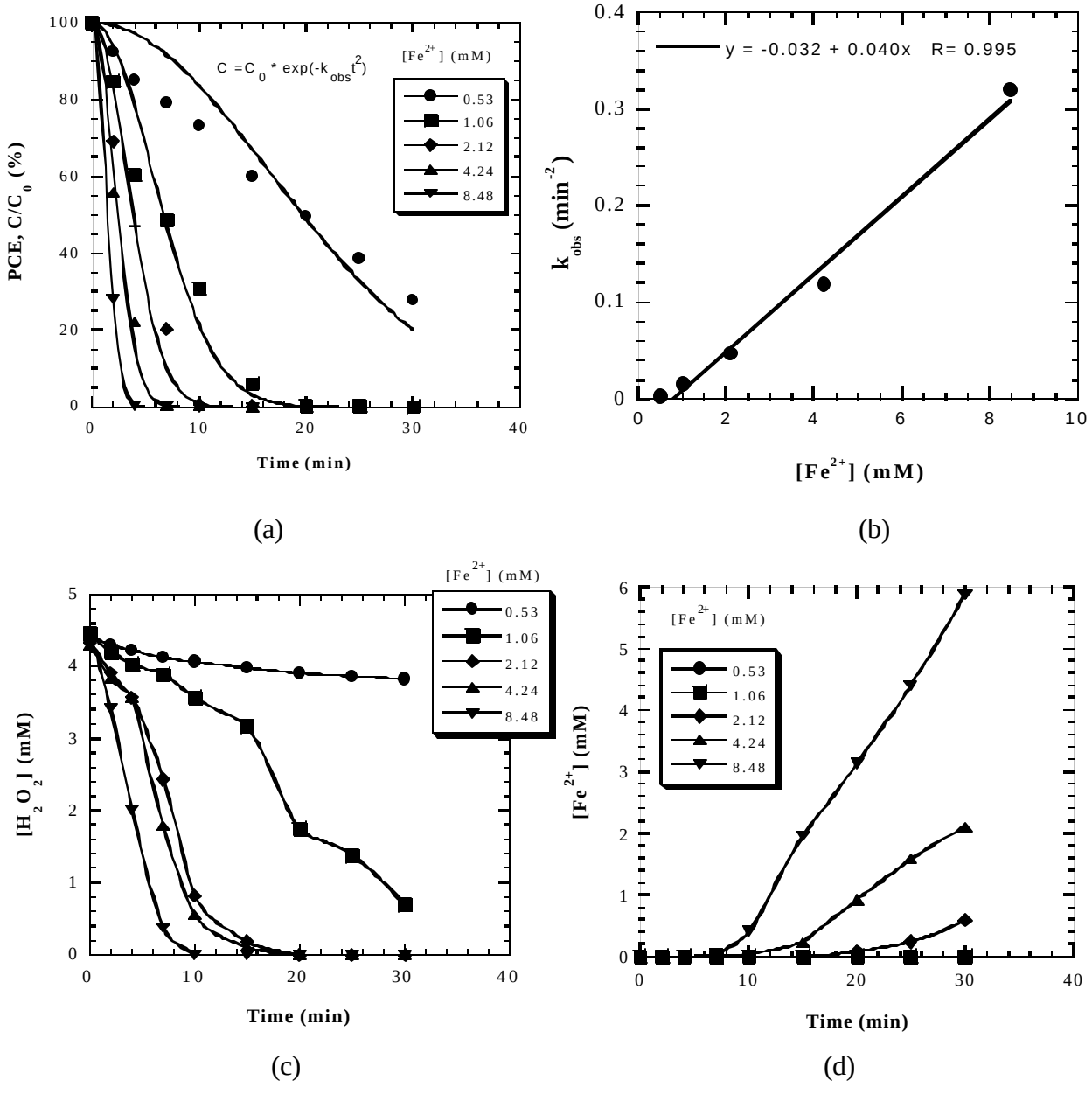

Figure 5.3. Oxidation of PCE --H_2O_2 batch, Fe^{2+} continuous: (a) PCE, (b) observed rate constant, (c) H_2O_2, (d) Fe^{2+}. Experimental conditions: $C_{0,PCE}$ = 0.45~0.48mM, $[H_2O_2]$ = 4.24mM, $[Fe^{2+}]$ = varying, pH = 3, ionic strength = 0.05M $NaClO_4$.

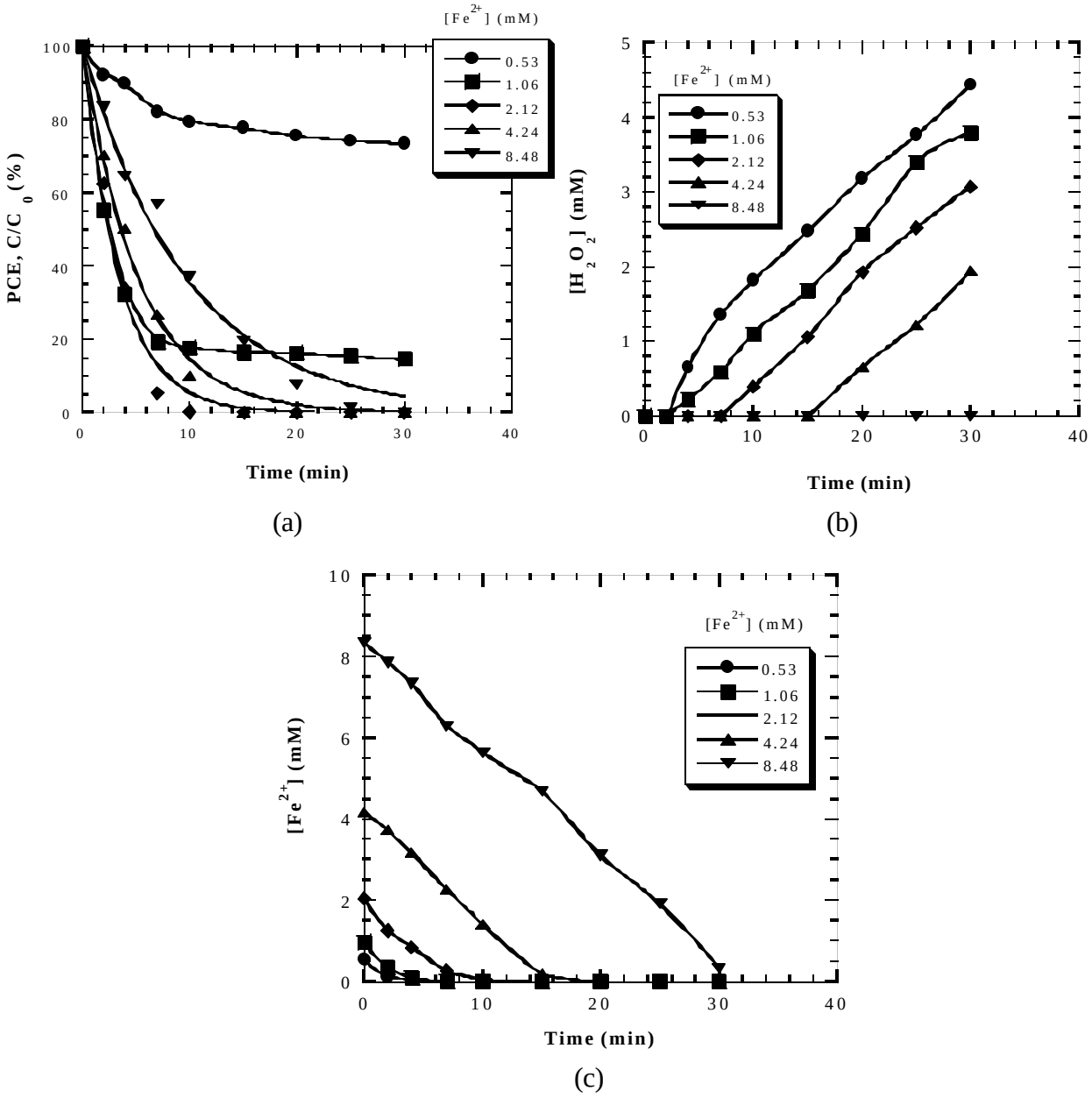

Figure 5.4. Oxidation of PCE --H_2O_2 continuous, Fe^{2+} batch: (a) PCE, (b) H_2O_2, (c) Fe^{2+}. Experimental conditions: $C_{0,PCE}$ = 0.43~0.47mM, $[H_2O_2]$ = 4.24mM, $[Fe^{2+}]$ = varying, pH = 3, ionic strength = 0.05M $NaClO_4$.

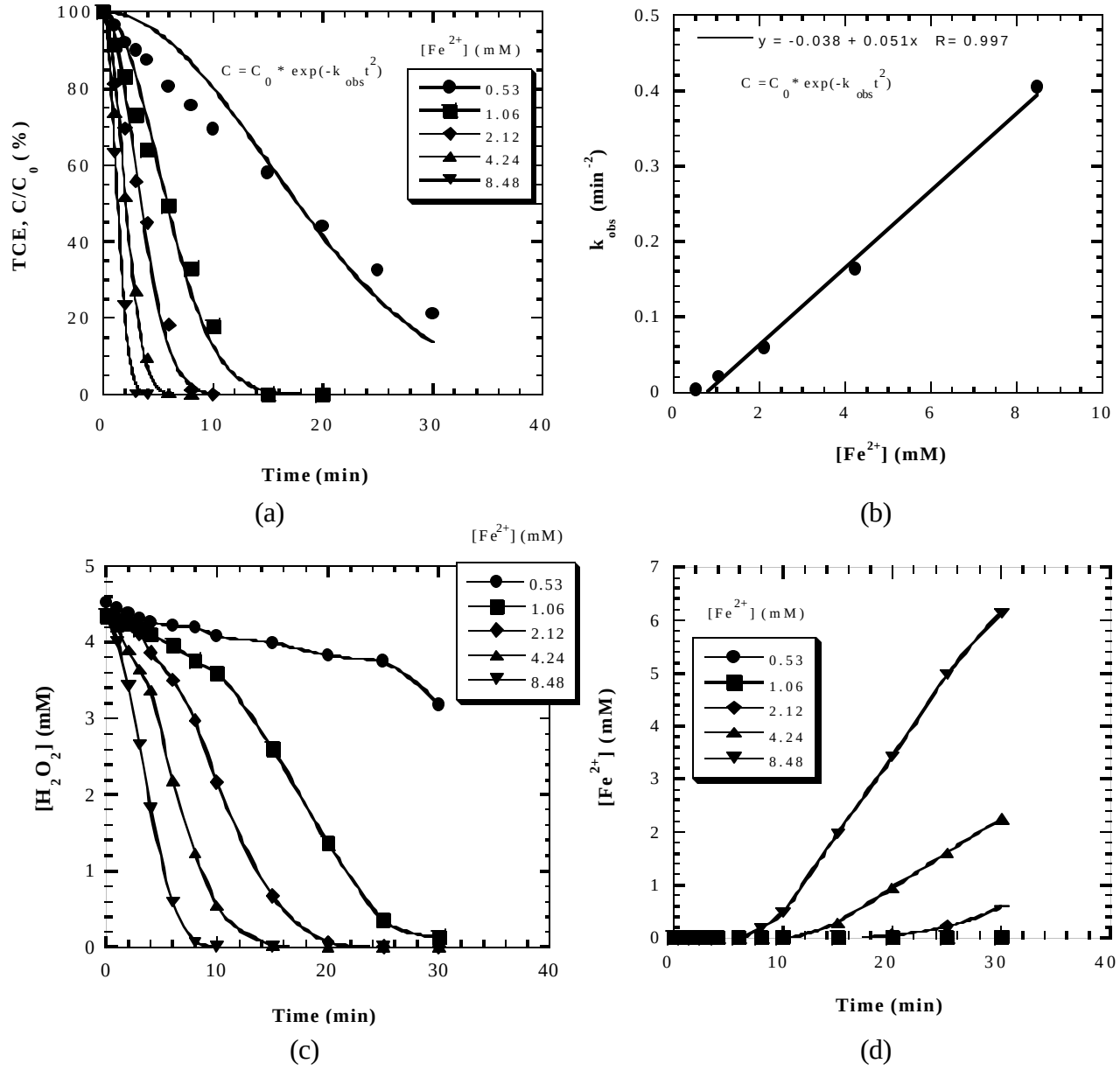

Figure 5.5. Oxidation of TCE--H_2O_2 batch, Fe^{2+} continuous: (a) TCE, (b) k_{obs}, (c) H_2O_2, (d) Fe^{2+}. Experimental conditions: $C_{0,TCE}$ = 0.42~0.46mM, $[H_2O_2]$ = 4.24mM, $[Fe^{2+}]$ = varying, pH = 3, ionic strength = 0.05M $NaClO_4$.

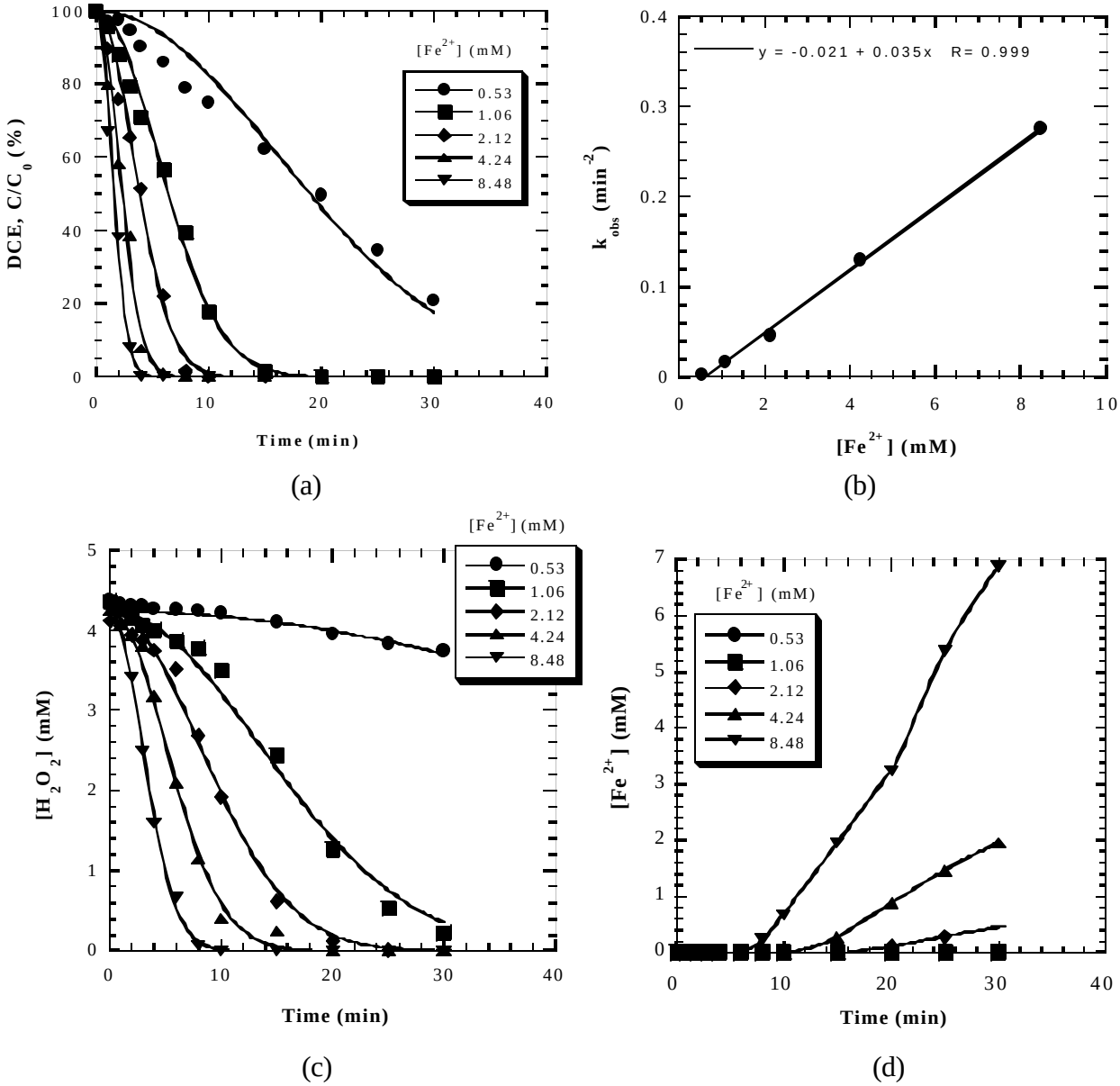

Figure 5.6. Oxidation of DCE--H_2O_2 batch, Fe^{2+} continuous: (a) DCE, (b) k_{obs}, (c) H_2O_2, (d) Fe^{2+}. Experimental conditions: $C_{0,DCE}$ = 0.42~0.44mM, $[H_2O_2]$ = 4.24mM, $[Fe^{2+}]$ = varying, pH = 3, ionic strength = 0.05M $NaClO_4$.

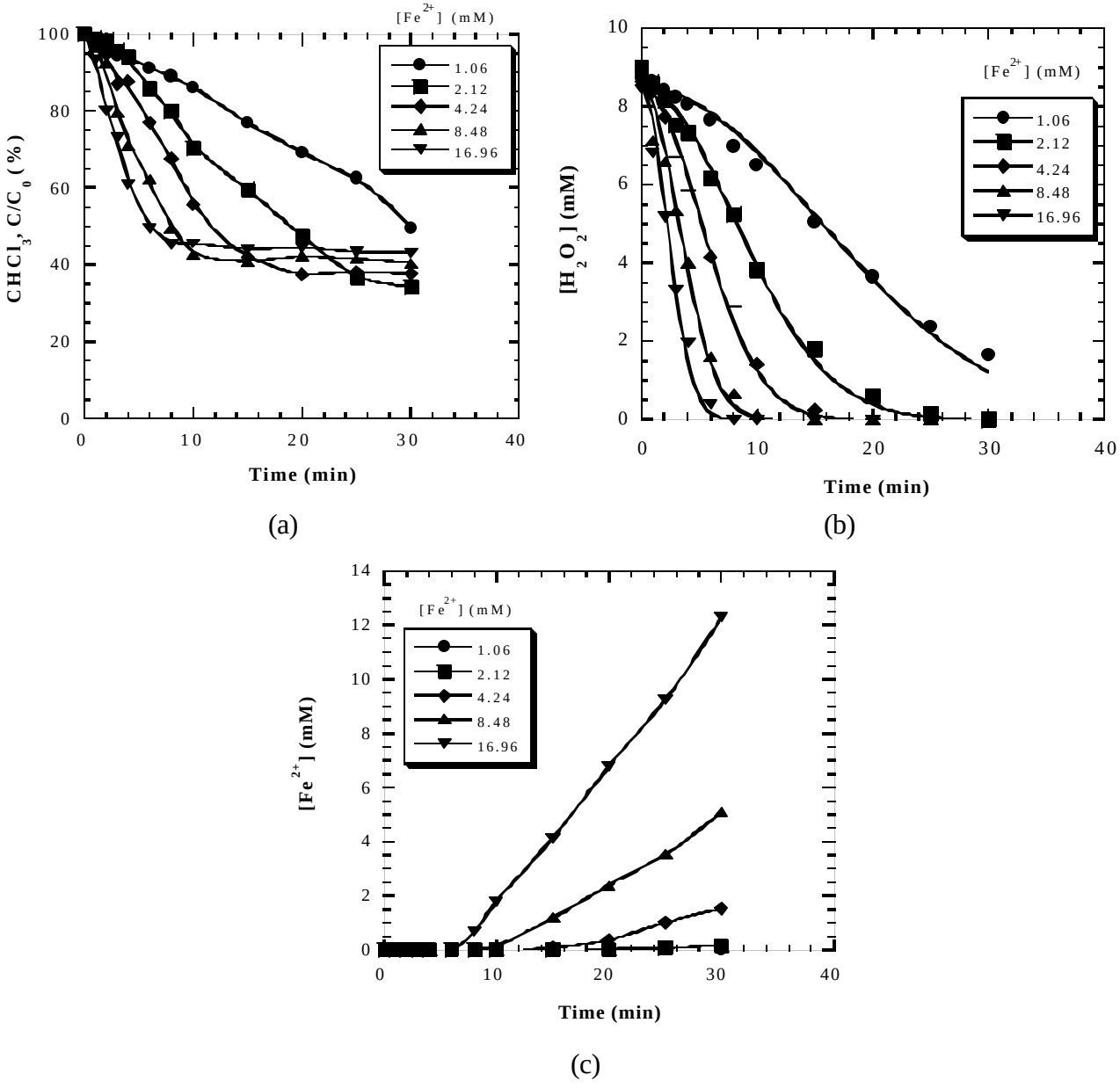

Figure 5.7. Oxidation of chloroform--H_2O_2 batch, Fe^{2+} continuous: (a) chloroform, (b) H_2O_2, (c) Fe^{2+}. Experimental conditions: $C_{0,chloroform}$ = 0.43~0.47mM, $[H_2O_2]$ = 8.48mM, $[Fe^{2+}]$ = varying, pH = 3, ionic strength = 0.05M $NaClO_4$.

The pseudo-continuous mode, specifically, with batch dosing H_2O_2 and continuous doing Fe^{2+} was employed to investigate the oxidation of TCE, DCE and chloroform since this mode yields a better organic removal efficiency. Experimental results are shown in Figures 5.5, 5.6 and 5.7 for TCE, DCE and chloroform, respectively. Results indicate that both TCE and DCE can be completely removed at a certain dosage of Fe^{2+} (Figures 5.5a and 5.6a). However, the complete removal of chloroform is impossible despite of the dosage of Fe^{2+} (Figure 5.7a). A high dosage will not enhance the removal efficiency but stress the competition from Fe^{2+}. The optimal molar ratio of H_2O_2 to Fe^{2+} for the oxidation of chloroform is about 4:1. Further increasing the Fe^{2+} dosage will reduce the removal efficiency of chloroform. The removal efficiency depends on the molecular structure of organic compound. Since hydroxyl radical is electron-deficient, it likes to attack those organic compounds with an electron-rich structure containing double bond or aromatic ring. PCE, TCE and DCE all have a double bond and thus can be effectively oxidized by hydroxyl radical. However, chloroform has only single bonds. Moreover, the highly chlorinated structure draws the electrons away from the carbon center. Therefore, chloroform reacts with hydroxyl radical more slowly than chlorinated ethenes. Results indicate that the "time-squared" model can be used to fit the experimental data of TCE and DCE, but not suitable for chloroform.

The change of H_2O_2 and Fe^{2+} concentrations as a function of reaction time is shown in Figures 5.5c, 5.5d, 5.6c, 5.6d, 5.7b and 5.7c. Figures 5.5b and 5.6b show the linear relationship between k_{obs} and Fe^{2+} dosage, i.e., $k_{obs} = -0.038 + 0.051[Fe^{2+}]$ for TCE, and $k_{obs} = -0.021 + 0.035[Fe^{2+}]$ for DCE.

(c) Continuous Dosing Mode

In the continuous dosing mode, H_2O_2 and Fe^{2+} were continuously added into the reaction solution using separate dosing pumps. In this dosing mode, it is expected that the competition of both H_2O_2 and Fe^{2+} for hydroxyl radicals can be minimized. As a consequence, more hydroxyl radicals can be used for organic degradation.

Figure 5.8 show the oxidation of PCE using the continuous dosing mode at various dosages of Fe^{2+}, while the dosage of H_2O_2 is maintained constant, i.e., 4.24 mM totally. Figures 5.8a, c and d show the concentration change of normalized PCE residual, H_2O_2 and Fe^{2+}, respectively. Results indicate that the degradation rate of PCE increases with increasing dosage of Fe^{2+}, and the experimental data can be well fitted by the proposed "time-squared" kinetic model above the Fe^{2+} dosage of 1.06 mM. The accumulated concentration of H_2O_2 decreases with increasing Fe^{2+} dosage as expected. At $[Fe^{2+}] = 0.53$mM which corresponds to a molar ratio (H_2O_2/Fe^{2+}) of 4:1, H_2O_2 concentration increases almost linearly with reaction time. At $[Fe^{2+}] = 1.06$ mM and 2.12 mM, H_2O_2 concentration first increases with reaction time, and then drops gradually. The flexing point on the H_2O_2 curve corresponds to the time when PCE approaches the complete removal. After PCE no longer consumes hydroxyl radicals, the decomposition of H_2O_2 by hydroxyl radicals becomes stressed. At $[Fe^{2+}] = 4.24$ mM, a constant low H_2O_2 concentration of about 0.3 mM is observed. At $[Fe^{2+}] = 8.48$ mM, there is no H_2O_2 detected in the solution since all H_2O_2 is decomposed by Fe^{2+} and hydroxyl radicals. Results in Figure 5.8d indicate that a notable accumulation of Fe^{2+} only occurs at $[Fe^{2+}] = 8.48$ mM. At the end of reaction, the Fe^{2+} concentration reaches 0.95 mM. This means that about 40% of the dosed Fe^{2+} is oxidized by hydroxyl radicals. At $[Fe^{2+}] = 4.24$ mM, a low Fe^{2+} concentration of 0.08 mM is detected. Compared to the corresponding 0.3

mM of H_2O_2 concentration in Figure 5.8c, it is again seen that hydroxyl radical oxidizes Fe^{2+} more rapidly than it oxidizes H_2O_2. The observed rate constants, k_{obs}, at various Fe^{2+} dosages are summarized in Figure 5.8c. It is seen that the k_{obs} increases as a linear function of Fe^{2+} dosage, i.e., $k_{obs} = -0.044 + 0.011[Fe^{2+}]$. The negative effect of Fe^{2+} dosage on PCE degradation has not yet appeared under the stated experimental conditions since the accumulated concentration of Fe^{2+} is not significant, as shown in Figure 5.8d.

Figure 5.9 show the oxidation of PCE at various dosages of H_2O_2, while the dosage of Fe^{2+} is maintained constant, i.e., 2.12 mM totally. The results are similar to those observed in Figure 5.8. It should be pointed out that the k_{obs} reaches the maximum at $[H_2O_2] = 8.48$ mM which corresponds to the molar ratio (H_2O_2/Fe^{2+}) of 4:1. Further increasing the H_2O_2 dosage to 16.96 mM will slightly reduce the k_{obs}. Since H_2O_2 accumulates rapidly in the solution at this dosage (Figure 5.9c), its suppression on PCE degradation by competing for hydroxyl radicals is signified. Compared Figure 5.8b and 5.9b, it is clearly seen that Fe^{2+} dosage affects PCE degradation more significantly than H_2O_2 dosage.

The results of oxidation of TCE and DCE by the continuous dosing mode at various Fe^{2+} dosages are shown in Figures 5.10 and 5.11, respectively. The H_2O_2 dosage is maintained constant at 4.24 mM. The experimental data of TCE and DCE degradation can be fitted by the proposed kinetic model, and the accumulation of H_2O_2 and Fe^{2+} with reaction time are similar to that observed in the degradation of PCE. Again, a linear relationship between k_{obs} and Fe^{2+} dosage can be established, i.e., $k_{obs} = -0.028 + 0.012[Fe^{2+}]$ for TCE, and $k_{obs} = -0.048 + 0.0127[Fe^{2+}]$ for DCE. Comparing the slopes, it is seen that the rate constant of the reaction between the selected chlorinated ethens and hydroxyl radicals increases in the following order: DCE > TCE > PCE. Generally speaking, organic compounds containing electron-withdrawing functional groups (such as chloride) are resistant to oxidative decomposition by hydroxyl radicals. The chloride substituent on an aliphatic chain draws electrons away from the carbon center due to its electronegative nature and thus deactivates the compound toward hydroxyl radical attack. The more chlorides present on the structure, the lower reaction rate constant towards hydroxyl radicals. The effective oxidation of selected chlorinated ethenes by hydroxyl radicals is due to their electron-rich double bond structure. The chlorine substituent plays a negative role. For chloroform, with a highly chlorinated and saturated structure, it can not provide easily attackable sites to hydroxyl radicals. As a result, the oxidation of chloroform by hydroxyl radicals is considerably slow.

Figure 5.12 show the oxidation of chloroform by the continuous dosing mode at various Fe^{2+} dosages, while the dosage of H_2O_2 is maintained constant at 8.48 mM. Since chloroform is difficult to oxidize, the dosages of H_2O_2 and Fe^{2+} are doubled. Figure 5.12a show the degradation of chloroform with reaction time. Results indicate the optimal molar ratio of H_2O_2 to Fe^{2+} is 1:1, and the maximum removal efficiency reaches about 90%. Further increasing the Fe^{2+} dosage will decreases the degradation rate of chloroform. This differs from the results obtained in the oxidation of PCE, TCE and DCE because chloroform reacts with hydroxyl radicals more slowly than the selected chlorinated ethenes. At $[Fe^{2+}] \leq 8.48$ mM, H_2O_2 accumulates in the reaction solution. Meanwhile, Fe^{2+} starts to accumulate at $[Fe^{2+}] = 16.96$ mM. It is noted that most of chloroform can be removed in the continuous dosing mode, though it is impossible in the batch dosing mode. It is also pointed out that the optimal molar ratio of H_2O_2 to Fe^{2+} is 1:1 for either chlorinated ethenes or chloroform. At this ratio, both H_2O_2 and Fe^{2+} can be effectively used and their residuals in the solution are insignificant.

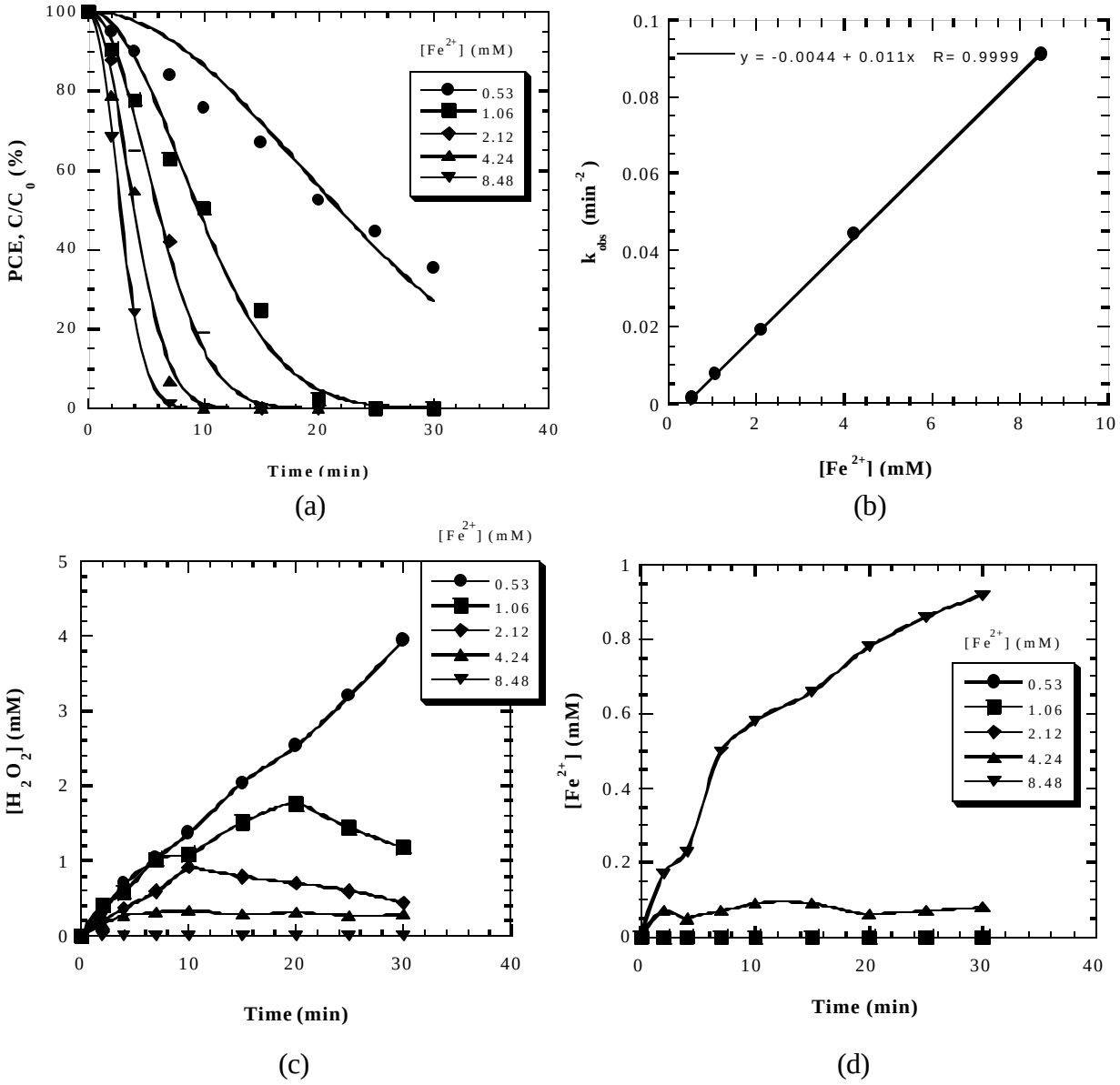

Figure 5.8. Oxidation of PCE --H_2O_2 continuous, Fe^{2+} continuous: (a) PCE, (b) k_{obs}, (c) H_2O_2, (d) Fe^{2+}. Experimental conditions: $C_{0,PCE}$ = 0.44~0.50mM, $[H_2O_2]$ = 4.24mM, $[Fe^{2+}]$ = varying, pH = 3, ionic strength = 0.05M $NaClO_4$.

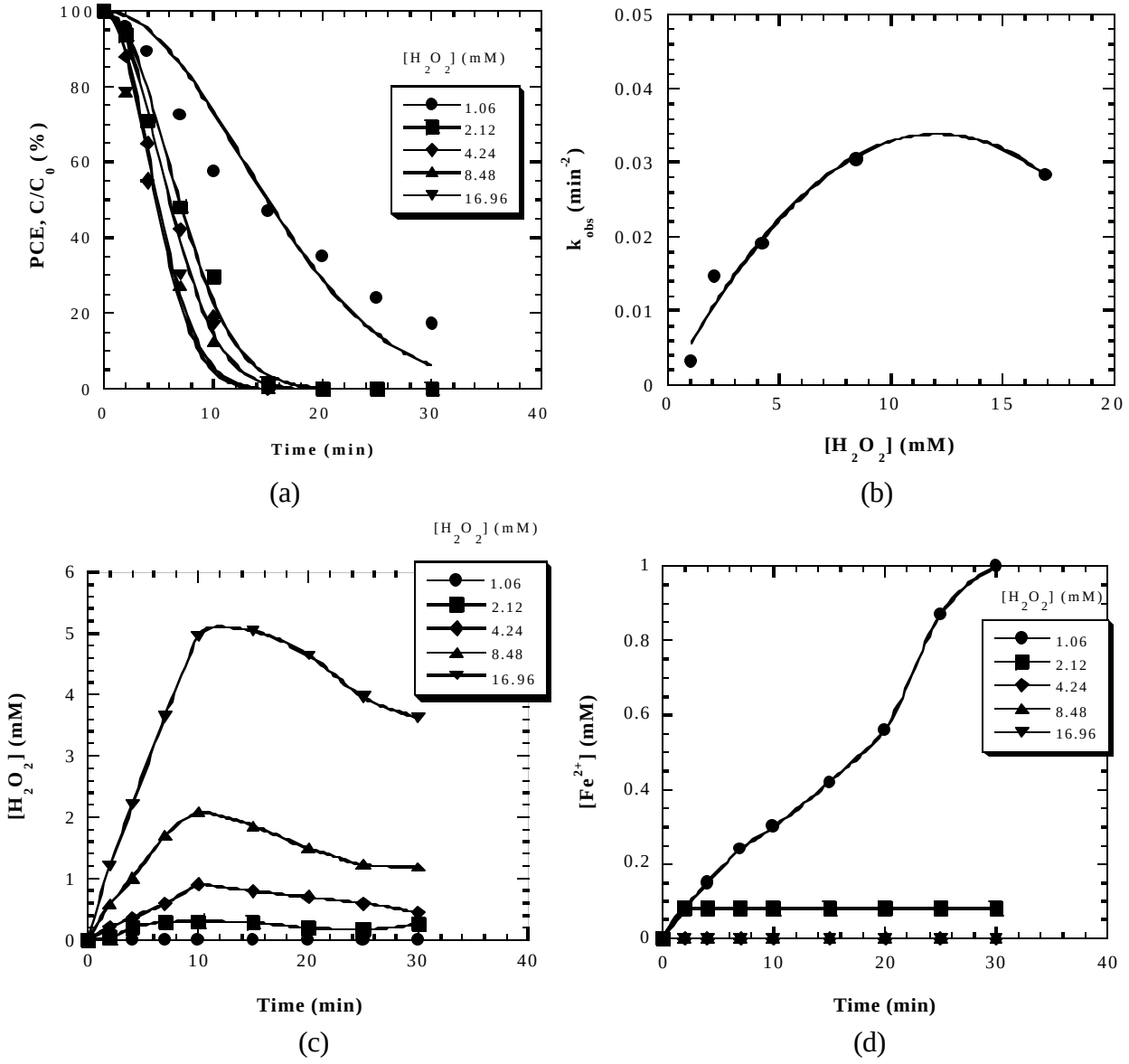

Figure 5.9. Oxidation of PCE --H_2O_2 continuous, Fe^{2+} continuous: (a) PCE, (b) k_{obs}, (c) H_2O_2, (d) Fe^{2+}. Experimental conditions: $C_{0,PCE}$ = 0.43~0.48mM, $[H_2O_2]$ = varying, $[Fe^{2+}]$ = 2.12mM, pH = 3, ionic strength = 0.05M $NaClO_4$.

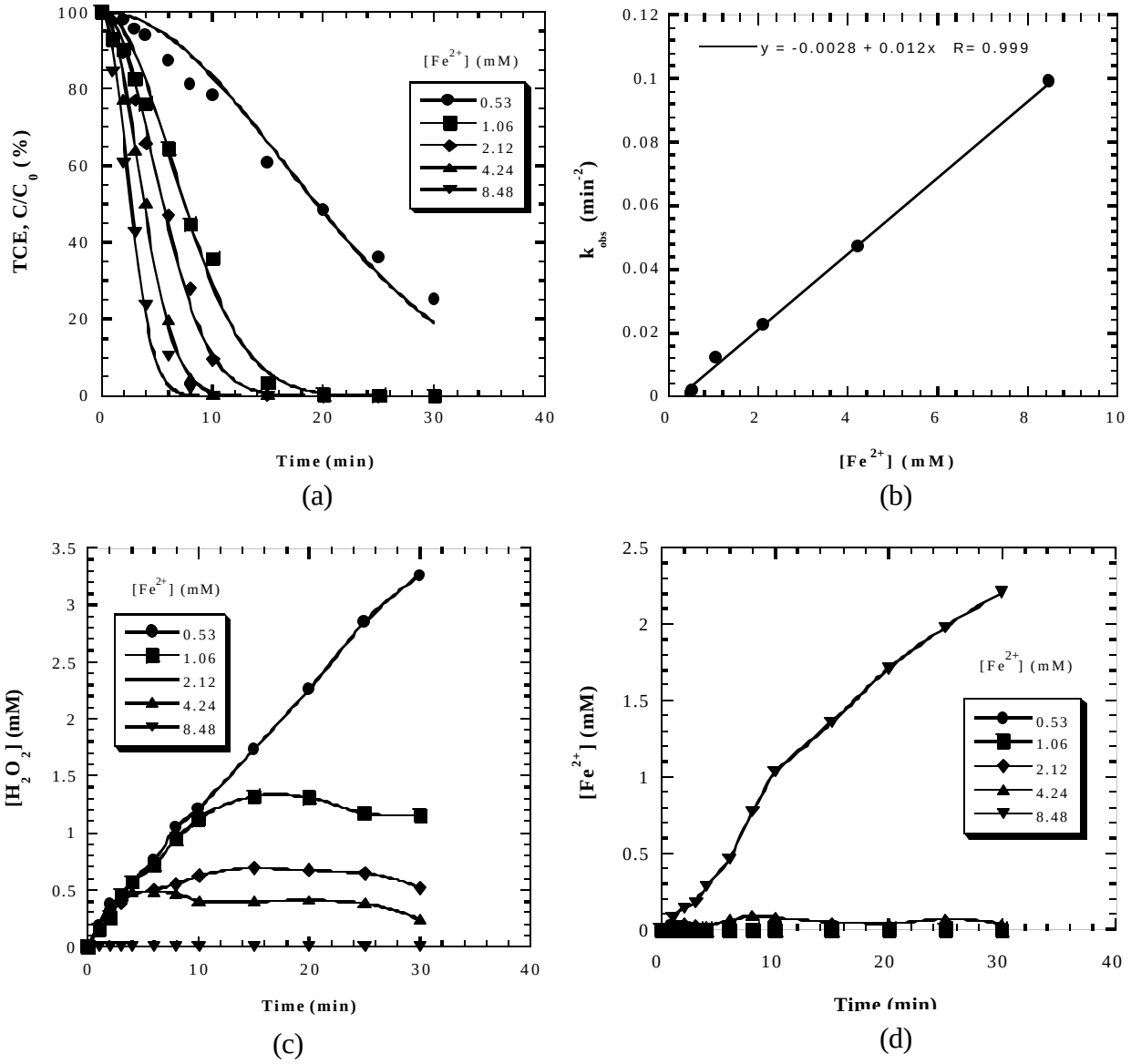

Figure 5.10. Oxidation of TCE--H_2O_2 continuous, Fe^{2+} continuous: (a) TCE, (b) k_{obs}, (c) H_2O_2, (d) Fe^{2+}. Experimental conditions: $C_{0,TCE}$ = 0.43~0.46mM, $[H_2O_2]$ = 4.24mM, $[Fe^{2+}]$ = varying, pH = 3, ionic strength = 0.05M $NaClO_4$.

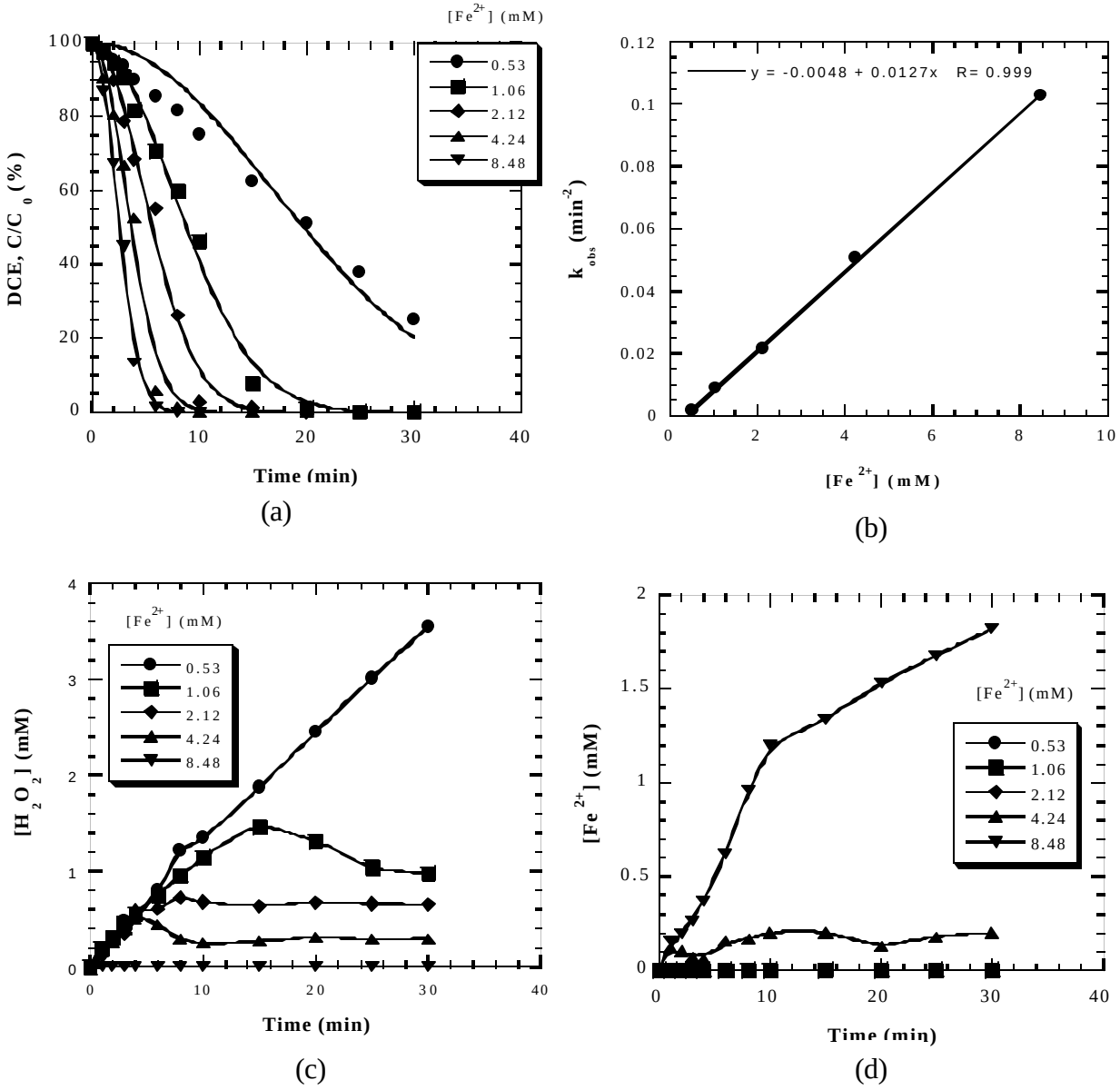

Figure 5.11. Oxidation of DCE--H_2O_2 continuous, Fe^{2+} continuous: (a) DCE, (b) k_{obs}, (c) H_2O_2, (d) Fe^{2+}. Experimental conditions: $C_{0,DCE}$ = 0.42~0.44mM, $[H_2O_2]$ = 4.24mM, $[Fe^{2+}]$ = varying, pH = 3, ionic strength = 0.05M $NaClO_4$.

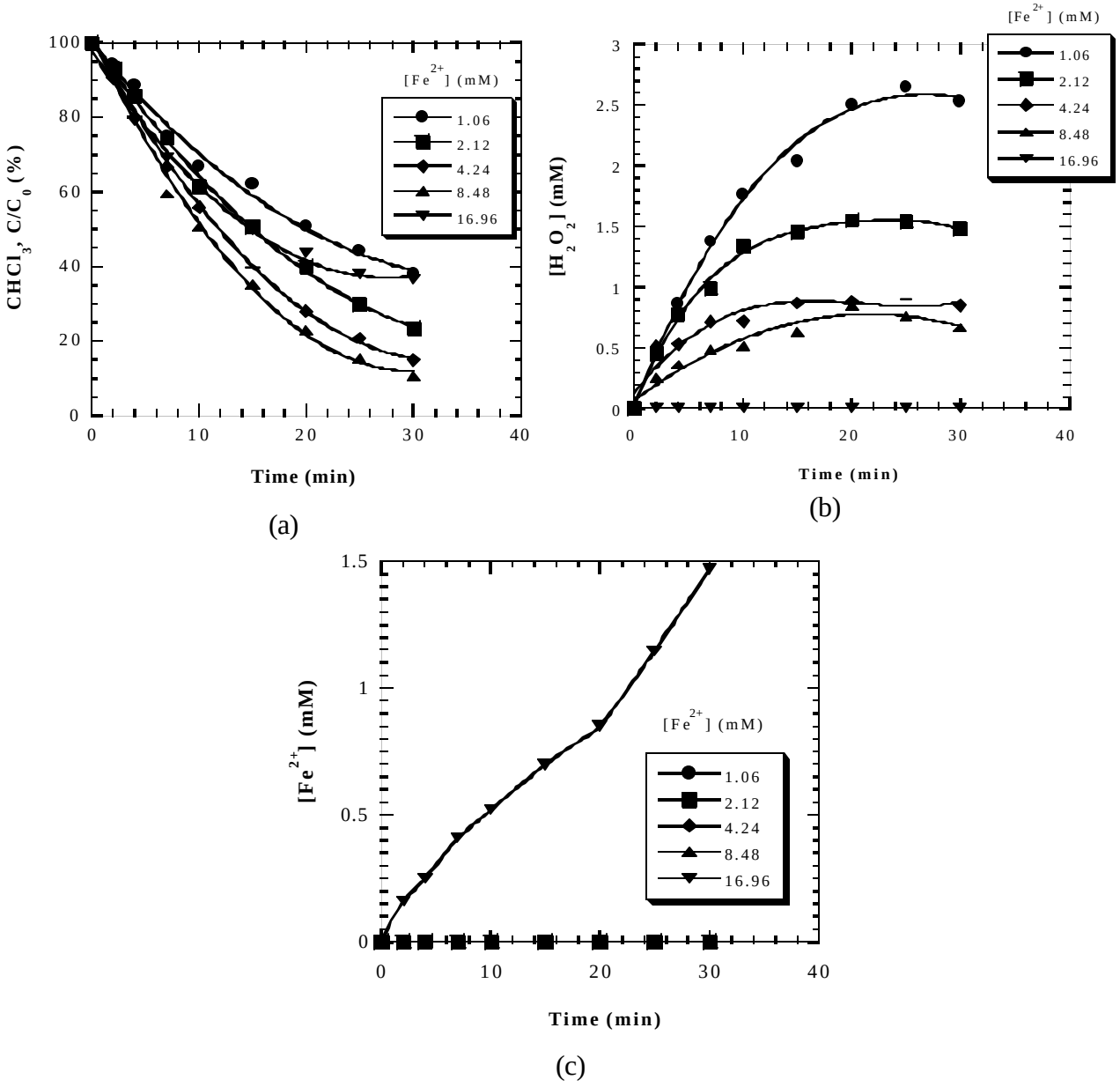

Figure 5.12. Oxidation of chloroform--H_2O_2 continuous, Fe^{2+} continuous: (a) chloroform (b) H_2O_2, (c) Fe^{2+}. Experimental conditions: $C_{0,chloroform}$ = 0.41~0.44mM, $[H_2O_2]$ = 8.48mM, $[Fe^{2+}]$ = varying, pH = 3, ionic strength = 0.05M $NaClO_4$.

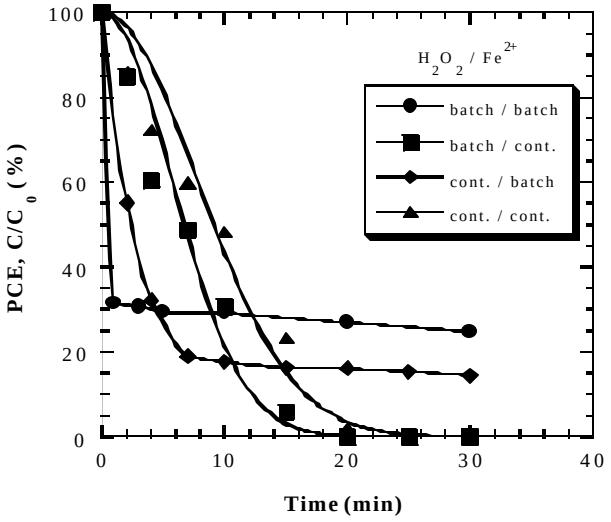

Figure 5.13. Effect of dosing mode on the oxidation of PCE. Experimental conditions: $C_{0,PCE}$ = 0.43~0.47mM, $[H_2O_2]$ = 4.24mM, $[Fe^{2+}]$ = 1.06mM, pH = 3, ionic strength = 0.05M $NaClO_4$.

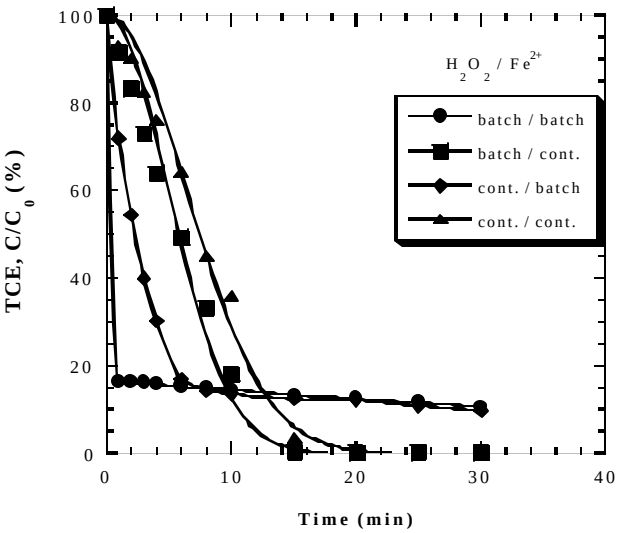

Figure 5.14. Effect of dosing mode on the oxidation of TCE. Experimental conditions: $C_{0,TCE}$ = 0.42~0.44mM, $[H_2O_2]$ = 4.24mM, $[Fe^{2+}]$ = 1.06mM, pH = 3, ionic strength = 0.05M $NaClO_4$.

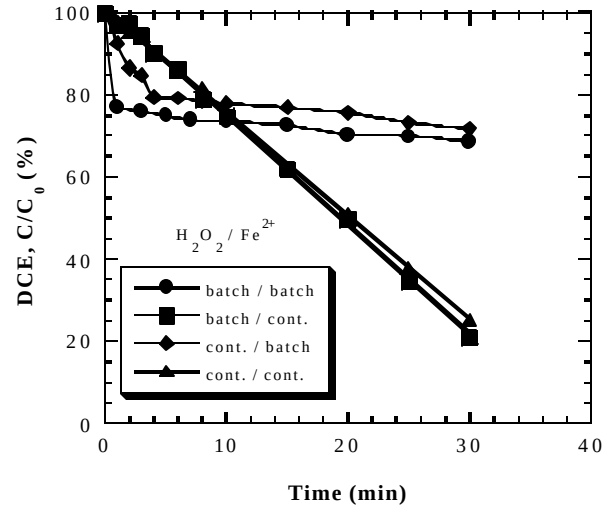

Figure 5.15. Effect of dosing mode on the oxidation of DCE. Experimental conditions: $C_{0,DCE}$ = 0.42~0.44mM, $[H_2O_2]$ = 4.24mM, $[Fe^{2+}]$ = 0.53mM, pH = 3, ionic strength = 0.05M $NaClO_4$.

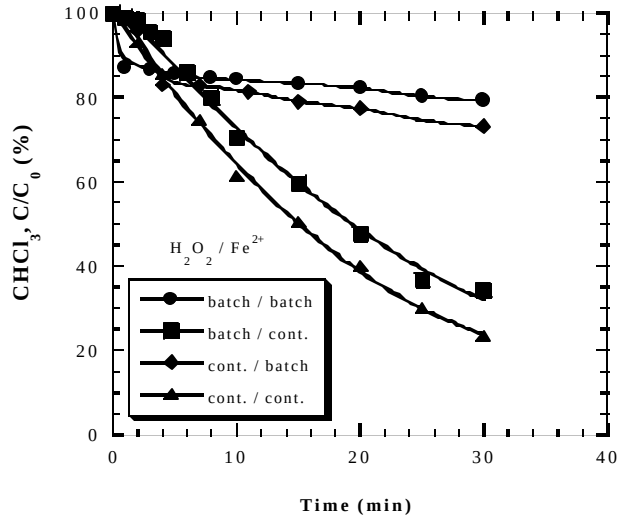

Figure 5.16. Effect of dosing mode on the oxidation of chloroform. Experimental conditions: $C_{0,chloroform}$ = 0.40~0.45mM, $[H_2O_2]$ = 8.48mM, $[Fe^{2+}]$ = 2.12mM, pH = 3, ionic strength = 0.05M $NaClO_4$.

Chen *et al.* (1990) studied the dechlorination of chloroform in aqueous solution by ultrasound in the presence of hydrogen peroxide. It is reported that the optimal H_2O_2 concentration has a molar ratio of H_2O_2 to $CHCl_3$ being 50:1. The addition of Fe^{2+} (20 mg/L) into the solution increases the removal efficiency. Under optimal conditions the removal efficiency of chloroform is 94%. In this experiment, a removal efficiency of 90% can be achieved at the molar ratio ($H_2O_2/CHCl_3$) of 20:1 by the continuous dosing mode.

(d) Comparison of Different Dosing Modes

Figures 5.13, 5.14, 5.15 and 5.16 show the effect of dosing mode on the degradation of PCE, TCE, DCE and chloroform, respectively. Results indicate that the organic removal efficiency primarily depends on the dosing mode of Fe^{2+}. It is seen that when Fe^{2+} is batch dosed, similar results are obtained for either batch or continuous dosing of H_2O_2. In addition, when Fe^{2+} is continuously dosed, batch and continuous dosing of H_2O_2 produce similar results again. This is still due to the fact that Fe^{2+} competes for hydroxyl radicals more strongly than H_2O_2. Changing the dosing mode of Fe^{2+} affects its suppression on organic degradation. For the selected chlorinated ethenes, batch H_2O_2 yields a slightly better removal efficiency than continuous H_2O_2 despite the dosing of Fe^{2+}. However, for chloroform, continuous H_2O_2 achieves a better removal efficiency than batch H_2O_2 despite the dosing of Fe^{2+}. This may be due to that the selected CAHs react more rapidly than H_2O_2 towards the hydroxyl radicals, while chloroform reacts more slowly than H_2O_2 towards the hydroxyl radicals. Therefore, the suppression of high concentration H_2O_2 on organic degradation is only signified in the oxidation of chloroform. It is generalized that the pseudo-continuous dosing mode, specifically, with batch H_2O_2 and continuous Fe^{2+} is optimal for the oxidation of the selected chlorinated ethenes, while the continuous dosing mode is optimal for the oxidation of chloroform.

5.3.1.2. Effect of pH

The effect of pH was investigated from pH 1 to 4.5 using the continuous dosing mode. Alkaline pH range was not studied since $Fe(OH)_2(s)$ will precipitate out at high pH and reduce the reaction efficiency. Figures 5.17a and b show the degradation of PCE and the decomposition of H_2O_2 as a function of reaction time at various pH values, respectively. The degradation of TCE and the decomposition of H_2O_2 at various pH values are shown in Figure 18a and b, respectively. Results indicate that the optimal pH range is 2~3 for the oxidation of PCE and TCE. Either above pH 3 or below pH 2, the reaction efficiency is reduced. The effect of pH on the organic removal by Fenton's reagent has been discussed previously in the oxidation of PAHs. Results also indicate that the decomposition rate of H_2O_2 is accelerated as the reaction proceeds. The residual PCE or TCE in the solution decreases with reaction time so that more hydroxyl radicals are consumed by H_2O_2 decomposition. In particular, the flexing point at the apex of H_2O_2 accumulation curve corresponds to the time when all PCE or TCE is removed. There is no residue Fe^{2+} detected in the solution since the molar ratio of H_2O_2 to Fe^{2+} is 4:1. All Fe^{2+} is rapidly oxidized to Fe^{3+} upon its dosing.

5.3.1.3. Degree of Dechlorination and Mineralization

The concentration of chloride ion released from selected CAHs by Fenton's reagent oxidation was measured to evaluate the degree of dechlorination. It is the chlorine

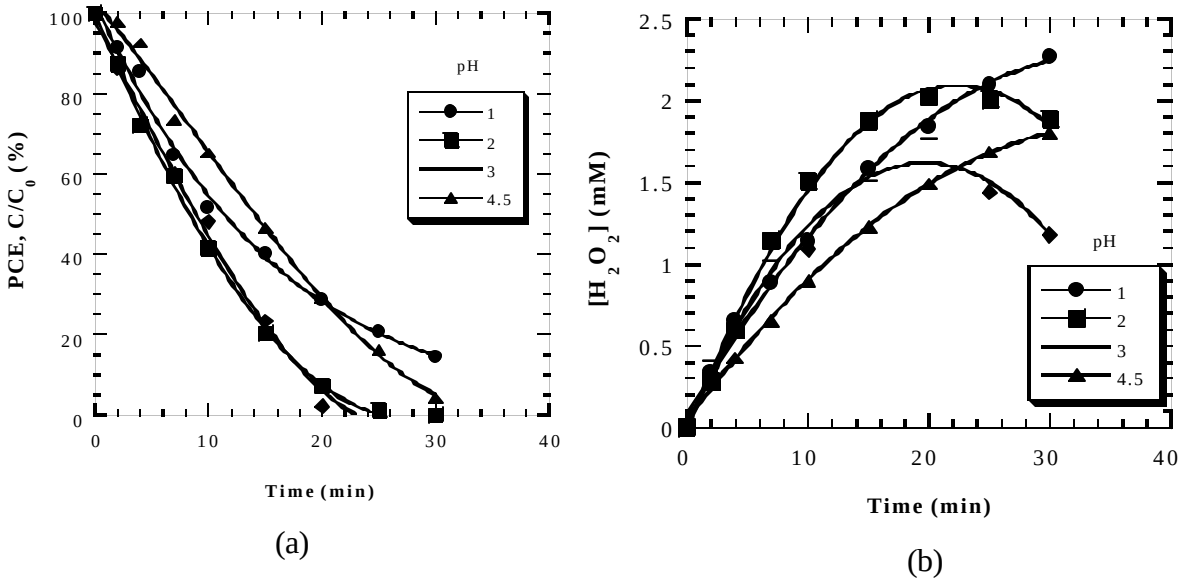

Figure 5.17. Effect of pH on the oxidation of PCE: (a) PCE, (b) H_2O_2. Experimental conditions: $C_{0,PCE}$ = 0.43~0.48mM, $[H_2O_2]$ = 4.24mM, $[Fe^{2+}]$ = 1.06mM, ionic strength = 0.05M $NaClO_4$.

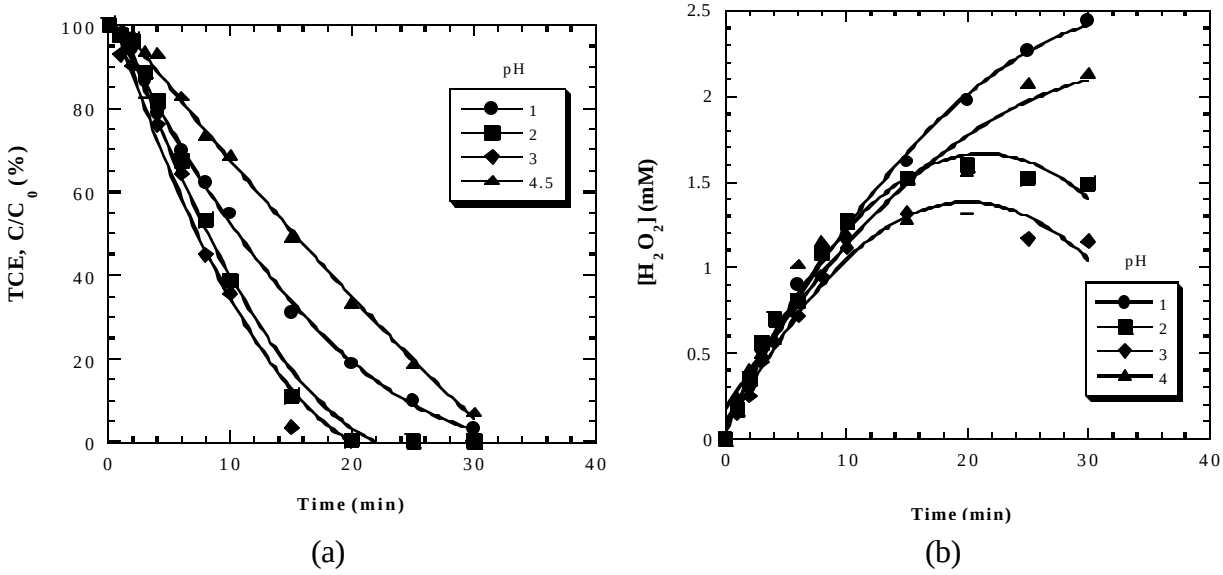

Figure 5.18. Effect of pH on the oxidation of TCE: (a) TCE, (b) H_2O_2. Experimental conditions: $C_{0,TCE}$ = 0.41~0.43mM, $[H_2O_2]$ = 4.24mM, $[Fe^{2+}]$ = 1.06mM, ionic strength = 0.05M $NaClO_4$.

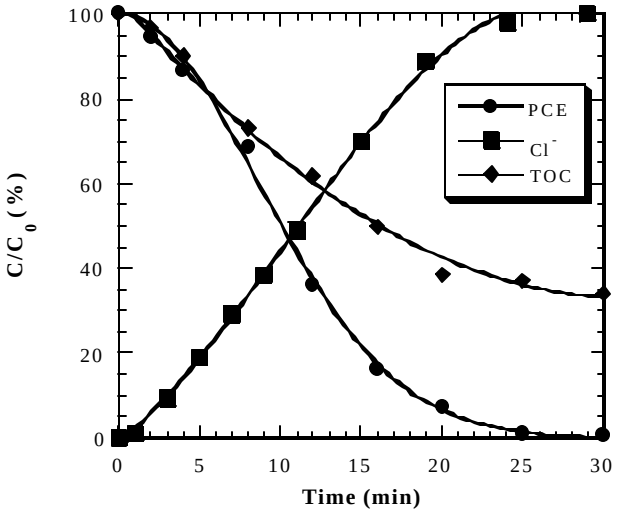

Figure 5.19. Dechlorination and mineralization of PCE. Experimental conditions: $C_{0,PCE}$ = 1.01mM, $[H_2O_2]$ = 4.24mM, $[Fe^{2+}]$ = 2.12mM, pH = 3, ionic strength = 0.05M $NaClO_4$.

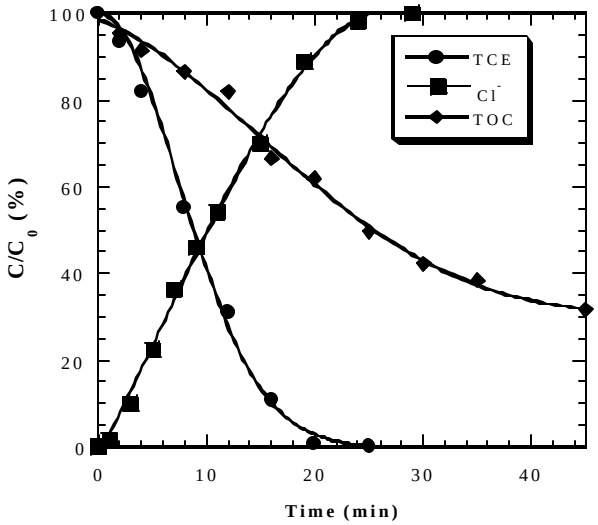

Figure 5.20. Dechlorinatyion and mineralization of TCE. Experimental conditions: $C_{0,TCE}$ = 0.89mM, $[H_2O_2]$ = 4.24mM, $[Fe^{2+}]$ =2.12mM, pH = 3, ionic strength = 0.05M $NaClO_4$.

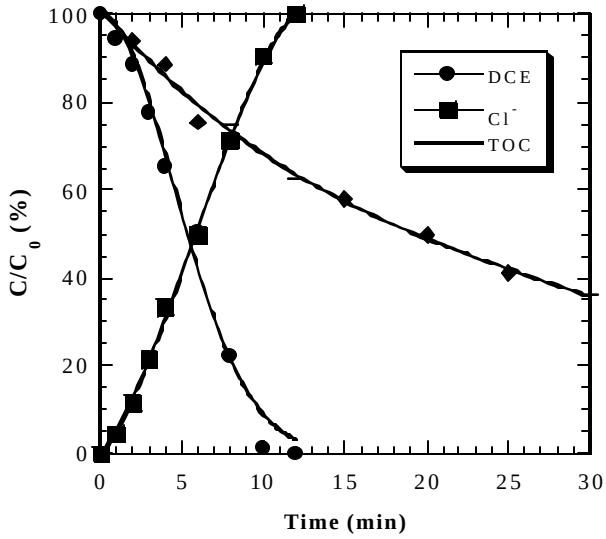

Figure 5.21. Dechlorination and mineralization of DCE. Experimental conditions: $C_{0,DCE}$ = 0.46mM $[H_2O_2]$ = 4.24mM, $[Fe^{2+}]$ = 2.12mM, pH = 3, ionic strength = 0.05M $NaClO_4$.

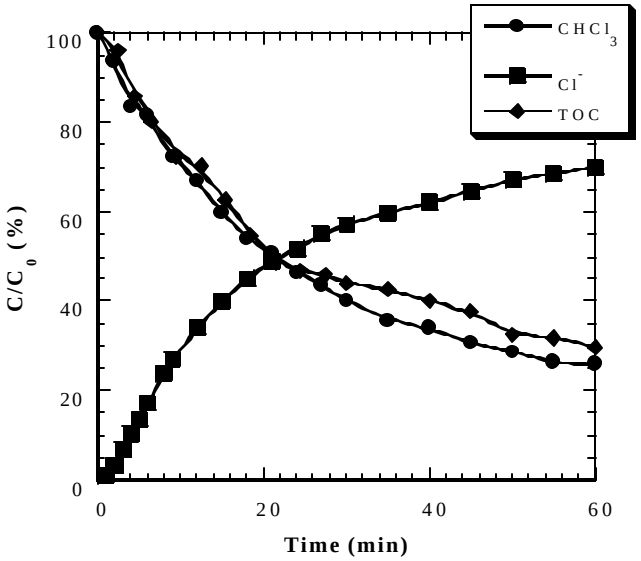

Figure 5.22. Dechlorination and mineralization of chloroform. Experimental conditions: $C_{0,chloroform}$ = 1.73mM, $[H_2O_2]$ = 8.48mM, $[Fe^{2+}]$ = 1.06mM, pH = 3, ionic strength = 0.05M $NaClO_4$.

substituents that mainly account for the toxicity of CAHs towards the environment. Therefore, the degree of dechlorination indirectly represents the degree of detoxification of the hazardous CAHs. In experiments, the initial pH of reaction solution was adjusted to 3.0. There was no pH control during the course of reaction. Since the stock solutions of H_2O_2 and Fe^{2+} were preserved in an acidic condition, the pH of reaction solution gradually dropped with the continuous dose of H_2O_2 and Fe^{2+}. The final pH was measured as around 2.1 which is still in the optimal range. Figures 5.19, 5.20 and 5.21 show the chloride release together with the organic degradation as a function of reaction time for PCE, TCE and DCE, respectively. Results clearly indicate that as the organic compound is completely removed, all chloride is effectively released from its molecular structure. A complete dechlorination can be readily achieved. However, only 70% of chlorine can be released from chloroform at the end of reaction, as shown in Figure 5.22. Correspondingly, there is still ca. 25% of chloroform remaining in the final solution.

Mineralization means a complete decomposition of organic compound to carbon dioxide and water. The total organic carbon (TOC) was measured to represent the degree of organic mineralization. Figures 5.19, 5.20 and 5.21 show the degradation of TOC with reaction time for PCE, TCE and DCE, respectively. Results indicate that the TOC degradation significantly lags behind the compound degradation due to the formation of organic intermediates. The residual TOC in the final solution is about 30-35%. In other words, the degree of mineralization reaches to about 65-70%. It is seen that the TOC can be further removed after the completion of parent compound removal if more H_2O_2 and Fe^{2+} are dosed. Since all chlorine is released from the chlorinated ethenes, the residual TOC is expected to be low molecule organic acids that are amenable to biological degradation. Figure 5.22 show the TOC degradation of chloroform. Results indicate that the residual TOC accounts for about 30%. Considering that there is 25% of chloroform remaining in the final solution, the reaction intermediates only occupy 5% of the residual TOC. It implies that less organic intermediates are formed in the oxidation of chloroform than in the oxidation of selected chlorinated ethenes. The degree of mineralization is approximately 75%.

5.3.2. Electro-Fenton Oxidation Process

In the previous chapters, we have clarified the optimal conditions for the electro-generation of H_2O_2, the electro-regeneration of Fe^{2+}, and the degradation of selected CAHs by conventional Fenton oxidation process. With the fundamental knowledge achieved, the oxidation of CAHs by the electro-Fenton oxidation process was investigated. PCE and TCE were selected as the model compounds.

The electro-Fenton process was carried out in the following procedures:

(a) produce 4 mM of H_2O_2 at $-E_c$ = 0.5 V and pH 2.5 (about 4 hours);
(b) turn off the potentiostat; spike the solution with 0.45 mM PCE and 0.45 mM TCE;
(c) batch dose 1.0 mM Fe^{2+};
(d) turn on the DC power supply to regenerate Fe^{2+} at 50 mA;
(e) determine the concentrations of PCE, TCE, H_2O_2, Fe^{2+}, Cl^- and TOC at pre-selected time intervals.

Though pH 2 is the optimal value for H_2O_2 generation, pH 2.5 is chosen to reduce acid consumption. The 50 mA current for Fe^{2+} regeneration is obtained by multiplying the dosage of Fe^{2+} and the effective cathode surface area by the slope of 8.48×10^{-3} $(A/m^2)(mg/L)^{-1}$ which is previously determined.

Figure 5.23a shows the degradation of PCE, TCE, TOC and the release of Cl^- by the electro-Fenton oxidation processes. Figure 5.23b shows the change of H_2O_2 and Fe^{2+} concentrations as a function of reaction time. For the purpose of comparison, the results from the conventional oxidation process are also presented. Results indicate that in the

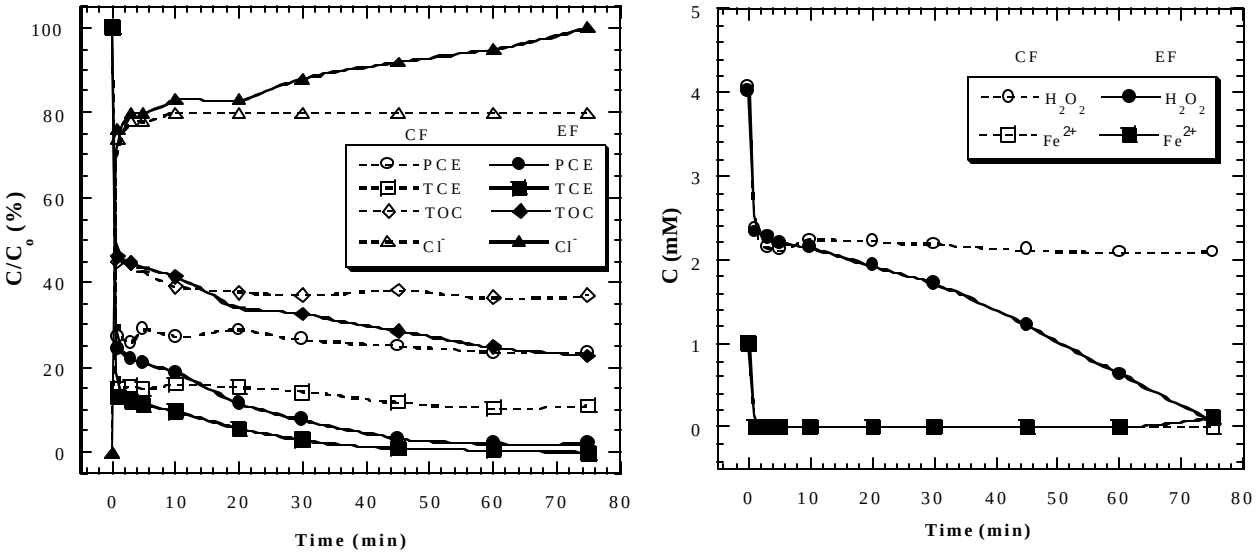

Figure 5.23. Comparison of PCE and TCE degradation by conventional Fenton and electro-Fenton oxidation processes: a. change of PCE, TCE, TOC and Cl^- concentrations; b. change of H_2O_2 and Fe^{2+} concentrations. Experimental conditions: $[H_2O_2]_0$ = 4.0 mM, $[Fe^{2+}]_0$ = 1.0 mM, $[PCE]_0$ @ 0.45 mM, $[TCE]_0$ @ 0.45mM, pH = 2.5, ionic strength = 0.05M $NaClO_4$.

conventional Fenton process, the reaction stops very quickly (within one minute) due to the immediate depletion of Fe^{2+}. Though the residual H_2O_2 concentration remains at 2.2mM (Figure 5b), no further removal of PCE. TCE and TOC is observed since Fe^{2+} can not be effectively regenerated. However, in the electro-Fenton process, PCE, TCE and TOC are continuously removed after the initial rapid reaction due to the effective regeneration of Fe^{2+} at the cathode of the electrolytic cell. The gradual decomposition of H_2O_2 demonstrates a continuous regeneration of Fe^{2+}. All PCE and TCE can be removed, with a complete dechlorination and 77% of mineralization. Though the mineralization is not complete, it is reasonably deduced that only C_1 and C_2 carboxylic acids remain in the solution as the byproducts. Since all chlorine is released, these simple carboxylic acids are less toxic to the environment than the parent compounds and these acids are readily biodegradable.

5.4. Conclusions

This study investigated the oxidation of selected chlorinated aliphatic hydrocarbons, namely, tetrachloroethylene (PCE), trichloroethylene (TCE), 1,1-dichloroethylene (DCE) and chloroform by the conventional and electrochemical Fenton processes. The conventional Fenton process was used to determine the optimal conditions for the oxidation of selected CAHs by hydroxyl radicals. The electro-Fenton process first generated H_2O_2 on site, and then degraded PCE and TCE after the external dose of Fe^{2+}. In the meantime, Fe^{2+} was continuously regenerated at the cathode once oxidized to Fe^{3+}.

The conventional Fenton oxidation process reveals that:

- PCE, TCE and DCE can be effectively removed by hydroxyl radicals, while the removal of chloroform is more difficult. The removal rate is primarily affected by the molecular structure of organic compound. The chlorinated ethenes can be readily oxidized by hydroxyl radicals due to their electron-rich double bond structure. On the contrary, chloroform is difficult to remove due to its highly chlorinated and saturated structure. The reaction rate of the chlorinated ethenes decreases as the chlorine substitution degree increases, i.e., DCE > TCE > PCE.
- The dosing mode of H_2O_2 and Fe^{2+} significantly affects the degradation of selected CAHs. Especially, the dosing mode of Fe^{2+} plays a more important role than that of H_2O_2.
- For the oxidation of PCE, TCE and DCE, the experimental data in the continuous dosing mode can be well fitted by the proposed "time-squared" kinetic model, i.e., $C = C_0 \exp(-k_{obs} t^2)$. A complete dechlorination can be readily achieved, and the minerailzation degree reaches about 65-70%. Since all chlorine is released from the molecular structure of the chlorinated ethenes, the residual TOC is only composed of low molecule (C_1 or C_2) carboxylic acids that are less toxic to the environment.
- For the oxidation of chloroform, the maximum removal efficiency achieved is about 90% by the continuous dosing mode. The dechlorination and mineralization degrees are both around 70%.
- The optimal pH range is 2~3, as exemplified by the oxidation of PCE and TCE.

The electro-Fenton oxidation process yields a higher removal efficiency of PCE and TCE since Fe^{2+} can be effectively regenerated at the cathode of the electric cell. This demonstrates that the electro-Fenton oxidation process is an effective technology for the removal of hazardous organic contaminants in aqueous solutions.

5.5. References

1. *ATSDR Biannual Report to Congress*: *October 17, 1986 ~ September 30, 1988* (1989) Agency for Toxic Substances and Disease Registry, U. S. Public Health Service: Atlanta, GA.
2. Chen J. R., Xu X. W., Lee A. S. and Yen T. F. (1990) *Environ. Technol.*, **11**: 829-836.
3. Higgins T. E. (1989) *Hazardous Waste Minimization Handbook*, Lewis Publishers: Chelsea, MI.
4. Keith L. H. and Telliard W. A. (1979) Environ. Sci. and Technol., **13**: 416-423.
5. Lou J. C. and Lee S. S. (1995) *Hazardous Waste and Hazard. Materials*, **12** (2): 185-193.
6. Macay D. and Shiu W. Y. (1981) *J. Phys. Chem. Ref. Data*, **10**: 1175.
7. Saxe J. K., Allen H. E. and Nicol G. R. (2000) *Environmental Engineering Science*, **17** (4): 233-244.
8. Schwarzenbach R. P., Gschwend P. M. and Imboden D. M. (1993) *Environmental Organic Chemistry*, John Wiley & Sons, Inc: New York, NY.
9. Tamura H., Goto K., Yotsuyanagi T. and Nagayama M. (1974) *Talanta*, **21**: 314-318.
10. Watts R. J. (1998) *Hazardous Wastes: Sources, Pathways, Receptors*, John Wiley & Sons, Inc.: New York, NY.

6. CONCLUSIONS

6.1. Electrochemical Generation of Hydrogen Peroxide from Dissolved Oxygen in Acidic Solutions

Hydrogen peroxide (H_2O_2) was electro-generated in a parallel-plate electrolyzer by reduction of dissolved oxygen (DO) in acidic solutions containing dilute supporting electrolyte. Operational parameters such as cathodic potential, oxygen purity and mass flow rate, cathode surface area, pH, temperature, and inert supporting electrolyte concentration were systematically investigated as to improve the Faradic current efficiency of H_2O_2 generation. Results indicate that significant self-decomposition of H_2O_2 only occurs at high pH (>9) and elevated temperatures (>23^{o}C). Results also indicate that the optimal conditions for H_2O_2 generation are cathodic potential of –0.5V vs. saturated calomel electrode (SCE), oxygen mass flow rate of $8.2x10^{-2}$ mol/min, and pH 2. Under the optimal conditions, the average current density and average current efficiency are 6.4 A/m^2 and 81%, respectively. However, when air is applied at the optimal flow rate of oxygen, the average current density markedly decreases to 2.1 A/m^2, while the average current efficiency slightly increases to 90%. The limiting current density is 6.4 A/m^2, which is independent of cathode geometry and surface area. H_2O_2 generation is favored at low temperatures. In the concentration range studied (0.01~0.25M), the inert supporting electrolyte ($NaClO_4$) affects the total potential drop of the electrolyzer, but does not affect the net generation rate of H_2O_2.

6.2. Electrochemical Regeneration of Fe(II) for Fenton Oxidation Processes

Fenton oxidation process, though efficient in degrading organic contaminants, is limited by the considerable amount of iron sludge generated. The present study is to regenerate Fe(II) from ferric salt or iron sludge by electrochemical method as a means to minimize the iron sludge generation. Experiments were carried out in a parallel-plate electrolyzer using both constant potential and constant current modes. Results indicate that the optimal cathodic potential for the electro-regeneration of Fe(II) is –0.1V vs. the saturated calomel electrode (SCE). In the constant potential mode, the average current density obtained at –0.1V (vs. SCE) is approximately equal to the optimal current density applied in the constant current mode, provided an identical initial Fe(III) concentration ($[Fe^{3+}]_0$). The suitable pH range is determined by the hydrolysis of Fe(III) ions, which depends on Fe(III) concentration. Above the pH domain of Fe(III) hydrolysis, $Fe(OH)_3(s)$ precipitates and significantly inhibits Fe(II) regeneration. As expected, increasing cathode surface area and solution temperature markedly accelerates Fe(II) regeneration rate. At the optimal cathodic potential (-0.1V vs. SCE), the average current density is in linear proportion to $[Fe^{3+}]_0$, showing a slope of 8.48 x 10^{-3} $(A/m^2)(mg/L)^{-1}$ (or 4.74 x 10^2 $(A/m^2)(M)^{-1}$). The average current efficiency varies with $[Fe^{3+}]_0$, i.e., 75% at $[Fe^{3+}]_0$ = 100 mg/L and 96~98% at $[Fe^{3+}]_0 \geq 500$ mg/L, during the course of electrolysis for 3 hours . Once reaching 75% of the Fe(II) regeneration capacity (ca. 4 hours of extended electrolysis), further regeneration becomes difficult due to Fe(III) mass transfer limitation. Fe(II) can also be effectively regenerated from iron sludge, though a much lower pH (usually < 1) is required for sludge dissolution. Oxygenation of Fe(II) by pure oxygen gas is kinetically negligible at pH < 4. The unit energy consumption is 2.0~3.0 kWh per kg Fe(II) regenerated.

6.3. Oxidation of Selected Polycyclic Aromatic Hydrocarbons (PAHs) by Conventional Fenton Oxidation Process

Fenton's oxidation process can effectively degrade all selected PAHs, i.e., naphthalene, fluorene, phenanthrene, fluoranthene, pyrene and anthracene. The optimal pH value is pH 3. The extent of mineralization exemplified by naphthalene is around 85%. A "time-squared" kinetic model, $C = C_0 \exp(-k_{obs} t^2)$, can be used to describe the degradation kinetics of selected PAHs in the continuous dosing mode. This model assumes that the concentration of hydroxyl radicals increases linearly with reaction time. The observed rate constant, k_{obs}, follows the order: fluorene < phenanthrene < fluoranthene ≈ pyrene < anthracene, which reverses the order of water solubility. Methanol or ethanol significantly inhibits the degradation of PAHs by competing for hydroxyl radicals.

6.4. Oxidation of Selected chlorinated Aliphatic Hydrocarbons (CAHs) by Conventional Fenton and Electro-Fenton Oxidation Processes

The oxidation of selected chlorinated aliphatic hydrocarbons, namely, tetrachloroethylene (PCE), trichloroethylene (TCE), 1,1-dichloroethylene (DCE) and chloroform was investigated by the conventional Fenton and electro-Fenton oxidation processes. The conventional Fenton process was used to determine the optimal conditions for the oxidation of selected CAHs by hydroxyl radicals. The electro-Fenton process first generated H_2O_2 on site, and then degraded PCE and TCE after the external dose of Fe^{2+}. In the meantime, Fe^{2+} was continuously regenerated at the cathode once oxidized to Fe^{3+}.

Results of the conventional Fenton oxidation process indicate that PCE, TCE and DCE can be effectively removed by hydroxyl radicals, while the removal of chloroform is more difficult. The removal rate is primarily affected by the molecular structure of organic compound. The chlorinated ethenes can be readily oxidized by hydroxyl radicals due to their electron-rich double bond structure. On the contrary, chloroform is difficult to remove due to its highly chlorinated and saturated structure. The reaction rate of the chlorinated ethenes decreases as the chlorine substitution degree increases, i.e., DCE > TCE > PCE. The dosing mode of H_2O_2 and Fe^{2+} significantly affects the degradation of selected CAHs. Especially, the dosing mode of Fe^{2+} plays a more important role than that of H_2O_2. For the oxidation of PCE, TCE and DCE, the experimental data in the continuous dosing mode can be well fitted by the proposed "time-squared" kinetic model, i.e., $C = C_0 \exp(-k_{obs} t^2)$. A complete dechlorination can be readily achieved, and the minerailzation degree reaches about 65-70%. Since all chlorine is released from the molecular structure of the chlorinated ethenes, the residual TOC is only composed of low molecule (C_1 or C_2) carboxylic acids that are less toxic to the environment. For the oxidation of chloroform, the maximum removal efficiency achieved is about 90% by the continuous dosing mode. The dechlorination and mineralization degrees are both around 70%. The optimal pH range is 2~3, as exemplified by the oxidation of PCE and TCE.

Results of the electro-Fenton oxidation process indicate that a higher removal efficiency of PCE and TCE can be achieved since Fe^{2+} is effectively regenerated at the cathode of the electric cell. This demonstrates that the electro-Fenton oxidation process is an effective technology for the removal of hazardous organic contaminants in aqueous solutions.